EXPERIMENTS ON VORTEX SHEDDING FROM STATIONARY AND OSCILLATING CABLES IN A LINEAR SHEAR FLOW

by

H. G. C. Woo*, J. E. Cermak** and
J. A. Peterka***

for

Civil Engineering Laboratory
Naval Construction Battalion Center
Port Hueneme, California 93043

Contract N68305-78-C-0055

Fluid Mechanics and Wind Engineering Program
Fluid Dynamics and Diffusion Laboratory
Department of Civil Engineering
Colorado State University
Fort Collins, Colorado 80523

CSU Project 5-32453

July 1981

*Graduate Research Assistant
**Professor-in-Charge, Fluid Mechanics
and Wind Engineering Program
***Associate Professor

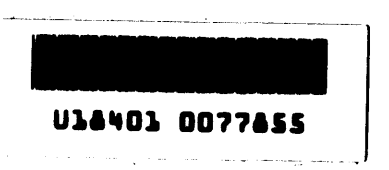

CER81-82HGCW-JEC-JAP7

TABLE OF CONTENTS

LIST OF TABLES

LIST OF FIGURES

LIST OF SYMBOLS

Symbol	Definition
A, B, n	Hot-film anemometer calibration constants
a	Amplitude of vibration
a*	$a^* = \sqrt{S/\mu}$
C_{pb}	Base pressure coefficient $C_{pb} = (P_b - P_\infty)/\frac{1}{2}\rho U^2$
D	Diameter of cylinder or cable
D'	Vortex wake width at the end of the vortex formation region
E	Mean anemometer bridge voltage
E_{rms}	Root-mean-square anemometer bridge voltage
f	The synchronized frequency
f_c	Vibration frequency of a cable
f_n	Natural frequency of vortex shedding for a stationary cylinder
f_s	Natural frequency of vortex shedding for a stationary cylinder or cable
$\tilde{f}_S$	Vortex shedding frequency for a vibrating cable
H	The distance between the inner faces of end plates (also called the effective height of the wind tunnel)
H*	Height of the wind-tunnel test section
K	Base pressure parameter $K^2 = U_b/U = 1 - C_{pb}$
L*	Length of cable
L_f	Vortex street formation length
ℓ	Half wave length of a vibrating cable
P_b	Local base pressure of a cylinder ($\theta = 180°$)
P_f	Local leading edge pressure of a cylinder ($\theta = 0°$)
P_∞	The static pressure of the undisturbed flow
Re	Reynolds number $Re = \frac{UD}{\nu}$

Symbol	Definition
Re*	Wake Reynolds number $Re^* = \frac{U_b D'}{\nu}$
r	Integers (1,2,3,...)
S_c	Strouhal frequency for a vibrating cable $S_c = \frac{f_c D}{U}$
S_s	Strouhal frequency of natural vortex shedding for a stationary cylinder or cable
$\tilde{S}_s$	Strouhal frequency of vortex shedding for a vibrating cable
St	Strouhal frequency $St = \frac{fD}{U}$
St*	Universal Strouhal number $St^* = \frac{f_s D'}{U_b}$
St**	Synchronized wake parameter $St^{**} = (\frac{f}{f_s})(1 + \frac{a}{D})St_n$
St_n	Strouhal number for natural shedding $St_n = \frac{f_n D}{U}$
s	Prestressing force in the cable
U	Mean velocity in the x or X direction
U_b	Velocity at the edge of the boundary layer at the separation point
u	Fluctuation velocity in the x or X direction
u'	Root-mean-square of fluctuation velocity in x or X direction
W	Width of the wind-tunnel test section
x,y,z	Space coordinates centered at midpoint of the downstream shear flow generator (Figure 3.6)
X,Y,Z	Space coordinates measured from stationary cylinder (or cable) center; X is in the mean flow direction, Y is in the direction perpendicular to the mean flow direction and cylinder (or cable) axis, and Z is in the axial direction of the cylinder (or cable)

Greek Symbols	Definition
β	Steepness parameter $\beta = \frac{dU}{dZ}\frac{D}{U}$
ν	Kinematic viscosity
λ	Shear parameter $\frac{U}{U_m} = 1 + \lambda(\frac{Z}{H^*} - \frac{1}{2})$
μ	Mass per unit length of the cable
ω_r	Natural circular frequency of a cable
θ	Angular position on cylinder, origin being the front stagnation point ($\theta = 0°$)
ρ	The fluid density

Subscripts	
ℓ	Local values
m	Values at mid-height of the tunnel (Z = 0)

Chapter 1

INTRODUCTION

The dynamics of slender bodies in interaction with fluid flow has received increasing attention in the last two decades. These effects include buffeting, galloping, vortex-induced motions and wake-turbulence-induced motions. In the area of vortex-induced motions, the subject of this report, it has been recognized that lock-on phenomena can significantly increase the fluid forces acting on a body oscillating at or near the natural shedding frequency. Loading due to vortex shedding from slender bodies has a number of important engineering applications including strumming of cables in water, smokestack motions, and suspension or cable-stayed bridge motions. In each of these applications, lock-on phenomena and the existence of mean velocity gradients along the body axis can importantly influence the resulting motion amplitude.

From the fluid dynamics point of view, it is important to understand the flow field about a bluff body in shear flow, before further problems associated with the coupling of the oscillations and the flow field can be adequately addressed. Due to the complicated nature of vortex-excited oscillations and their important consequences, with present knowledge theoretical attempts must rely heavily on experimental observation and measurement.

The problems associated with bluff bodies placed in a stream of fluid with uniform approach velocity have been extensively studied for many years. Attention has been concentrated primarily on the vortex shedding process, the pressure distribution and hence the drag coefficient, the effect of turbulence level in the approach flow and the

roughness of the cylinder surface, and vortex-induced oscillations. Some excellent review papers and reports have been published by Morkovin (2.1), Marris (2.2), Küchemann (2.3), Mair and Maull (2.4), Berger and Wille (2.5), Bearman (2.6), McCroskey (2.7), and recently by Sarpkaya (2.8).

Although the important features of the nonuniform flow problem have long been recognized, little investigation has been conducted. Little has been known of the basic features of the flow around a cylinder immersed in a shear flow, especially on the effect of shear on the vortex shedding process.

In this study, the characteristcs of vortex shedding from large L/D rigid cylinders was studied to understand more about the nature of vortex shedding in the presence of a strong velocity shear along the cylinder axis. In addition, the characterstics of vortex shedding from a vibrated cable in a velocity gradient were studied. In both cases, the primary methods for investigation included high-speed flow visualization motion pictures and measurement of shedding frequency at many points along the cylinder or cable axis. Some base pressure and vortex formation length measurements were obtained for comparison with the uniform flow case.

Chapter 2

SUMMARY OF RELATED INVESTIGATIONS

2.1 Cylinders in Shear Flows

The first exploratory investigation to study the effects of shear flow past a circular cylinder was probably the work of Masch and Moore (2.9). A general experimental investigation of the variation of drag coefficient on a circular cylinder in water flows with roughly linear velocity distributions was made. The shear flow was generated with a variable shutter gate. No information about the turbulence level of the incidence flow was reported. The important concept of velocity gradient parameter $(\frac{\Delta U}{\Delta Z}\ \frac{D}{U})$ in this type of study was considered. The flow visualization study showed the presence of strong secondary flow effect in the wake due to the velocity gradient. The three-dimensional aspects of the flow were described qualitatively by the authors. Due to the effect of the longitudinal velocity gradient, a variation of up to 40 percent from the uniform flow values of the drag coefficient was reported. In this study, the steepness factor $(\beta = \frac{dU}{dZ}\ \frac{D}{U})$ ran from 0.058 to 0.117 and the H to D ratio was only 9.6. It is quite apparent that the whole flow field along the test cylinder was dominated by the end effects.

Chen and Mangione (2.10) reported the results of their experiment on vortex shedding from two steel circular cylinders in a linear shear flow in 1969. They found that within the accuracy of their measurement (approximately ±10 percent scatter in the data attributed to the relatively high turbulence level, which was about 4 percent, in the shear flow), the local Strouhal number was constant along the length of the cylinder. Based on this result, they suggested that a good

estimate of the shedding frequency behind a circular cylinder in a shear flow might be obtained by using the correlation of Roshko

$$S_t \equiv f \frac{D}{U} = 0.212 - (\frac{4.5}{Re})$$

with the local approaching velocity as the characteristic velocity in both the Strouhal and Reynolds number. In his Ph.D. thesis on shear flows past circular cylinders, Starr (2.11) proposed three possible modes of vortex shedding:

Mode 1: A zone or zones of regular vortex shedding, with a different frequency in each zone. These zones could overlap.

Mode 2: Vortex shedding with unstable frequency: a burst at one frequency, followed by a burst at another.

Mode 3: Completely a-periodic vortex shedding.

Starr concluded that the steepness of the velocity gradient relative to the slenderness ratio of the cylinder and the value of the local Reynolds number were probably the significant factors which determined which mode was developed.

Starr's studies were mainly concerned with identifying design guidelines for use in practical engineering problems. He gave no detailed results for the vortex shedding frequency and simply stated that "synchronized shedding" occurred over part of the cylinder. However Starr (2.11) and Shaw and Starr (2.12) did emphasize the importance of characterizing the nonuniform flow in terms of a "steepness factor" for the incident velocity gradient.

Maull and Young (2.13,2.14) first verified that the vortex shedding from a bluff body in shear flow broke down into a number of coherent spanwise cells in each of which the frequency was constant. The model

used was D-shaped with a semi-elliptic nose, followed by a parallel-sided section. With only one value of upstream shear, the vortex shedding from the bluff body (by examining the power spectral density of the velocity fluctuations) and the base pressure coefficient were measured. They explained the presence of four distinct cells by stating "that the coherence of the shed vortices requires a constant frequency over certain lengths." They theorized that the division between the cells was marked by a longitudinal vortex in the stream direction and that these longitudinal vortices came from the rolling up of the initial vorticity in the shear flow. This was supported by evidence from experiments that the presence of a longitudinal vortex in an otherwise uniform flow could cause a jump in vortex shedding frequency along the span of the body with a consequent variation in the base-pressure coefficient.

A study on the effects of turbulent shear flow on the critical Reynolds number of a circular cylinder was reported by Davies (2.15). He approached the problem by analyzing the variation of base pressure coefficient C_{pb} for a highly sheared ($\lambda = 0.8$, $\beta = 0.18$), turbulent (4 percent to 7 percent) flow about a circular cylinder of low aspect ratio (H/D = 6). The flow around the cylinder was found to be strongly Reynolds number dependent in the region around $Re = 10^5$. The high turbulence intensity of the shear flow reduced the onset of the critical number by a factor of ten. It is quite clear that such effects should be considered in the design of experimental facilities intended to produce shear flows for study of vortex shedding. The strong tendency for the vortex shedding to develop into spanwise cells was also mentioned by the author.

The first major effort to study the vortex wakes of bluff cylinders in shear flow was perhaps the work of Mair and Stansby (2.16). A series of measurements of vortex-shedding frequency and base pressure were made with circular cylinders and D-shaped models of different sizes and aspect ratio spanning the wind tunnel with their axes normal to the vorticity vector. The vortex wake measurements showed a number of coherent cells across the span of the test models. They attributed the lack of a measured cellular shedding pattern in some of their results to fluctuations in cell boundaries. Since the data were obtained based on successive time-averaged spectra, the results showed a continuous change in peak frequency. The influences of the boundaries at both ends of the test body on the whole flow field along the span were carefully demonstrated and discussed. They determined an optimum dimension for an end plate to minimize interference with coherent vortex shedding behind the test model. With some forms of end plate, the position of the cell boundaries fluctuated with time.

Rooney and Peltzer (2.17) recently reported their experimental results on vortex shedding and surface pressure measurements from both smooth and rough cylinders in shear flows. A series of tests were conducted to determine the length over which highly correlated vortex shedding occurred as a function of upstream shear and cylinder surface roughness. The minimum shear level producing cellular shedding patterns was also investigated. The experiments were conducted with a cylinder of aspect ratio H/D = 16 at Reynolds numbers in the range of 1.5×10^5 to 3×10^5. Based on the results of their weakest steepness factor ($\beta = 0.007$) for which an incipient cellular pattern of vortex shedding was observed, they concluded that any linear shear, however slight, in

the approaching flow would trigger a cellular vortex-shedding pattern. They also found that a general trend toward decreasing cell length with increasing shear parameter, although the results were partially obscured due to the effect of unsteady cell boundaries. The average cell length for a rough cylinder was greater than for a smooth cylinder was also reported.

2.2 Cables in Shear Flows

To the best knowledge of the present authors, no result which is directly applicable to large aspect ratio flexible cable in shear flow is presently available. The closest to this type of study is probably the work of Stansby (2.18). In 1976, Stansby published some of his studies concerning the vortex shedding characteristics of circular cylinders both in uniform and linear shear flow (at Re less than 10^4). The cylinder was forced to vibrate at various frequencies and amplitudes. The bounds of the locking-on between the cylinder vibration and the vortex shedding were measured for both the uniform and shear flow cases. He found that the "lock-on" phenomenon was somewhat similar for a circular cylinder in both the uniform and shear flow situations. Stansby further showed that uniform flow results were applicable to the problem of vortex shedding lock-on in shear flows. He developed an approximate method for estimating the spanwise extent over which the vortex shedding locked into the oscillation of a cylinder in a shear flow. For a vibrating cable, the vortex wake structure is complicated due to the variation of the vibration amplitude along the span of the body. In view of the findings by Stansby (2.18) relating lock-on phenomena between oscillating cylinders in uniform and shear flows, existing information concerning vibrating cylinders and cables in

uniform flow was examined. Ferguson and Parkinson (2.19) presented measurements of fluctuating pressures on the surface and in the wake of a circular cylinder in vortex-excited oscillation at subcritical Reynolds numbers. Throughout the synchronization range (where cylinder was forced to oscillate with amplitudes greater than 10 percent of the cylinder diameter), an increase in correlation length of vortex shedding along the cylinder was reported. Toebes (2.20) examined the correlation of velocity fluctuation and base pressure for a forced vibrating cylinder at Reynolds numbers of 10^4 to 10^5. Increasing axial flow correlation due to cylinder oscillation was also reported. Koopman (2.21) demonstrated that lock-on encompasses a range of ±25~30 percent of the natural vortex shedding frequency. Above the threshold amplitude (0.1 D), the transverse vibration of a cylinder at the natural frequency of its wake induces increasing correlation of vortex shedding spanwise along the cylinder. This results in an increase of the vortex strength and a greater instantaneous lift force. The geometry of the vortex wake is altered appreciably due to the transverse vibration of the cylinder which in general causes a reduction in the lateral spacing of the vortex wake.

The vortex street wake of vibrating cylinders has also been studied by Griffin (2.22), Griffin (2.23), Griffin and Votaw (2.24), and Griffin and Ramberg (2.25). They investigated the dependence of the formation length and wake structure on the amplitude and frequency of vibration. The vortex wake formation length is shown to be an appropriate scaling length for the vortex wake of an oscillating body. The formation region length is also shown to be dependent on a synchronized wake parameter,

St^{**} which is defined as

$$St^{**} = \left(\frac{f}{f_s}\right)\left(1 + \frac{a}{D}\right) St_n$$

where $St_n = \left(\frac{f_n D}{U}\right)$ is the Strouhal number for natural shedding

f = the synchronized frequency

f_s = natural frequency of vortex shedding for a stationary cylinder

a = amplitude of vibration

More recently Ramberg and Griffin (2.26), Griffin (2.27), and Ramberg and Griffin (2.28) have reported studies on the vortex wake behind a forced vibrating cable in uniform flow. The von Kármán vortex streets formed behind vibrating, flexible cables were studied using a hot-wire anemometer and flow visualization. The experiments were concentrated in the flow region where the vortex shedding and vibration of the cable synchronize to control the wake formation.

Although the wake is inherently three-dimensional for a vibrating cable due to the variation of amplitude of vibration, similarities are found to exist with the wakes of rigid cylinders. The bounds of the lock-on regime for oscillating cables are found to compare well with vibrating cylinder results. The near-wake properties such as the formation region length, etc., at any point along a vibrating cable are similar to the wake behind a cylinder oscillating under the same conditions of Reynolds number, frequency and amplitude. They have also shown that the synchronized wake parameter St^{**} is also a useful parameter in characterizing vortex-excited cable vibrations. Furthermore, the downstream longitudinal vortex spacing and induced street velocity are also found to compare well with the results of vibrating

cylinders. Ramberg and Griffin (2.29) further identify three distinct spanwise regions according to wake structure of a synchronized oscillating cable. Near the cable nodal points, the flow is found to resemble that of a stationary cable. Adjacent to the node is a transition regime which extends up to the synchronized region about the cable antinode. Each regime is characterized by its spectral content, spanwise correlation coefficient, and local vortex street geometry. The vortex strength and drag force on the oscillating cable are found to be as much as 65 percent larger for lock-in conditions than in the stationary case.

Chapter 3

3.1 Wind Tunnel

All the experiments were conducted in an open-return type wind tunnel in the Fluid Dynamics and Diffusion Laboratory at Colorado State University (Figure 3.1). The wind tunnel has a width of 24 in., a height of 24 in. and a test-section length of 96 in. The tunnel is driven by a 36 in. diameter commercial fan which is directly connected to a 15 HP induction motor which runs at a constant speed of 1150 rpm. Variation of the wind speed is obtained by remotely adjusting the pitch of the fan blades.

The walls of the wind tunnel were rebuilt with 1/4 in. and 1/2 in. thick transparent Plexiglas. Vibration caused by the wind-tunnel fan was also effectively eliminated by installing a vibration-resistant connection between the fan and the test section.

3.2 Generation of Uniform Shear Flow in a Wind Tunnel

At the early stages of this study, a number of methods had been tried for generating a strong linear shear flow with low-turbulence level in the wind tunnel. Methods such as a grid of rods, suggested by Owen and Zienkiewicz (3.1), can be used to generate relatively strong shear flows, but the disadvantage is a high turbulence intensity.

By modifying a theoretical work of Elder (3.2), Maull (3.3) was able to generate a shear flow of moderate strength with fairly low turbulence level. The shear flow was generated by means of a curved screen gauze. This method was later adopted by Maull and Young (2.13,2.14), Mair and Stansby (2.16), and Stansby (2.18) in their studies. Our initial efforts with this technique showed that, to

prevent high turbulence intensities associated with incipient separation near the low-speed boundary, the lowest velocities in the linear shear flow zone could not be brought below about 65-70 percent of the test section average velocity. For the experiments desired for this study, minimum velocities within the linear shear region had to be 20-30 percent of the test section mean velocity. In addition, a turbulence intensity much below one percent was desired.

For the present work, a pair of curved sheets of cloth screens with nonhomogeneous properties were used to generate the linear shear flow. The cloth-screen gages have a shape described by Figure 3.2 which was experimentally modified from that of Maull (3.3). Figure 3.3 shows a magnified view of the cloth used for the screen. It is approximately 75 strands per inch. Each strand is about 0.006 in. in diameter. The cloth porosity β^* is about 0.31. The nonhomogeneous property of each screen was obtained by selectively spraying the screens with an acrylic spray to decrease the screen porosity (and therefore increasing the resistance coefficient). This was performed by means of trial and error.

The pair of screen gauzes were placed parallel to each other near the upstream end of the working section of the wind tunnel. The distance between the gauzes was 3.0 in. (Figures 3.4 and 3.5).

Vertical and horizontal profiles of mean velocity and longitudinal turbulence intensity without the experimental cylinders or cables in position were taken to determine the spatial uniformity of the linear shear flow. Figure 3.6 shows the coordinate system and the measurement locations. Vertical profiles of mean velocity at three longitudinal locations are shown in Figure 3.7. Note that the linear shear extends

to the low velocity boundary without evidence of separation. The wall boundary-layer thicknesses at bottom and ceiling of the tunnel at these locations are less than 0.5 in.

Vertical profiles of turbulence intensity are shown in Figure 3.8. Turbulence intensities $(\sqrt{u'/U})$ 4.0 in. above the floor and 1.0 in. below the ceiling are all less than 0.4 percent. Horizontal profiles of mean velocity and turbulence intensity are shown in Figures 3.9 to 3.11. Lateral uniformity of velocity is considered acceptable. The vertical distribution of the streamwise velocity component and the uniformity in the lateral direction did not change significantly with the range of wind speed adopted in this study.

The streamlines were deflected upwards by the curved gauze. Flow visualization showed that they were parallel at the cylinder test location at $x/H^{*} = 1.94$. Careful survey of the static pressure field at the test section location was also performed. The results indicated that the static pressure was essentially constant in all directions.

It was discovered that the characteristics of the linear shear flow were very sensitive to the treatment of the screens, such as dust accumulation on the screens. Therefore it was necessary to regularly clean the screens with air jets supplied by an air compressor.

The effects of the tunnel wall boundary layer on test results have long been noticed. Stansby (3.4) has shown that boundary layers on the tunnel wall have considerable effect on base pressure measurement for a circular cylinder. He continuously pointed out that most of the published pressure distributions for circular cylinders were obtained without end plates and this probably explains their inconsistency.

The common practice of eliminating this so called "end effects" is by using end plates--by making the boundary layers at both junctions of the cylinder as thin as possible, therefore a test condition which is very nearly two-dimensional may be achieved.

Based on the results of the wind-tunnel vertical velocity profiles, it was estimated that the boundary layer thickness at the ceiling and bottom of the wind tunnel at the test section ($x/H^* = 1.94$ from the center of the curved gauze) did not exceed 0.5 in. The end plates were installed 4 in. from the floor (where the turbulence level exceeded 0.4 percent) and 2 in. from the ceiling.

The dimensions of the rectangular end plates were based on the results of Stansby. The width was 10.5 in., the length was 11.25 in., and the thickness was 0.125 in.. The distance, $H^* = 18.0$ in., between the inner faces of the end plates was regarded as being the effective height of the wind tunnel.

3.3 Velocity, Pressure, and Wake Frequency Measurements

Measurements of the longitudinal velocities were made with a Thermo-System, Inc., Model 1050 anemometer unit with a TSI-10 quartz-coated cylindrical hot-film probe. This sensor has a sensing length of 0.02 in. and is 0.001 in. in diameter. The anemometer unit was operated without filtering or linearization.

The probe was calibrated before each experiment. A Thermo-Systems, Inc., Model 1125 calibrator and an MKS Baratron pressure meter were used for the calibration. Calibration data were fit to a variable exponent form of King's law

$$E^2 = A + BU^n$$

using a least-square curve fitting program. From this equation it follows, to the first order approximation, that the local turbulence intensity can be given by

$$\frac{\sqrt{u^2}}{U} = \frac{2E\ E_{rms}}{Bn\ U^{n-1}}$$

Mean values of the anemometer bridge output were obtained using a 60-second time constant circuit, TSI Model 1047. Root-mean-square voltages were obtained with a DISA Model 55D35 rms voltmeter.

A method suggested by Bearman (3.5) was used to correct the error due to the temperature difference between calibration and measurements.

The traverse mechanism supporting the hot-film probe was manufactured by Uni Slide Assemblies. The traverse controls permit positioning of a probe mount to within 0.02 in.

The cylinder surface pressure measurements were performed with 3/64-in. diameter pressure taps on the surface of the rigid test cylinder. No pressure measurement was attempted on the oscillating cables. Vinyl tubes were used to connect the pressure tap to an MKS Baratron (Type 77) pressure measuring head. The DC outputs from the Baratron were then recorded on a XY recorder (positions versus pressure) for later analysis.

Measurements of vortex shedding frequencies were carried out with a General Radio Company Type 1564-A sound and vibration analyzer. The wave analyzer has a range from 2.5 cps to 25 kcps in four decade ranges. For all the frequency measurements of this study, the analyzer filter was set at 1/10 octave bandwidth (at least 40 db attenuation at one-half and twice the selected frequency, the ultimate attenuation is greater than 70 db). Because the output from this analyzer is a rectified mean

rather than a true rms of the output from the bandpass filter, the analyzer output can be used to accurately select frequencies containing high energy, but should not be considered as a true spectrum.

The wave analyzer outputs were recorded continuously on chart paper. The measurements of vortex shedding frequency were obtained by placing a hot-film probe at a position outside the turbulent wake but in a position such that it would record the velocity fluctuations due to the vortex shedding. This position is generally at a distance of about 1.0 D downstream of the base of the test cylinder (or cable) and about 2.0 D away from the centerline as suggested by Mair and Stansby (2.16).

3.4 Flow Visualization Studies

Motion pictures served as an excellent method for understanding the kinematics of the flow using smoke as an indicator. A 16 mm high-speed motion picture camera manufactured by Red Lake Labs, Inc., was used for the flow visualization study. With Kodak ASA 400 color film (100 ft in length for each reel), the motion pictures were taken at either 500 or 1000 frames per second.

The smoke was released from holes 3/64-in. in diameter on the surface of the experimental body. Special care was taken so that the relative velocity between the jet from these small holes and the flow over the cylinder was minimized. Smoke was generated using a simple apparatus which forced the burning of low-tar, low-nicotine tobacco with compressed air. The smoke was filtered and cooled before it reached the test section.

In addition to four 1000 Watt tungsten photo lamps, a new high intensity lamp was used to help visualize flow patterns in this study. The lamp, developed by General Electric, is called a MARC-350 and is a

metallized arc lamp of very small size enclosed in a heavy quartz envelope. A regulated power supply applies an 8-kilovolt starting potential and then automatically drops to a steady DC running voltage. Color temperature produced by this system is of the order of 5000°K and lamp surface temperature is about 1000°C. A dichroic reflector, virtually transparent to infrared, is used to direct the visible light. Because of the high temperatures involved and the high brightness of the source, air cooling of both the bulb and its reflector is required.

3.5 Test Cylinders, Cables, and Support Mechanism

Hard brass tubes of five different diameters (0.25 in., 0.50 in., 0.75 in., 1.0 in., and 1.50 in.) were used as the rigid test cylinders in this study. The surfaces of the hard brass tubes were all carefully sanded with fine steel wool and were considered as very smooth. Because the flow was not expected to be a significant function of surface roughness at the Reynolds numbers used for this test, a quantitative evaluation of cylinder roughness was not made.

Three O-ring rubber cords were used as the cables for the oscillating cable tests. The surface of the rubber cord was fairly smooth and the diameter was reasonably uniform.

Since the natural frequency of a cable is a function of the following: 1) length of the cable (L*), 2) prestressing force in the cable(s), 3) mass per unit length of the cable (μ), and 4) the mode of vibration, the equation for the frequency of an ideal cable in which the stiffness of the cable has been ignored is

$$w_r = \frac{r-0.5}{L^*} \pi a^* \quad (r = 1,2,3,\ldots)$$

where $a^* = \sqrt{s/\mu}$

The stiffness of the O-ring rubber cord prevented use of diameters larger than 0.50 in. when a half wavelength of 10 in. was used. The reason for choosing 10 in. as the half wavelength with antinode at the center of the wind-tunnel test section was based on the earlier vortex wake measurements using rigid brass cylinders. In this region, the vortex shedding process was reasonably free from end effects.

In order to vibrate the cables at the required frequencies, the prestress required was often sufficiently high to induce rupture or continuous creep. In addition, the rubber cord under high tension tended to "fatigue" easily, therefore precautions were taken during the test to assure the vibrating mode, vibrating frequency, etc., were unchanged.

The cylinders and cables all spanned the working section of the wind tunnel vertically with the velocity gradient along the cylinder axis.

The experimental setup is shown in Figure 3.12 for the vibrating cable studies. One end of the cable is connected to a turnbuckle for adjustment of the cable stress. The other end of the cable is connected to a strain gauze. The output of the strain gauze is directly displayed on the oscilloscope and under frequent observation.

A type AV-50 vibrator of AGAC-Derritron, Inc., was used to vibrate the cable with the selected frequency. The vibrator has a continuous frequency range from 5 Hz to 20,000 Hz with a maximum excursion of 0.50 in. (±0.25 in.). Since the vibrator uses a lightweight moving table, cast in magnesium alloy with an extremely stiff and robust suspension assembly, it provides a very smooth and useful frequency response.

The vibrator is driven by a 300-Watt solid state amplifier (Model N-300, manufactured by the same company), which is specially designed to drive electromechanical vibrators, and includes a sine wave oscillator suitable for this application.

For the rigid-cylinder tests, the cylinders were directly supported by the heavy steel frame which was set directly on the ground and had no direct contact with the wind tunnel.

Rubber diaphragms were used to prevent the air leaking for both the cylinders and cables at the junctions with the wind tunnel.

3.6 The Range of Experiments

Table 4.1.1 shows the test scheme of base pressure measurements and the related parameters.

Table 4.1.2 shows the test scheme of wake characteristics measurements at midsection of the cylinders.

Table 4.1.3 describes the rigid cylinders and their associated parameters which were tested for vortex shedding characteristics along the span. These data points are also shown on a dimensional plot of the available parameter domain in Figure 4.1.21a.

A list of stationary cylinders and their related parameters for flow visualization studies is shown in Table 4.1.4.

For vibrating-cable studies the range of experiments is shown in Table 4.2.1 and Figure 4.2.1. For flow visualization studies of vibrating cables, the tested cables and their related parameters are shown in Table 4.2.3.

The Cartesian coordinate system x.y.z. which will be used in the following discussion of the test results is shown in Figure 3.12. The origin of the coordinate is located at the central axis of the test cylinders or cables when they are in neutral position.

Chapter 4

RESULTS AND DISCUSSION

4.1 Stationary Circular Cylinders in Linear Shear Flows

4.1.1 Surface Pressure Measurements and End Effects

As has been discussed by Masch and Moore (2.9) and Mair and Stansby (2.16), based on a simple dimensional analysis, the local base pressure coefficient, $C_{pb\ell}$ (or local drag coefficient and Strouhal number) for a circular cylinder spanned vertically in a shear flow can be formulated as

$$C_{pb\ell} = F_1(Re_\ell, \beta_\ell, Z/D) \tag{4.1}$$

where $Re_\ell = \frac{U_Z D}{\nu}$ and $\beta_\ell = \frac{dU}{dZ}\frac{D}{U_Z}$

For a moderate shear flow, the variations of Re and β with Z are small and can be neglected. Re and β may be replaced by a mean value, i.e., the value at the middle span

$$Re_m = \frac{U_m D}{\nu} \quad \text{and} \quad \beta_m = \frac{dU}{dZ}\frac{D}{U_m}$$

then we can write

$$C_{pb\ell} = F_2(Re_m, \beta_m) \tag{4.2}$$

This formula has been generally adopted to correlate the experimental results. For a range of Reynolds numbers between 10^4 to 10^5 (in the sub-critical range), the base pressure coefficient is practically constant, (4.2) has even been simplified as (Masch and Moore (2.9))

$$C_{pb\ell} = F_3(\beta_m) \tag{4.3}$$

For a circular cylinder spanned vertically in a shear flow, along the front stagnation line, the stagnation pressure is higher at the top

end of the cylinder than that at the bottom end. This is simply because the approaching velocity is higher at the top than at the bottom. A downward secondary flow following the front stagnation line is induced due to this pressure gradient. On the lee side of the cylinder, the induced secondary flow is in the opposite direction. At the higher velocity end, due to the higher entrainment rate of the separating free shear layer, the base pressure is much lower than that at the lower velocity end. Therefore, the secondary flow runs upward. These secondary flows in the neighborhood of a circular cylinder in an approach stream which had shear had been demonstrated previously by Masch et al. (2.9).

For the present study, based on the flow visualization results of a selected case investigation, this upward mean flow velocity of the secondary flow in the base region has been found to be as high as 0.43 to 0.44 U_m. The cylinder used has a diameter D = 0.48 in. with $\beta_m = 0.035$ and $Re_m = 960$ ($U_m = 4.60$ ft/sec). This result was obtained by tracing an individual eddy frame after frame, from the movies taken with a high-speed movie camera (at 500 frames per second). Consequently, the velocity was calculated based on the distance that particular eddy had traveled and the time it had taken. The eddies are not traveling at constant speed, instead, their velocity slightly fluctuates. This is apparently caused by the fluctuation of pressure due to vortex shedding. This mean flow velocity was obtained by the average of more than ten values.

Two prints from separated frames of the 16 mm film of this secondary flow are shown in Figures 4.1.1 and 4.1.2.

Based on a simple consideration of continuity of mass, one can easily see that this upward velocity in the lee side will induce a recirculation bubble at the lower end of the cylinder, if the junction between the cylinder and wind-tunnel wall (or end plate) is completely tight. This phenomenon is clearly demonstrated in Figures 4.1.3 and 4.1.4.

As the flow proceeds upward toward the upper "dead end," it will gradually encounter an adverse pressure gradient. At a point where the upward velocity has been sufficiently retarded, and the momentum is balanced by the adverse pressure, the flow will separate from the surface of the cylinder. This upper end recirculation bubble is shown in Figures 4.1.5 and 4.1.6.

It is apparent, that in the shear flow case, end plates will always create this type of end effect, if the junction between cylinder and base plate is completely tight.

During the course of this study, it was planned to leave some gaps around the cylinders at the junctions with the end plates. In other words, the cylinders were not connected to the end plates. In addition to this, at the top end of the cylinder, in the lee side, an air pump was used to reduce the pressure by continuously drawing out the air. Therefore, a smooth and continuous passage for these secondary flows at both the upstream and downstream side of the cylinder could properly be maintained.

The primary difference between a uniform flow and a shear flow is the presence of vorticity in the shear flow case. In the undisturbed shear flow, the vortex lines are all normal to the plane of the flow. As the shear flow approaches the test cylinder, the vorticity vector is

progressively turned until eventually the vorticity near the body is bent into the flow direction.

It will be shown later that apparently, at both ends of the cylinder, the vorticities have accumulated and formed horseshoe vortices. The streamwise vorticity at each side of the cylinder will induce a downward velocity component in the base region of the cylinder. This downward velocity component can be quite high at both ends of the cylinder due to considerable vorticity concentration there.

It should be noted here that the boundary layer thickness on the inner face of the end plate at the test site with the present experimental setup, is on the order of a couple of millimeters. It's effect on the base region at both ends of the cylinder is believed to be effectively cancelled out with its image due to inviscid effect.

Measurements of base pressure were made at various spanwise positions on circular cyclinders of diameter 0.50 in., 0.75 in., and 1.0 in. The local base pressure coefficient, $C_{pb\ell}$ is defined as $(P_b - P_\infty)/\frac{1}{2}\rho U_\ell^2$ where P_b is the local base pressure, P_∞ is the static pressure of the undisturbed flow, and U_ℓ is the local free stream velocity. The pressure measurements reported in this segment were taken with the wind tunnel running only at one speed, U_m = 9.20 ft/sec. The related parameters for these measurements are shown in Table 4.1.1.

The result of these base pressure measurements is shown in Figure 4.1.7. The base pressure distributions along the cylinders follow the same pattern--at the top of the cylinder a high pressure region, at the bottom of the cylinder a low pressure region, and in between the pressure coefficient is fairly constant.

As has already been mentioned, the streamwise vorticity at each side of the cylinder will induce a downward velocity component in the base region. These vertical velocities can be quite high at both ends of the cylinder where concentrated vortices rest. At the lower end of the cylinder in the base region, both the flow induced by the pressure gradient (moving upward) and the flow induced by the concentrated vortex (moving downward) all act as directing fluid away from the base region therefore, create a low pressure region. At the upper end of the cylinder both flows serve as bringing fluid into that region. Two streams converge, therefore create a higher pressure region. In between the local flow conditions are relatively free from the effects coming from both ends.

It is still unknown how these secondary flows in the neighborhood of a cylinder in an approach stream which has shear, modify the vortex shedding mechanism, modify the velocity distribution and hence the pressure distribution and wake characteristics (such as wake width, formation length, etc.). How this secondary flow phenomenon is related to Reynolds number effect and steepness factor effect, etc., is still open as a challenge to researchers. In view of all these uncertainties, it was decided to leave the test results uncorrected for wind-tunnel blockage effect. Therefore, it should be stressed here, that any interpretation of the test results presented in this report should bear this fact in mind.

As shown in Figure 4.1.7, the base pressure coefficient is fairly constant for each test cylinder in the middle region. Namely, the local base pressure coefficient is not effected by Re_{ℓ}, β_{ℓ} and Z/D. However, there is a systematic shift in the values for different test cylinders.

4.1.2 Wake Characteristics Measurements at Midsection of the Cylinders

For a bluff body in a stream, the importance of the region in the wake where vortices are formed and the close relation between the flow dynamics in this region and the fluid-induced force on the bluff body have been recognized for quite some time. Roshko (4.1) has discussed the importance of the vortex dynamics on the cylinder base pressure and the cylinder drag. Bloor (4.2) and Bloor and Gerrard (4.3), Gerrard (4.4), and Bearman (4.5) etc., have intensively studied the cylinder wake from a basic perspective.

There are numerous publications on this subject. One thing in common among these publications is that they are all restricted to bodies in uniform flow. There is no quantitative work existing at present related to the shear effects on the near wake. In view of this, it was decided during the course of this study to do some exploratory measurements of some of the characteristics associated with a vortex wake. The results presented in this section should be considered as a quantitative supplimentation to the results presented in the last section, where the highly three-dimensional characteristics of the flow around a circular cylinder in shear flow were discussed qualitatively.

The front stagnation and base pressure, as well as vortex shedding frequency, wake formation length and wake width were included in the measurements. The measurements were all conducted at midspan of the test cylinders only.

The initial position of the fully formed vortex defines the end of the formation region. A list of the criteria can be found in the work of Griffin (2.22), Griffin (2.23), and Ramberg and Griffin (2.26). According to Griffin and Votaw (2.24), some of the criteria yield

essentially the same value for the vortex formation length L_f. The criterium proposed by Bloor and Gerrard (4.3) was adopted in our measurement. Thus the position of the maximum of the second harmonic of the fluctuating velocity, u' on the wake axis is defined as the end of the vortex formation region. In this study, the length of the formation region was determined by hot-wire traverses along the wake axis. The output of the hot-wire anemometer was connected to a band-pass filter set at the second harmonic of the vortex shedding frequency f_s. The fluctuating velocity was consequently read on a rms meter. Once the location of the end of the vortex formation region was found, the wake width at that particular point was measured by searching for the point of maximum wide-band turbulence intensity (hot-wire was traversed in the Y direction).

The maximum of u'/U_m on the wake axis marking the end of the vortex wake formation region for the test cylinders at several Reynolds numbers are shown from Figures 4.1.8 to 4.1.12, and the corresponding wake widths are shown from Figures 4.1.13 to 4.1.17. The results are also summarized in Table 4.1.2.

The data show the general dependency of the wake formation length and wake width with Reynolds number. The formation length as well as the wake width decreases as the Reynolds number increases. This tendency can more readily be seen in Figure 4.1.18a. Griffin (2.22) has also found that the formation length decreases as Re is increased within the range $120 < Re < 350$ for stationary cylinder in uniform flow. Very interestingly, in a later study Ramberg and Griffin (2.26) found that the formation length L_f/D increases from 2.80 to 3.25 as the Reynolds number is increased from 350 to 650. The results of Griffin

(2.22) and Ramberg and Griffin (2.26) have also been included in Figure 4.1.18a for the purpose of comparison.

As for the velocity gradient effects, the data are not very conclusive. For the compatible cases: (1) D = 0.50 in., Re_m = 2,230; (2) D = 0.75 in., Re_m = 2.130, (3) D = 1.00 in., Re_m = 2,200; the formation length practically does not vary (~ 2.38, Table 4.1.2) while the wake width increases from 0.84 to 1.08, the base pressure coefficient decreases from -0.81 to -1.00, as the steepness factor increases from 0.034 to 0.070. For the cases D = 0.50 in., Re_m = 4,330 and D = 1.00 in., Re_m = 4,150, again the vortex formation length practically remains the same (~ 2.05) while the wake width increases from 0.82 to 1.0 and the base pressure coefficient decreases from -0.86 to -0.97 as the steepness factor increases from 0.034 to 0.068.

Let us further examine the effect the secondary flow around a cylinder has on the local pressure. If we neglect the region at both ends of the cylinder where the end effects dominate and confine as in the central region where the flow conditions are free from end effects, we will see that along the leading edge of the cylinder, the downward velocity component induced by the pressure gradient will deflect the streamline downward. This would force the fluid with higher velocity down and therefore, increase the local stagnation pressure. However, the results from the present measurements show that this effect is very weak. The measured front stagnation pressure coefficients are all practically equal to 1.0. The front stagnation pressure coefficient is defined as $(P_f - P_\infty)/\frac{1}{2}\rho U_m^2$, where P_f is the front stagnation pressure measured at a point on the nominally stagnation line ($\theta = 0°$). Based on the results of his extensive and careful measurements, Toebes

(2.20) reported a shifting of the front stagnation line at the Strouhal frequency. The unstable and unsteady nature of the flow field along the leading edge of the cylinder has prevented a fluid particle from traveling a significant distance downward. This resulted in an unsuccessful attempt during this study to estimate this downward velocity by introduction and visualization of smoke.

On the lee side of the cylinder, the upward velocity component will bring in fluid from the higher pressure region and therefore increase the local pressure. Therefore for a circular cylinder in a shear flow, it is believed that the overall effects of the secondary flow will tend to reduce the local drag force and hence to reduce the local drag coefficient.

From the results of present measurements (Table 4.1.2 and Figure 4.1.18a) this secondary flow has not much effect on the wake formation length while it does cause some variation in wake width. However, it should be stressed again that the tunnel blockage effect has not been taken into account, therefore the quantitative evaluation of this effect should be made with great care.

Results of base pressure measurement are somewhat confusing. As shown in Table 4.1.2, it seems that for each cylinder (with practically unchanged steepness factor), the base pressure coefficient and hence possibly the secondary flow are functions of Reynolds number. However, this variation in base pressure coefficient can also be directly due to the result of uncorrection of U_m. For the compatible cases: (1) D = 0.50 in., Re_m = 2,230; (2) D = 0.75 in., Re_m = 2,130; and (3) D = 1.00 in., Re_m = 2,200, as the value of steepness factor, β_m increases from 0.034 to 0.052 and then to 0.070, the local base pressure

coefficient $C_{pb\ell}$ decreases from 0.81 to -0.93 and then to -1.0. For the cases with D = 0.50 in., Re_m = 4,330 and D = 1.00 in., Re_m = 4,150, as the value of steepness factor β_m increases from 0.034 to 0.068, the local base pressure coefficient decreases from -0.86 to -0.97. These results apparently contradict the previous discussion that the secondary flow in the base region due to the existence of shear in the approach flow (this factor is expressed as β_m) should raise the base pressure and hence the base pressure coefficient. It is suggested that a more systematic study with a larger wind tunnel be undertaken so that the blockage effect can be reduced.

Many authors have tried to introduce a universal Strouhal number to collapse the experimental data of various bluff bodies.

In 1967, Calvert (4.8) introduced a universal Strouhal number St*, which is defined as

$$St^* = \frac{f_s D'}{U_b}$$

where D' is the vortex width at the end of the vortex formation region, U_b is the velocity at the edge of the boundary layer at the separation point, and f_s is the vortex shedding frequency. If Bernoullis equation is applied to the flow just outside the boundary layer at separation, then the base pressure coefficient

$$C_{pb} = \frac{P_b - P_\infty}{\frac{1}{2} \rho U^2} = 1 - \left(\frac{U_b}{U}\right)^2$$

If the base pressure parameter $K = U_b/U$ is introduced, then

$$K^2 = 1 - C_{pb}$$

and

$$St^* = \frac{St}{K} \left(\frac{D'}{D}\right)$$

where $St = f_s D/U$

We also can define a wake Reynolds number

$$Re^* = \frac{U_b D'}{\nu}$$

Based on his measurements of the wake formation behind cones with different vertex angles, Calvert (4.8) found that if the universal Strouhal number was defined in this way, then the value was about constant and $St^* = 0.19$. Simmons (4.9) and Griffin (4.6) adopted such a concept and showed that $St^* = 0.163$ and $St^* = 0.178$ respectively.

Following this idea, attempts to collapse the present data have been initiated and the results are shown from Figure 4.1.18 to Figure 4.1.20. The summarized results presented by Griffin (4.7) are also shown in the figures for the purpose of comparison. The present St^* values range from .160 to .115. This scattering of the data can be due to the secondary flow effects which have been discussed previously.

Further study of the effect of this secondary flow on the vortex formation is needed in order to clarify this point.

4.1.3 Vortex Shedding Characteristics

The tests described in this section were primarily focused toward seeking to identify cellular organization of eddy shedding frequencies behind the circular cylinder in linear shear flow. Hopefully, based on this series of test results, some relationship can be established between the eddy shedding correlation length and the shear parameter β_m and/or possibly Reynolds number effect. The test scheme is shown in Table 4.1.3 and Figure 4.1.21a.

For each of the cases studied, the results are presented in three separate figures. The first figure is a plot of the frequency spectra at various spanwise positions (Z/D). Following this figure are two plots of Strouhal number based on center-line (or mid-span) and local free-stream velocity as a function of Z/D.

At some particular stations for which two separate identifiable peaks are measured, the Strouhal data are represented by unconnected points. At some locations for which the spectra data has a broad peak, the Strouhal data are represented by points at the upper and lower limits of the top of the broad peak connected by a bar.

In order to insure that the wave analyzer gave peak frequencies similar to a spectral analysis, the case with D = 1.50 in., Re_m = 7,800 was selected to test. The output from the hot-film anemometer sensing the vortex shedding was directed simultaneously to the wave analyzer and an analog-to-digital converter which digitized (sample rate 500 per second, length of time series 60 seconds) and stored the signal on a HP 1000 disc for later spectral analysis. The power spectra density of vortex shedding frequency obtained using a digital computer are shown in Figure 4.1.62. The wave analyzer data and Fast Fourier Transformation

data are shown together in Figure 4.1.64. Their agreement was found to be within the frequency resolution of each method.

A repeat test on one cylinder was also made in order to determine whether after a time lapse of several weeks with many disturbances to the test conditions, such as setting and resetting the test cylinders, wind speed readjustment, and cleaning the shear flow generator, etc., the vortex shedding characteristics along a cylinder could be reproduced. The results of the retest with $D = 1.0$ in. and $Re_m = 3,950$ are shown in Figure 4.1.57 and Figure 4.1.58. Comparison of Figure 4.1.54 with Figure 4.1.57 and Figure 4.1.55 with Figure 4.1.58 show that the reproducibility of the data is quite satisfactory.

Small variations of the β_m value for each test cylinder are due to small changes in the distribution of mean velocity in the shear flow caused by variation of the wind-tunnel speed and the conditions of the shear flow generating gauze, such as accumulation of dust on the screen, variation of the tension imposed on the screen, etc. The β_m value for each test was obtained based on the best fit of the mean velocity data for that particular run.

Except under very strictly controlled test conditions in the pure Kármán vortex shedding range ($80\text{-}90 < Re < 150\text{-}300$), the Kármán vortex almost always bears its three-dimensionality and randomness (both in amplitude and period), even in a nominally two-dimensional flow case. This point has been discussed in numerous papers such as those by Hama (4.10) and Gerrard (4.11). At $Re = 6.8 \times 10^4$, Toebes (2.20) has shown that on occasions as large as 15 percent variation in period has occurred.

A vortex that is shed from a cylinder in shear flow must have some finite length in the spanwise direction. The time interval between two

adjacent vortices must also be a finite value. As a vortex is shed at a certain range along the span of the body, it must create some pressure fluctuations which then propagate in both directions. Thus, one would expect that a very long cylinder in shear flow would always generate vortex cells with fluctuating boundaries. And, as the cell boundaries change (the cell lengths may also change), the frequency of shedding for each cell may also change. However, if some kind of constraint such as end plates are used, this will impose some limitation on the fluctuation of boundaries. Due to this forced, fixed boundary by the presence of end plate, the end cells, therefore must shed in a far more "stable" manner. As will be seen later in the results, the end cell generally has a well defined boundary and sharper peak in the spectrum.

I. $D = 0.25$ in., $\beta_m = 0.016 \sim 0.017$, $Re_m = 900$ and 1,830

Based on extrapolation of the results of base pressure measurements for cylinders with $D = 0.50$ in., 0.75 in., and 1.0 in. (Section 4.1.1), for the $D = 0.25$ in. cylinder, the region which is free from end effects is located somewhere between $Z/D = 28$ and $Z/D = -30$.

Figure 4.1.21 shows the frequency spectra for $Re_m = 900$ at various spanwise positions. The data clearly depict the general characteristics of the vortex wake. It is quite evident that the two cells at both ends of the cylinder, which start from $Z/D = 38$ to 28 and $Z/D = -25$ to -30 are dominated by end effects. These two end cells are fairly well defined, both in shedding frequency and extent.

For this particular study with $D = 0.25$ in. cylinder, the ratio of effective tunnel height to cylinder diameter (H/D) is 72. This is the largest length to diameter ratio used in this type of study. The frequency at the peak appears to shift gradually from 145 Hz at $Z/D = 28$ to

47 Hz at Z/D = -25. As the boundaries of the cells are changing with time, cells of possibly several frequencies can shed from some specific locations on the cylinder. Since the data were obtained based on an average over a period of time, the data will show a broad peak if more than one frequency is present. For this kind of wide band spectrum, as stated before, the data are represented by a bar.

Due to the fluctuating nature, as has been shown in Figure 4.1.21, the peak of the spectrum shifts more or less smoothly and somewhat continuously. This sometimes makes the data appear to be ambiguous and increases difficulty in defining the cell boundaries. However, a tendency toward some organized cell structure is still quite evident. This tendency can be seen in Figure 4.1.22 where the Strouhal number S_{sm} is based on the mid-span (Z = 0) velocity U_m.

The longest cells appear to be about 5D in length. There are three of them with this length, one located from Z/D = 20 to 15 at 120 Hz (S_{sm} = 0.301), one located from Z/D = 6 to 1 at 90 Hz (S_{sm} = 0.226), and one located from Z/D = 0 to -5 at 84 Hz (S_{sm} = 0.211). Figure 4.1.23 shows the Strouhal number based on the local free-stream velocity U_ℓ. The upper and lower bounds of local Strouhal number ($S_{s\ell}$) for the three above mentioned cells are 0.217 to 0.233, 0.204 to 0.223 and 0.211 to 0.227.

Figure 4.1.24 shows the frequency spectra at various spanwise positions for the Re_m = 1,830 test case. Again judging from the general tendency of the peak, the cells from Z/D = 38 to 29 and Z/D = -25 to -31 are apparently dominated by end effects.

By comparing these two sets of experimental results (Re_m = 900 and 1,830), doubling the Reynold's number apparently does not change the general characteristics except at certain span-wise regions where the

vortex shedding is uncorrelated along the span of the cylinder (without cell structure as shown in Figure 4.1.25). Possibly, increasing the wind-tunnel test speed will induce more uncertainty factors in the approach flow, and possibly also will cause some random vibrations of the test cylinder.

The longest cells are 5D in length. They are located from Z/D = 21 to 16 at 250 Hz (S_{sm} = 0.305) and Z/D = 6 to 1 at 185 Hz (S_{sm} = 0.225). The respective ranges of $S_{s\ell}$ (as shown in Figure 4.1.26) are 0.222 to 0.237 and 0.204 to 0.222.

II. D = 0.50 in., β_m = 0.33 ~ 0.37, Re_m = 970, 1,770, 3,600 and 4,500

For D = 0.50 in. at Re_m = 1,960, the results of base pressure measurement indicates that $-14 \leq Z/D \leq 12$ is the region that is free from end effects.

The results of vortex-wake measurements for Re_m = 970 test case are shown from Figure 4.1.27 to Figure 4.1.29. As can be seen in Figure 4.1.28, there is no discernible cell structure along most span of the test cylinder where it is free from end effects, except the one from Z/D = -3 to -5 at 21.5 Hz which is also barely identifiable. The spectral peaks appear to shift gradually. Since the wind tunnel used for the present experiment is of the open type and the wind-tunnel speed, U_m, set for this specific run is only about 4.5 ft/sec, any slight disturbance of the environment can cause considerable fluctuations at the test section. This is believed to be an important factor that can add to the fluctuation of the cell boundaries. It should be noted also, that for D = 0.50 in., the ratio of effective tunnel height to cylinder diameter is 36. Therefore, even for very stable test conditions cells with considerable boundary fluctuations will be produced.

The cell from Z/D = -3 to -5 at 21.5 Hz has a length of 2D. The Strouhal number based on mid-span tunnel speed S_{sm} is 0.196 and the Strouhal number based on local velocity $S_{s\ell}$ ranges from 0.218 to 0.236.

The results for Re_m = 1.770 test case are shown from Figure 4.1.30 to Figure 4.1.32. By comparing the results with those of the Re_m = 970 case, one can see that increasing the wind-tunnel test speed does result in stabilizing the test conditions.

From Z/D = 12 to Z/D = -2, there are only a few barely identifiable short cells. The spectral peaks still shift in a smooth fashion as the Re_m = 970 case in this region. From Z/D = -2 to -6, there is a cell at 38 Hz (S_{sm} = .191) and from Z/D = -7 to -11 there is another cell at 30 Hz (S_{sm} = .151). The former has a length of 4D with $S_{s\ell}$ varying from 0.203 to 0.229 and the later also has a length of 4D with $S_{s\ell}$ varying from 0.189 to 0.229.

As the Re_m reaches 3,600 (Figure 4.1.33 to Figure 4.1.35), except the upper end cell, for Z/D > 4, it is still difficult to identify any cell structure. From Z/D = 3 to -1, there is a fairly well defined cell of length 4D at 90 Hz (S_{sm} = 0.223 and $S_{s\ell}$ = 0.202 to 0.231) followed by a cell of length 2D at 80 Hz and then an unstable cell at about 76 Hz.

The results for the Re_m = 4,500 case are shown from Figure 4.1.36 to Figure 4.1.38. One cell extended from Z/D = 11 to 7 is fairly identifiable. This cell has a length of 4D with a frequency of about 140 Hz (S_{sm} = 0.278, $S_{s\ell}$ = 0.208 to 0.223). The one from Z/D = -5 to -9 is very well defined. This cell has a length of 4D and is shed at 90 Hz (S_{sm} = 0.179, $S_{s\ell}$ = 0.204 to 0.233).

III. D = 0.75 in., β_m = 0.050 ~ 0.052, Re_m = 1,950, 2,920, 3,900, 6,730

The results from base pressure measurements show that the end effect is very much confined in Z/D > 7 and Z/D < -7.4 at Re_m = 2,950.

For Re_m = 1,950, the results are shown from Figure 4.1.39 to Figure 4.1.41. Within the 7 > Z/D > -7 region, there are four cells. They are from Z/D = 7 to 4 at 27 Hz, from Z/D = 2 to 0 at 22.5 Hz, from Z/D = 0 to -2 at 19.5 Hz, and from Z/D = -4 to -6 at 15 Hz. The first one with a length of 3D is the longest . The corresponding S_{sm} is 0.278 and $S_{s\ell}$ = 0.199 to 0.228.

For Re_m = 2,920, the results are shown from Figure 4.1.42 to Figure 4.1.44. Aside from the two end cells, there are four discrete cells along the span. From Z/D = 7 to 4, this one has a frequency of 39.5 Hz with length 3D, the corresponding S_{sm} = 0.271 and $S_{s\ell}$ = 0.198 to 0.222. The next one ranges from Z/D = 4 to 1 which has a length of 3D with frequency 33.0 Hz, the corresponding S_{sm} = 0.226 at $S_{s\ell}$ = 0.186 to 0.214. The third one ranges from Z/D = 0 to -3 which also has a length of 3D with shedding frequency at 28.5 Hz and the corresponding S_{sm} = 0.195 and $S_{s\ell}$ = 0.195 to 0.222. The fourth one ranges from Z/D = -4 to -6 at 22.5 Hz. This one is only two diameters long.

The results for Re_m = 3,900 case are shown from Figure 4.1.45 to Figure 4.1.47. There are three discrete cells in the region free from end effect. The first one which extends from Z/D = 6 to 4 is only 2D in length. The second one extended from Z/D = 4 to 1 has a length of 3D and the shedding frequency is 40 Hz (S_{sm} = 0.206, $S_{s\ell}$ = 0.176 to 0.198). The third one which ranges from Z/D = -1 to -4 also has a length of 3D and the shedding frequency is 33.5 Hz (S_{sm} = 0.172, $S_{s\ell}$ = 0.179 to 0.206).

As the Reynolds number Re_m is raised to 6,730, the lower end effects apparently extend up to Z/D = -3. This is shown from Figure 4.1.48 to Figure 4.1.50. There is only one possible cell which extends from Z/D = 3 to 0 at about 73 Hz. The corresponding S_{sm} and $S_{s\ell}$ are about 0.217 and 0.195 to 0.214 respectively.

IV. D = 1.0 in., β_m = 0.065 ~ 0.075, Re_m = 1,950, 3,900, 7,800

The pressure data show that for D = 1.0 in. at Re_m = 3,930, the region which is free from end effects extends only from Z/D = 4 to -4 (Figure 4.1.7).

Figure 4.1.51 to Figure 4.1.53 show the results for Re_m = 1,950 case. The upper end cell extends down to about Z/D = 5.0, while the lower end cell reaches up to Z/D = -3.0. There are two well defined cells. One ranges from Z/D = 4.0 to 2.0 at 15 Hz (S_{sm} = 2.74, $S_{s\ell}$ = 0.202 to 0.234) and the other one ranges from Z/D = 1.0 to -1.0 at 10.5 Hz (S_{sm} = 0.192, $S_{s\ell}$ = 0.175 to 0.203).

There are two sets of results for Re_m = 3,900 case. One set is the original and the other set is a rerun which as a check of the repeatability of the data. By comparing these two sets of data (Figure 4.1.54 and 4.1.56 and Figure 4.1.57 and 4.1.58), one can see that the wake pattern is very much the same. Very interestingly, both sets of data show two upper end cells, one at 32 Hz and the other at 27 Hz (Figures 4.1.54 and 4.1.55) for the original data, one at 33 Hz and the other one nominally at about 28 Hz for the rerun data (Figure 4.1.57 and 4.1.58). The slight difference is due primarily to a slightly different test wind speed.

The only well defined cell in the region free from end effect is the one from Z/D = 1 to -1.5 at 20.5 Hz (S_{sm} = 0.187, $S_{s\ell}$ = 0.174 to

0.206) for the original results. For the rerun data, it is from Z/D = -0.5 to -3 at 21.0 Hz (S_{sm} = 0.192, $S_{s\ell}$ = 0.197 to 0.240; not shown in a separate figure).

The Re_m = 7,800 results are shown from Figure 4.1.59 to Figure 4.1.61. In the $-4 \leq Z/D \leq 4$ region, there is no well defined cell.

V. D = 1.50 in., β_m = 0.10, Re_m = 7,800 and 13,460

This is the largest cylinder used in the present test matrix. The shear parameter β_m is 0.10 which is the highest value attained in this series of test. The cylinder blockage ratio is 6.3 percent. With the present wind-tunnel fan, the maximum Reynolds number that can be achieved under this test set-up is 13,460.

Although the effective wind-tunnel height to cylinder diameter ratio (H/D) is 12, a region of only about three inches exist at the mid-span ($-0.7 \leq Z/D \leq 1.4$) where the flow can be considered as free from end effects. This estimation is obtained based on the extrapolation of the base pressure data described in Section 4.1.1.

The results of Re_m = 7,800 are shown from Figure 4.1.63 to Figure 4.1.65. The lower end cell at 12.5 Hz predominates from Z/D = -0.5 to -5.0. This can evidently be seen in Figure 4.1.64. The peaks are very well defined and the energy levels are high. The upper end cell with a frequency of about 27 Hz extends down to Z/D = 3.5. From Z/D = 3.5 to 1.5, the spectra have rather broad peaks.

Although somewhat ambiguous, from Z/D = 1.5 down to Z/D = -0.5, the peaks are sharper and better defined. This is the region where the flow conditions are believed to be free from end effects. A cell with a frequency of 19 Hz and length 2D tends to form in this region. The corresponding S_{sm} = 0.206 and $S_{s\ell}$ ranges from 0.174 to 0.193.

As the Reynolds number is raised to 13,460, the general wake pattern very much stays the same as is shown from Figure 4.1.66 to Figure 4.1.68. The cell which starts at Z/D = 2.0 and ends at Z/D = 0.0 has a frequency of 36 Hz. The corresponding S_{sm} = 0.214 and $S_{s\ell}$ ranges from 0.177 to 0.208.

VI. Effect of Shear Parameter β_m on Eddy Shedding Correlation Lengths

The results discussed from Section I to V show that the greatest cell lengths free from end effect are at the same level for a specific shear parameter. Based on these experimental results, an attempt to correlate the greatest cell lengths for each test case to its corresponding shear parameter was made. The result plotted in cell length (normalized by the cylinder diameter) as a function of shear parameter, β_m is shown in Figure 4.1.69. The curve is drawn based on the best fit of present results. As the shear parameter increases, the cell length decreases correspondingly. This trend has also been reported by Rooney and Peltzer (2.17). Their data are also shown in the same figure. It should be noted that the data of Rooney and Peltzer were obtained at Reynolds number from 1×10^5 to 4×10^5 and some of the results were subject to end effects. Mair and Stansby (2.16) have also reported that the greatest cell lengths are usually in the range 4D to 6D. Their β_m values are believed to be from 0.012 to 0.048 and Reynolds numbers range from 1.3×10^4 to 2.6×10^4. It should also be noted that some of the results reported by Mair and Stansby also show end effects.

The present experimental results have also shown that for each test cylinder with shear parameter almost constant, change of Reynolds number has no significant effect on the greatest cell length.

4.1.4 Flow Visualization Results

It can be postulated that, since vortex shedding is occurring (as evidenced by the spectral peaks shown in Section 4.1.3), it must shed at any instant over a finite length of the cylinder in the shear flow cases. At any one location along the cylinder, competition from a range of frequencies may result in shedding at one frequency (for example, associated with a "cell" below that point) at another time. In other words, while a discrete cell with a single shedding frequency may act at a particular location at one point in one time, it will be replaced at another time with a discrete cell at a slightly different frequency. Support for this argument is seen in the data discussed in Section 4.1.3 in the width of the spectral peak and in the lack of clearly defined cells. Even in the region where the vortex shedding is comparatively "stable" (with better defined boundaries and frequencies), it is believed that the vortex shedding correlation length and frequency etc., can only be determined and discussed in the statistical sense.

Figure 4.1.70(a) and Figure 4.1.70(b) show two photographs of smoke flow behind the 0.50 in. diameter cylinder at a Reynolds number of about 1,770. The region observed is roughly from the centerline to 4 inches below the centerline where no clear indication of a cell structure is evident in Figures 4.1.31 or 4.1.32. The smoke was illuminated by a strobe light set to the shedding frequency. An exposure time, long enough to cover about six or seven shedding cycles was used. Periodic structure seen in the smoke pattern along the cylinder length is a result of smoke introduction through equally spaced holes in the cylinder. If a coherent cell shedding at the strobe frequency for seven or eight cycles existed during during the exposure time, the result

would appear as a banded system as seen in Figure 4.1.70(a). If cells with frequencies different from the strobe frequency existed, the result would look like Figure 4.1.70(b). The photos in Figure 4.1.70(a) and Figure 4.1.70(b) were, in fact, taken at two different times using the same strobe frequency. These photos further support the postulation that cells of finite size, but different in frequency and probably position, exist at different times in the wake.

A list of five reels of motion pictures which show the vortex shedding process for stationary cyclinders in shear flows is shown in Table 4.1.3. Reel 1 and Reel 2 show side views of the vortex shedding process. The shed vortices appear to form lines across the span inclined in sympathy with the approaching shear flow. The point of detachment of the vortex from the cylinder is moving down the span of the body.

Reel 3 and Reel 4 show the top views of the Kármán vortices at two different positions along the span of the cylinder.

Reel 5 shows the secondary flow which is induced by the incident shear flow on the lee side of the cylinder.

4.2 Oscillating Cables in Linear Shear Flows

A detailed, quantitative set of hot-wire measurements of vortex shedding frequency from cables forced to oscillate transversely in low turbulence shear flow was performed in this study. The test scheme is shown in Table 4.2.1 and Figure 4.2.1. The measurements were designed to examine the locking-on length of the vortex shedding to the cylinder frequency as a function of cable vibrating frequency, amplitude, Reynolds number and steepness parameter of the approaching flow.

The maximum Reynolds number that has been achieved for this vibrating cable study is only 1,725 (Table 4.2.1). The reasons are: (1) As has already been discussed in Chapter 3, the stiffness of the rubber cords that were used as the test cable prevented the adoption of diameters greater that 0.50 inch when a half-wavelength of 10 inches was desired. (2) The inertia of the rubber cord increases rapidly as the diameter of the cord increases. Large inertia makes it impossible to shake the cable at a desired high frequency unless a tension exceeding material strength is applied on the cable. The prestress that is required on the rubber cord is often beyond the breaking point or has reached such an extent that severe creep occurs. Thus with the present experimental setup, unless some lightweight, less stiff, round and smooth material which can withstand high tension for a long duration without significant change in diameter can be found, the test range will remain quite limited.

The largest cable used was about 0.5 inch in diameter. The effective wind-tunnel blockage by the cable, even at the extreme test case with $a_m/D = 0.6$, was only about 3 percent at the antinode. Without

correction of the experimental results the discrepancy due to the wind-tunnel blockage effects is believed to be well within the measurement error in most of the test cases. Therefore, no attempt has been made to correct the experimental results for blockage.

By comparing the experimental results of both smooth and stranded cables, Votaw and Griffin (4.16) have reported that as long as the helix angle or the ratio of strand to total diameter of the cable remain small, there is little difference in vortex shedding frequency and the wake formation processes. For the present vibrating cable study, three O-ring rubber cords were used as the test cables. The surface of the rubber cord is fairly smooth and the diameter is reasonably uniform. Based on the finding of Votaw and Griffin (4.15), any possible effect on the vortex shedding frequency and the wake formation processes, due to the rubber-cord surface being not extremely smooth or the diameter being not perfectly uniform, is therefore considered as negligible.

In order to model a resonant self-excited (strumming) oscillating condition, the cables were physically oscillated at either the center-line (Z = 0, where the antinode is located in the vibrating situation) vortex shedding frequency when the cable is stationary or at a frequency slightly below this value. For tests No. 1, No. 3, or No. 5, the cable oscillation frequency $S_{cm}(= f_c D/U_m)$ was set equal to the mid-span vortex shedding frequency S_{sm} $(= f_c D/U_m)$ when the cable was in stationary condition. For tests No. 2, No. 4, or No. 6, the value of S_{cm} was set to be lower then S_{sm}.

It should be noted that since the wind tunnel used for this study is of the open-return type, small fluctuations in the air pressure in

the laboratory (caused by gusts outside the building, opening or closing of doors) affects the test conditions at the working section. This distrubance becomes more pronounced as the wind tunnel is run at a lower speed. It was found at the early stage of this study that whan the tunnel was run at a speed no less that 4.5 ft/sec, a well-developed constant shear flow with reasonably steady test condition could be maintained when the environment was also reasonably calm. The minimum wind speed shown in Figure 4.2.1 was determined based on this practical consideration.

4.2.1 The Spanwise Distribution of Shedding Frequency for Cables with Different d, a_m/D, S_{cm}, and Re_m

For each of the test cases for which the spectrum measurement has been measured at certain intervals along the whole span of a half-wavelength (listed in Table 4.2.1), the results are presented in two separate figures. The first figure is a plot of power spectra for various spanwise positions along the cable. The corresponding values of $\tilde{S}_{sm}$ $(= \tilde{f}_s D/U_m)$ along the span are plotted in the second figure. The corresponding figures for the results of each test run are also listed in Table 4.2.1.

For test No. 2 and test No. 4, the cable was not run in a stationary $(a_m/D = 0)$ state. The results of test No. 1 with $a_m/D = 0$ were used in the data analysis for test No. 2, the results of test No. 3 with $a_m/D = 0$ were used in the data analysis for test No. 4.

The results of the 0.25 inch cable held stationary $(a_m/D = 0)$ at the test section (shown in Figures 4.2.54, 4.2.55 and Figures 4.2.64, 4.2.65) indicate lack of cell structure of vortex shedding along the span.

Bishop and Hassan (4.12) investigated the lift and drag forces on a circular cylinder in a flowing fluid. They reported that vortex shedding could lock on at a half and a third of the cylinder oscillaiton frequency. Stansby (2.18) also found that the vortex shedding frequency locked on at the cylinder vibration frequency and to sub-multiples of the cylinder vibration frequency. For convenience, Stansby referred to locking-on at the cylinder vibration frequency, at a half of the cylinder vibration frequency and a third of the cylinder vibration frequency as primary, secondary and tertiary lockin-on, respectively.

Vortex shedding at a third of the cable frequency has not been observed with any of the test cases of present experimentation. Vortex shedding at one half of the cable frequency occurred in only one case ($a_m/D = 0.20$) of test No. 4 and four cases ($a_m/D = 0.63$, 0.47, 0.37 and 0.23) of test No. 6. This study is directed mainly at primary locking-on, therefore no further discussion will be pursued on the subject of secondary and tertiary locking-on.

The cable oscillation wlll cause the wake to assume a roughtly sinusoidal oscillation with various amplitudes along the span. The spectrum peaks at double the cable oscillation frequency, for example, as shown in Figure 4.2.46, were caused by the hot-wire probe being set too close to the wake centerline and therefore picked up the signal from the other side of the wake.

4.2.2 On Complete "Locking-On"

Before discussion of the concept of complete locking-on, there are two concepts which are closely related to complete locking-on which must be reviewed. These are (1) modulation of vortex shedding process due to forced oscillation of the cable, and (2) motion induced vortex.

Through his extensive and well-developed experimental study, Toebes (2.20) has reported the results of multiprobe measurements in the wake and adjacent unsteady flow of an oscillating circular cylinder in the Reynolds number range $Re = 0.2 \sim 1.2 \times 10^5$. For a circular cylinder spanning a uniform stream, the Kármán vortex street occurs in its purest, most regular form only at Reynolds number up to a few hundred. At higher Reynolds numbers the Kármán vortex wake becomes more complicated due to the presence of turbulence. Concurrent random variations in periods, that on occasion are as large as 15 percent per cycle, are reported by Toebes (2.20). Consequently, Toebes comments that thinking of the vortex shedding frequency as reasonably constant may stem from emphasis on low Reynolds number studies wherein flow fluctuations are nearly harmonic. Deduced from his correlation measurements farther from the cylinder, Toebes explains this difference by the fact that the unsteady flow is influenced by the wake boundary. At higher Reynolds number appreciable turbulent distortion of that boundary in the axial direction has come fairly close to the cylinder. Toebes further comments that one can but indicate an average Strouhal frequency of vortex formation. Cylinder oscillation might merely alter the phase amplitude distribution, rather than force the vortex shedding frequency away from its natural value.

If f_s is the vortex shedding frequency (wide band, more precisely should be called the average vortex shedding frequency) for a stationary cylinder in a stream, vibration of the cylinder at a frequency f_c which is close enough to f_s ("threshold frequency" as it is called by Ramberg and Griffin (2.28)) and with vibration amplitude large enought ("threshold amplitude" as it is also called by Ramberg and Griffin

(2.28)), may modulate the vortex formation process and cause the vortices to shed at a well-defined frequency f_c (narrow band). This effect of vibration in making the vortices shed at much better defined frequency than that of stationary case can obviously be seen in the figures of frequency spectra at various spanwise positions presented in Section 4.2.1.

The concepts of motion induced vortex and oscillation by motion induced vortex have been discussed by Kobayashi (4.13) and Komatsu and Kobayashi (4.14). Both wake velocity measurement and the flow visualization test were conducted for a set of bluff cylinders oscillated freely in a air flow. From these tests two types of vortex oscillations were reported by Kobayashi. One is a small amplitude restricted oscillation caused by Kármán vortex. The other is a relatively large amplitude restricted oscillation caused by motion induced vortex. This oscillation by motion induced vortex occurs independently of Kármán vortex.

From the high speed movie of the present flow visualization study (Reel 3b and Reel 3c as are lsited in Table 4.2.3), it can be seen that the vortices are shed intermittently at the cable frequency (synchronizing with the motion of the cable) which are not seen in the steady cable case (Reel 3a). Hence the vortex shed at cable frequency can be called a motion induced vortex, distinguishing it from Kármán vortex.

For a stationary cylinder (or cable) in a shear flow, the fluctuating forces produced by regularly shed spanwise organized vortices from the body may excite the body into resonant oscillations, if the damping of the body is sufficiently low and if the vortex shedding frequency is close to one of the natural frequencies of the

body. As there will be range of values of vortex shedding frequency f_s along a cylinder (or cable) in constant shear flow, oscillation of the cylinder (or cable) at a frequency f_c which is close to f_s may cause vortex shedding within certain regions of the body all at the frequency f_c. Oscillation of the body also induces vortices which are in perfect synchronization with the motion of the body. The strength of the vortices shed from the body will be amplified due to this synchronization of Kármán vortex and motion induced vortex. This is believed to be the fundamental mechanism of complete locking-on.

The complete locking-on of the vortex shedding to the cable oscillating frequency in a shear flow depends on Reynolds number, steepness parameter, local amplitude of vibration and the ratio of S_s/S_c.

$$\tilde{S}_s = \tilde{f}_s D/U_m = F\ (Re_m,\ \beta_m,\ a_Z/D,\ S_s/S_c)$$

where $$Re_m = \frac{U_m D}{\nu}\ ,\ \beta_m = \frac{\lambda D}{U_m}\ ,\ S_s = f_s D/U_m\ ,\ S_c = f_c D/U_m$$

Since for a vibrating cable, the amplitude of vibration varies across the span,

if expressed on the antonode amplitude, then

$$\tilde{S}_s = \tilde{f}_s D/U_m = F^*\ (Re_m,\ \beta_m,\ a_m/D,\ \Pi/D,\ z/D,\ S_s/S_c)$$

4.2.3 Discussion

A notable feature shown by the spanwise distributions of vortex shedding frequency (aside from the motion induced vortex) for the vibrating cable is the effect due to the oscillation on the vortex shedding frequencies adjacent to the complete locking-on region. The values of $\tilde{S}_s$ for the upper region adjacent to the complete locking-on

region are greater than those of the corresponding locations under the stationary situation. For the lower region adjacent to the complete locking-on region, the values of $\tilde{S}_s$ are lower than those of the corresponding locations while the cable is in stationary state.

The vortex shedding frequencies adjacent to the complete locking-on region, although not as well defined (represented by a sharper spectrum peak) as those of the motion-induced vortices, are in general much better defined than those of the stationary case. In other words, although the vortex sheddings are slightly unsteady, the vortex shedding process modulated by the motion of the cable, has become more stable in frequency and the ranges of possible vortex shedding frequency are much smaller than the corresponding stationary case.

For a cylinder engaged in cross flow oscillation, there are three factors that will affect the vortex shedding process. The first factor is the apparent increase in diameter due to the motion of the boundary. The second factor is that owing to the cross-flow velocity of the cylinder, the magnitude and direction of the fluid velocity relative to the cylinder will change continuously. As a consequence, the locations of the boundary layer separation points on both sides of the cylinder may also change. The third factor is that when the cylinder performs oscillatory motion it imposes an oscillatory motion on the wake. The periodic mass transport right behind the cylinder, as can vividly be seen in the high speed movie (Reel 3b and Reel 3c) carried circulation of different sign to the opposite shear layer.

The location of the boundary-layer separation point on a circular cylinder has been investigated experimentally for both stationary and vortex-excited oscillations by Mei and Currie (4.15). For the vibrating

cylinder, the range of angular displacement of the separation point was found to depend upon the vibration amplitude and frequency.

For a vibrating cable in a shear flow, the problem is far more complicated than that of a rigid cylinder. The vibration amplitude and all the above mentioned three factors are functions of positions along the span of the cable. Added to the complication of the problem is the secondary flow induced by the approaching shear flow.

At the lower region adjacent to the complete locking-on, since the cable vibrating frequency, f_c, is much higher than the vortex shedding frequency, f_s, while the cable is stationary, it is believed that in this region the effect of apparent increase in diameter surpass the effect of increase in relative velocity. Based on a quasi-two-diamensional consideration, the vortices therefore will be shed at a lower frequency. At the upper region adjacent to the complete locking-on, the effect is opposite. In this region f_s is larger than f_c, the effect of increasing in relative velocity due to the oscillation supersedes the effect of apparent increase in the diameter, therefore $\tilde{f}_s$ will be "forced" above that of the stationary case.

Table 4.2.2 gives the values of $\tilde{S}_{sm}$ at the boundaries of complete locking-on as well as the values of S_{sm} of the corresponding stationary state and the values of local oscillating amplitude (a_Z/D) and cable vibrating frequency S_c.

At the regions outside the complete locking-on region, vortex shedding is intermittent with motion induced vortex and Kármán vortex. Within these regions, for a given cable frequency, both the oscilloscope trace of the hot-wire signal and smoke pattern captured by high-speed motion pictures, showed the vortex shedding to change intermittently

(jump in a discrete manner) between with the cable frequency and the Kármán vortex frequency, $\tilde{f}_s$, which was "forced" away from the stationary value, f_s.

In uniform flow, the length of complete locking-on is found to be dependent on the amplitude of oscillation and Reynolds number (Stansby (2.18)). The complete locking-on length increases linearly as the amplitude of vibration increases. Close examination of the present experimental results show that this finding by Stansby cannot be applied to the vibrating cable cases. A notable feature shown by the experimental results of each test is that the spanwise extent of primary locking-on does not increase monotonically as a_m/D increases. When a_m/D reaches to a certain value, the length of complete locking-on ceases to increase. Instead, the complete locking-on region starts moving along the cable. This effect which is apparently caused by the curvature of the vibrating cable, should impose some limitation on applying the cylinder results to the cables.

The nature of complete locking-on as well as the characteristics of vortex shedding outside the complete locking-on, are now clear. Based on the experimental results, it is now possible to formulate a general procedure to predict the spanwise extent of primary complete locking-on for a vibrating cable in constant shear flow.

The values of $(S_{sm}/S_{cm})_+$ and $(S_{sm}/S_{cm})_-$ for each of the test runs are plotted as functions of local vibrating amplitude a_z/D in Figure 4.2.66. The suffix minus corresponds on the boundary at the high velocity end of locking-on. It appears from Figure 4.2.66 that the condition $S_{sm}/S_{cm} \geq 0.9$ must be satisfied for locking-on shedding to occur for a vibrating cable in a constant shear flow.

Since the boundary of complete locking-on is never a fixed point but a region, the above mentioned boundary is simply an approximation of its mean position. Within the Reynolds number range of the present experiments, no systematic effect of Reynolds number is observed with the test results.

The least-square curve fittings for $(S_{sm}/S_{cm})_-$ and $(S_{sm}/S_{cm})_+$ as functions of a_z/D are:

$$(S_{sm}/S_{cm})_- = 1.03 + 0.41(a_z/D)^{.452} \tag{4.1}$$

$$(S_{sm}/S_{cm})_+ = 0.96 - 0.88(a_z/D) + 3.88(a_z/D)^2 - 3.7(a_z/D)^3 \tag{4.2}$$

It should be noted that the curve fittings are valid only for $a_z/D \leq 0.6$.

The present experimental results on stationary cables show that $S_{s\ell} = f_s D/U_z$ (where $U_z = U_m[1 + \lambda\,(\frac{Z}{H^*} - 1/2)]$) is nearly constant along the span. The value of $S_{s\ell}$ is approximately .220. If $S_{s\ell}$ is assumed constant, then,

$$\begin{aligned} S_{sm} &= f_x D/U_m \\ &= S_{s\ell}\,\frac{U_Z}{U_m} \\ &= S_{s\ell}\,(1 + \frac{Z}{D}\,\beta_m) \\ &= 0.220\,(1 + \frac{Z}{D}\,\beta_m) \end{aligned} \tag{4.3}$$

For a flexible cable of diameter D vibrating at one of its natural frequencies, f_c, with certain mode and amplitude a_m/D in a constant shear flow, β_m, U_m, based on equation (4.3), one can obtain an equation for S_{sm}/S_{cm} as a function of a_z/D for each particular case. The common solutions of this equation with equation (4.1) and

equation (4.2) should give the upper and lower boundary of complete locking-on. The spanwise extent of primary complete locking-on can therefore be estimated.

4.2.4 Flow Visualization Results

A detailed flow visualization study of a cable forced to vibrate in a constant shear flow has been conducted. The cable used for the study was a d = 0.48 inch vinyl tube. The cable was properly tuned and forced to vibrate at f_c = 27.0 Hz. The half-wavelength was 10.0 inch with antinode at the center of the wind tunnel. The Reynolds number based on the wind velocity at mid-height of the wind tunnel was 960. The peak-to-peak amplitude of oscillation at the antinode was about 0.45 D. Figure 4.2.67 shows the frequency spectrum along the span of the cable. Nine reels of 16 mm film are included with this report. A list of the reels is given in Table 4.2.3.

Much of the detailed phenomena associated with a cable during forced vibrations in a constant shear flow has been captured by these high speed motion pictures. Unless specified, the motion pictures were taken at 500 frames per second. Reel 1 shows the side view of vortex shedding process along the span of the cable. Reel 2a shows the top view of the vortex shedding process for a cable in stationary state. The smoke is released at Z/D = 5.67. Reel 2b is the same as Reel 2a except the the cable is oscillating. The smoke is released well within the complete locking-on region (see Figure 4.2.67). The vortex shedding process is locked on to the cable oscillation.

Reel 3a shows the top view of the vortex shedding process for the cable in stationary state. The smoke is released at Z/D = -1.81. Reel 3b shows the cable in a vibrating state. The smoke is released at the

same position as Reel 3a. This position is outside the complete locking-on region. The camera speed was 1000 frames per second. The spectrum (Figure 4.2.67) shows the coexistance of two peaks. The motion pictures show the vortex shedding is intermittent between the cable frequency and the Kármán vortex frequency. Reel 3c is the same as Reel 3b, except that it was taken at 500 frames per second.

Reels 4a and 4b show the secondary flow (induced by the approach shear flow) in the lee side of the cable for the stationary and vibrating cases, respectively. The secondary flow speed discussed in Section 4.1.1 was calculated based on Reel 4a.

Reel 5 shows tha close-up view of the complete locking-on region. Notice the three band marks on the cable. The upper one is at $Z/D = 7.99$ and the lower one is at $Z/D = 3.21$. Figure 4.2.3 shows this is approximately the complete locking-on region. The middle one (slightly wider as compared with the upper and lower ones) is located at $Z/D = 5.67$ where some holes are covered. Smoke was released from these holes while Reels 2a and 2b were being taken.

Chapter 5

CONCLUDING REMARKS

An effective method of generating strong uniform shear flow with low turbulence level has been developed. A pair of curved screens with nonhomogeneous properties was used for the generation of shear flow. The method is based on a theoretical work of Elder (3.2) and the results of experimental modification by Maull

The highly three-dimensional characteristics of the secondary flow around a cylinder and the end effects have been discussed. The upward mean flow velocity of the secondary flow in the base region has been found to be as high as 0.44 U_m. Without taking into account the tunnel blockage effect, the local base pressure coefficients in the region free from end effects are found to be fairly constant and are not effected by Re_ℓ, β_ℓ, and Z/D. However, there is a systematic shift in the value of local base pressure coefficient for different test cylinders. This could be due to the difference in the degree of secondary flow effects and blockage.

The front stagnation and base pressures, as well as vortex shedding frequency, wake formation length and wake width have been measured at mid-span for a selected set of test cylinders and cases. The vortex formation length and the wake width are found to decrease as the Reynolds number increases. Effects of the incident velocity gradient on vortex formation length, wake width and base pressure are not conclusive.

Following the idea of a universal Strouhal number, St* initiated by Calvert, attempts to collapse the present data were made. The present St* values range from 0.160 to 0.115. This scattering of the data could be due to the secondary flow effects.

The vortices from a circular cylinder spanned across a uniform shear flow are found to shed discretely with finite span-wise length and different frequencies. The boundaries of the cells can be relatively stable or fluctuating vigorously. As the boundaries of the cell change, the vortex shedding frequency may also change. The stable cell length is found to decrease exponentially as the shear parameter increases.

The mechanism of complete locking-on has been discussed, based on the concepts of (1) modulation of vortex shedding process due to forced oscillation of the cable and (2) motion induced vortex. Oscillation of the cylinder (or cable) at a frequency f_c which is fairly close to f_s may cause vortex shedding within certain regions along the span of the body all at the frequency f_c. Oscillation of the body will also induce vortices which are in perfect synchronization with the motion of the body. The strength of the vortices shed from the body will be amplified due to this synchronization of Kármán vortex and motion induced vortex. This is believed to be the fundamental mechanism of complete locking-on.

Cable oscillation has a stabilizing effect on the Kármán vortex shedding process in the regions adjacent to the complete locking-on region. The vortex shedding frequencies near the complete locking-on region are found to be forced away from those values when the cable is in stationary state. The causes of this phenomenon have been postulated and discussed. At the regions outside the complete locking-on region, vortex shedding is intermittent with motion induced vortex and Kármán vortex.

The span-wise extent of complete locking-on for a cable oscillating in a shear flow does not increase monotonically as a_m/D increases. When a_m/D reaches a certain value, the span-wise extent of complete locking-on ceases to increase, instead, the complete locking-on region starts moving along the cable. This effect which is apparently caused by the curvature of the vibrating cable should impose some limitation on applying the results for stiff cylinders to flexible cables.

Based on a series of experimental results, a procedure is proposed to estimate the span-wise extent over which the vortex shedding locks onto the oscillation of a cable in a shear flow.

REFERENCES

2.1 Morkovin, M. V., "Flow Around Circular Cylinder--A Kaleidoscope of Challenging Fluid Phenomena," Symposium on Fully Separated Flows, Hansen, A. G., ed, ASME, New York, pp. 102-118, 1964.

2.2 Marris, A. W., "A Review on Vortex Streets, Periodic Wakes, and Induced Vibration Phenomenon," J. Basic Eng. (Trans. ASME) 86, pp. 185-196, 1964.

2.3 Küchemann, D., "Report on the I.U.T.A.M. Symposium on Concentrated Vortex Motions in Fluids," J. Fluid Mech. (1968), Vol. 21, Part 1, pp. 1-20.

2.4 Mair, W. A., and Maull, D. J., "Bluff Bodies and Vortex Shedding--A Report on Euromech 17," J. Fluid Mech. (1971), Vol. 45, Part 2, pp. 209-224.

2.5 Berger, E., and Wille, R., "Periodic Flow Phenomena," Annual Review of Fluid Mechanics, Vol. 4, pp. 313-340.

2.6 Bearman, P. W., "Some Recent Measurements of the Flow Around Bluff Bodies in Smooth and Turbulent Streams," Symposium on External Flows, Bristol University, July 1972, pp. B.1-B.15.

2.7 McCrosky, W. J., "Some Current Research in Unsteady Fluid Dynamics --The 1976 Freeman Scholar Lecture," Transactions of ASME, Journal of Fluids Engineering, Vol. 101, pp. 8-39.

2.8 Sarpkaya, T., "Vortex-Induced Oscillations--A Selective Review," Trans. of ASME, Journal of Applied Mech., Vol. 46, pp. 241-258, 1979.

2.9 Masch, F. D., and Moore, W. L., "Drag Forces in Velocity Gradient Flow," J. of the Hydraulics Division, Proceedings of the ASCE, Vol. 86, HY7, 1960, pp. 1-11.

2.10 Chen, C. F., and Mangione, B. J., "Vortex Shedding from Circular Cylinders in Sheared Flow," AIAA J. 7, pp. 1211-1212, June 1969.

2.11 Starr, M. R., "The Characteristics of Shear Flows Past a Circular Cylinder," Ph.D. Thesis, University of Bristol, Bristol, U.K. (1966).

2.12 Shaw, T. L., and Starr, M. R., "Shear Flows Past Circular Cylinder," J. of the Hydraulics Division, Proceedings of the ASCE, Vol. 98, HY3, pp. 461-473, March 1972.

2.13 Maull, D. J. and Young, R. A., "Vortex Shedding from Bluff Bodies in a Shear Flow," Flow-Induced Structural Vibrations, E. Naudascher, ed., pp. 717-729, 1974.

2.14 Maull, D. J., and Young, R. A., "Vortex Shedding from Bluff Bodies in a Shear Flow," J. Fluid Mech. (1973), Vol. 60, Part 2, pp. 401-409.

2.15 Davies, M. E., "The Effects of Turbulent Shear Flow on the Critical Reynolds Number of a Circular Cylinder," NPL Report Mar Sci R151, January 1976.

2.16 Mair, W. A., and Stansby, P. K., "Vortex Wakes of Bluff Cylinders in Shear Flow," SIAM J. Appl. Math, Vol. 28, No. 2, March 1975, pp. 519-540.

2.17 Rooney, D. M. and Peltzer, R. D., "The Effects of Shear and Roughness on Vortex Shedding Patterns Behind a Circular Cylinder at Critical Reynolds Numbers," A Report to the National Oceanic and Atmospheric Administration, Virginia Polytechnic Institute and State University, October 1979.

2.18 Stansby, P. K., "The Locking-On of Vortex Shedding Due to the Cross-Stream Vibration of Circular Cylinders in Uniform and Shear Flows," J. Fluid Mech., Vol. 74 (1976), Part 4, pp. 641-665.

2.19 Ferguson, N., and Parkinson, G. V., "Surface and Wake Flow Phenomena of the Vortex-Excited Oscillation of a Circular Cylinder, Transaction of the ASME, J. of Engineering for Industry, Vol. 89, November 1967, pp. 831-838.

2.20 Toebes, G. H., "The Unsteady Flow and Wake near an Oscillating Cylinder," Transaction of the ASME, J. of Basic Engineering, Vol. 91, 1969, pp. 493-505.

2.21 Koopmann, G. H., "The Vortex Wakes of Vibrating Cylinders at Low Reynolds Numbers," J. Fluid Mech. (1967), Vol. 28, Part 3, pp. 501-512.

2.22 Griffin, O. M., "The Unsteady Wake of an Oscillating Cylinder at Low Reynolds Number," Trans. ASME, Journal of Applied Mechanics, Paper No. 71-APM-33, December 1971, pp. 729-738.

2.23 Griffin, O. M., "Flow Near Self-Excited and Forced Vibrating Circular Cylinders," Trans. of ASME, Journal of Engineering for Industry, Vol. 94, May 1972, pp. 539-548.

2.24 Griffin, O. M., and Votaw, C. W., "The Vortex Street in the Wake of a Vibrating Cylinder," J. Fluid Mechanics (1972), Vol. 51, Part 1, pp. 31-48.

2.25 Griffin, O. M., and Ramberg, S. E., "The Vortex-Street Wakes of Vibrating Cylinders," J. Fluid Mechanics (1974), Vol. 66, Part 3, pp. 553-576.

2.26 Ramberg, S. E., and Griffin, O. M., "Vortex Formation in the Wake of a Vibrating Flexible Cable," Trans. ASME, Journal of Fluids Engineering, 96, December 1974, pp. 317-322.

2.27 Griffin, O. M., "Instability in the Vortex Street Wakes of Vibrating Bluff Bodies," Trans. ASME, Journal of Fluids Engineering, December 1973, pp. 579-581.

2.28 Ramberg, S. E., and Griffin, O. M., "Velocity Correlation and Vortex Spacing in the Wake of a Vibrating Cable," Trans. ASME, Journal of Fluids Engineering, Series 1, Vol. 98, No. 1, March 1976, pp. 10-18.

2.29 Ramberg, S. E., and Griffin, O. M., "The Effects of Vortex Coherence, Spacing and Circulation on the Flow-Induced Forces on Vibrating Cables and Bluff Structures," NRL Report 7945, January 1976.

3.1 Owen, P. R., and Zienkiewicz, K. H., "The Production of Uniform Shear Flow in a Wind Tunnel," J. Fluid Mech. (1957), Vol. 2, pp. 521-531.

3.2 Elder, J. W., "Steady Flow through Nonuniform Gauzes of Arbitrary Shape," J. Fluid Mech. (1959), Vol. 5, pp. 355-368.

3.3 Maull, D. J., "The Wake Characteristics of a Bluff Body in a Shear Flow," AGARD Conference Proceedings No. 48 (papers presented at the Fluid Dynamics Panel Specialists Meeting held at Munich, Germany, 15-17 September 1968, Paper #16).

3.4 Stansby, P. K., "The Effects of End Plates on the Base Pressure Coefficient of a Circular Cylinder," Aeronautical Journal, Vol. 78, No. 757, January, 1974, pp. 36-37.

3.5 Bearman, P. W., "Corrections for the Effect of Ambient Temperature Drift on Hot-Wire Measurements in Incompressible Flow," DISA Information Bulletin No. 11, 1970.

4.1 Roshko, A., "On the Drag and Shedding Frequency of Two-Dimensional Bluff Bodies," NACA Technical Note 3169, Washington D.C., 1954.

4.2 Bloor, M. S., "The Transition to Turbulence in the Wake of a Circular Cylinder, J. of Fluid Mech. (1963), Vol. 19, Part 2, pp. 290-303.

4.3 Bloor, M. S., and Gerrard, J. H., "Measurements on Turbulent Vortices in a Cylinder Wake," Proceedings of the Royal Society, London, England, Series A, Vol. 294, 1966, pp. 319-342.

4.4 Gerrard, J. H., "The Mechanics of the Formation Region of Vortices Behind Bluff Bodies," J. Fluid Mech. (1966), Vol. 25, Part 2, pp. 401-413.

4.5 Bearman, P. W., "On Vortex Shedding from a Circular Cylinder in the Critical Reynolds Number Regime," J. Fluid Mech. (1969), Vol. 37, Part 3, pp. 577-585.

4.6 Griffin, O. M., "A Universal Strouhal Number for the "Locking-On" of Vortex Shedding to the Vibrations of Bluff Cylinders," J. Fluid Mechanics, Vol. 85, Part 3, pp. 591-606, 1978.

4.7 Griffin, O. M., "Universal Similarity in the Wakes of Stationary and Vibrating Bluff Structure," Fifth International Conference on Wind Engineering (V-10), 8-14 July 1979, Colorado State University, Fort Collins, Colorado.

4.8 Calvert, J. R., "Experiments on Low Speed Flow Past Cones," J. Fluid Mechanis, Vol. 27, 1967, pp. 273-279.

4.9 Simmons, J. E. L., "Similarities Between Two-Dimensional and Axisymmetric Vorex Wakes," Aeronautical Quarterly, Vol. 26, 1977, pp. 15-20.

4.10 Hama, Francis, R., "Three-Dimensional Vortex Pattern Behind a Circular Cylinder," J. of the Aeronautical Sciences, pp. 156-158, February 1957.

4.11 Gerrard, J. H., "The Three-Dimensional Structure of the Wake of a Circular Cylinder," J. of Fluid Mechanics, Vol. 25, Part 1, pp. 143-164.

4.12 Bishop, R. E. D., and Hassan, A. Y., "The Lift and Drag Forces on a Circular Cylinder in a Flowing Fluid," Proc. Roy. Soc. London, Ser. A 277: pp. 32-50, pp. 51-75

4.13 Kobayashi, Hiroshi, "Vortex Oscillations of Bluff Cylinders in a Smooth Flow," Memoirs of the Research Institute of Science and Engineering, Ritsumeikan University, Kyoto, Japan, No. 37, 1979.

4.15 Komatsu, S., and Kobayashi, H., "Vortex Induced Oscillation of Bluff Cylinders," J. Wind Engng. and Ind. Aerodyn., Vol. 6, No. 3-4, 1980, pp. 335-382.

4.15 Mei, V. C., and Currie, I. G., "Flow Separation on a Bivrating Circular Cylinder," Physics of Fluids, Vol. 12, No. 11, pp. 2248-2254, 1969.

4.16 Votaw, C. W., and Griffin, O. M., "Vortex Shedding from Smooth Cylinders and Strand Cables," Journal of Basic Engineering, Trans. ASME, Series D, Vol. 93 pp. 457-460, 1971.

Table 4.1.1 Test Scheme of Base Pressure Measurements and the Related Parameters

D(in.)	H/D	D/W(%) Blockage Ratio	β_m	Re_m	Re'_ℓ	β''_ℓ
0.50	36	2.1	0.034	1,960	1,170-3,000	0.023-0.059
0.75	24	3.1	0.051	2,950	2,020-4,170	0.038-0.077
1.00	18	4.2	0.068	3,920	2,930-5,200	0.053-0.095

', " In the range where base pressure coefficient is constant

Table 4.1.2 Vortex Formation Length Wake Width and Their Related Parameters

D(in.)	Re_m	L_f/D	D'/D	β_m	$-C_{pb_\ell}$
0.25	1,075	2.75	1.00	0.017	0.65
	2,060	2.50	1.00	0.017	0.79
0.50	820	2.50	1.00	0.036	1.0
	2,230	2.38	0.84	0.034	0.81
	4,330	2.05	0.82	0.034	0.86
	4,670	1.80	0.82	0.034	0.88
0.75	2,130	2.33	1.00	0.052	0.93
	3,110	2.00	0.90	0.050	0.84
	3,810	1.83	0.86	0.050	0.86
	6,780	1.58	0.84	0.050	1.03
1.00	2,200	2.38	1.08	0.070	1.0
	4,150	2.07	1.00	0.068	0.97
	8,260	1.50	0.94	0.066	1.17
1.50	7,620	1.50	1.04	0.100	1.29
	13,650	1.22	1.00	0.100	1.43

Table 4.1.3 Experimental Scheme for Rigid Cylinders and their Associated Parameters

D(in.)	β_m	Re_m	H/D	D/W (blockage ratio in %)
0.25	0.017	900	72	1.0
	0.016	1,830	72	1.0
0.50	0.037	970	36	2.1
	0.034	1,770	36	2.1
	0.033	3,600	36	2.1
	0.034	4,500	36	2.1
0.75	0.052	1,950	24	3.1
	0.052	2,920	24	3.1
	0.050	3,900	24	3.1
	0.051	6,730	24	3.1
1.00	0.075	1,950	18	4.2
	0.069	3,900	18	4.2
	0.065	7,800	18	4.2
1.50	0.100	7,800	12	6.3
	0.100	13,460	12	6.3

Table 4.1.4 List of Movies Obtained with High Speed Movie Camera for Stationary Cylinders in Uniform Shear Flows

Reel 1	Side View:	$D = 1.0$ in., $Re_m = 1{,}950$, $\beta_m = 0.075$
Reel 2	Side View:	$D = 0.50$ in., $Re_m = 970$, $\beta_m = 0.037$
Reel 3	Top View:	$D = 0.48$ in., $Re_\ell = 1{,}140$, $\beta_\ell = 0.034$
		$Z/D = 5.67$
Reel 4	Top View:	$D = 0.48$ in., $Re_\ell = 880$, $\beta_\ell = 0.034$
		$Z/D = -1.81$
Reel 5	Side View:	$D = 0.48$ in., $Re_m = 960$, $\beta_m = 0.034$,
		$Z/D = -1.81$

Table 4.2.1 List of Test Runs and Results for Cables in Shear Flows

Test	D(in.)	Re_m	β_m	ℓ/D	f_c(Hz)	a_m/D	
1	0.49	1,000	0.035	20	26.5	0.60 (Fig. 4.2.2 & 4.2.3)	0.05 (Fig. 4.2.10 & 4.2.11)
						0.40 (Fig. 4.2.4 & 4.2.5)	0.025(Fig. 4.2.12 & 4.2.13)
						0.20 (Fig. 4.2.6 & 4.2.7)	0.00 (Fig. 4.2.14 & 4.2.15)
						0.10 (Fig. 4.2.8 & 4.2.9)	
2	0.50	1,000	0.036	20	19.5	0.20 (Fig. 4.2.16 & 4.2.17)	0.07 (Fig. 4.2.20 & 4.2.21)
						0.12 (Fig. 4.2.18 & 4.2.19)	0.045(Fig. 4.2.22 & 4.2.23)
3	0.45	1,700	0.031	22.2	51.0	0.35 (Fig. 4.2.24 & 4.2.25)	0.11 (Fig. 4.2.32 & 4.2.33
						0.25 (Fig. 4.2.26 & 4.2.27)	0.05 (Fig. 4.2.34 & 4.2.35)
						0.21 (Fig. 4.2.28 & 4.2.29)	0.0 (Fig. 4.2.36 & 4.2.37)
						0.15 (Fig. 4.2.30 & 4.2.31)	
4	0.46	1,725	0.031	22.0	43.0	0.54*	0.12(Fig. 4.2.40 & 4.2.41)
						0.37*	0.04(Fig. 4.2.42 & 4.2.43)
						0.20 (Fig. 4.2.38 & 4.2.39)	0.02 (Fig. 4.2.44 & 4.2.45)
						0.17*	
5	0.25	660	0.017	40.0	63.5	0.66 (Fig. 4.2.46 & 4.2.47)	0.13 (Fig. 4.2.52 & 4.2.53)
						0.50*	0.07*
						0.30 (Fig. 4.2.48 & 4.2.49)	0.03*

Table 4.2.1 (Continued)

Test	D(in.)	Re_m	β_m	ℓ/D	f_c(Hz)	a_m/D	
5						0.18 (Fig. 4.2.50 & 4.2.51)	0.0 (Fig. 4.2.54 & 4.2.55
6	0.25	735	0.016	40.0	63.5	0.63 (Fig. 4.2.56 & 4.2.57)	0.23 (Fig. 4.2.62 & 4.2.63)
						0.47 (Fig. 4.2.58 & 4.2.59)	0.08*
						0.37 (Fig. 4.2.60 & 4.2.61	0.0 (Fig. 4.2.64 & 4.2.65)

*Spectra data collected only at the boundaries of the complete locking-on region.

Table 4.2.2. List of $\tilde{S}_{sm}$ and S_{sm} at the Boundaries of Complete Locking-On for Cables in Uniform Shear Flows

Test	S_c	a_m/D	a_z/D	$\tilde{S}_{sm}$	S_{sm}
1	0.238	0.6	0.234	0.329	0.306
			0.570	0.158	0.238
		0.4	0.184	0.324	0.300
			0.398	0.153	0.232
		0.2	0.120	0.302	0.286
			0.20	0.180	0.220
		0.1	0.070	0.306	0.280
			0.097	0.185	0.212
		0.05	0.038	0.279	0.274
			0.049	0.194	0.212
		0.025	0.020	0.279	0.270
			0.025	0.205	0.220
2	0.178	0.20	0.186	0.238	0.204
			0.0	0.143	0.143
		0.12	0.186	0.219 - 0.238	0.204
			0.0	0.137 - 0.151	0.143
		0.07	0.063	0.210 - 0.228	0.203
			0.025	0.137 - 0.160	0.162
		0.045	0.039	0.215	0.198
			0.009	0.137 - 0.164	0.152
3	0.217	0.35	0.228	0.298	0.265
			0.343	0.160	0.200
		0.25	0.183	0.294	0.264
			0.233	0.158	0.204
		0.21	0.153	0.277	0.264
			0.187	0.164	0.196
		0.15	0.116	0.281	0.262
			0.113	0.170	0.183
		0.11	0.089	0.277	0.258
			0.098	0.170	0.196
		0.05	0.043	0.266	0.249
			0.045	0.175	0.196

Table 4.2.2. (Continued).

Test	S_c	a_m/D	a_z/D	$\tilde{S}_{sm}$	S_{sm}
4	0.185	0.54	0.456	0.285	0.252
			0.216	0.142	0.168
		0.37	0.329	0.280	0.240
			0.118	0.147	0.162
		0.20	0.162	0.272	0.227
			0.08	0.151	0.168
		0.17	0.167	0.267	0.224
			0.068	0.151	0.168
		0.12	0.12	0.259	0.222
			0.048	0.149	0.167
		0.04	0.039	0.229	0.212
			0.016	0.160	0.167
		0.02	0.020	0.229	0.215
			0.008	0.159	0.168
		0.01	0.009	0.211	0.204
			0.004	0.164	0.168
5	0.216	0.66	0.422	0.306	0.267
			0.620	0.163	0.228
		0.50	0.325	0.293	0.266
			0.495	0.157	0.208
		0.30	0.231	0.286	0.256
			0.285	0.167	0.204
		0.18	0.146	0.283	0.250
			0.173	0.167	0.203
		0.13	0.098	0.269	0.259
			0.121	0.174	0.202
		0.07	0.060	0.245	0.242
			0.065	0.184	0.202
		0.03	0.027	0.245	0.238
			0.029	0.197	0.204

Table 4.2.2. (Continued).

Test	S_c	a_m/D	a_z/D	$\tilde{S}_{sm}$	S_{sm}
6	0.192	0.63	0.479	0.288	0.260
			0.586	0.154	0.202
		0.47	0.381	0.288	0.256
			0.423	0.136	0.200
		0.37	0.307	0.285	0.252
			0.311	0.151	0.194
		0.23	0.211	0.257	0.226
			0.150	0.154	0.178
		0.08	0.079	0.227	0.213
			0.53	0.164	0.178

Table 4.2.3. List of Movies Obtained with High Speed Movie Camera for a Cable in Uniform Shear Flow

Reel 1	Side View:	$D = 0.48$ in.,	$Re_m = 960$,	$\beta_m = 0.034$
		$f_c = 27.0$ Hz,	$a_m/D = 0.45$	
Reel 2a	Top View:	$D = 0.48$ in.,	$Re_\ell = 1{,}140$,	$\beta_\ell = 0.034$
		$f_c = 0.0$ Hz,	$Z/D = 5.67$	
Reel 2b	Top View:	$D = 0.48$ in.,	$Re_\ell = 1{,}140$,	$\beta_\ell = 0.034$
		$f_c = 27.0$ Hz,	$a_\ell/D = 0.30$,	$Z/D = 5.67$
Reel 3a	Top View:	$D = 0.48$ in.,	$Re_\ell = 880$,	$\beta_\ell = 0.034$
		$f_c = 0.0$ Hz,	$Z/D = -1.81$	
Reel 3b	Top View:	$D = 0.48$ in.,	$Re_\ell = 880$,	$\beta_\ell = 0.034$
		$f_c = 27.0$ Hz,	$a_\ell/D = 0.43$,	$Z/D = -1.81$
Reel 3c	Top View:	$D = 0.48$ in.,	$Re_\ell = 880$,	$\beta_\ell = 0.034$
		$f_c = 27.0$ Hz,	$a_\ell/D = 0.43$,	$Z/D = -1.81$
Reel 4a	Side View:	$D = 0.48$ in.,	$Re_\ell = 880$,	$\beta_\ell = 0.034$
		$f_c = 0.0$ Hz,	$Z/D = -1.81$	
Reel 4b	Side View:	$D = 0.48$ in.,	$Re_m = 960$,	$\beta_m = 0.034$
		$f_c = 27.0$ Hz,	$a_m/D = 0.45$,	$Z/D = -1.81$
Reel 5	Side View:	$D = 0.48$ in.,	$Re_m = 960$,	$\beta_m = 0.034$
		$f_c = 27.0$ Hz,	$a_m/D = 0.45$,	$3.21 \leq Z/D \leq 7.99$

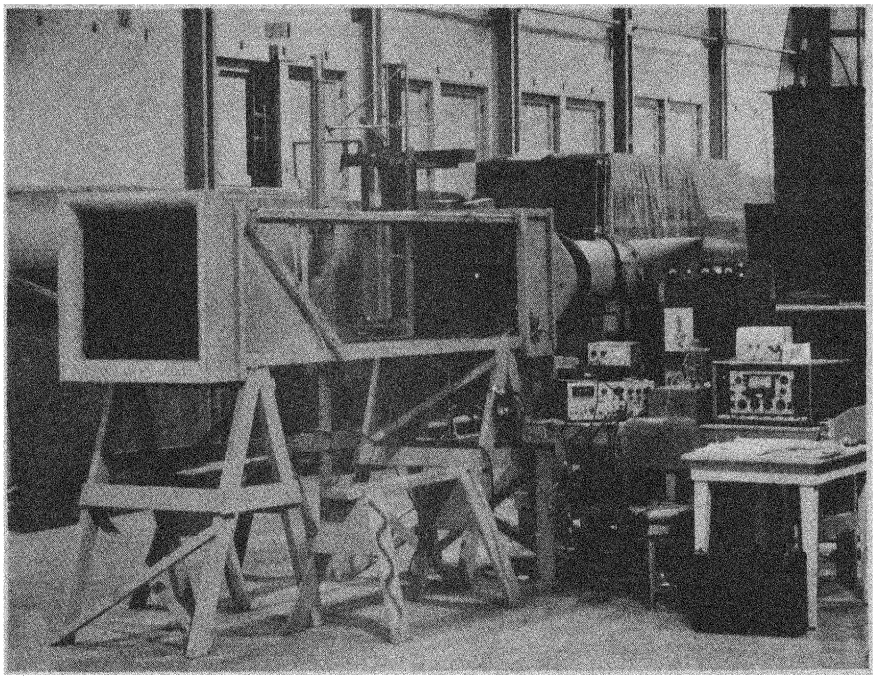

Figure 3.1. Wind-Tunnel Experimental Configuration

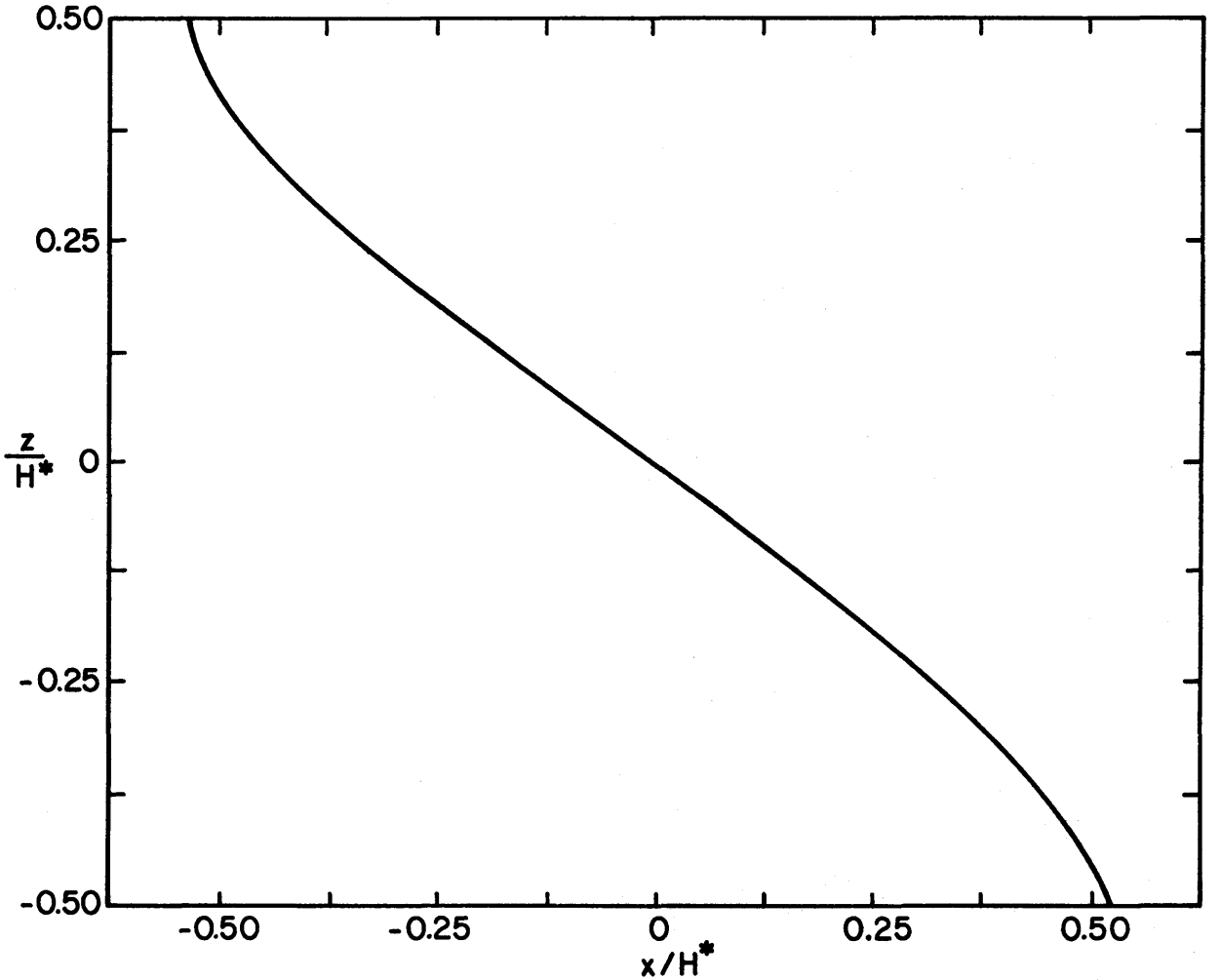

Figure 3.2. Shape of Gauze Used to Generate the Shear Flow

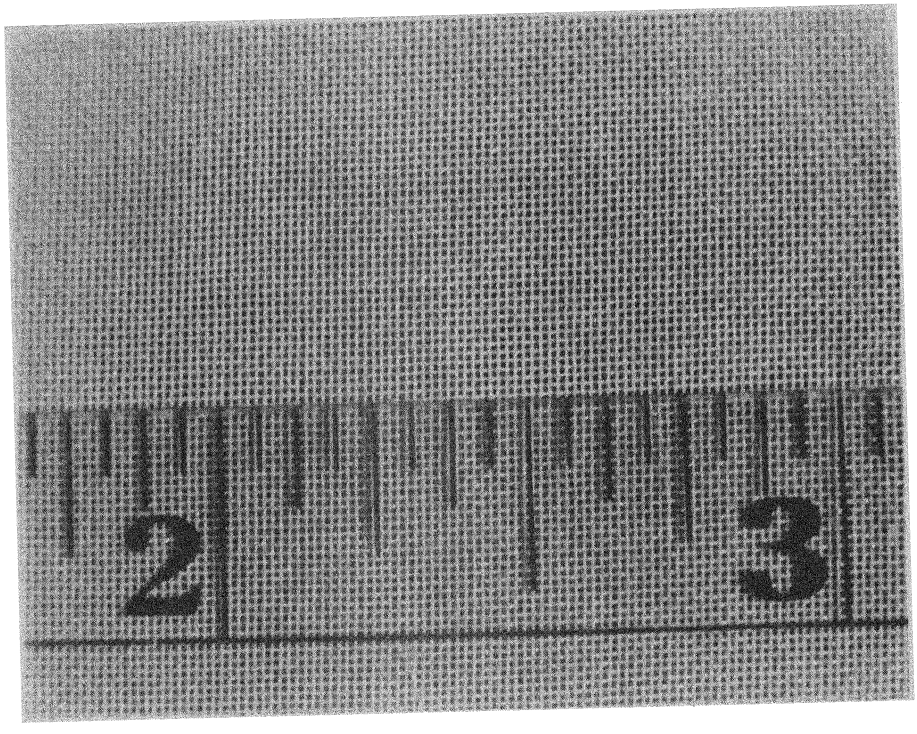

Figure 3.3. Magnified View of Screen Fabric (gauze)

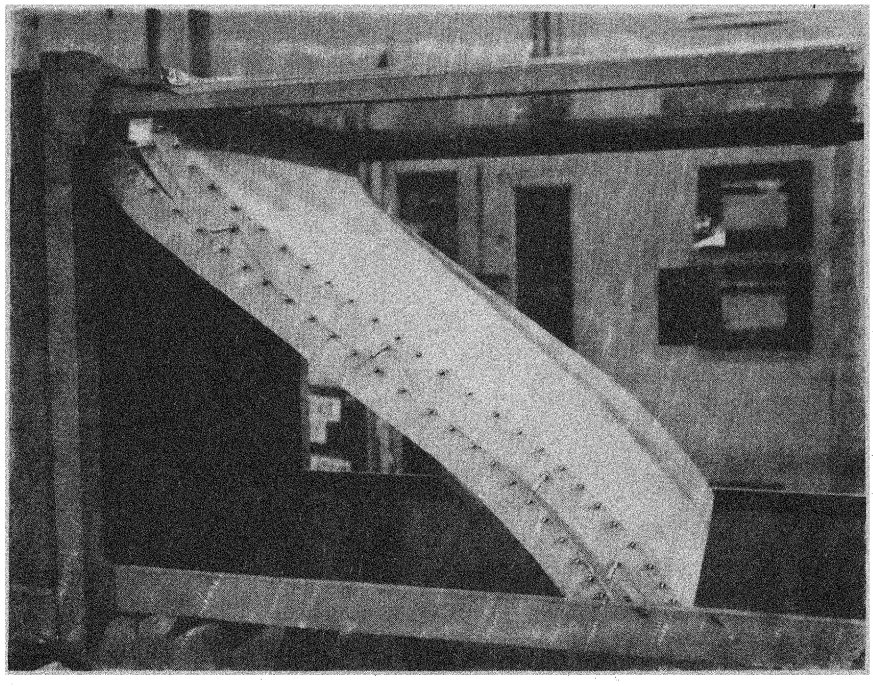

Figure 3.4. Double Curved Screen Gauze with Nonhomogeneous Properties

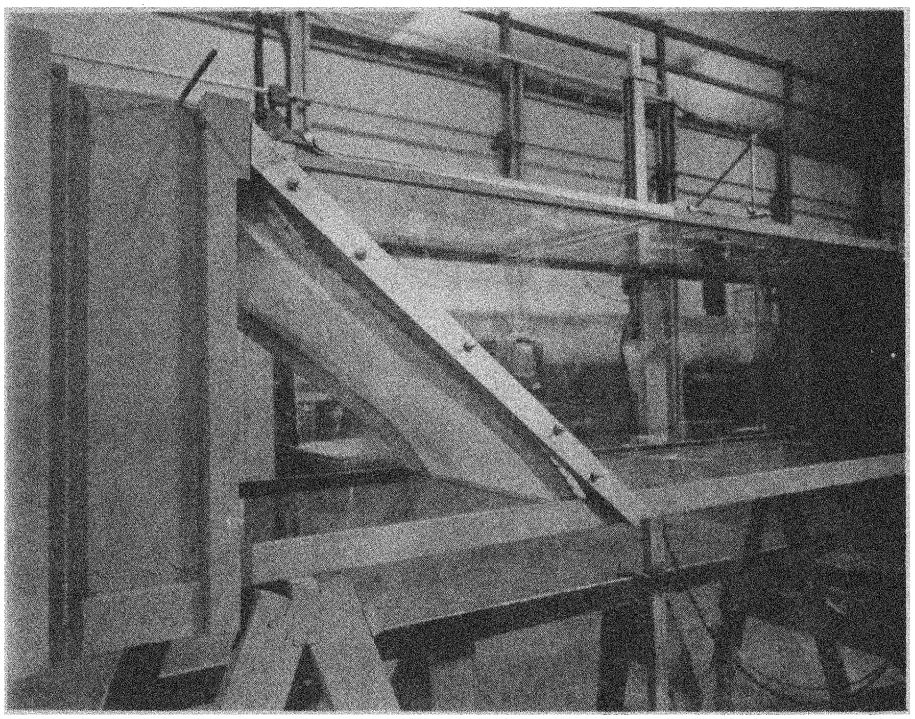

Figure 3.5. Experimental Set-up of Uniform Shear Flow Generator

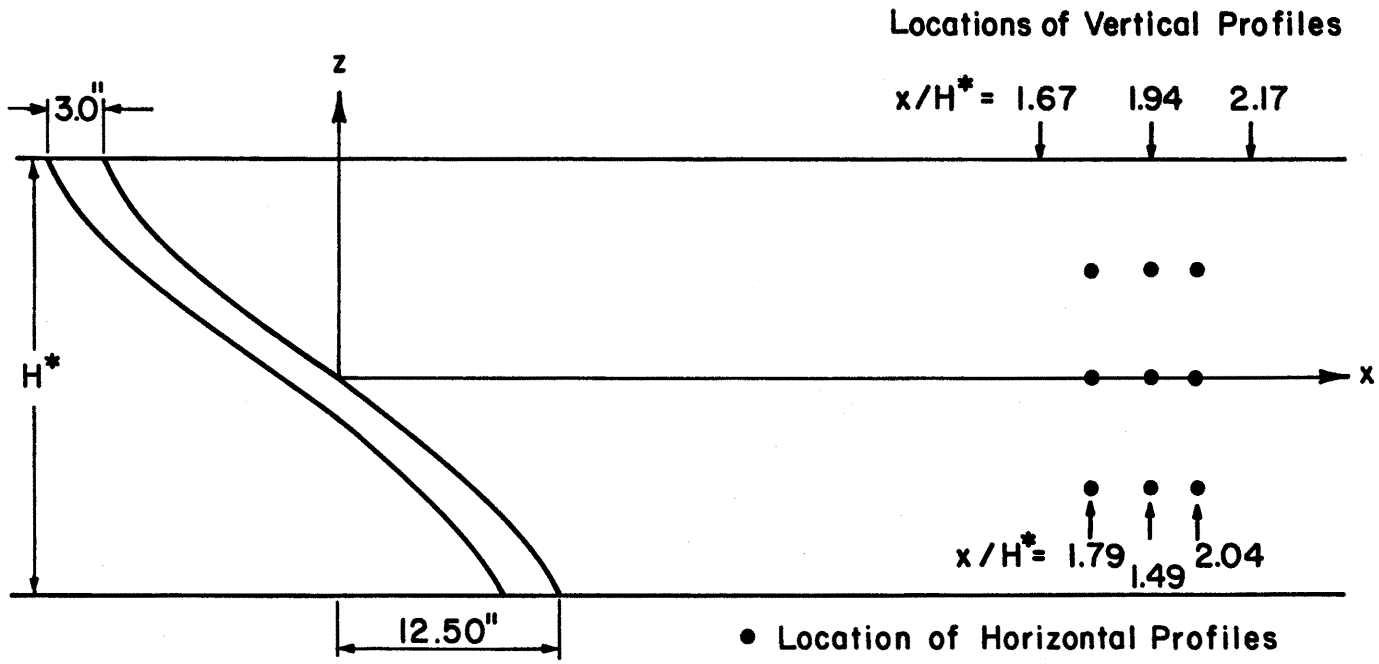

Figure 3.6. Coordinate System and Locations of Velocity Profile Measurements

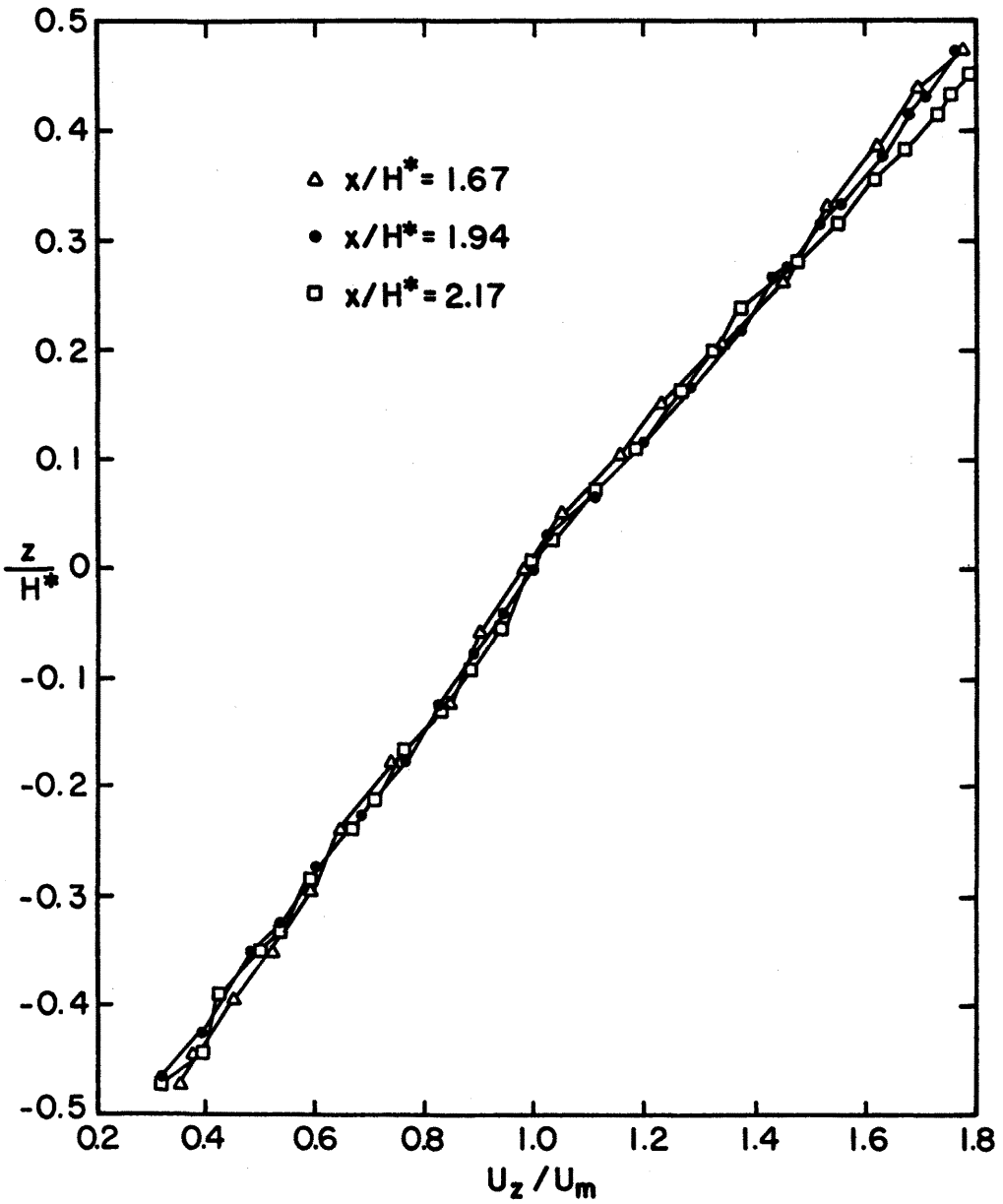

Figure 3.7. Vertical Profiles of Mean Velocity

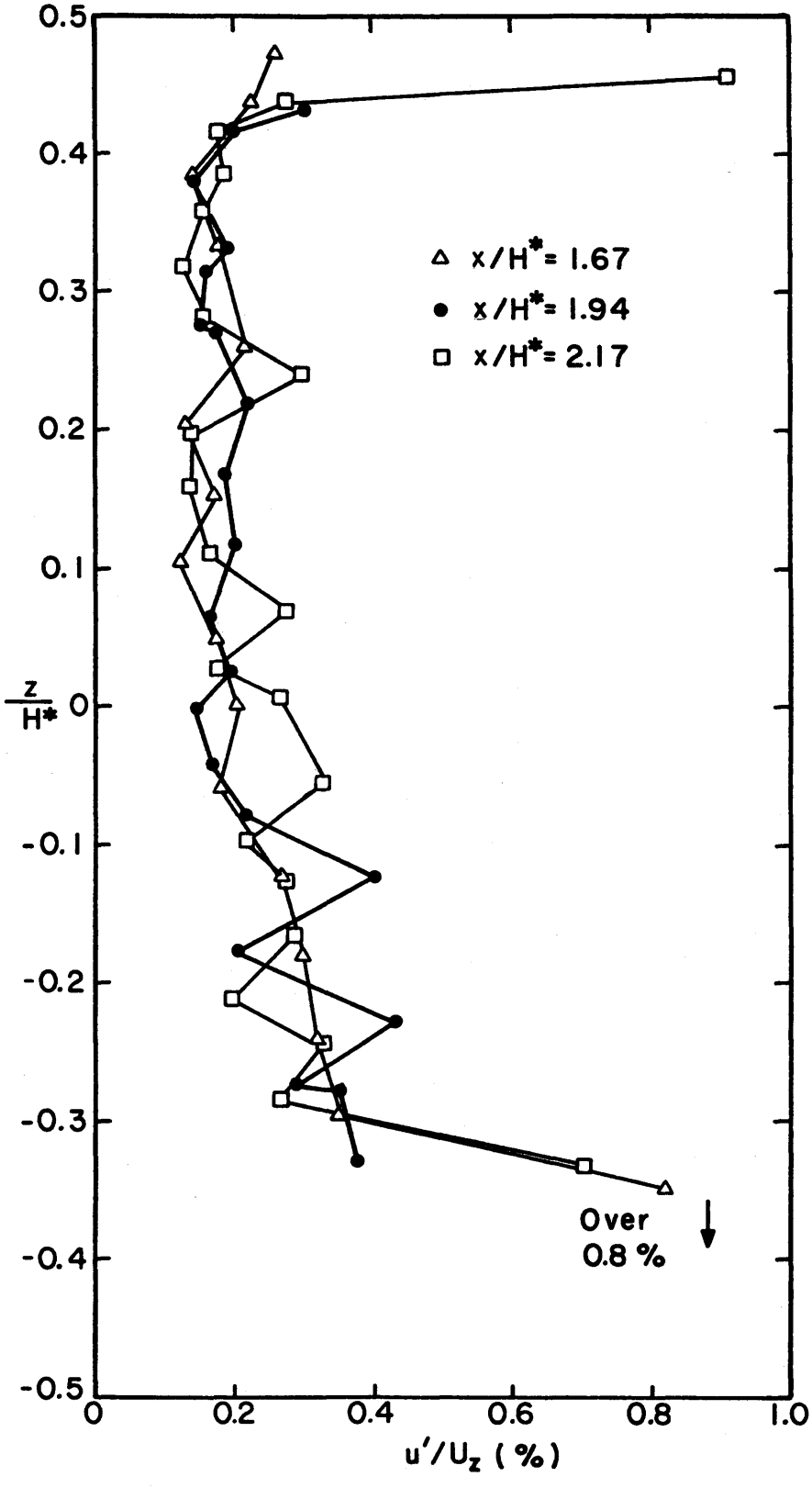

Figure 3.8. Vertical Profiles of Turbulence Intensity

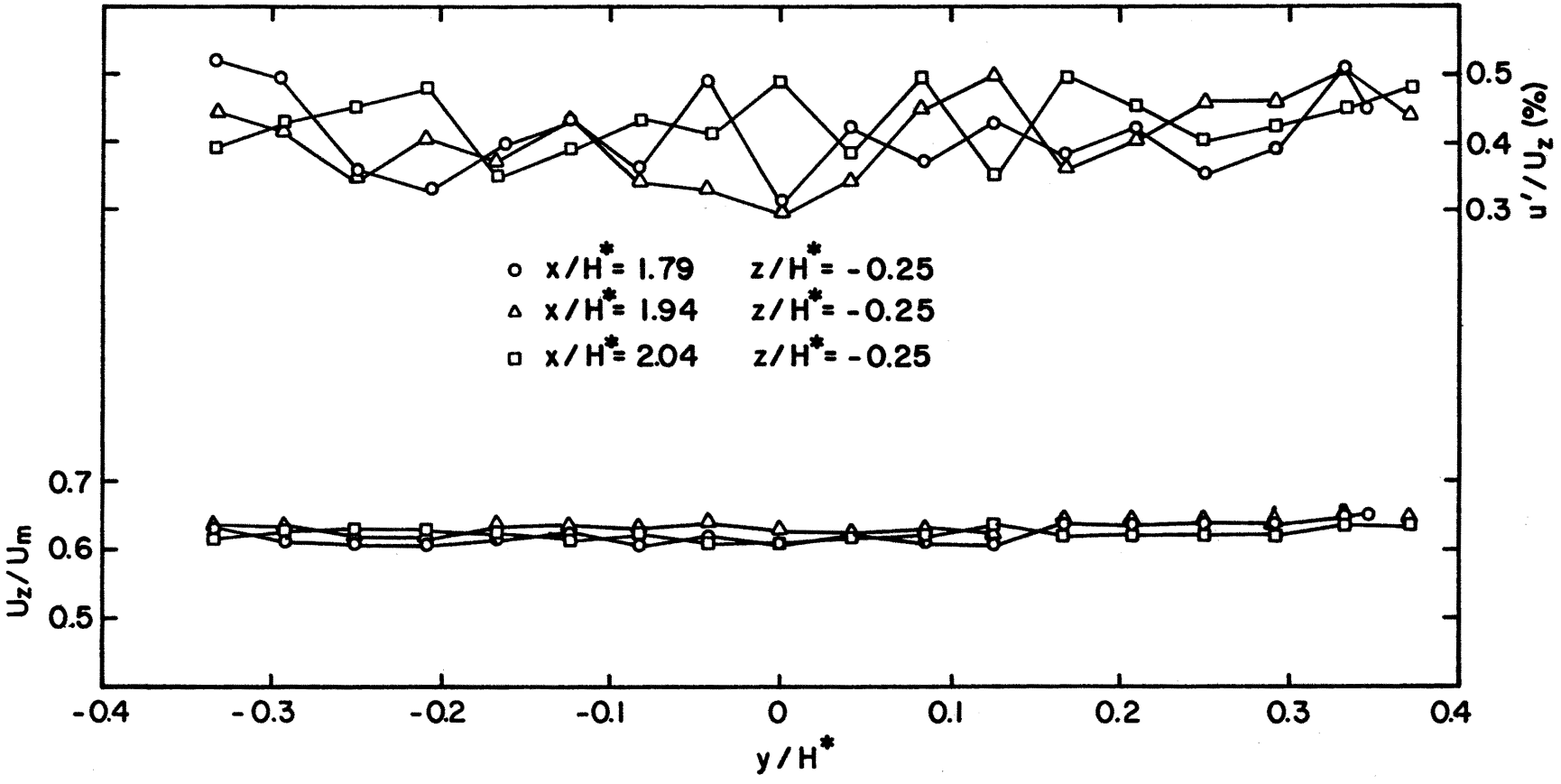

Figure 3.9. Horizontal Profiles at z/H* = 0.25

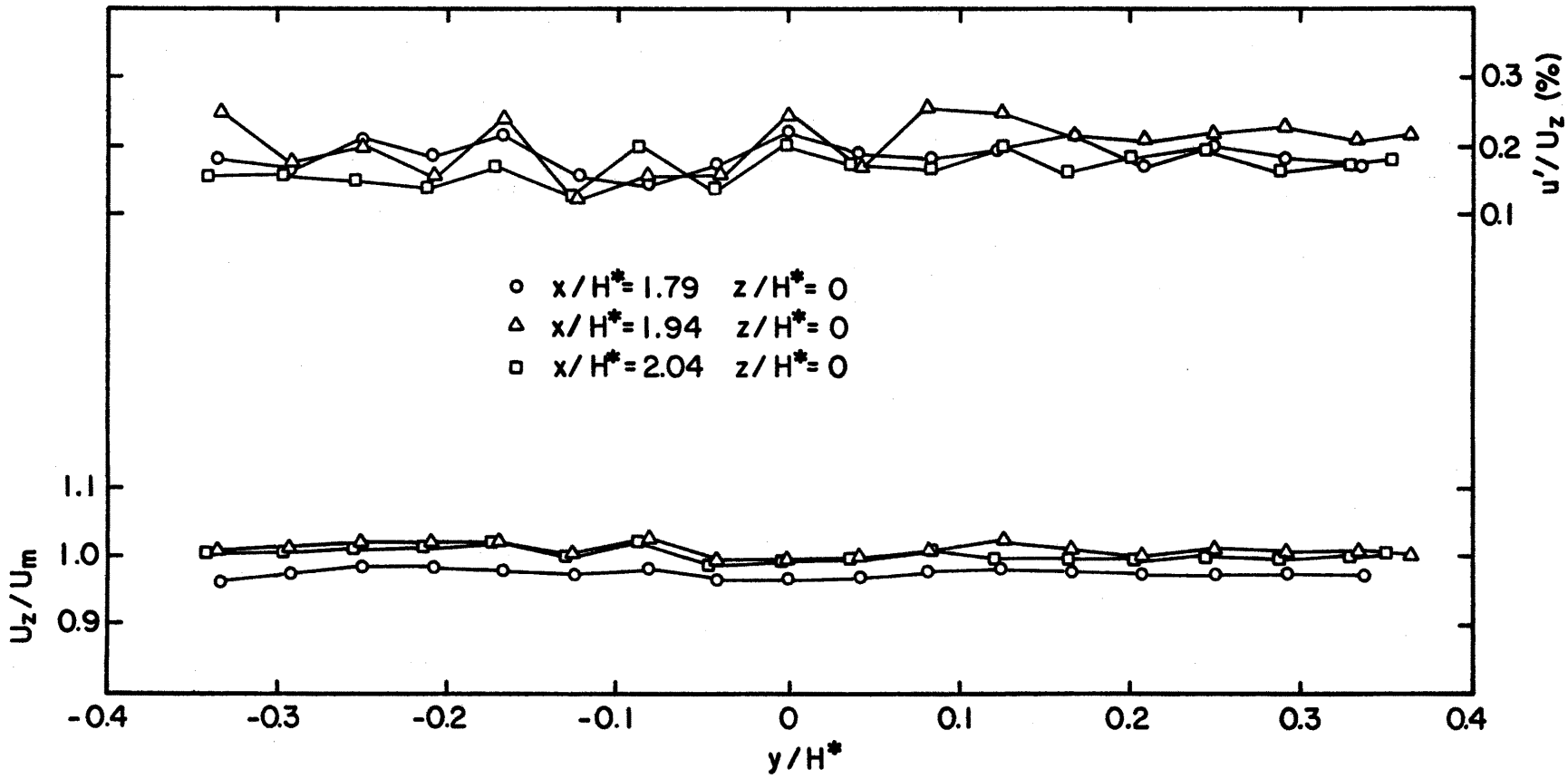

Figure 3.10. Horizontal Profiles at z/H* = 0.0

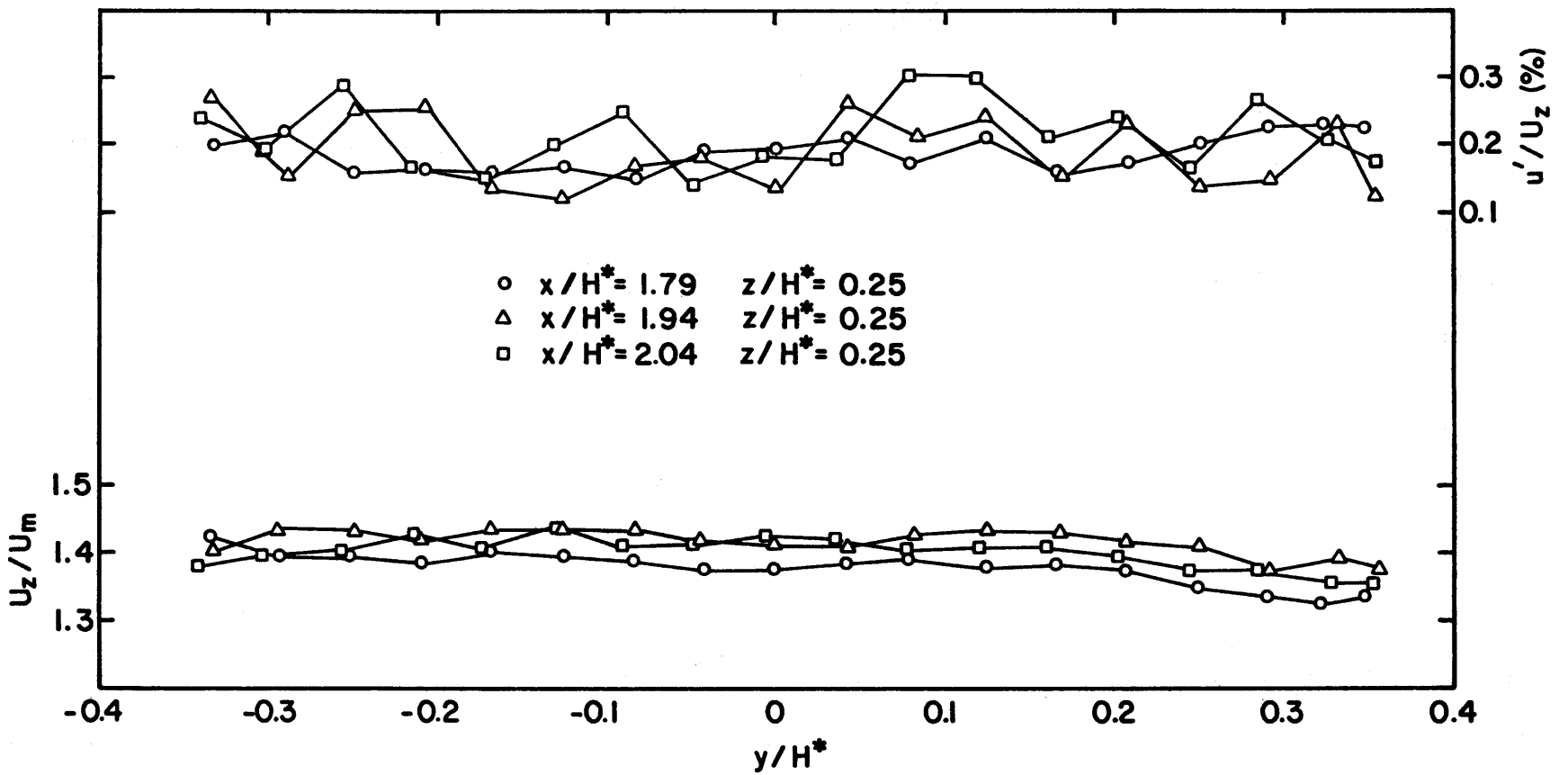

Figure 3.11. Horizontal Profiles at z/H* = 0.25

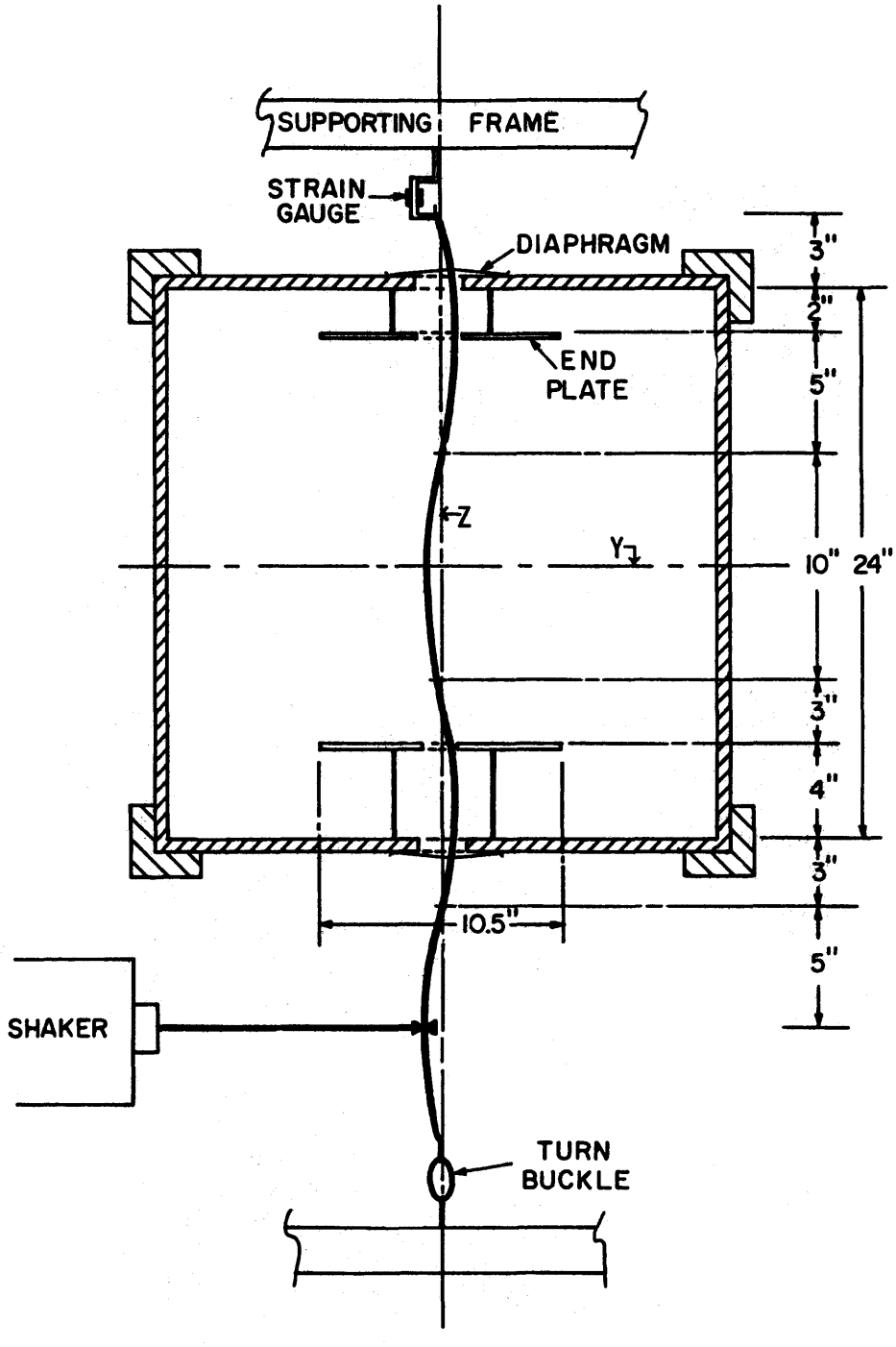

Figure 3.12. Diagram of Experimental Arrangement for Vibrating Cable (facing upwind)

Figure 4.1.1. Secondary Flow in the Lee Side of a Cylinder in a Uniform Shear Flow (t = 0)

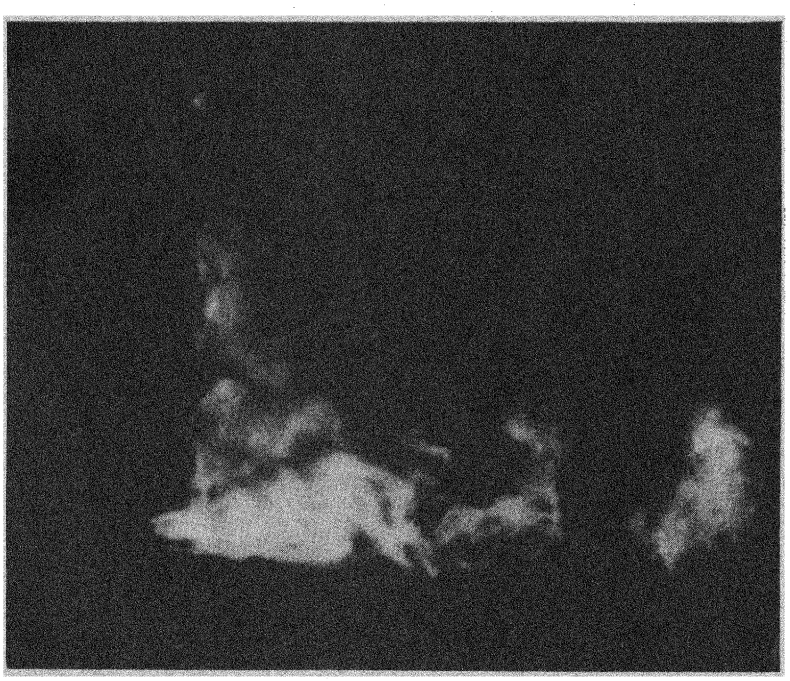

Figure 4.1.2. Secondary Flow in the Lee Side of a Cylinder in a Uniform Shear Flow (t = 0.1 sec)

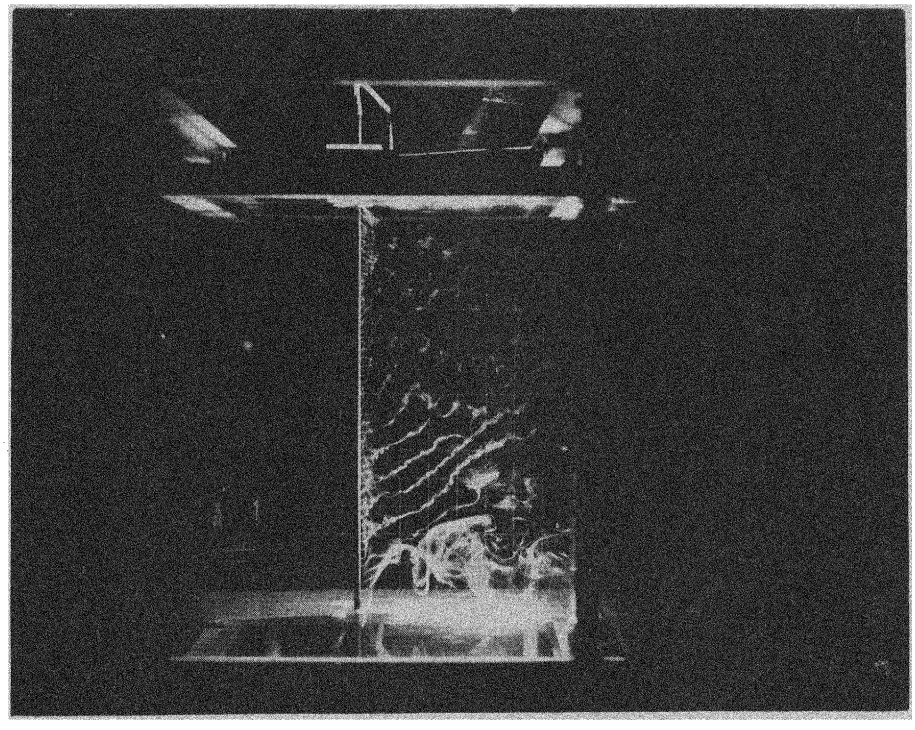

Figure 4.1.3. The Lower Separation Bubble

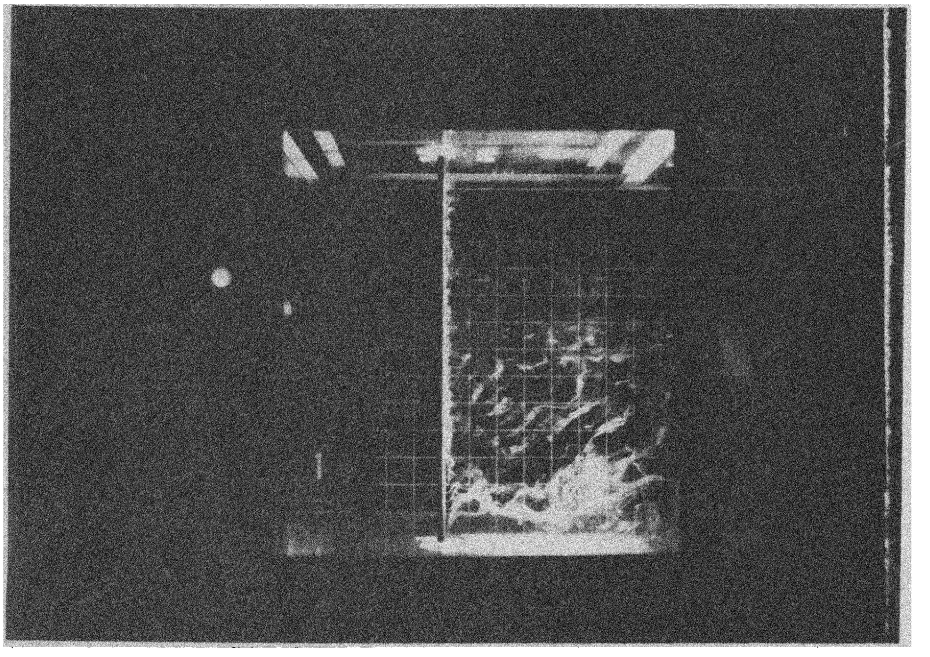

Figure 4.1.4. The Lower Separation Bubble

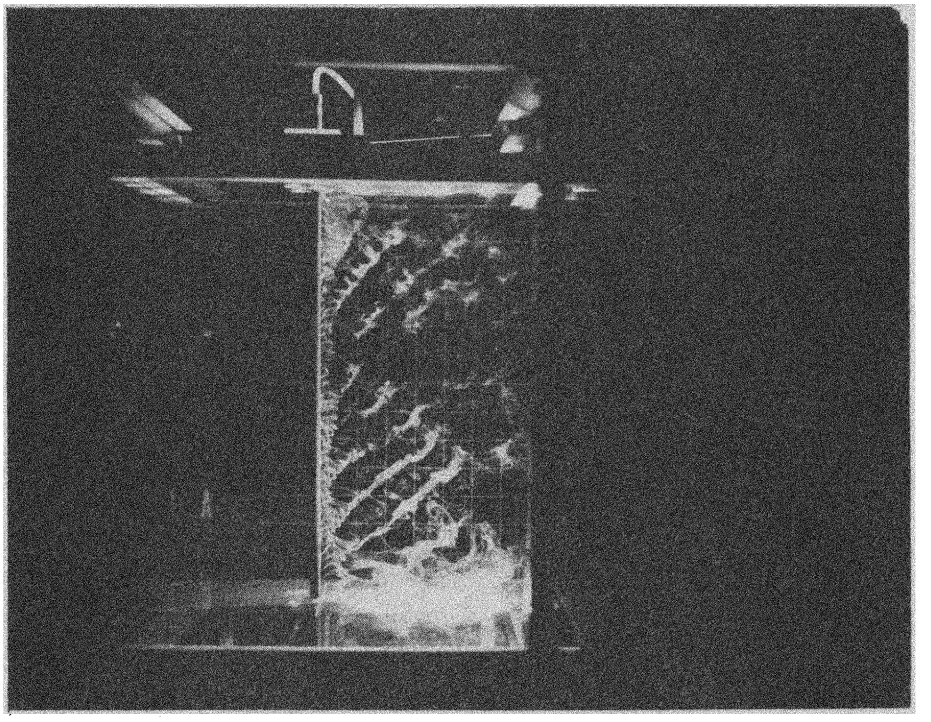

Figure 4.1.5. The Upper Separation Bubble

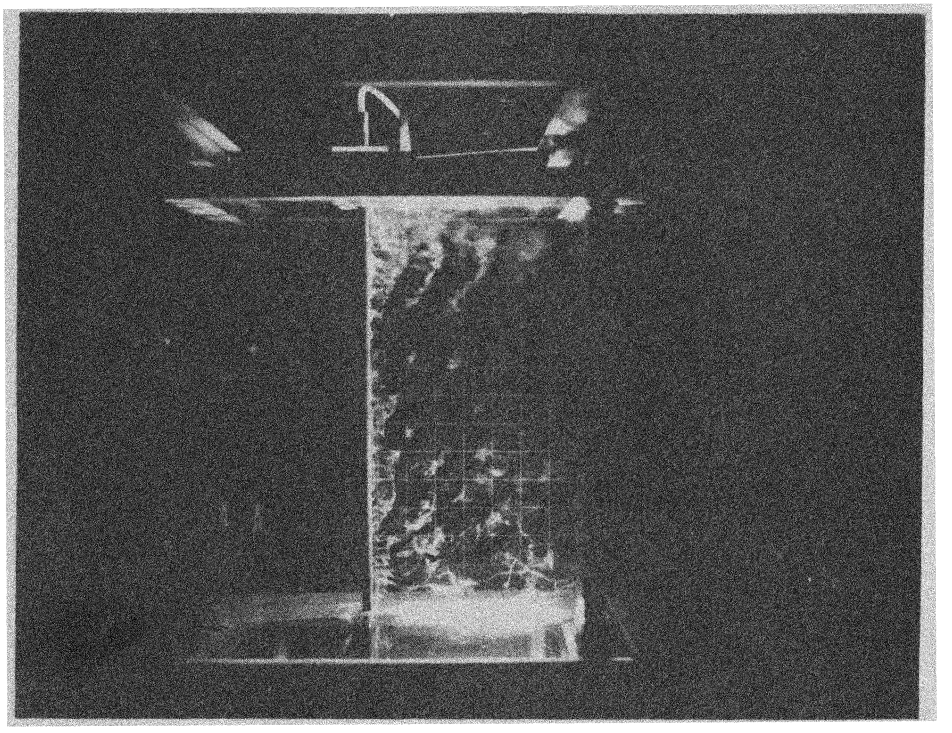

Figure 4.1.6. The Upper Separation Bubble

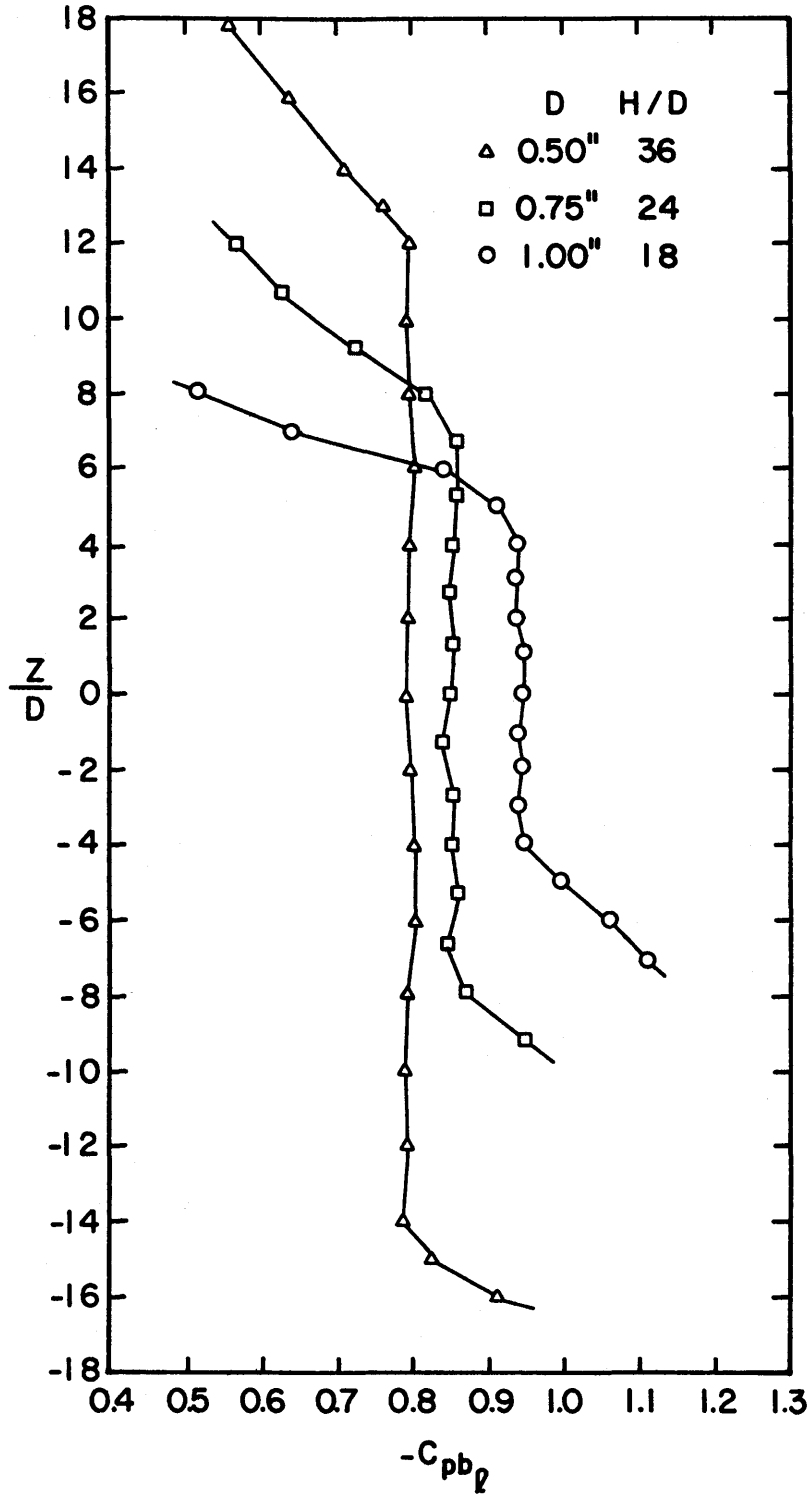

Figure 4.1.7. Base Pressure Coefficient, C_{pb_ℓ}, on Circular Cylinders in Uniform Shear Flow

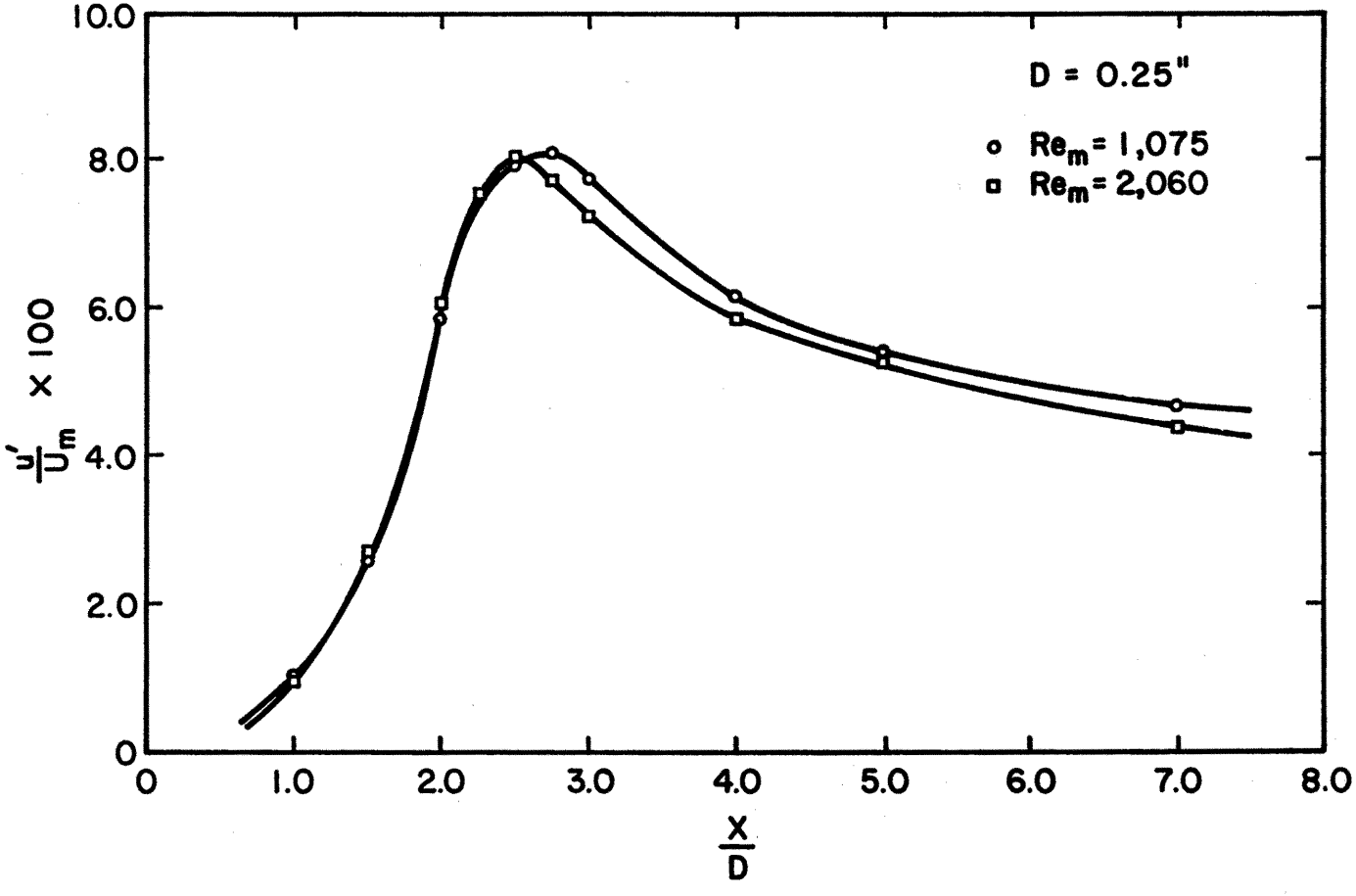

Figure 4.1.8. Turbulence Level (rms fluctuations at second harmonic of the vortex shedding frequency/U_m) on the Wake Axis

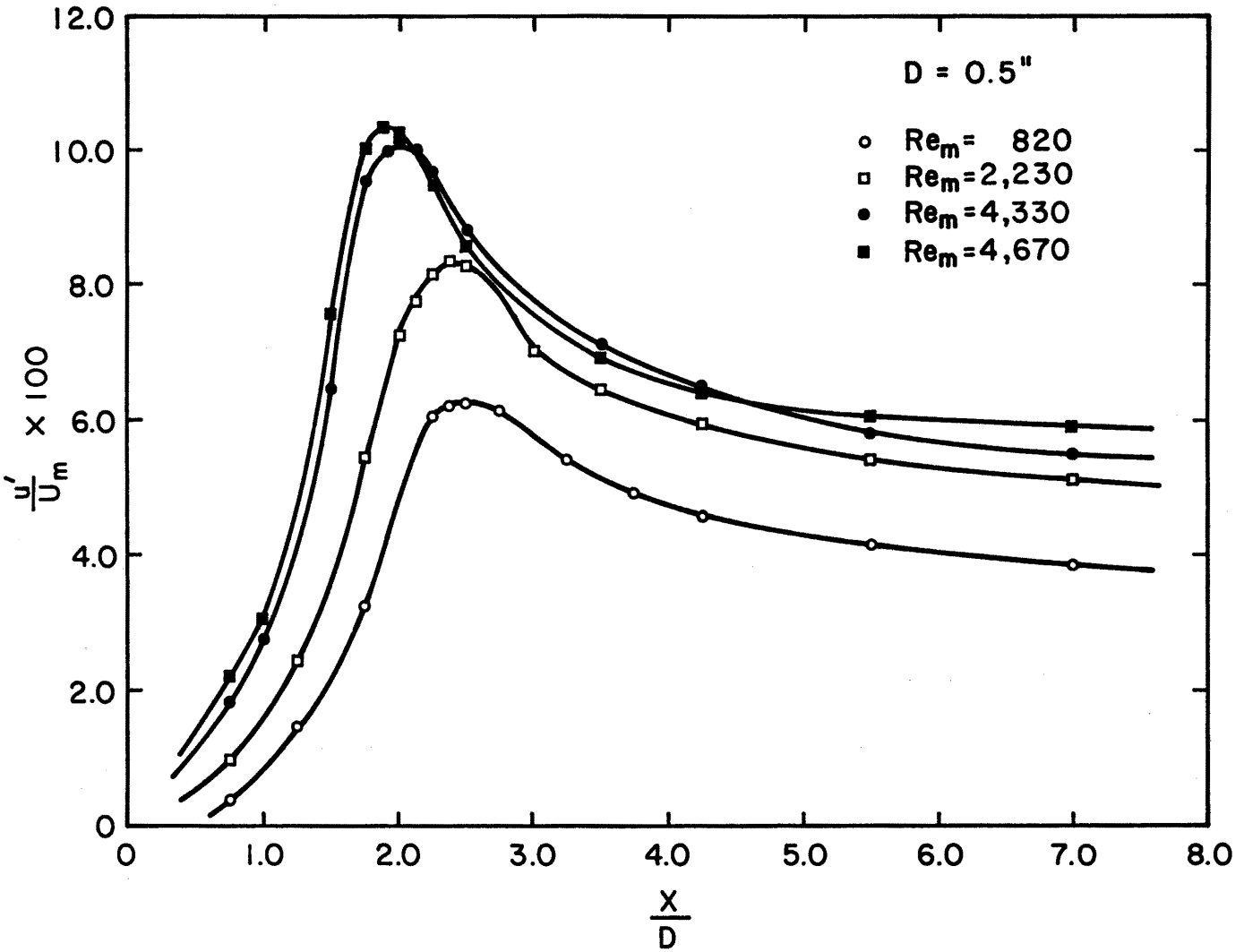

Figure 4.1.9. Turbulence Level (rms fluctuations at second harmonic of the vortex shedding frequency/U_m) on the Wake Axis

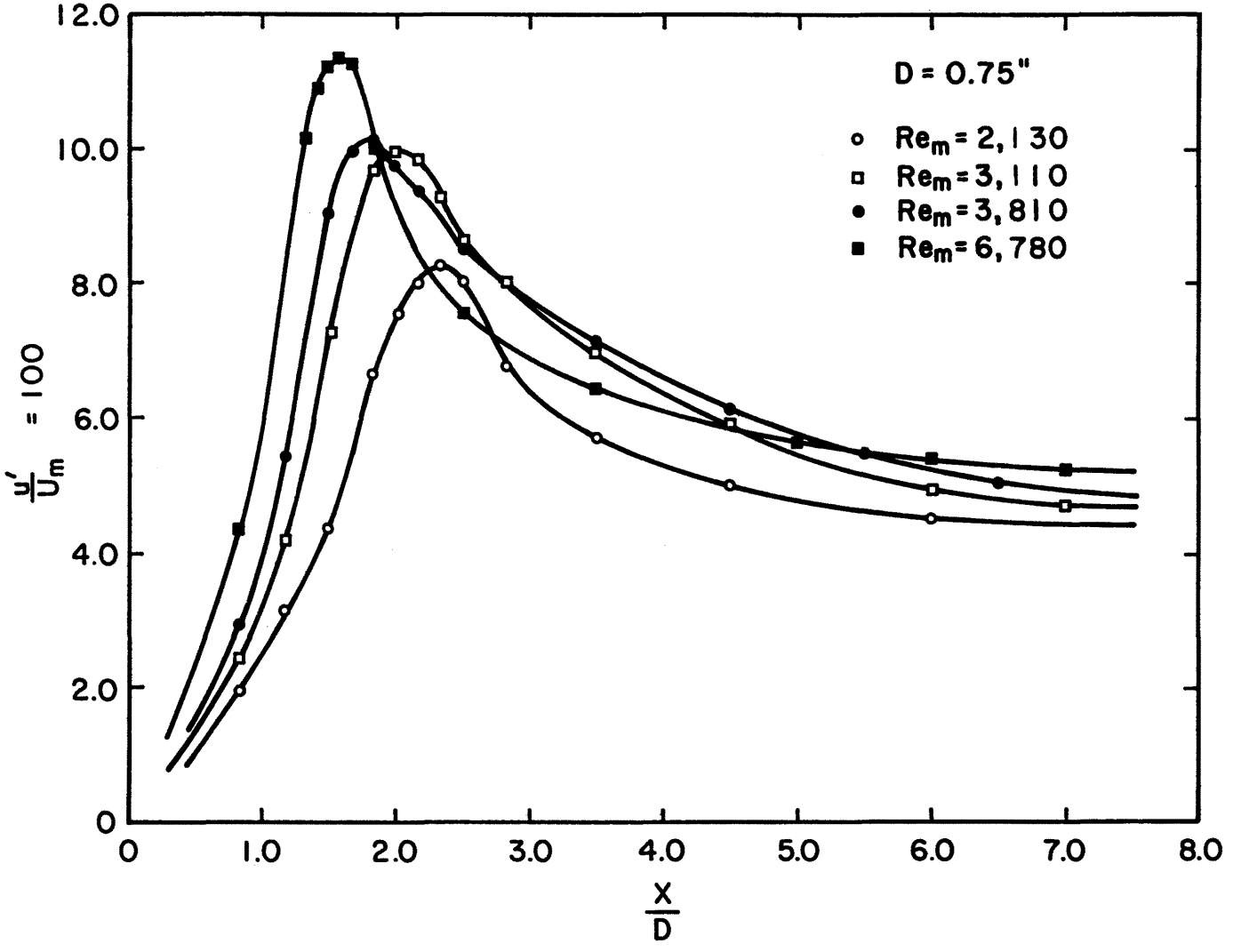

Figure 4.1.10. Turbulence Level (rms fluctuations at second harmonic of the vortex shedding frequency/U_m) on the Wake Axis

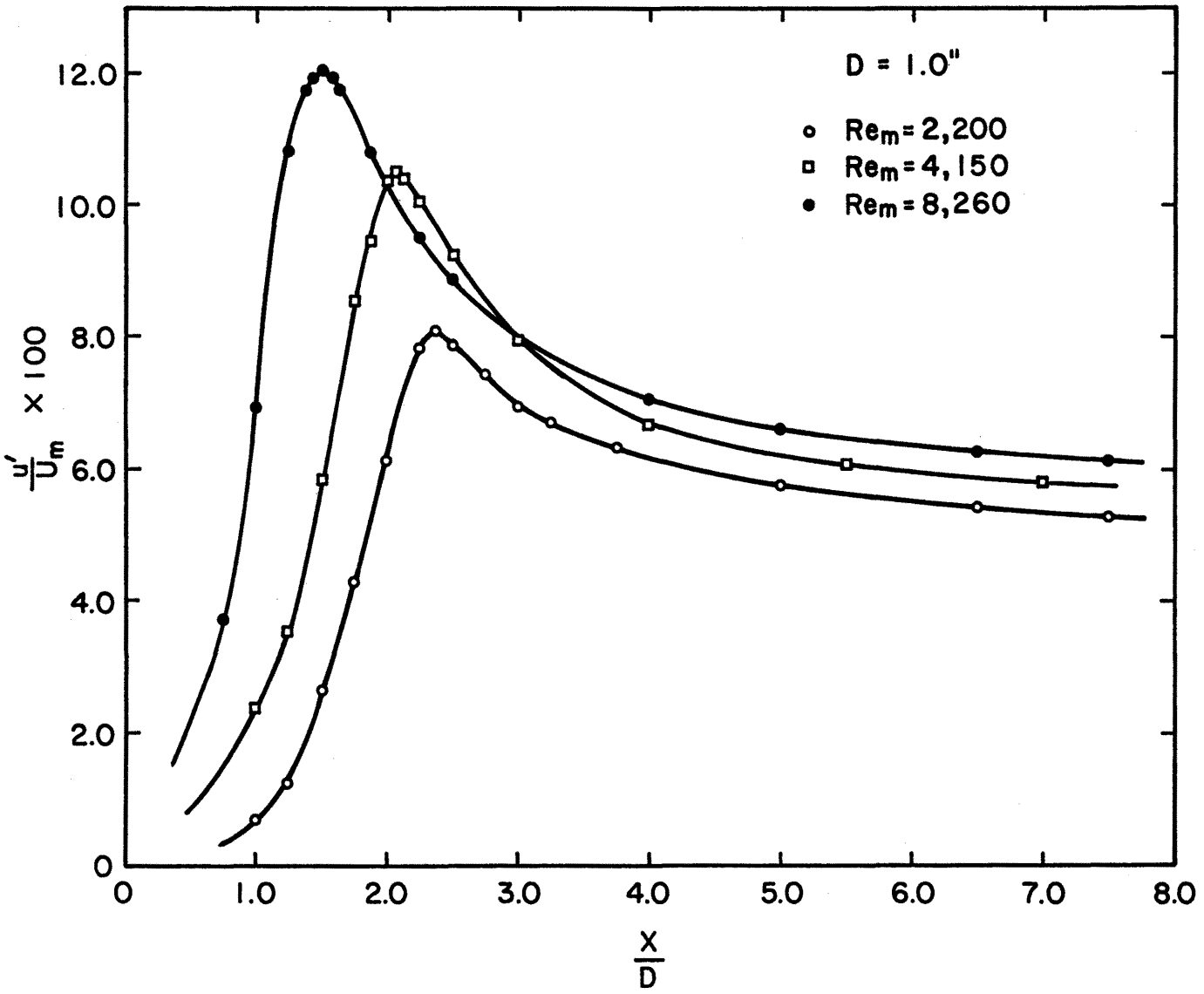

Figure 4.1.11. Turbulence Level (rms fluctuations at second harmonic of the vortex shedding frequency/U_m) on the Wake Axis

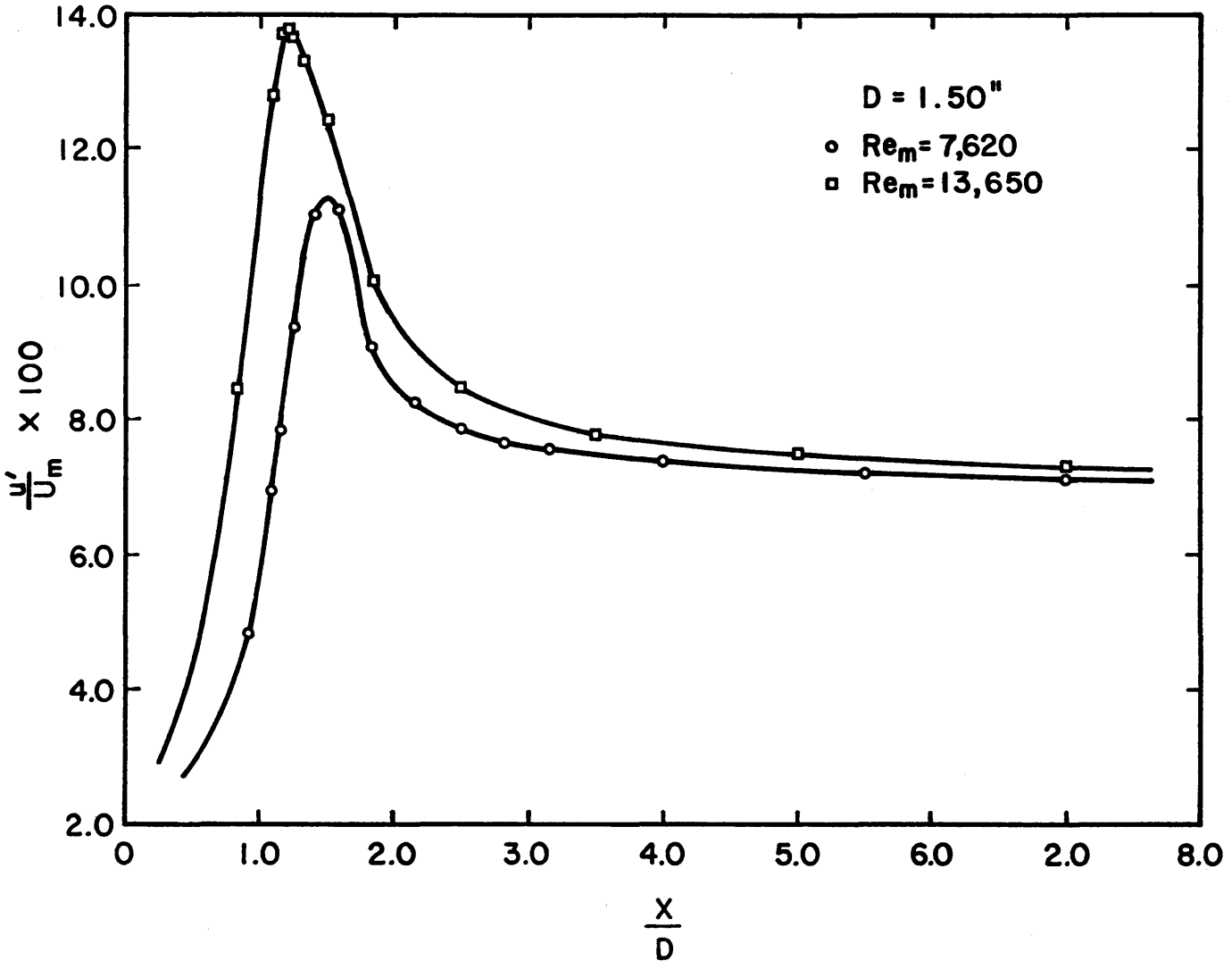

Figure 4.1.12. Turbulence Level (rms fluctuations at second harmonic of the vortex shedding frequency/U_m) on the Wake Axis

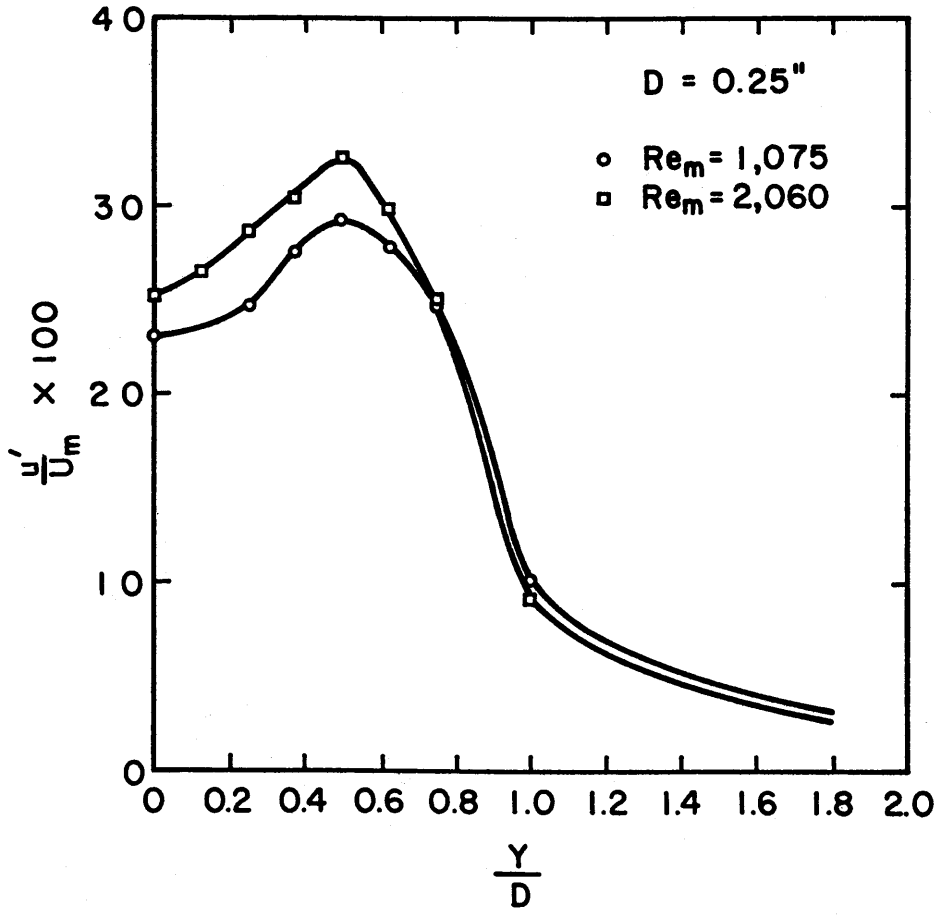

Figure 4.1.13. Turbulence Intensity Profile in the Crosswise Direction at the End of the Vortex Formation Region

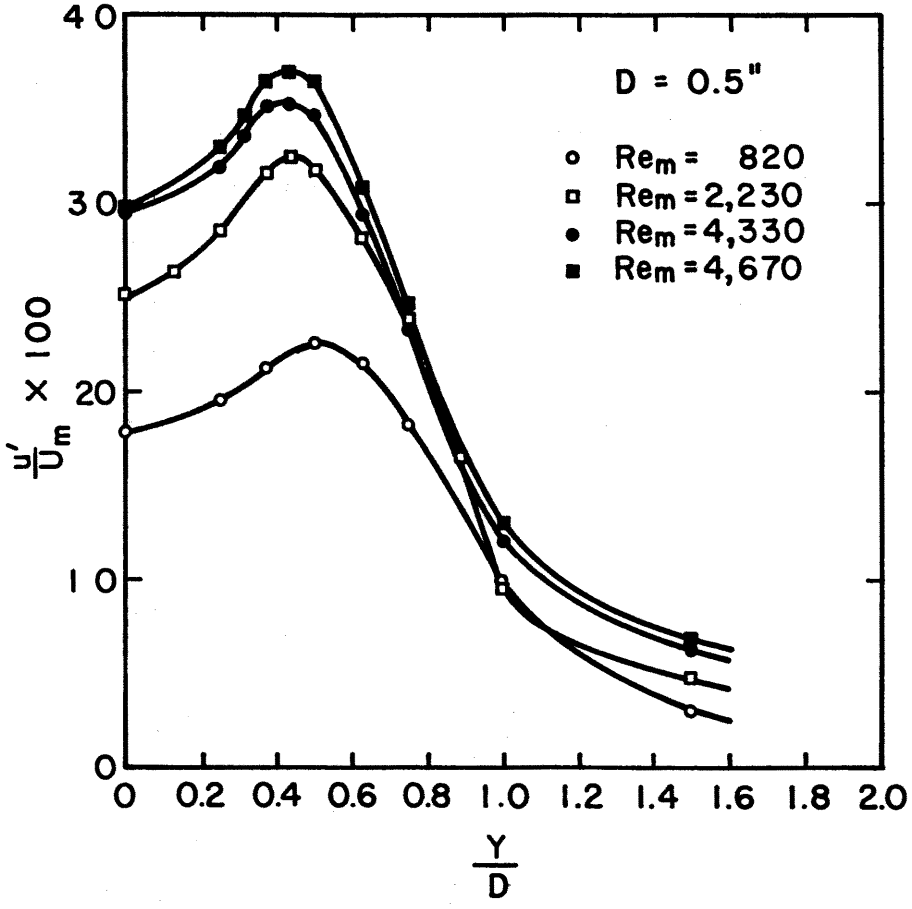

Figure 4.1.14. Turbulence Intensity Profile in the Crosswise Direction at the End of the Vortex Formation Region

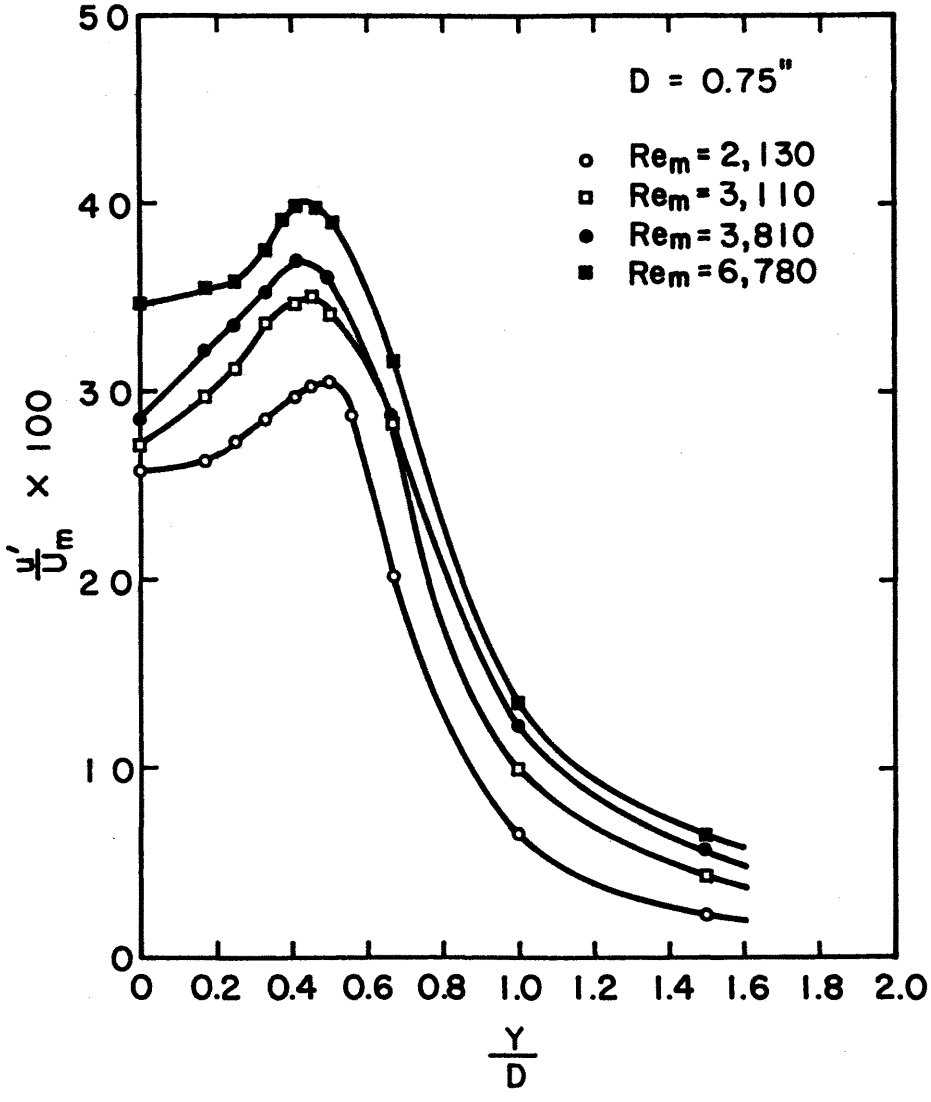

Figure 4.1.15. Turbulence Intensity Profile in the Crosswise Direction at the End of the Vortex Formation Region

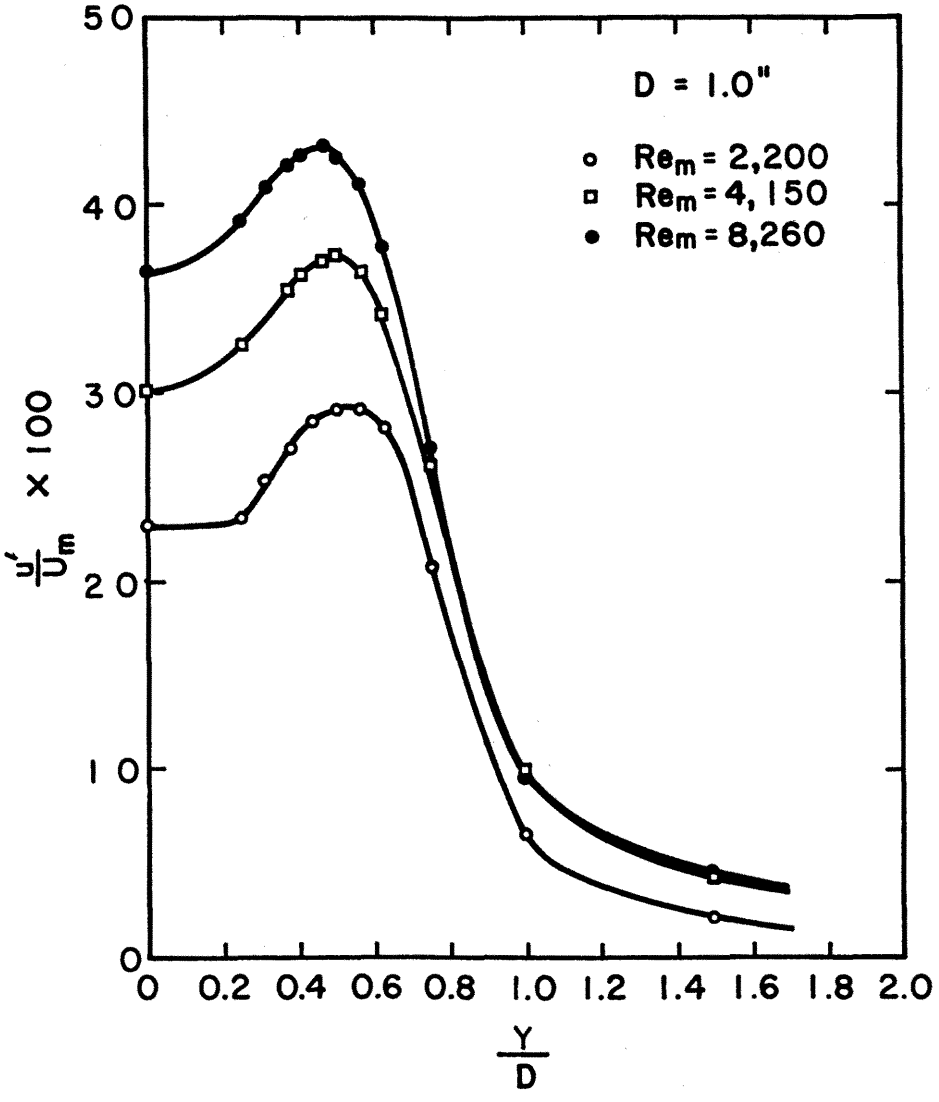

Figure 4.1.16. Turbulence Intensity Profile in the Crosswise Direction at the End of the Vortex Formation Region

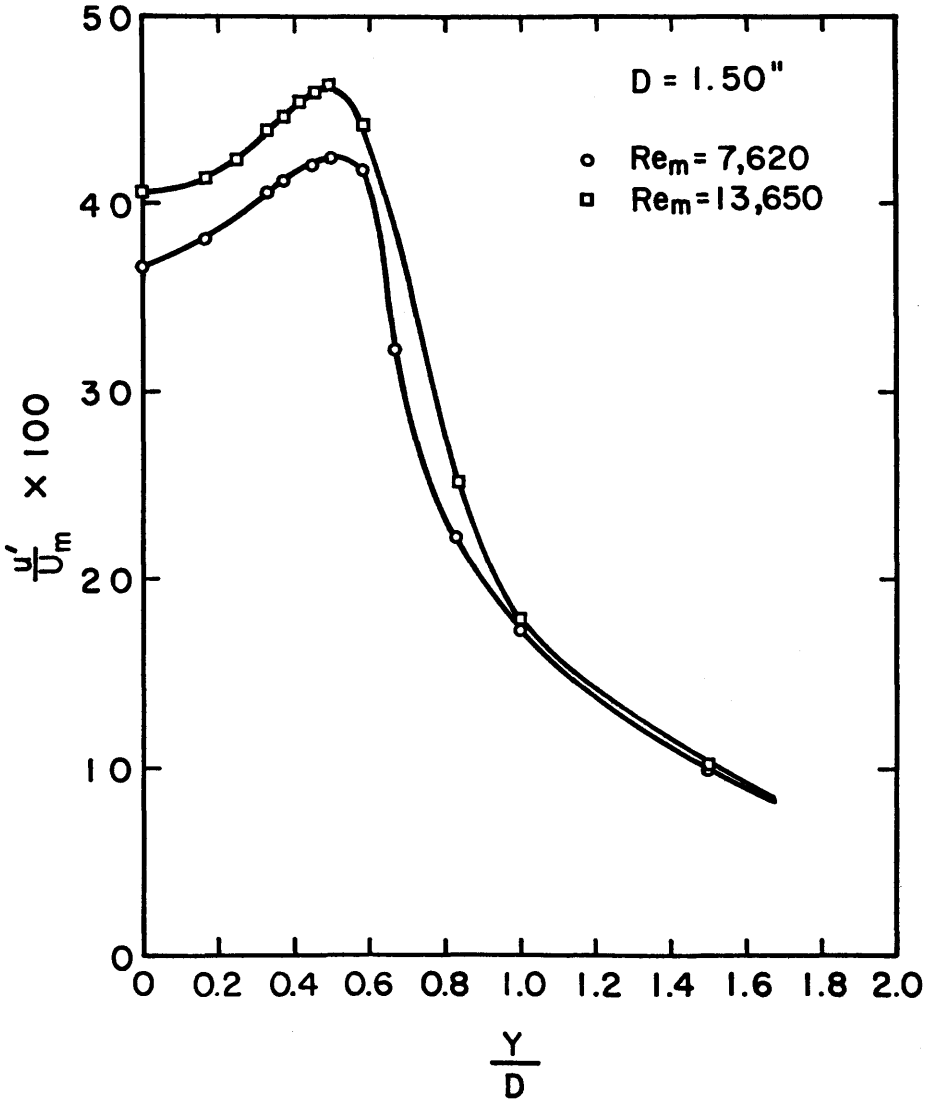

Figure 4.1.17. Turbulence Intensity Profile in the Crosswise Direction at the End of the Vortex Formation Region

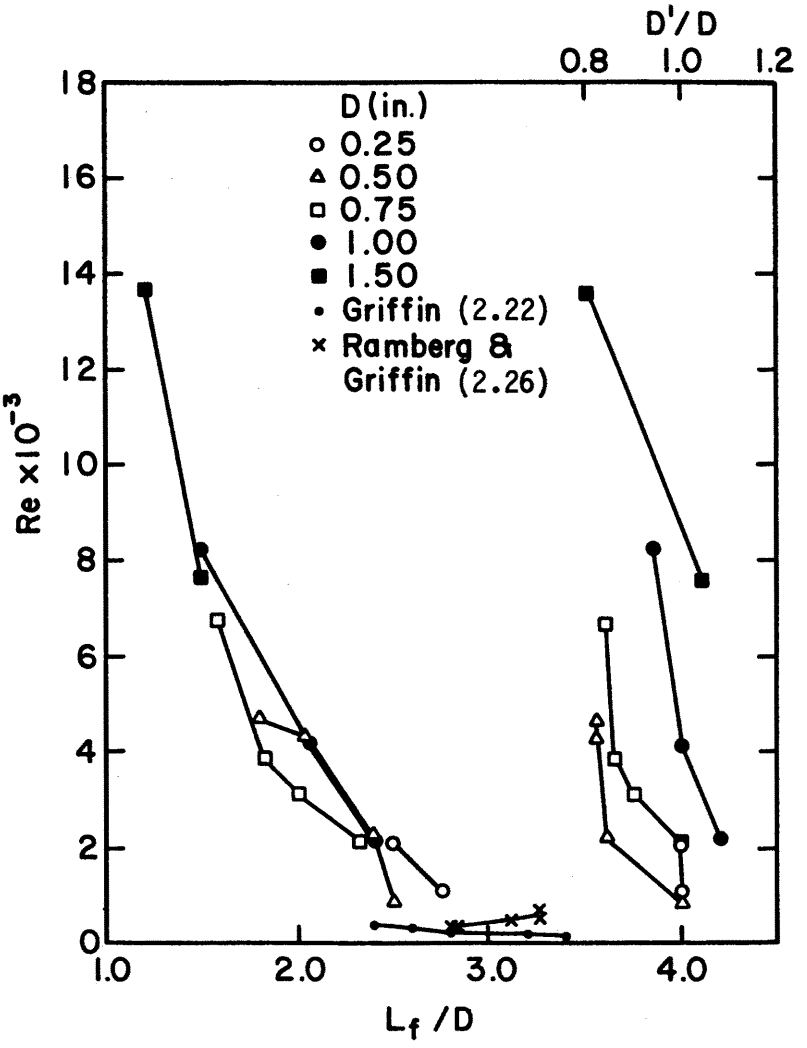

Figure 4.1.18a. Vortex Formation Length and Wake Width as Functions of Reynolds Number

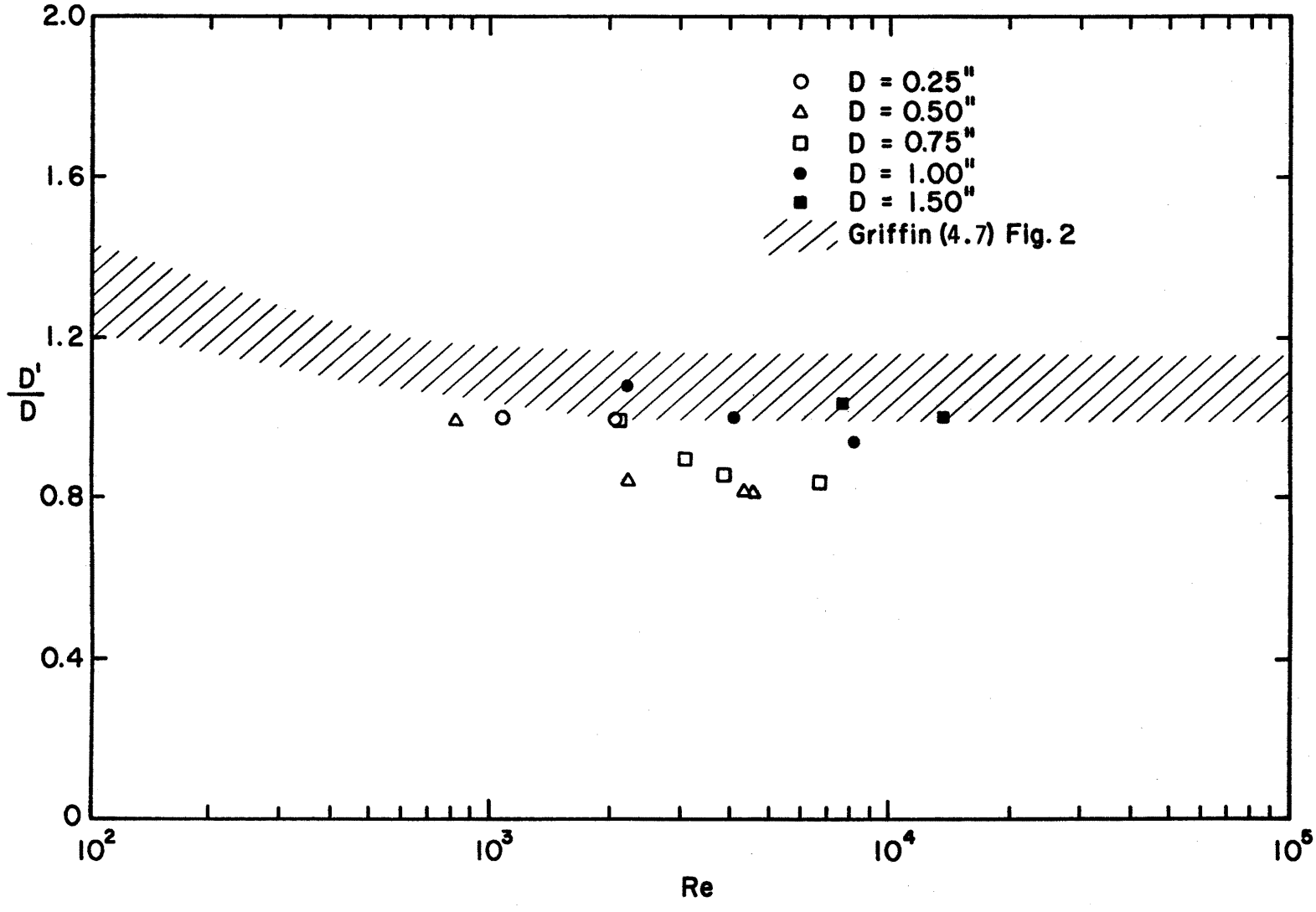

Figure 4.1.18. Wake Width, D'/D, for Circular Cylinders in Uniform Shear Flow Plotted against the Reynolds Number

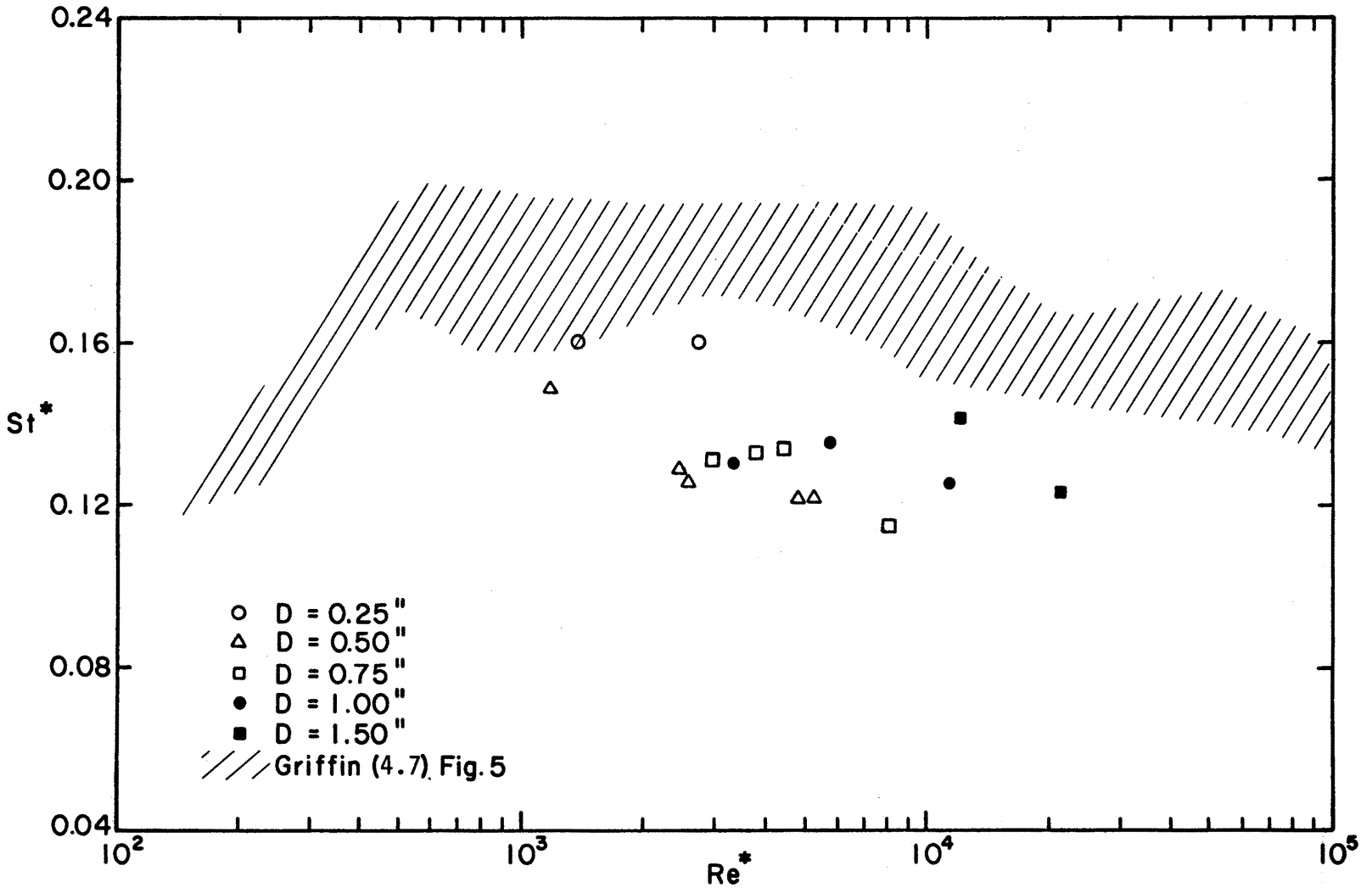

Figure 4.1.19. Universal Strouhal Number, $St^*(= f_s D'/U_b)$ Plotted against the Wake Reynolds Number $Re^*(= U_b D'/\nu)$

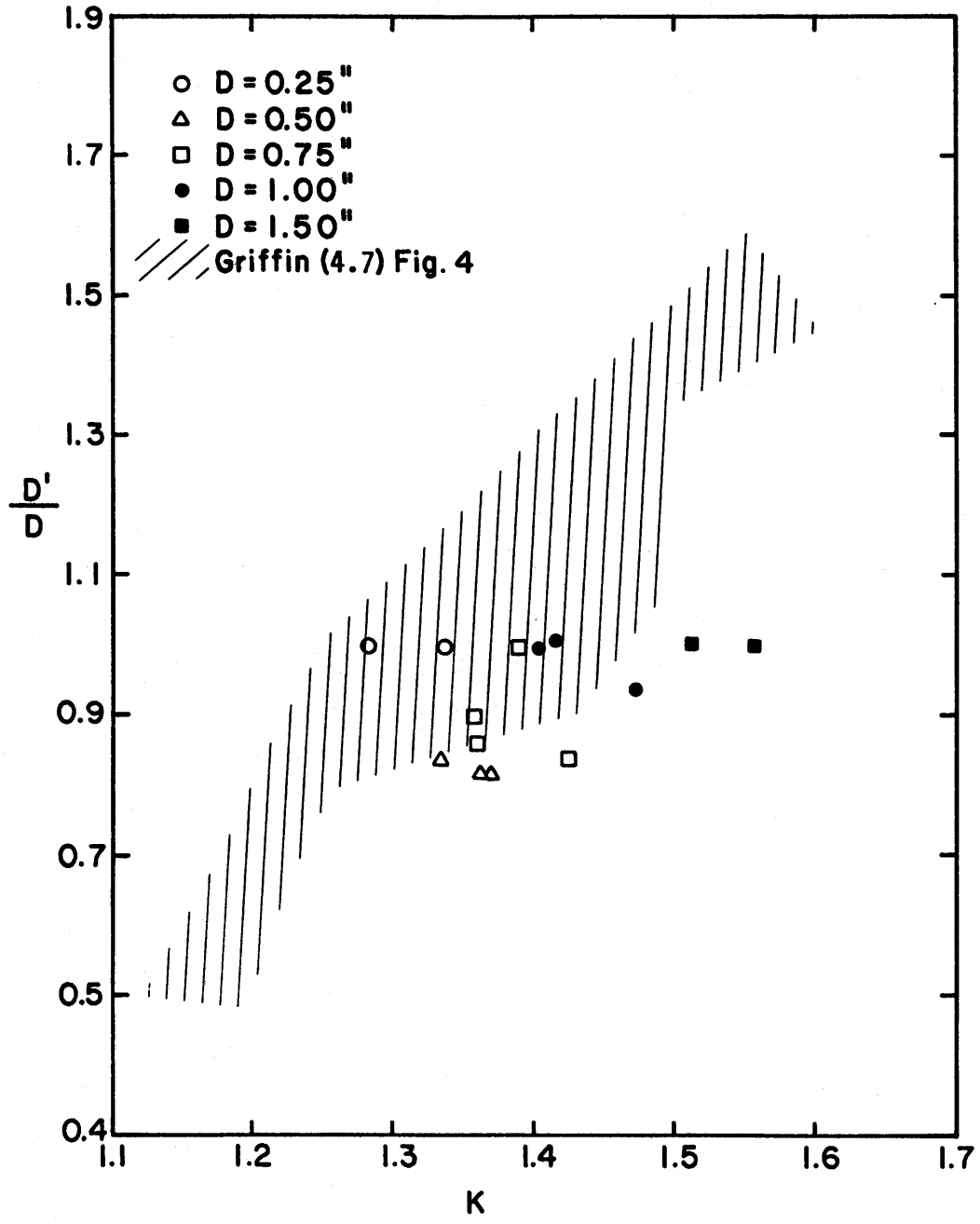

Figure 4.1.20. Wake Width, D'/D, for Circular Cylinders in Uniform Shear Flow Plotted against the Base Pressure Parameter K

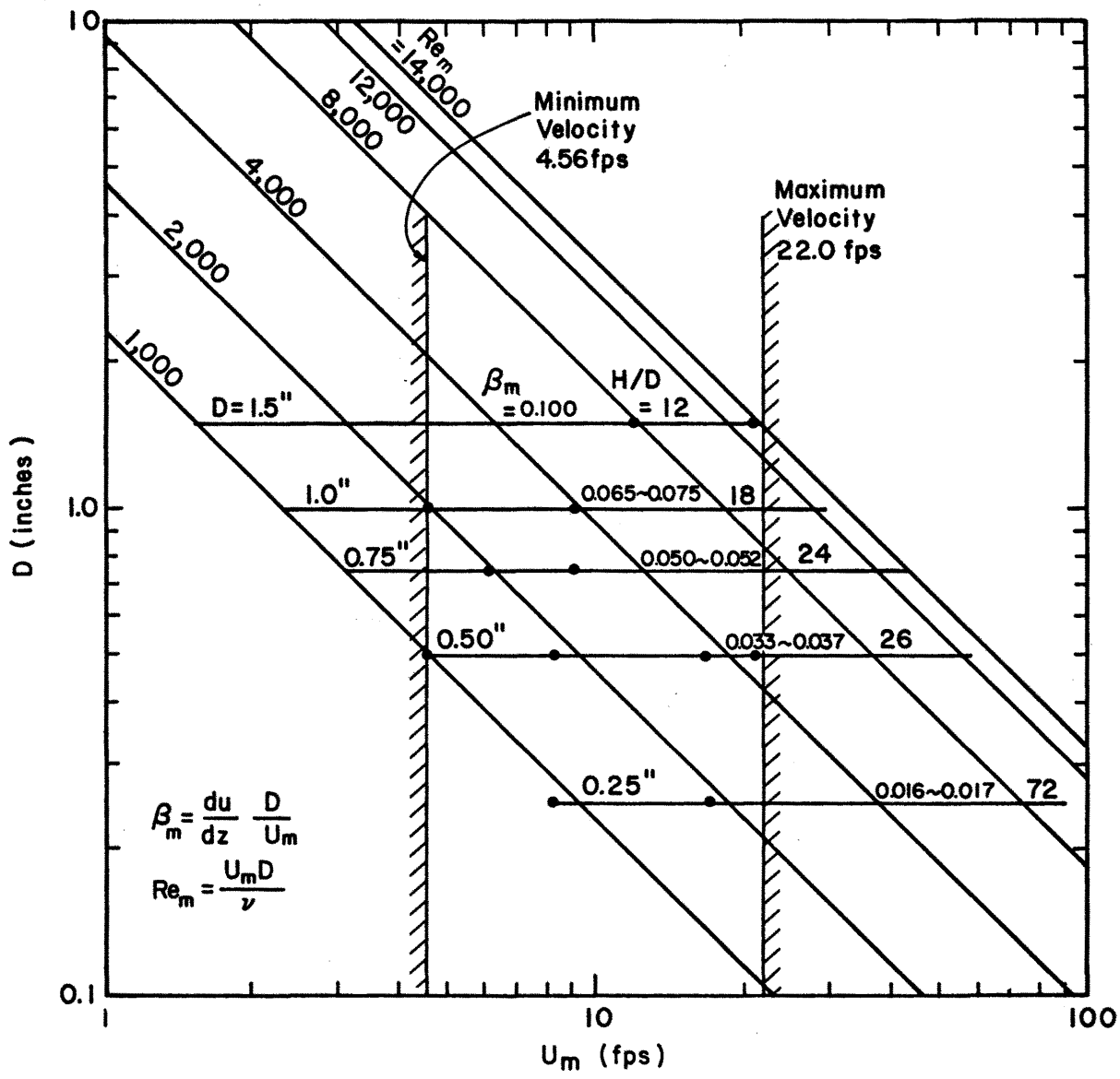

Figure 4.1.21a. Relation among Experimental Parameters for Cylinder

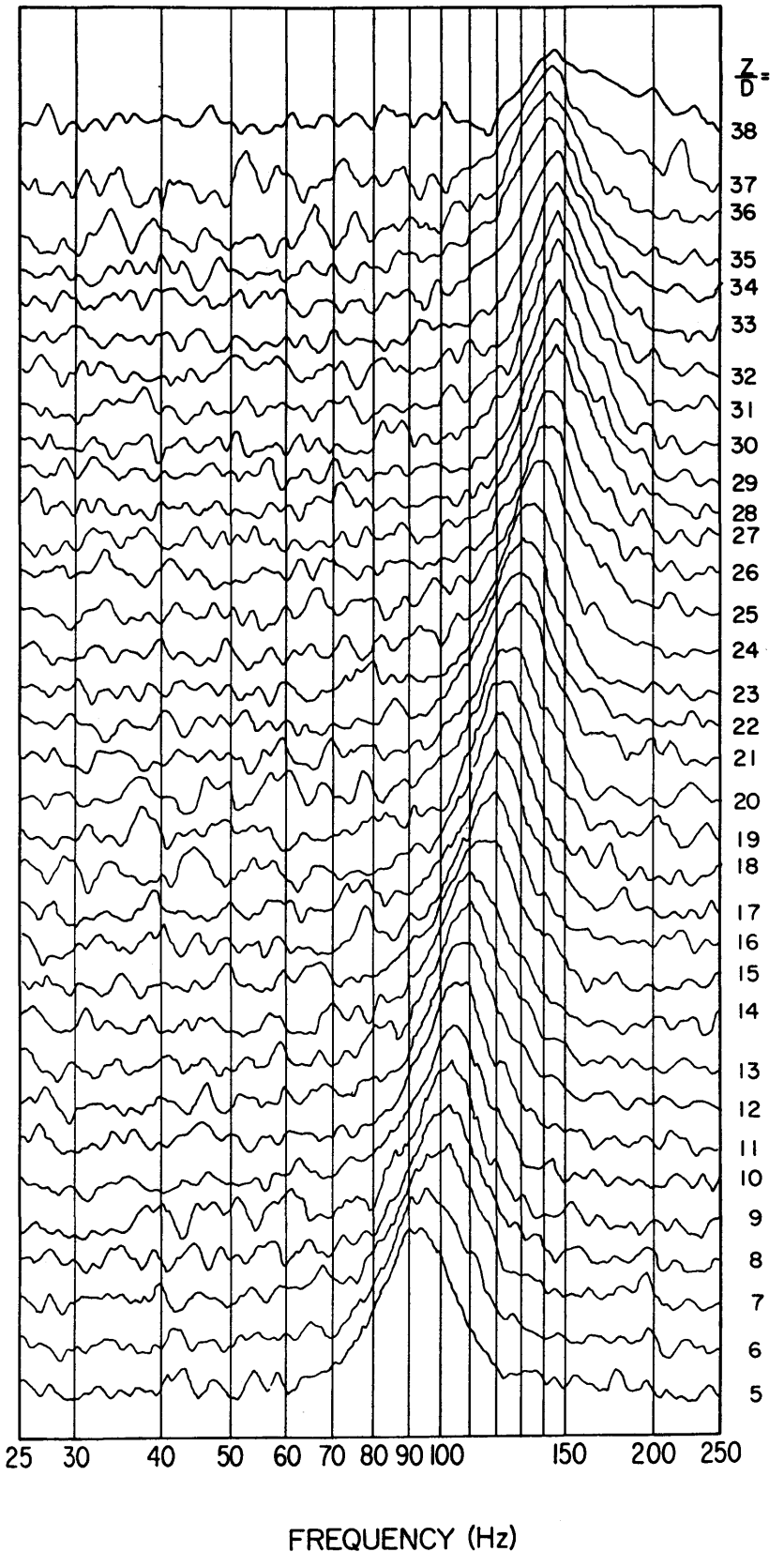

Figure 4.1.21. Frequency Spectra at Various Spanwise Positions for the Stationary Cylinder with D = 0.25 in., Re_m = 900, β_m = 0.017

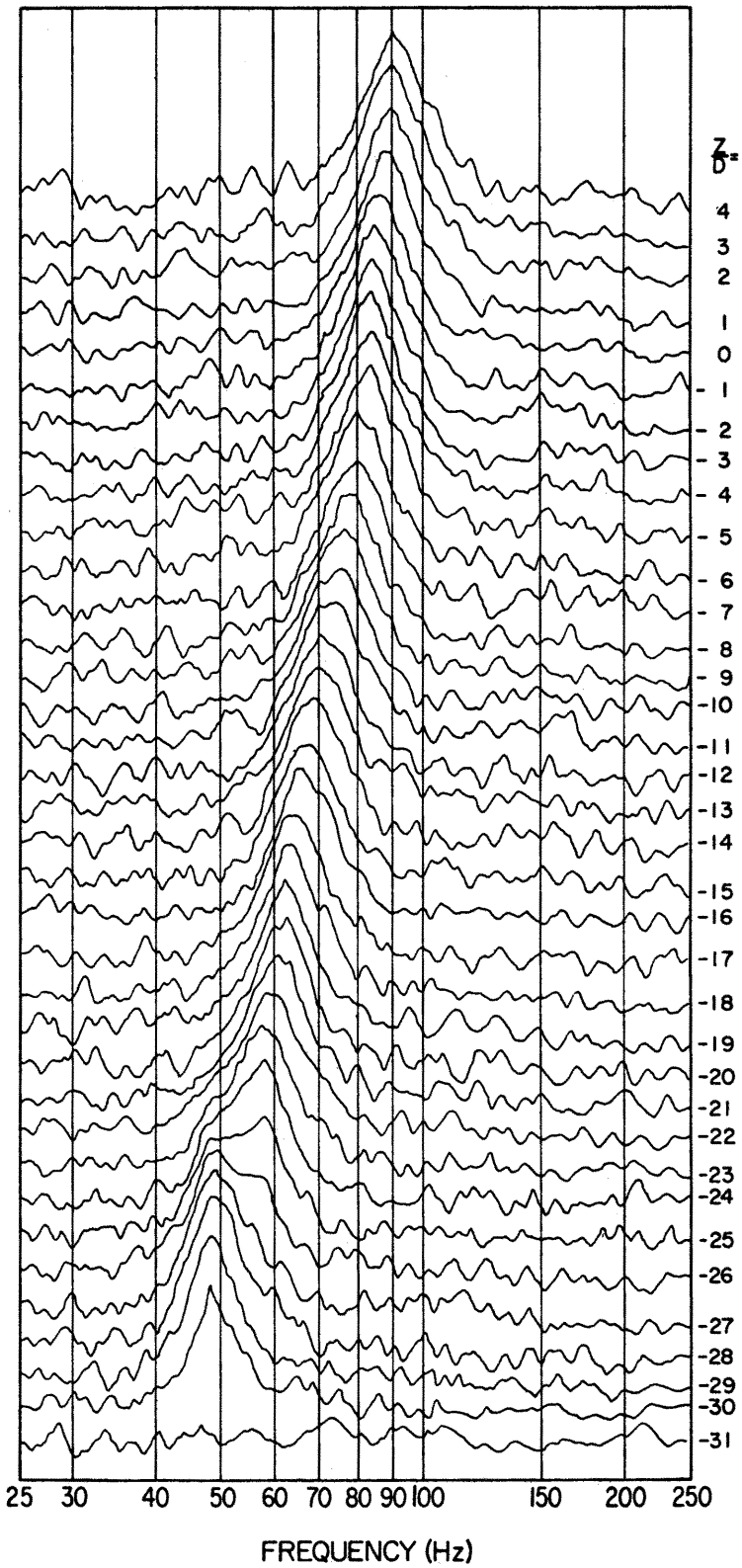

Figure 4.1.21. Continued

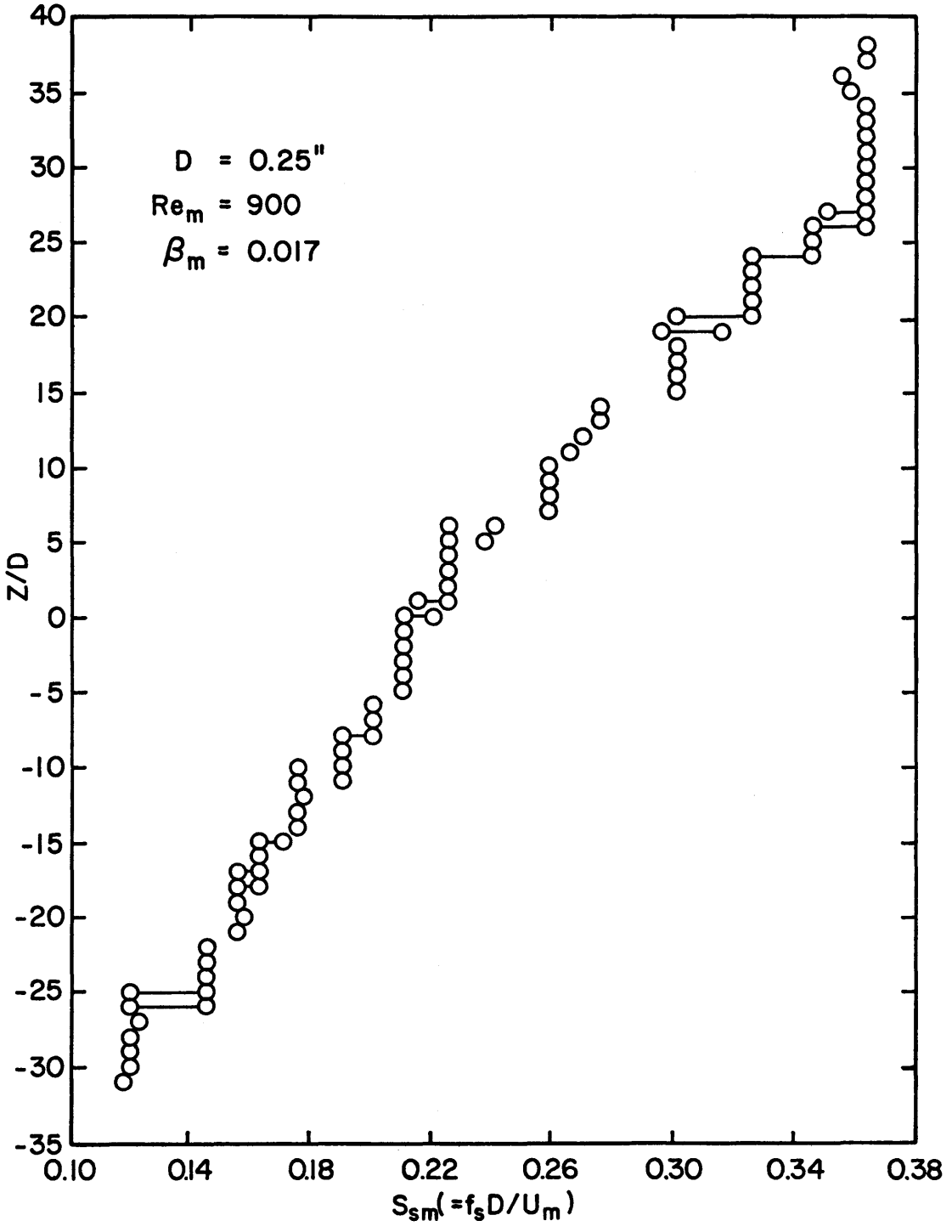

Figure 4.1.22. Spanwise Variation of S_{sm} for the Stationary Cylinder with D = 0.25 in., $Re_m \cong 900$, $\beta_m = 0.017$

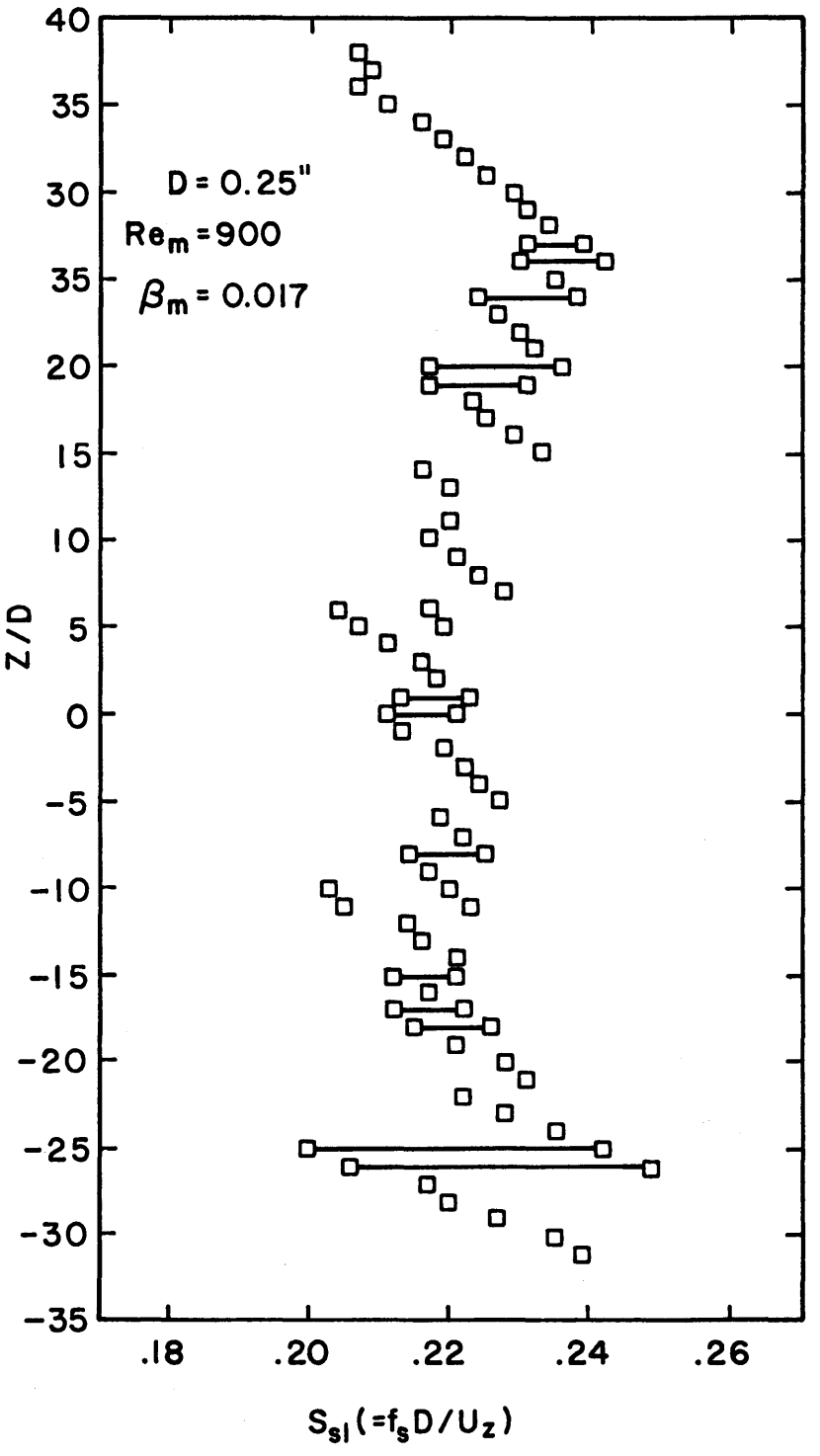

Figure 4.1.23. Spanwise Variation of $S_{s\ell}$ for the Stationary Cylinder with D = 0.25 in., Re_m = 900, β_m = 0.017

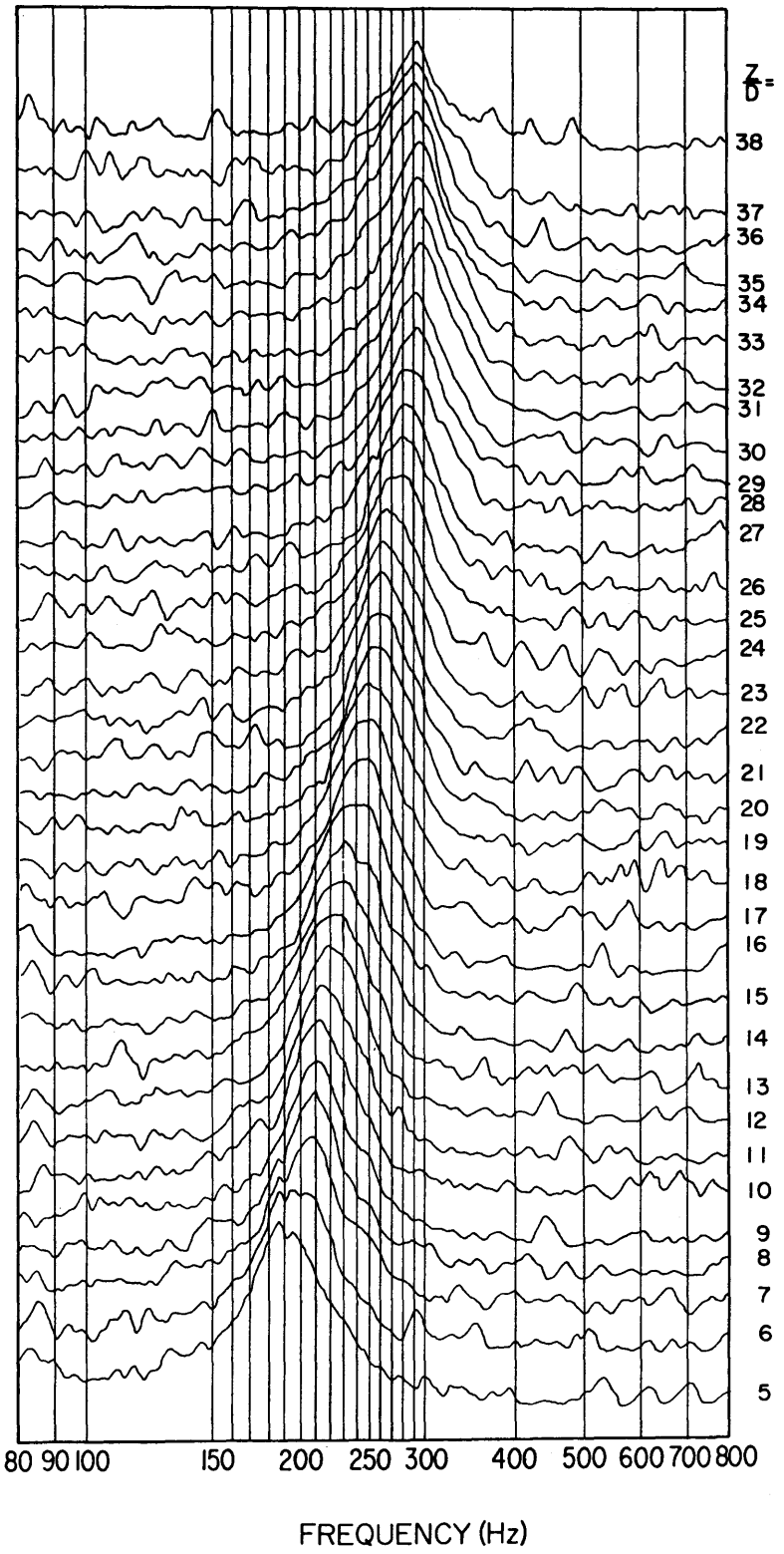

Figure 4.1.24. Frequency Spectra at Various Spanwise Positions for the Stationary Cylinder with D = 0.25 in., Re_m = 1,830, β_m = 0.016

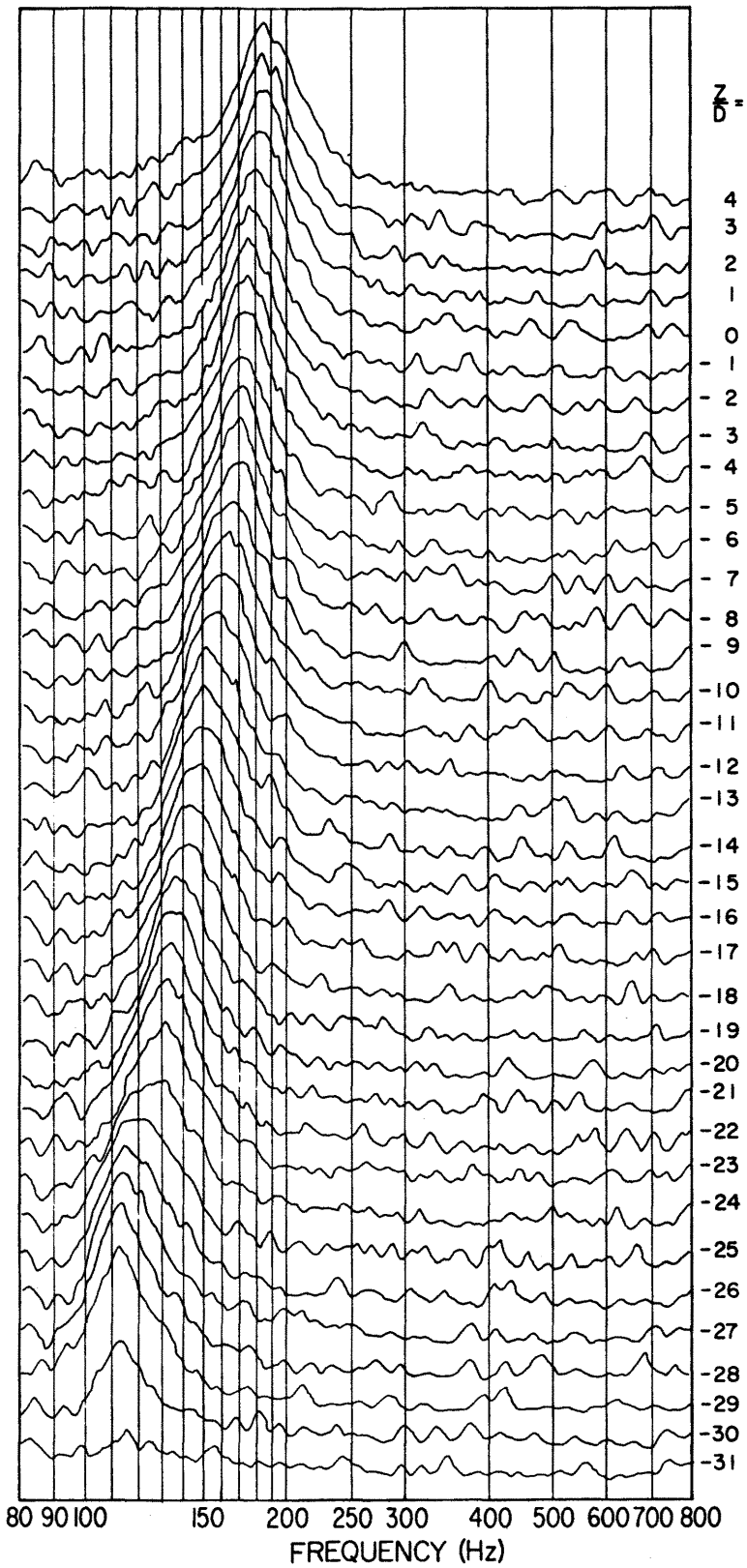

Figure 4.1.24. Continued

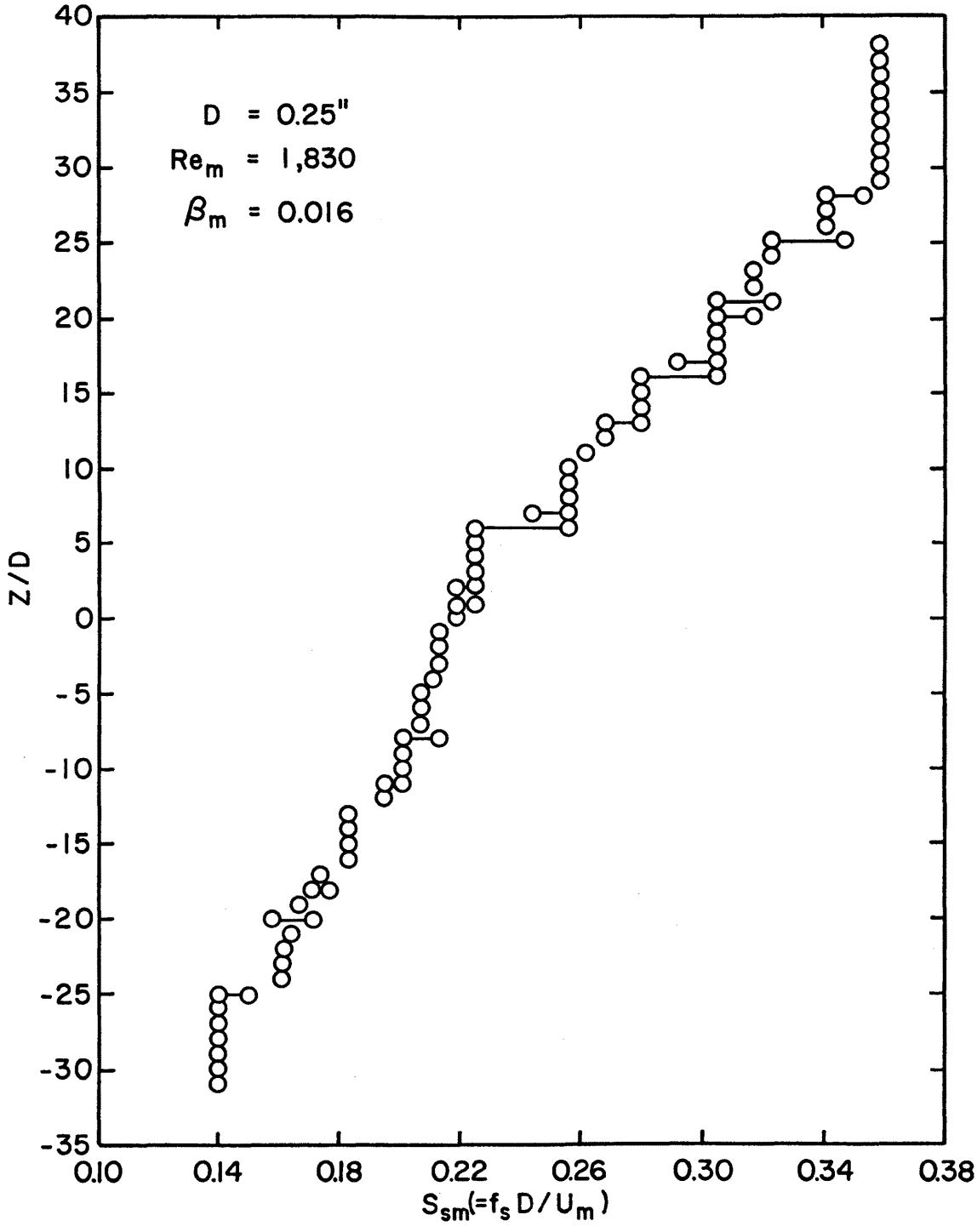

Figure 4.1.25. Spanwise Variation of S_{sm} for the Stationary Cylinder with D = 0.25 in., $Re_m \cong 1{,}830$, $\beta_m = 0.016$

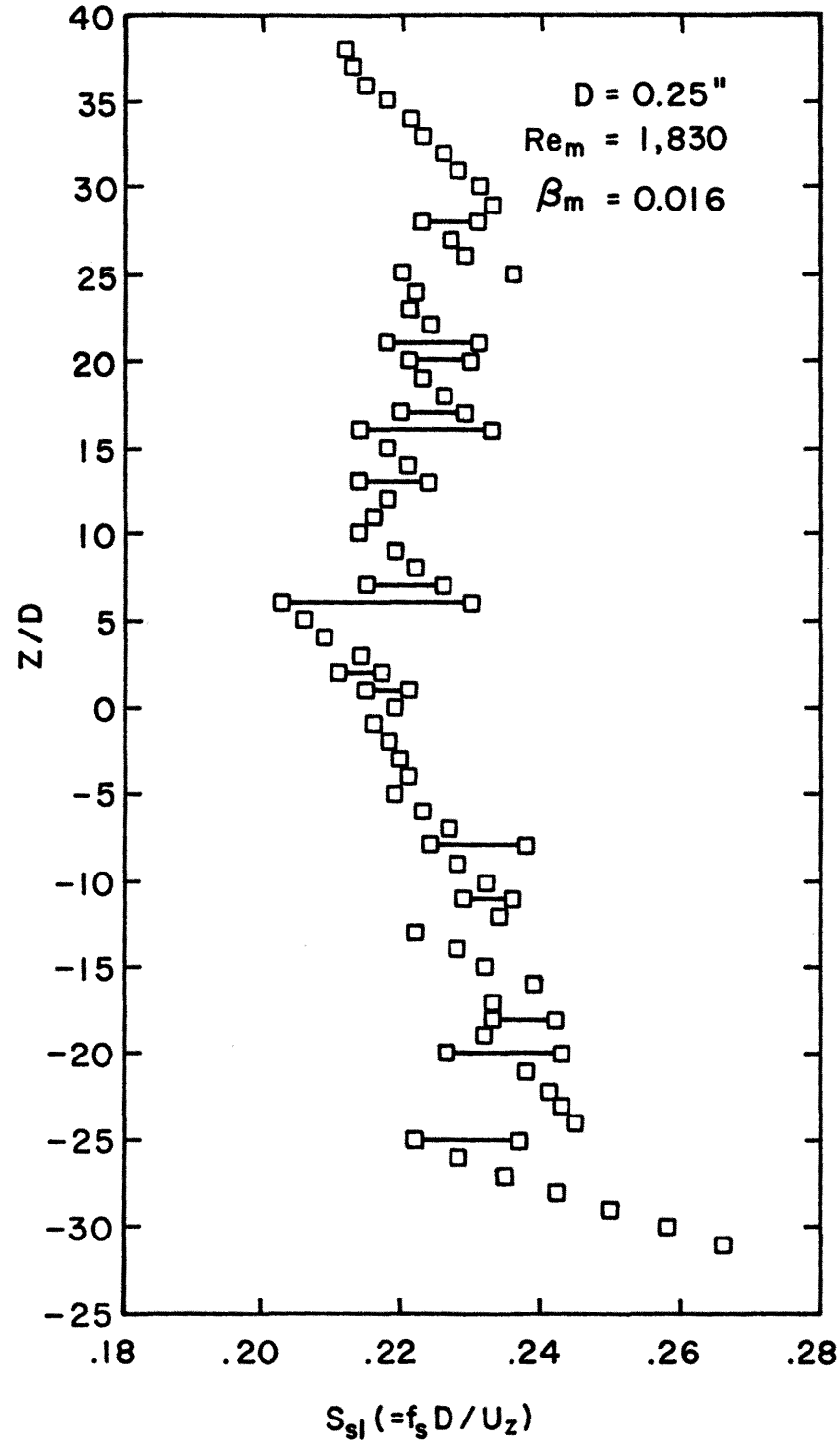

Figure 4.1.26. Spanwise Variation of $S_{s\ell}$ for the Stationary Cylinder with D = 0.25 in., Re_m = 1,830, β_m = 0.016.

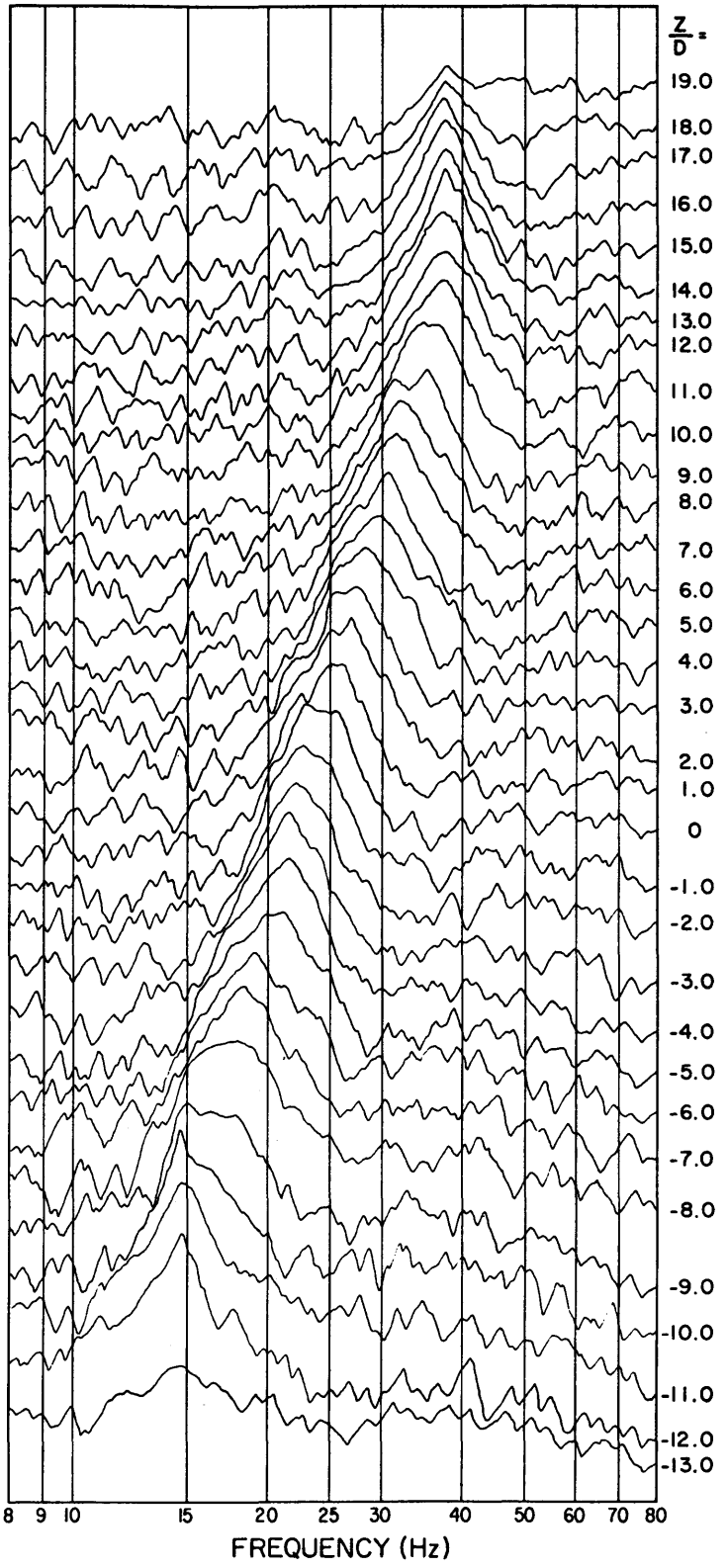

Figure 4.1.27. Frequency Spectra at Various Spanwise Positions for the Stationary Cylinder with D = 0.50 in., Re_m = 970, β_m = 0.037

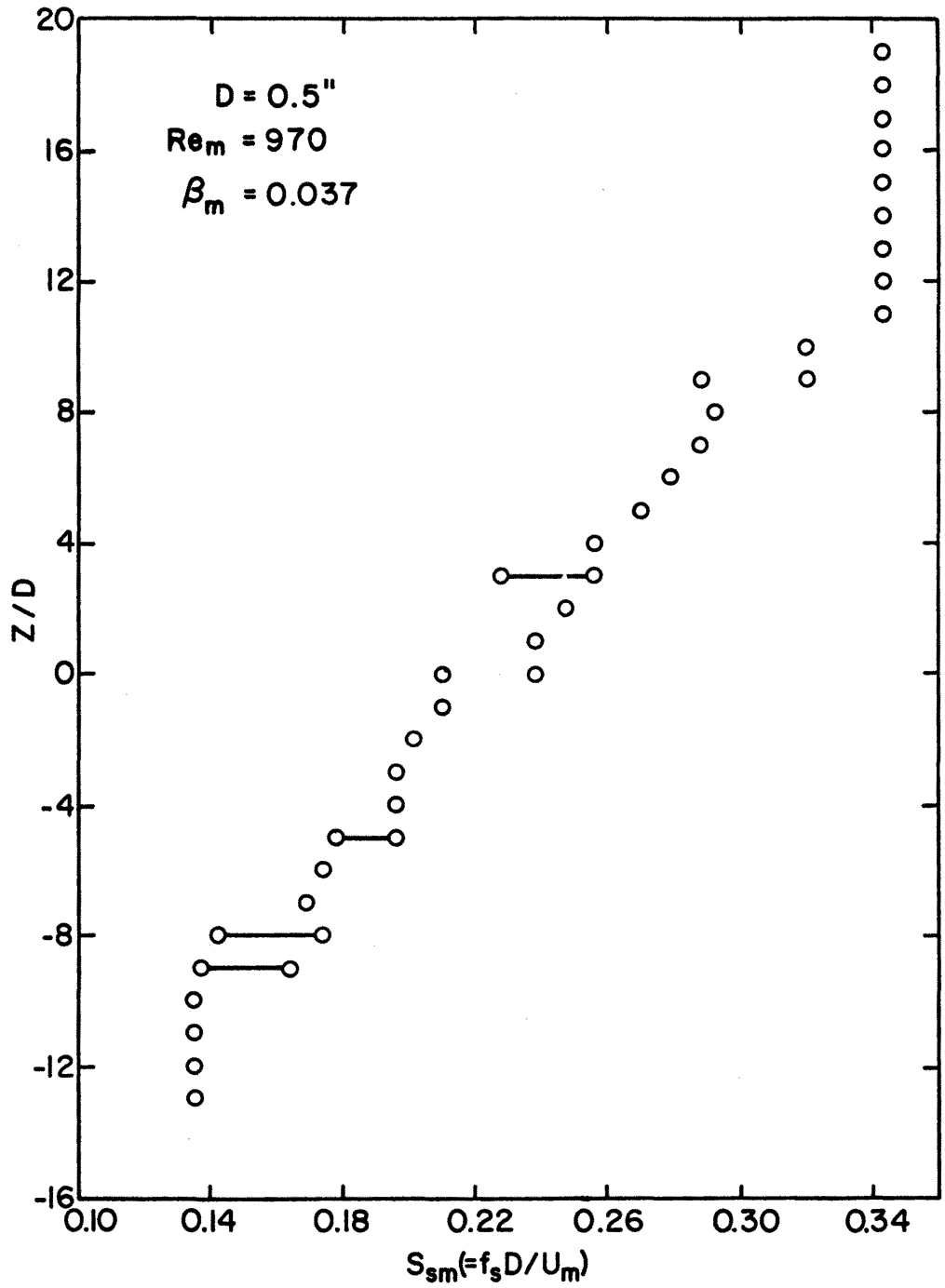

Figure 4.1.28. Spanwise Variation of S_{sm} for the Stationary Cylinder with D = 0.50 in., $Re_m = 970$, $\beta_m = 0.037$

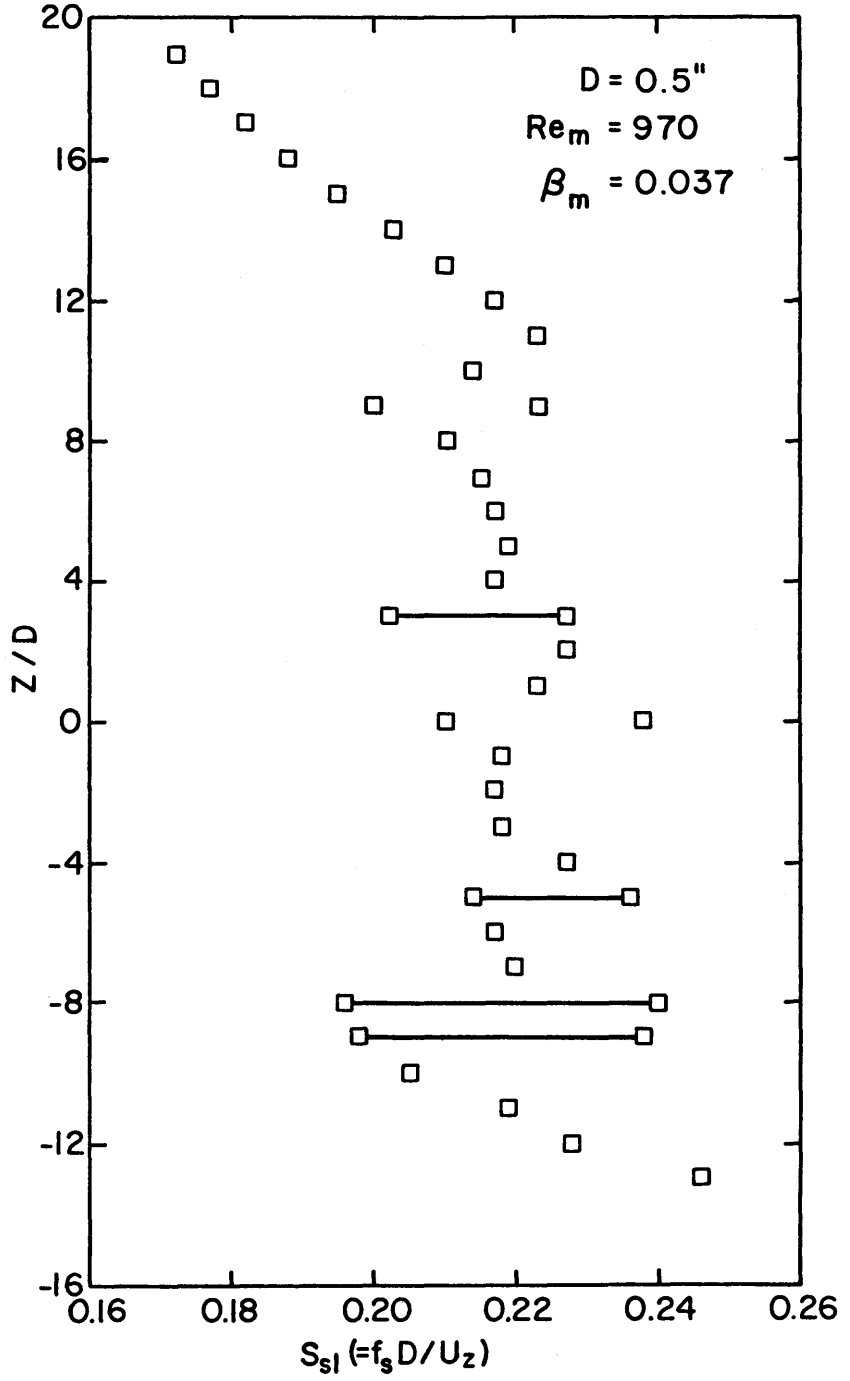

Figure 4.1.29. Spanwise Variation of $S_{s\ell}$ for the Stationary Cylinder with D = 0.50 in., Re_m = 970, β_m = 0.037

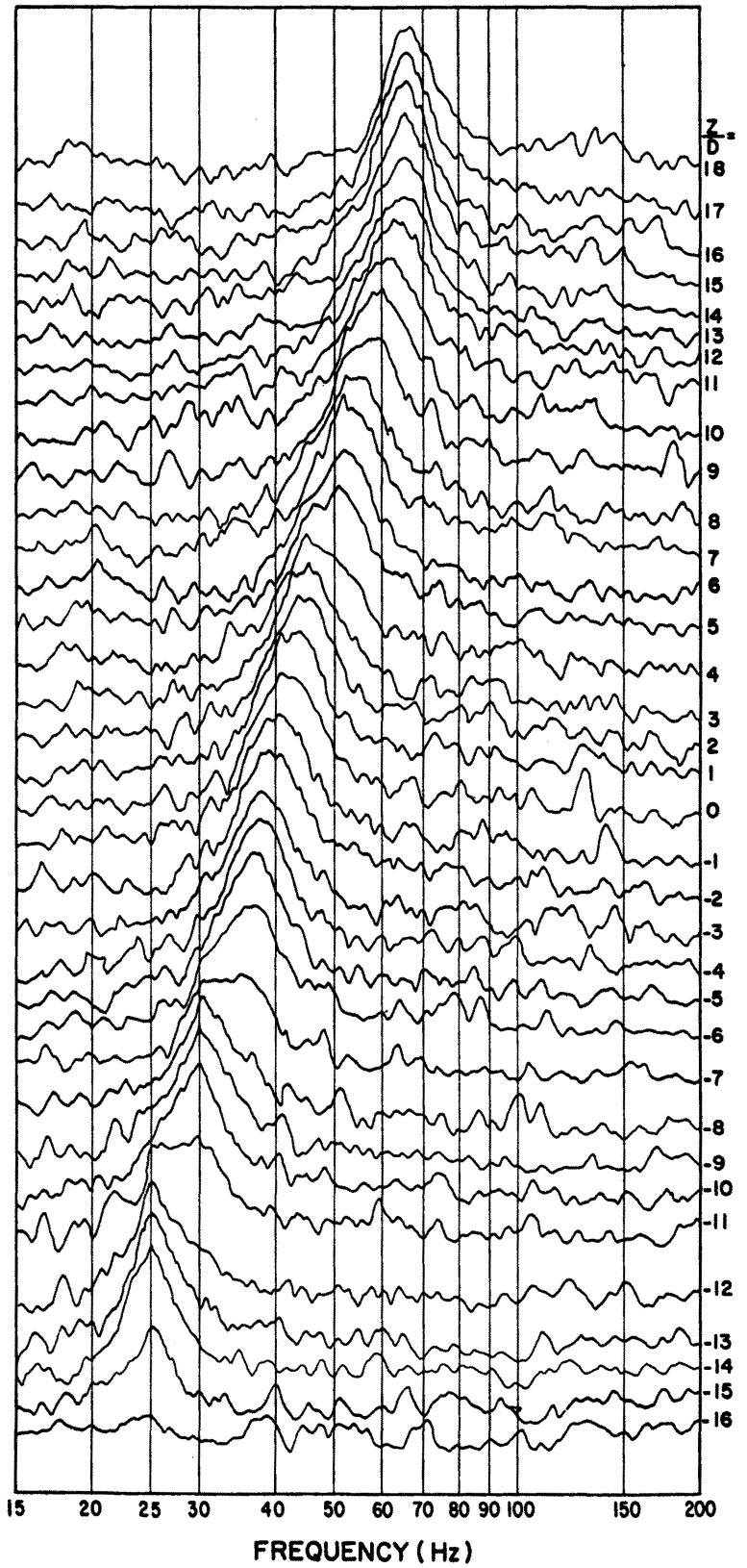

Figure 4.1.30. Frequency Spectra at Various Spanwise Positions for the Stationary Cylinder with D = 0.50 in., Re_m = 1,770, β_m = 0.034

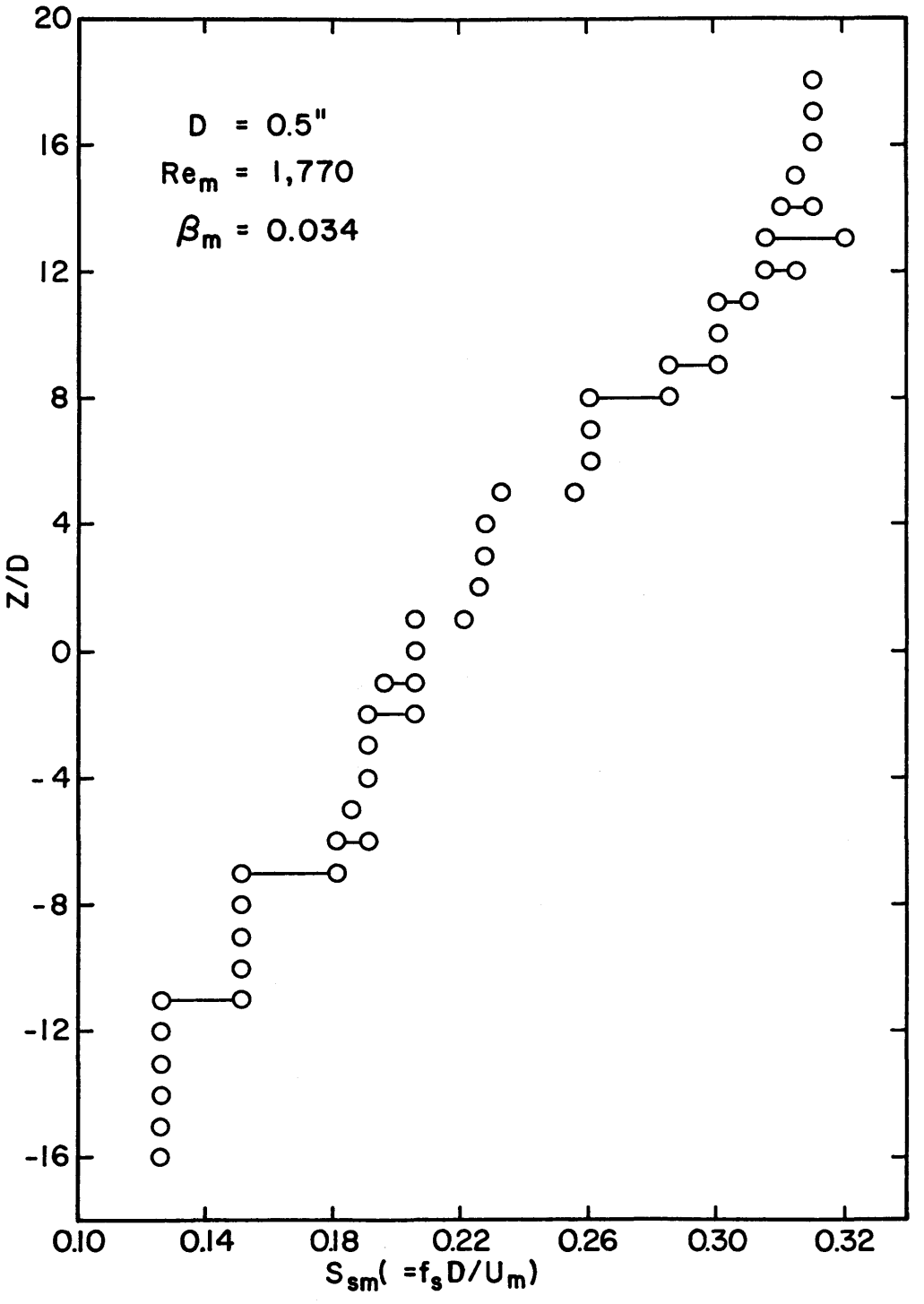

Figure 4.1.31. Spanwise Variation of S_{sm} for the Stationary Cylinder with D = 0.50 in., $Re_m \cong 1{,}770$, $\beta_m = 0.034$

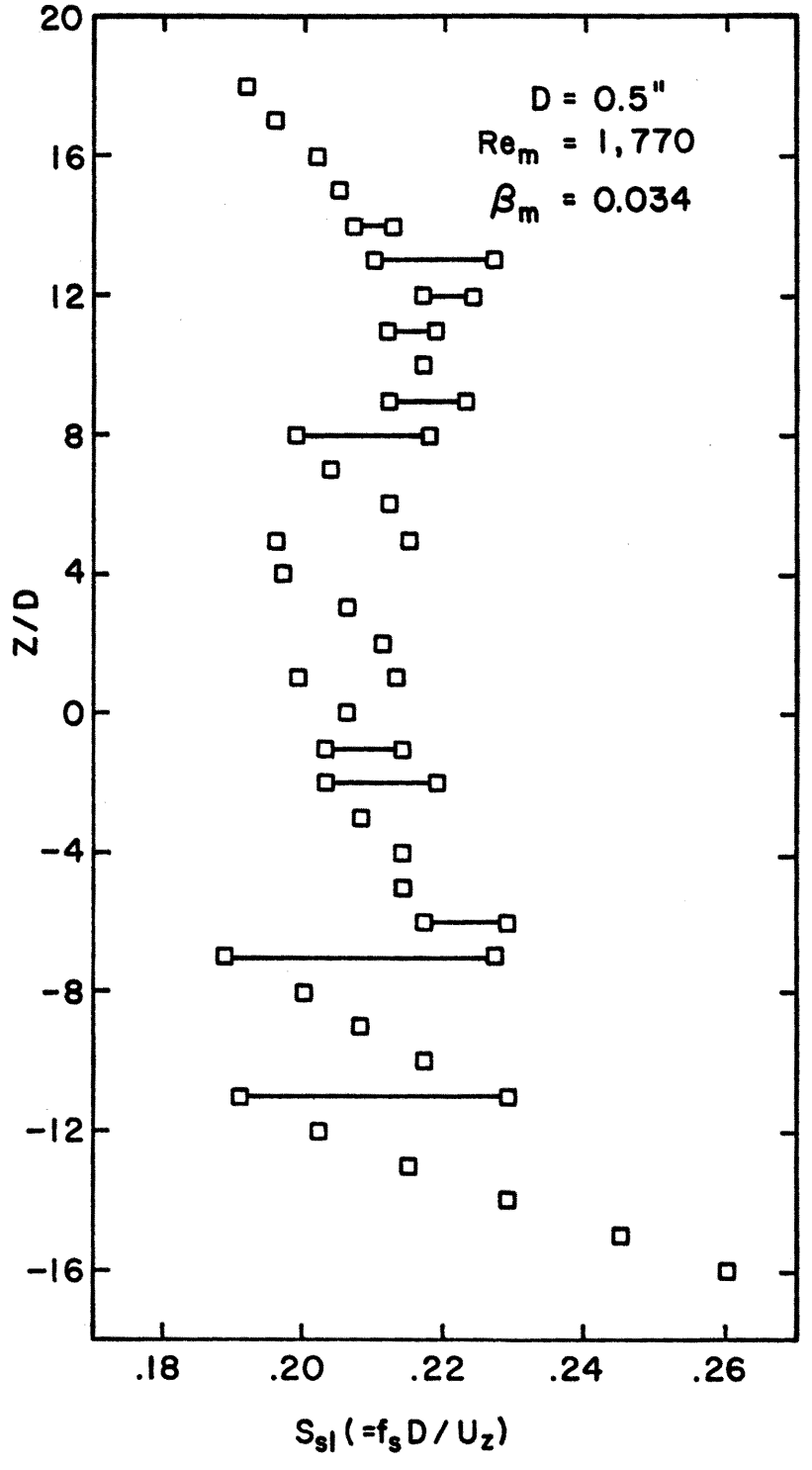

Figure 4.1.32. Spanwise Variation of $S_{s\ell}$ for the Stationary Cylinder with D = 0.50 in., Re_m = 1,770, β_m = 0.034

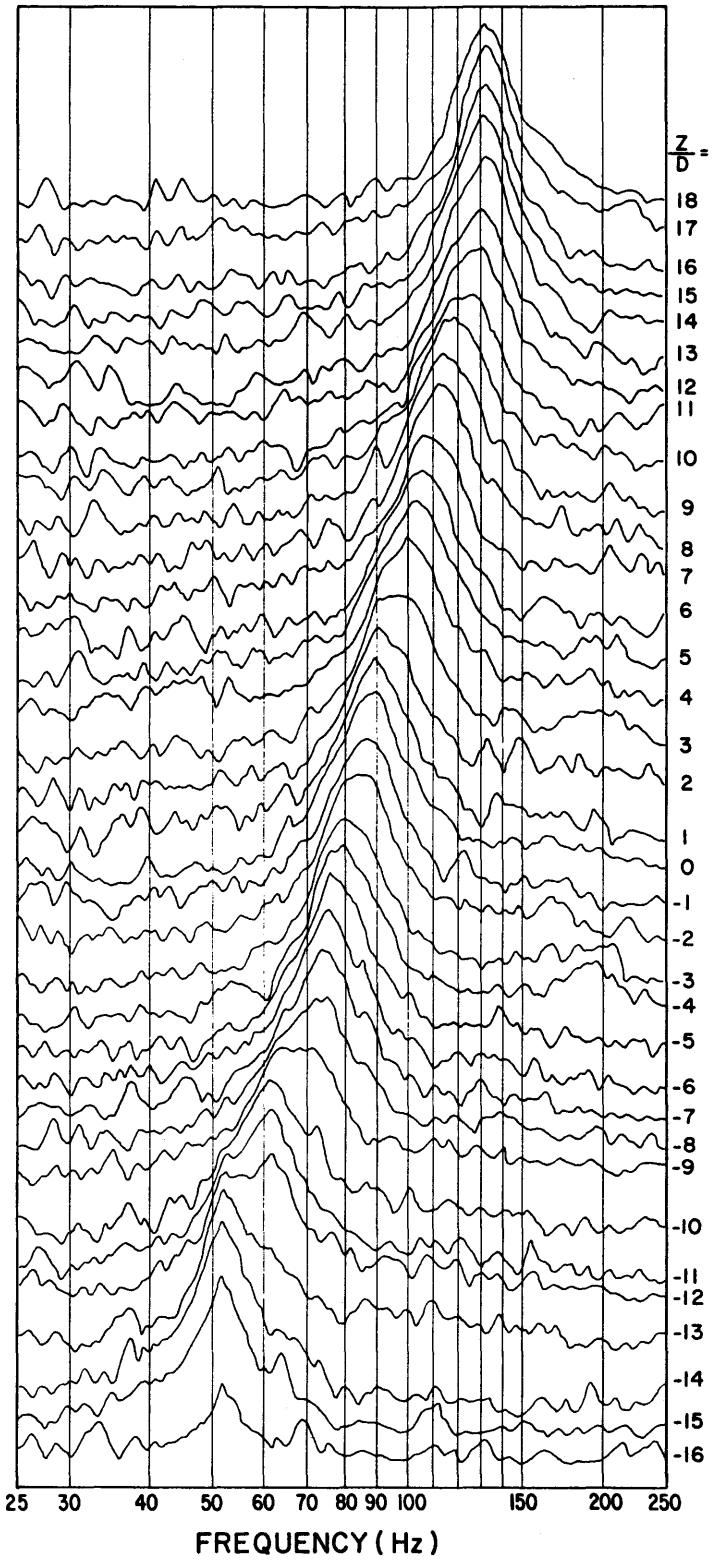

Figure 4.1.33. Frequency Spectra at Various Spanwise Positions for the Stationary Cylinder with D = 0.50 in., Re_m = 3,600, β_m = 0.033

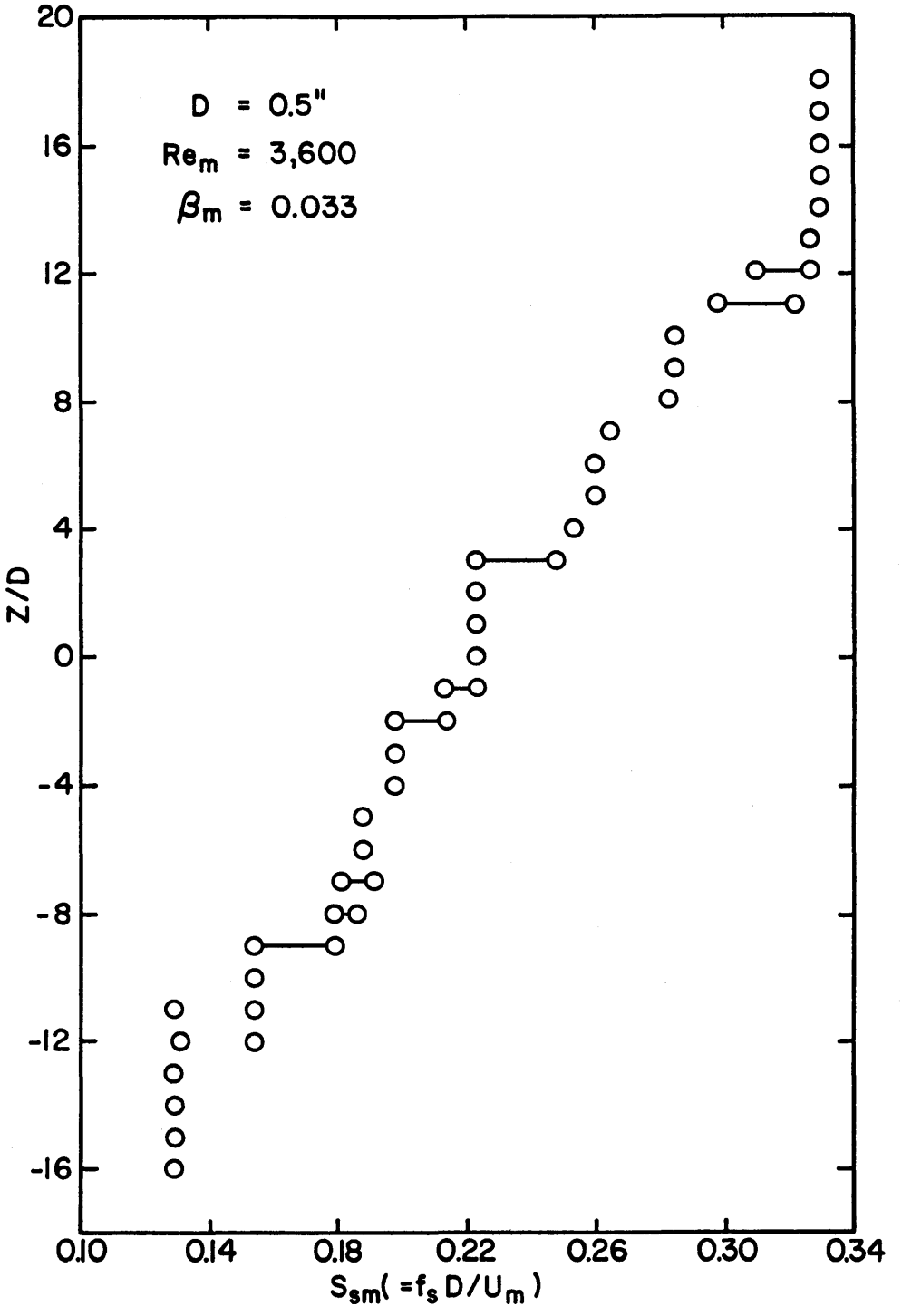

Figure 4.1.34. Spanwise Variation of S_{sm} for the Stationary Cylinder with D = 0.50 in., $Re_m \cong 3{,}600$, $\beta_m = 0.033$

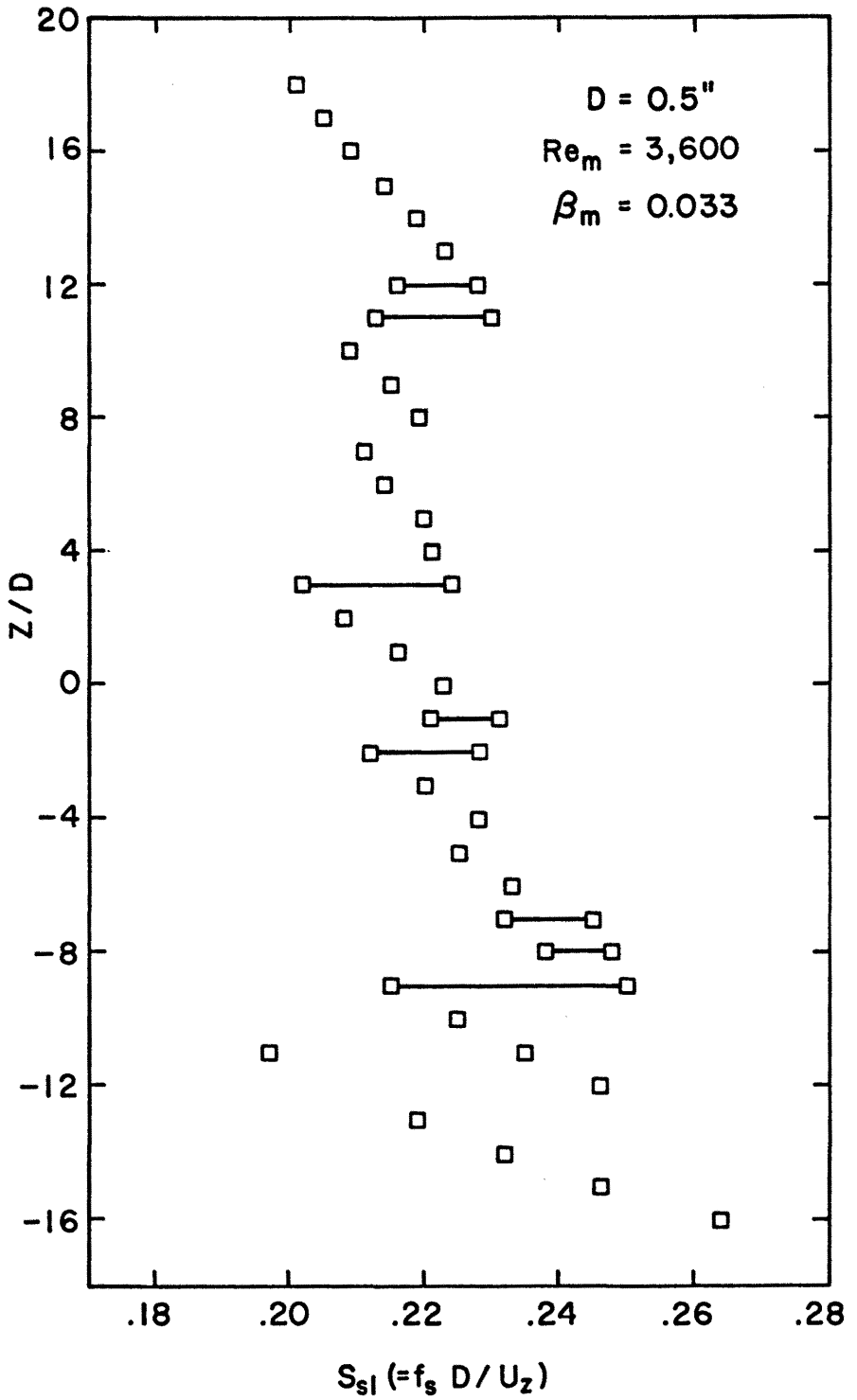

Figure 4.1.35. Spanwise Variation of $S_{s\ell}$ for the Stationary Cylinder with D = 0.50 in., Re_m = 3,600, β_m = 0.033

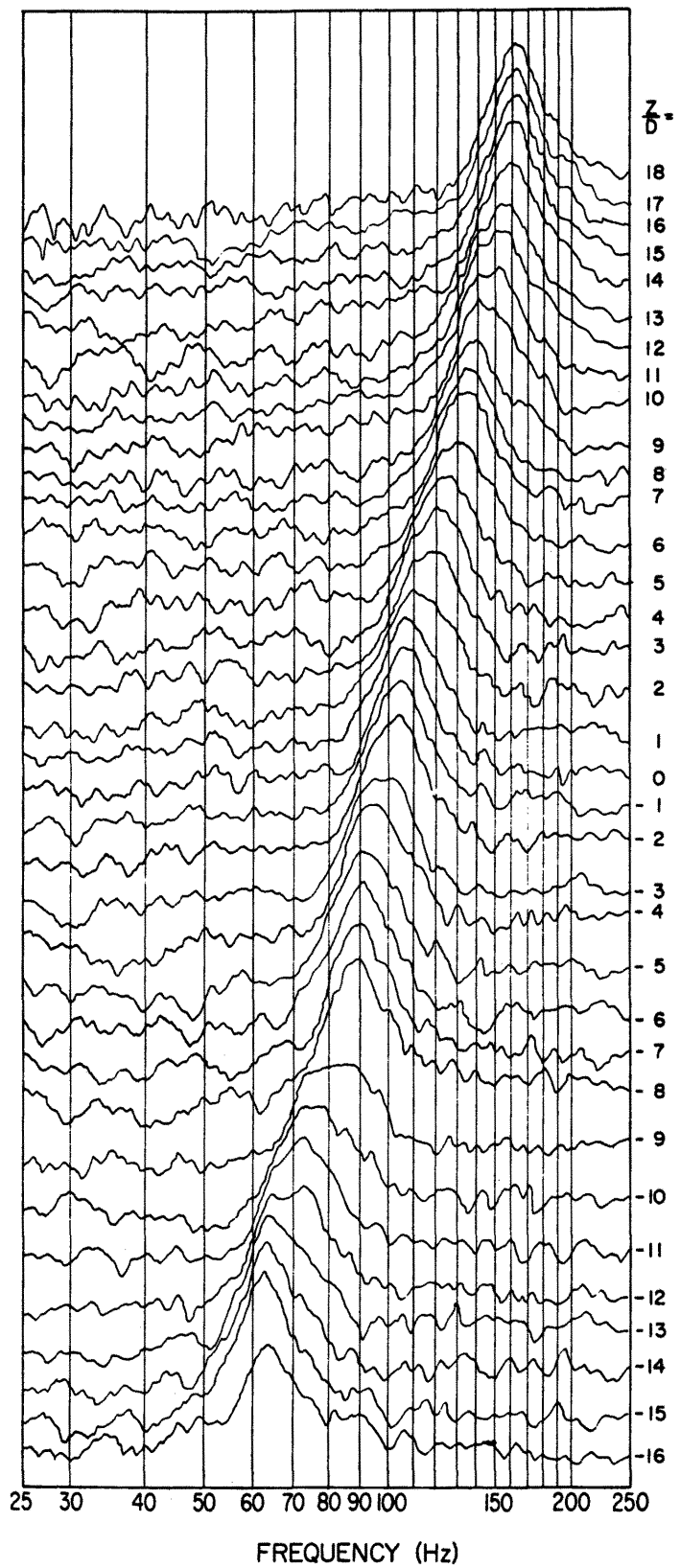

Figure 4.1.36. Frequency Spectra at Various Spanwise Positions for the Stationary Cyclinder with D = 0.50 in., Re_m = 4,500, β_m = 0.034

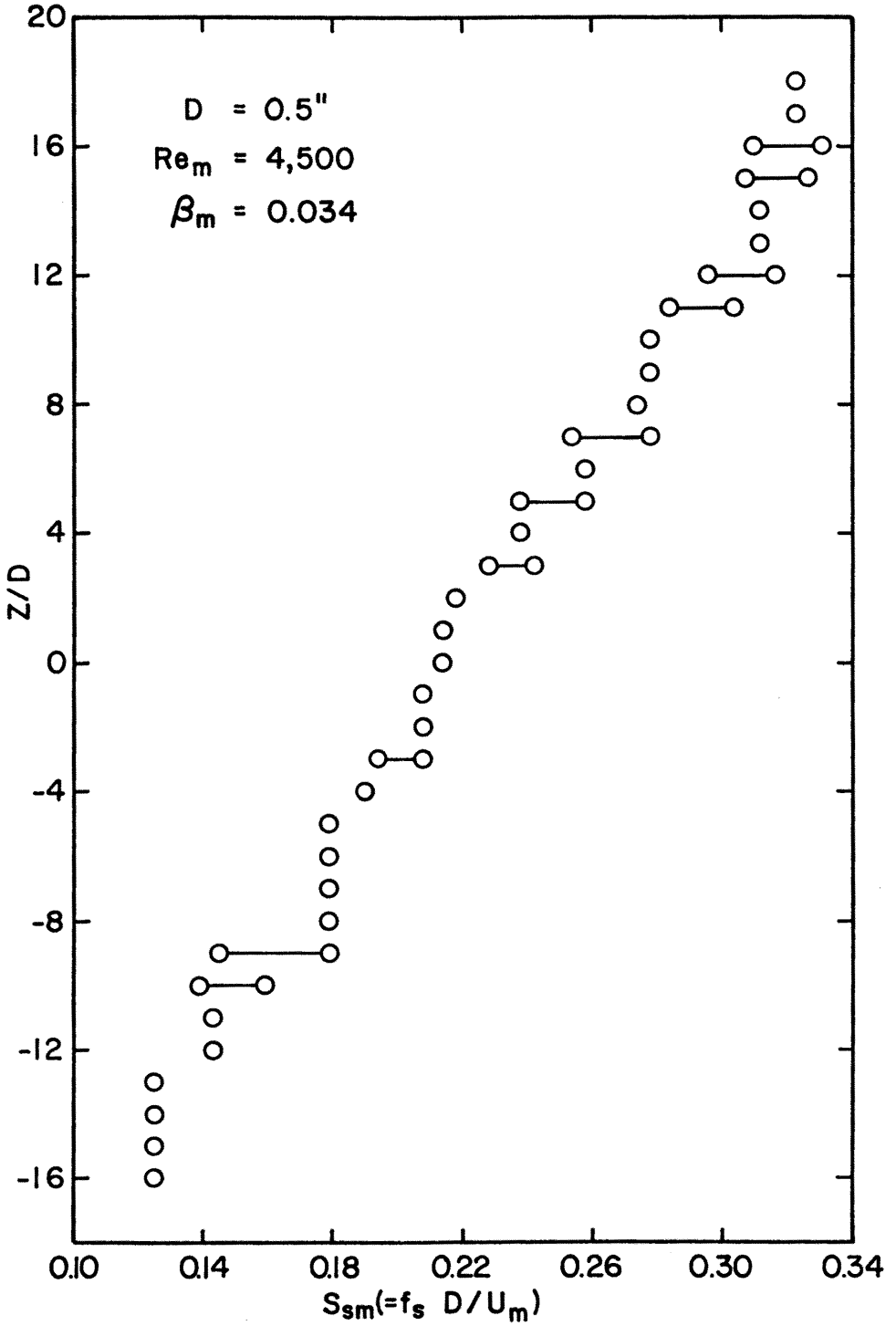

Figure 4.1.37. Spanwise Variation of S_{sm} for the Stationary Cylinder with D = 0.50 in., $Re_m = 4{,}500$, $\beta_m = 0.034$

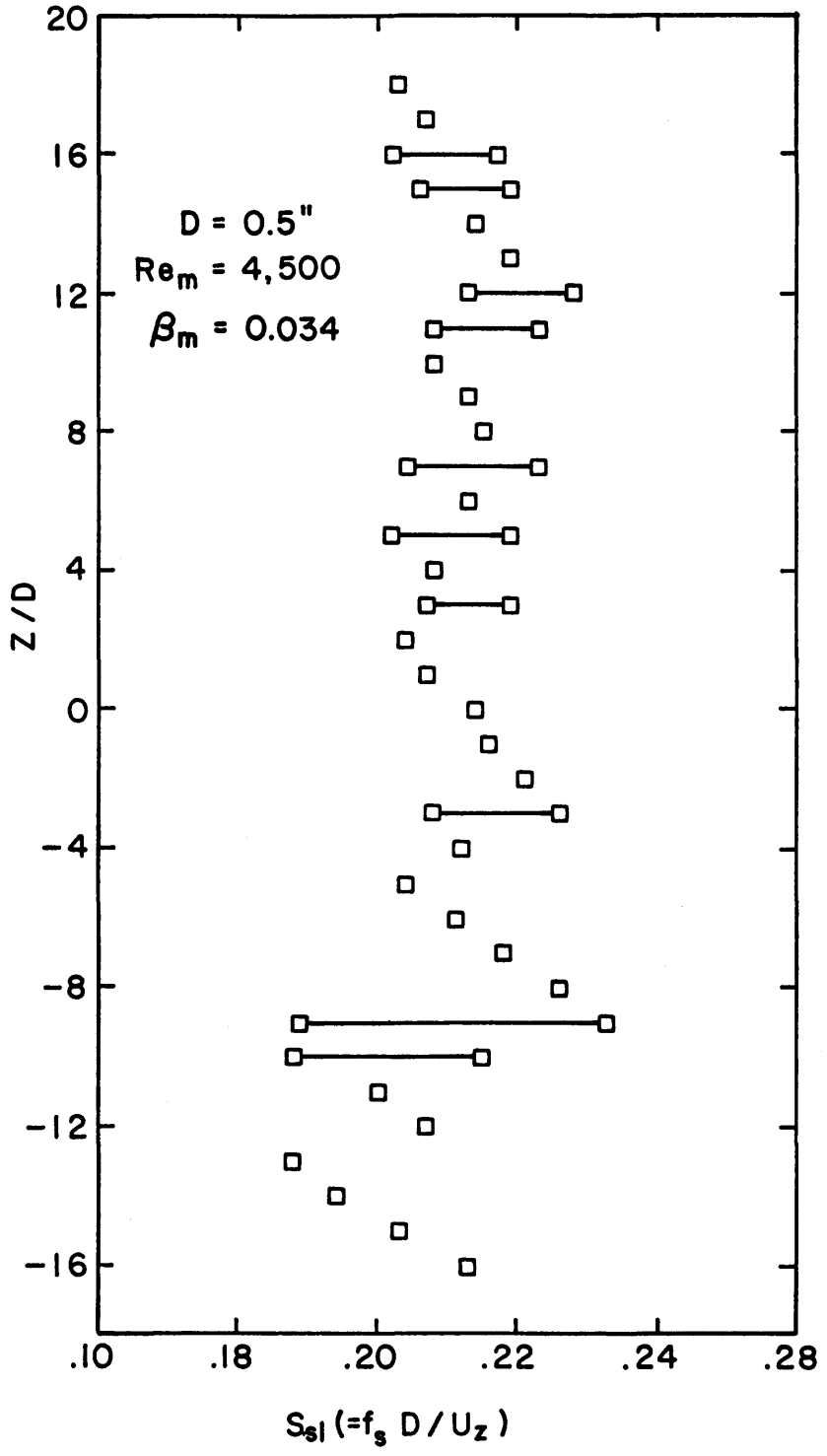

Figure 4.1.38. Spanwise Variation of $S_{s\ell}$ for the Stationary Cylinder with D = 0.50 in., $Re_m \cong 4{,}500$, $\beta_m = 0.034$

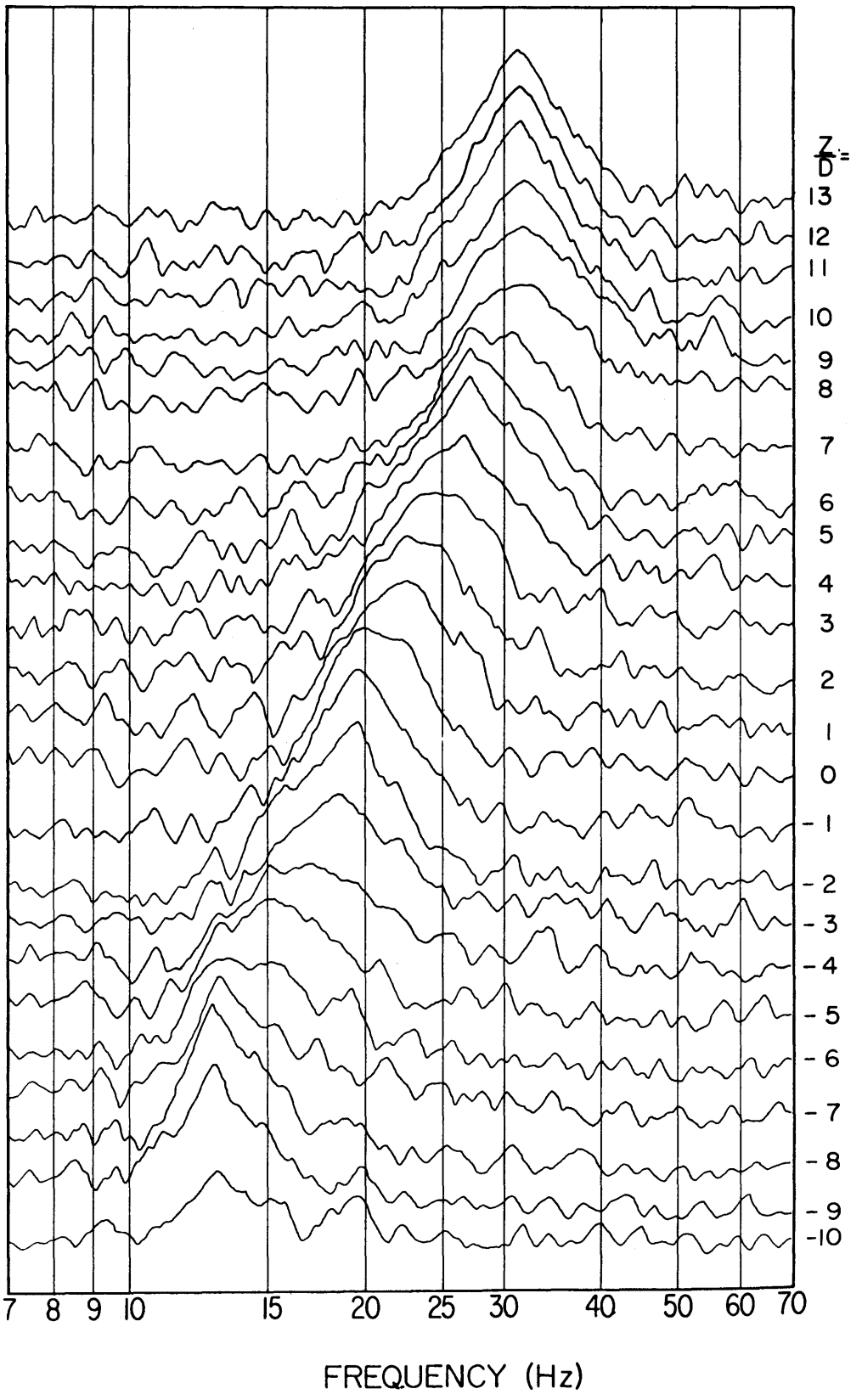

Figure 4.1.39. Frequency Spectra at Various Spanwise Positions for the Stationary Cylinder with D = 0.75 in., Re_m = 1,950, β_m = 0.052

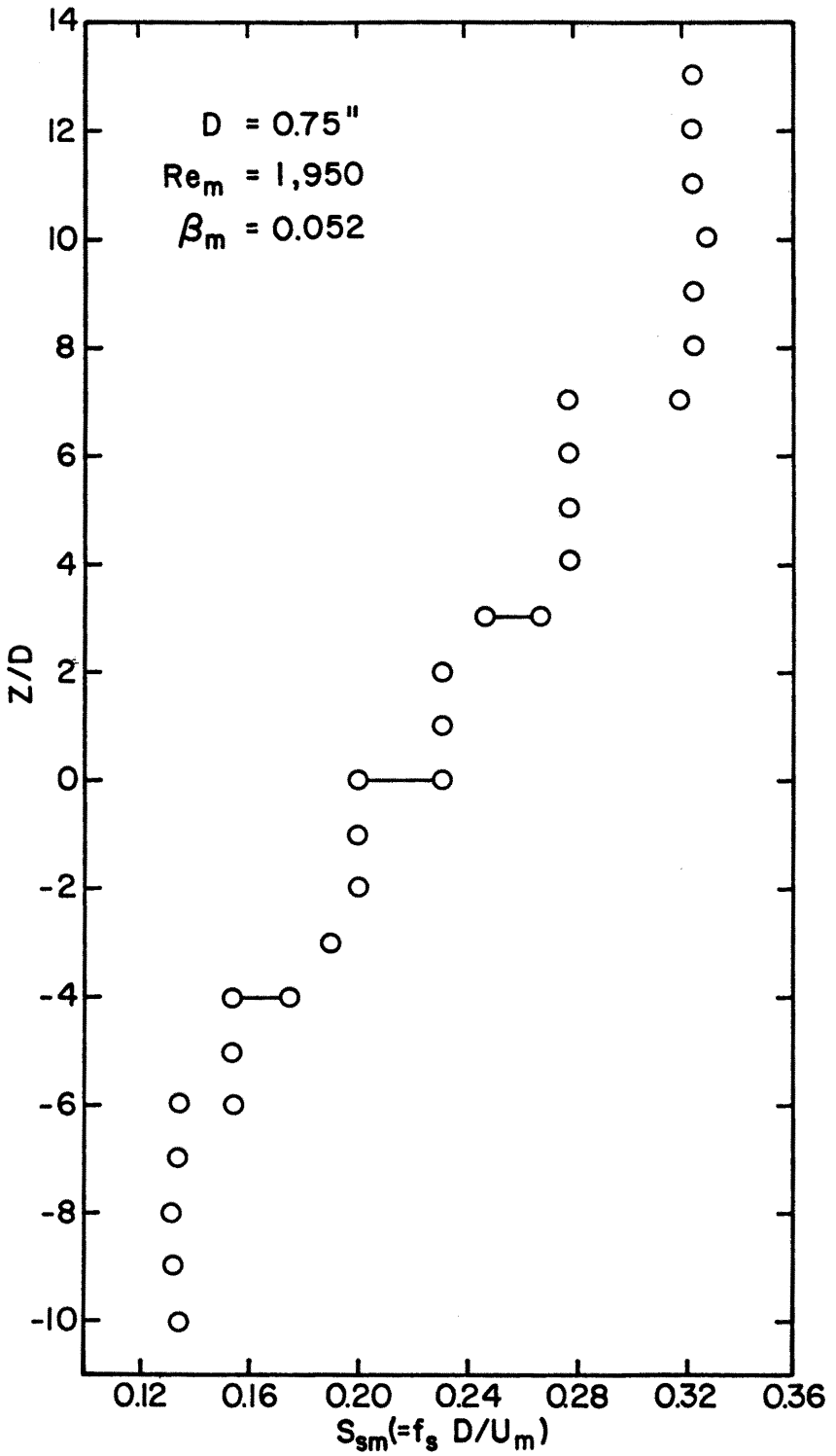

Figure 4.1.40. Spanwise Variation of S_{sm} for the Stationary Cylinder with D = 0.50 in., Re_m = 1,950, β_m = 0.052

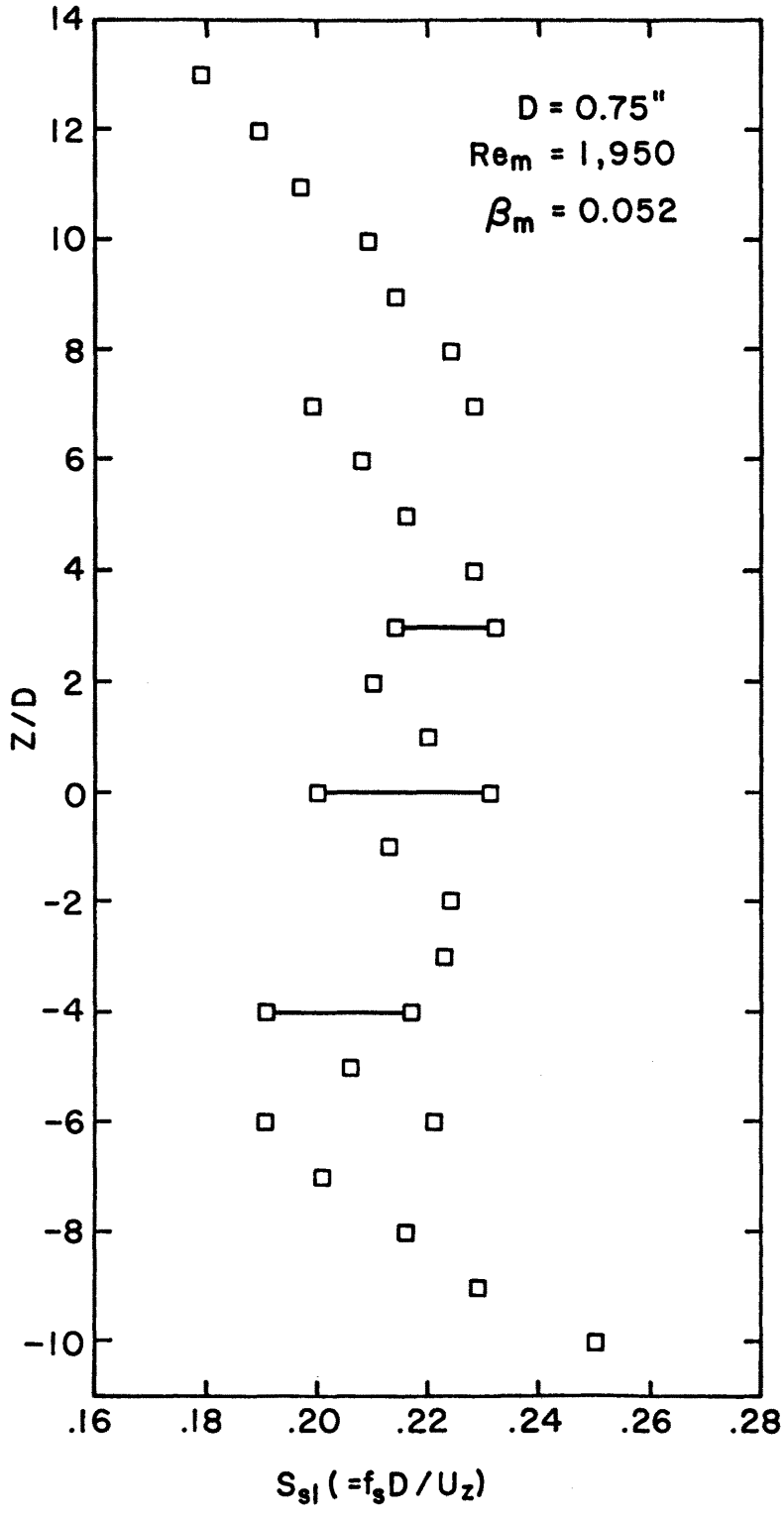

Figure 4.1.41. Spanwise Variation of $S_{s\ell}$ for the Stationary Cylinder with D = 0.50 in., $Re_m \cong 1{,}950$, $\beta_m = 0.052$

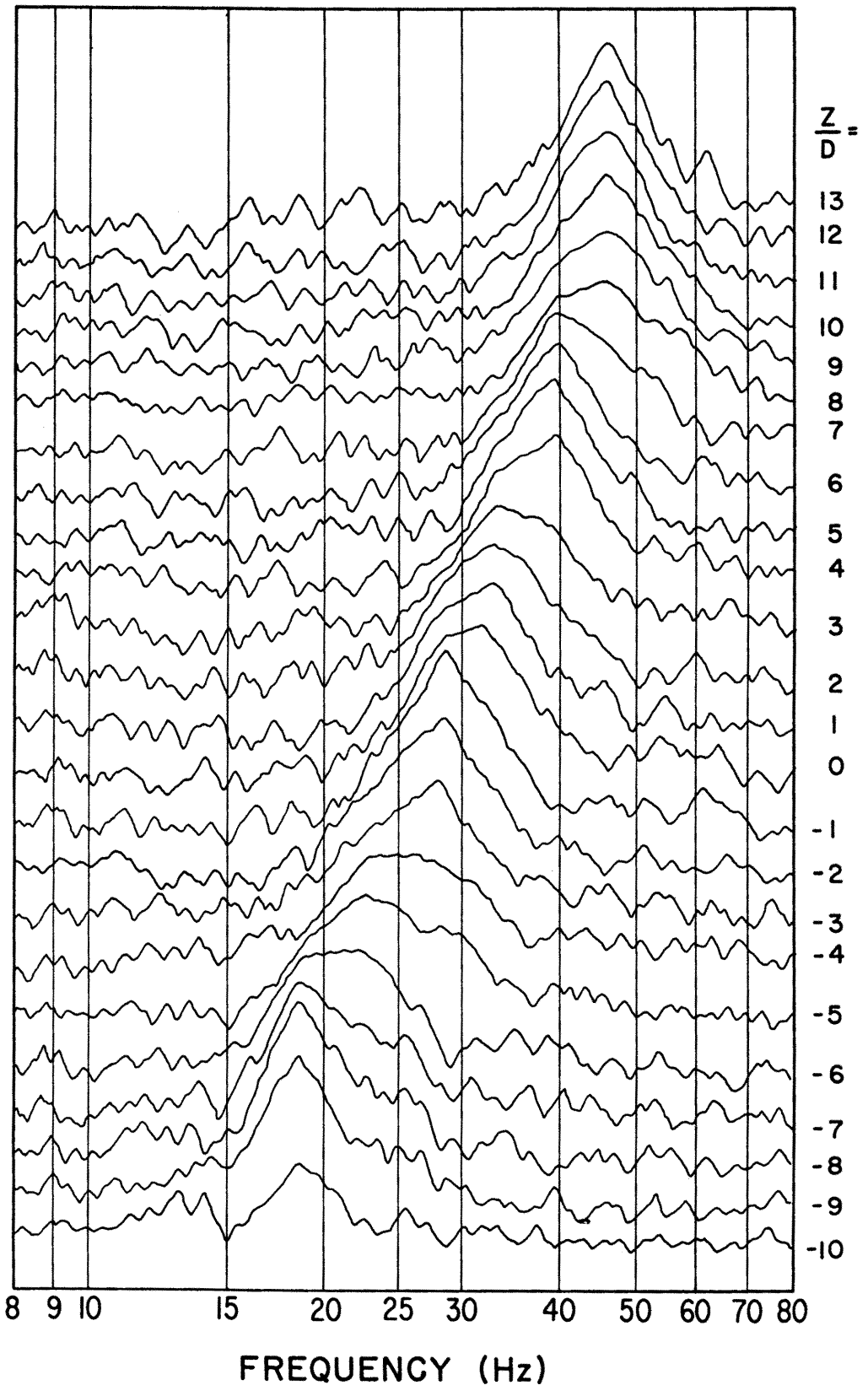

Figure 4.1.42. Frequency Spectra at Various Spanwise Positions for the Stationary Cylinder with D = 0.75 in., Re_m = 2,920, β_m = 0.052

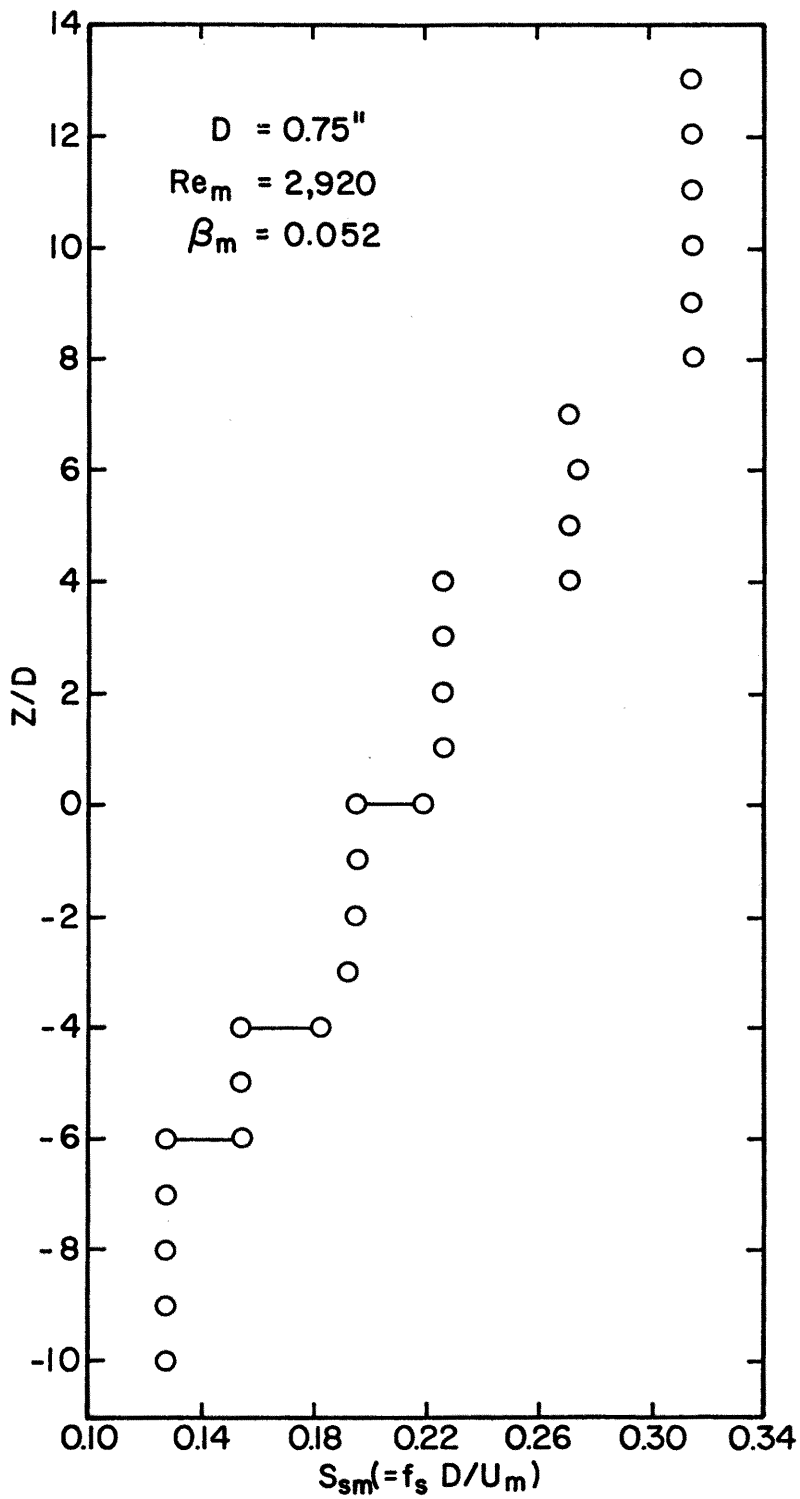

Figure 4.1.43. Spanwise Variation of S_{sm} for the Stationary Cylinder with D = 0.75 in., Re_m = 2,920, β_m = 0.052

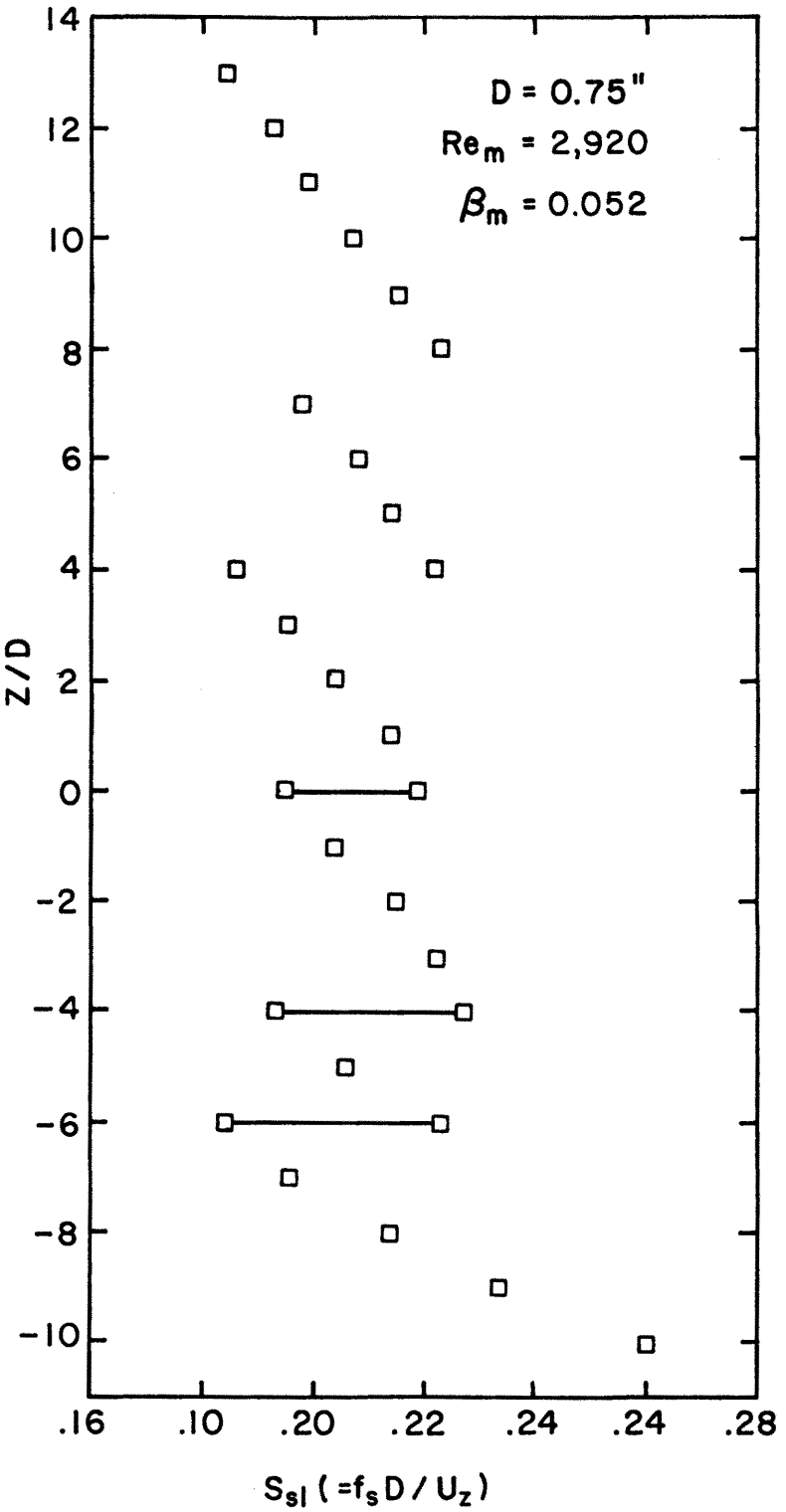

Figure 4.1.44. Spanwise Variation of $S_{s\ell}$ for the Stationary Cylinder with D = 0.75 in., Re_m = 2,920, β_m = 0.052

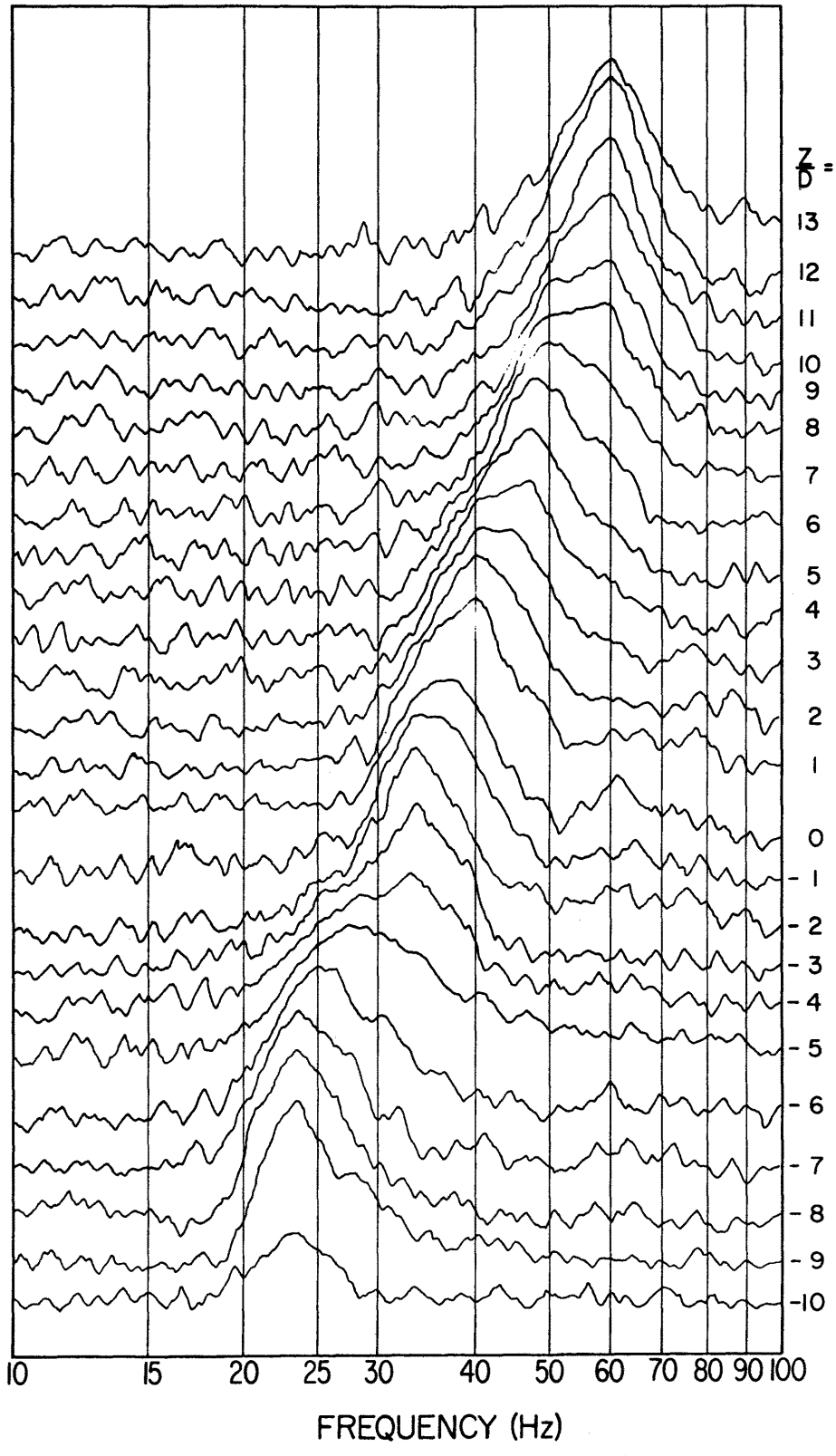

Figure 4.1.45. Frequency Spectra at Various Spanwise Positions for the Stationary Cylinder with D = 0.75 in., Re_m = 3,900 β_m = 0.050

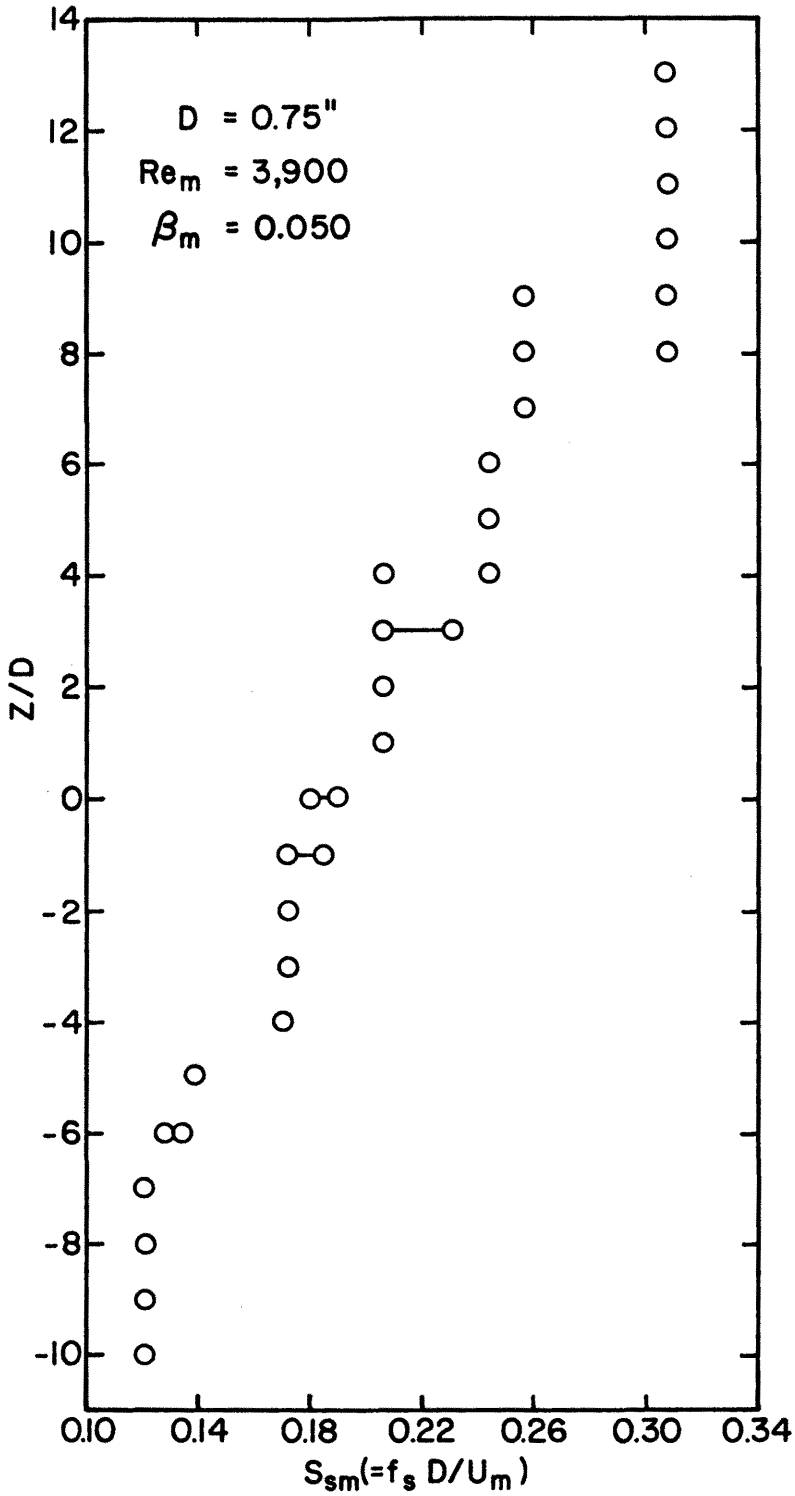

Figure 4.1.46. Spanwise Variation of S_{sm} for the Stationary Cylinder with D = 0.75 in., Re_m = 3,900 β_m = 0.050

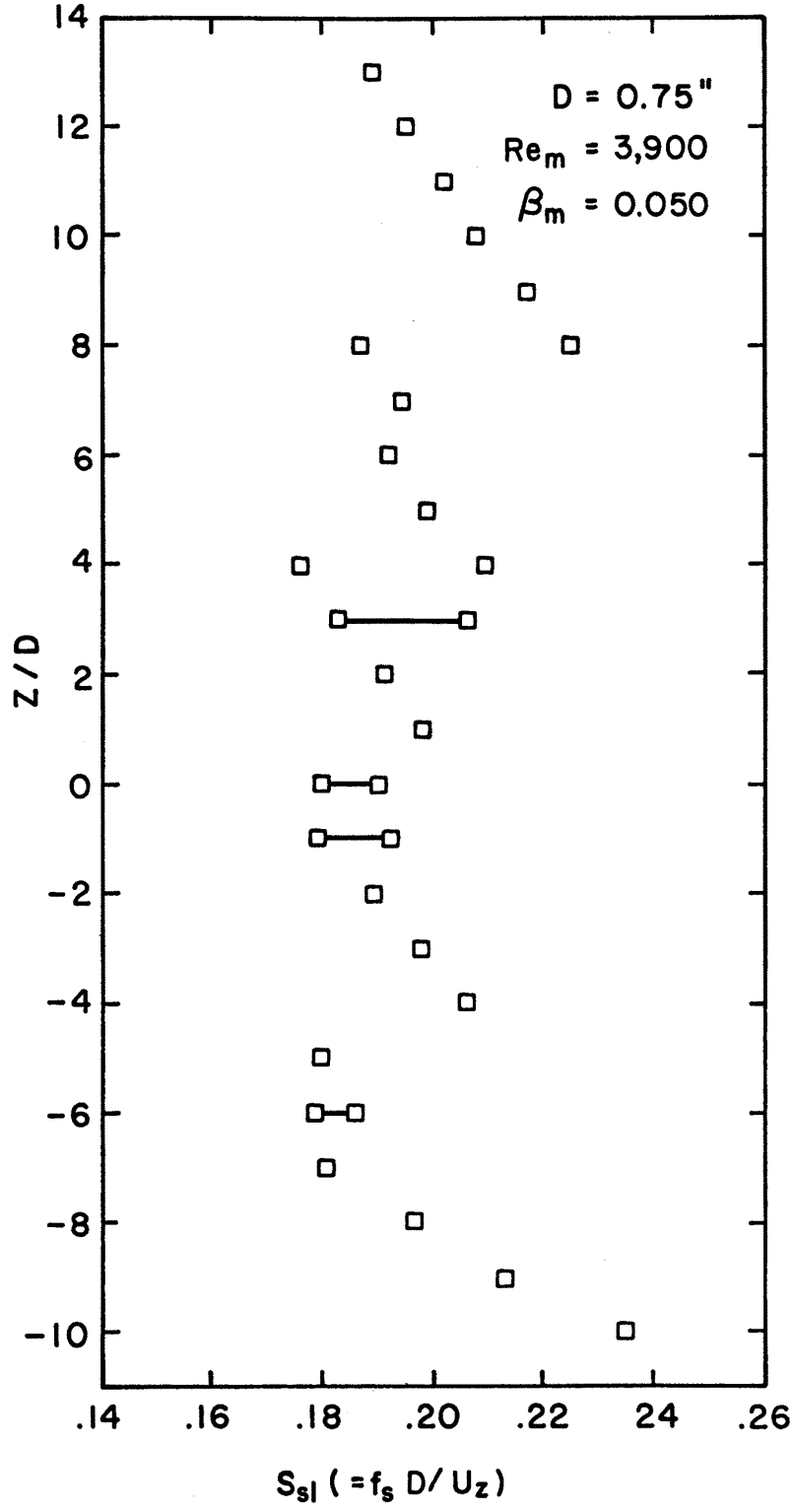

Figure 4.1.47. Spanwise Variation of $S_{s\ell}$ for the Stationary Cylinder with D = 0.75 in., Re_m = 3,900, β_m = 0.050

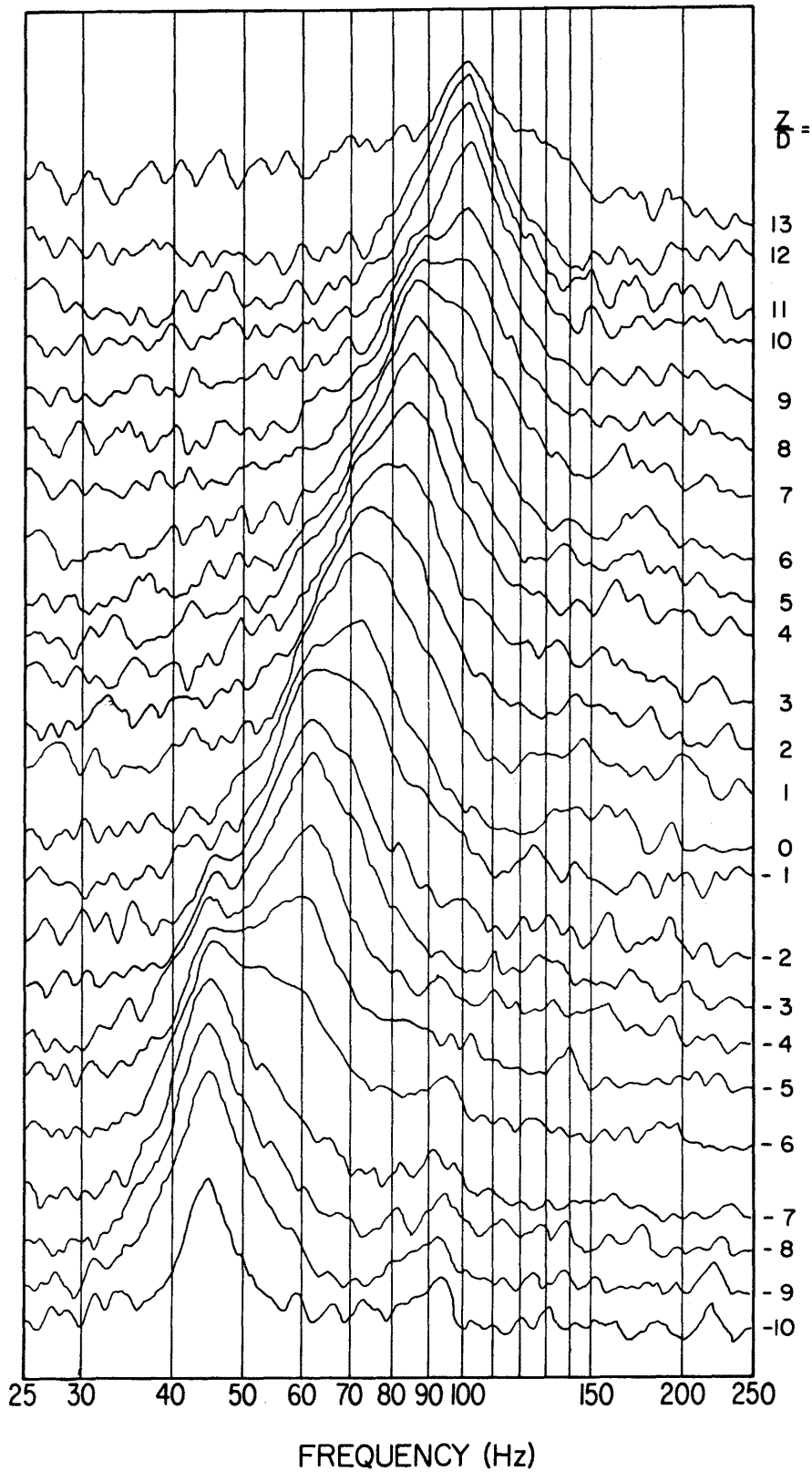

Figure 4.1.48. Frequency Spectra at Various Spanwise Positions for the Stationary Cylinder with D = 0.75 in., Re_m = 6,730, β_m = 0.051

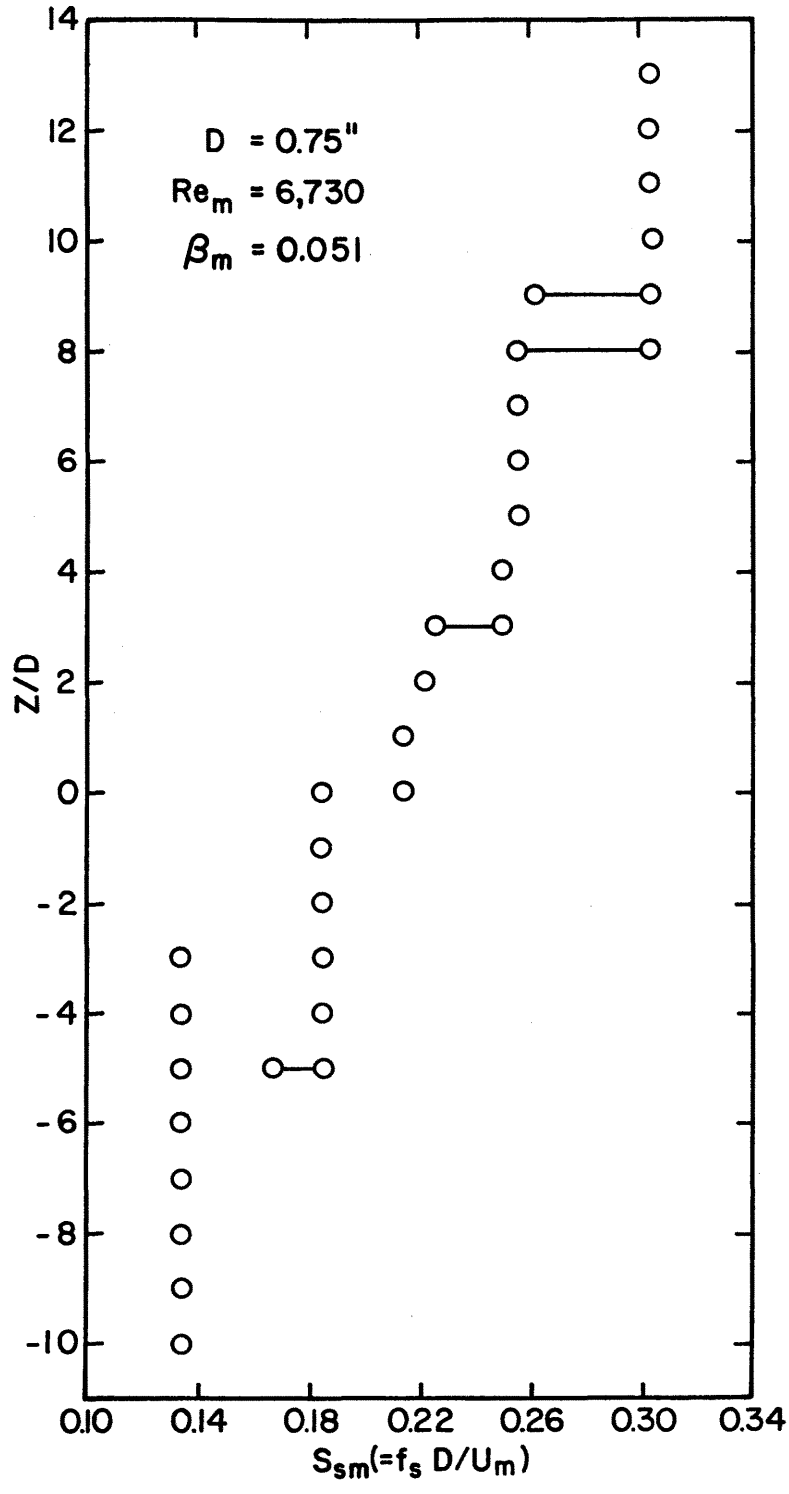

Figure 4.1.49. Spanwise Variation of S_{sm} for the Stationary Cylinder with D = 0.75 in., Re_m = 6,730, β_m = 0.051

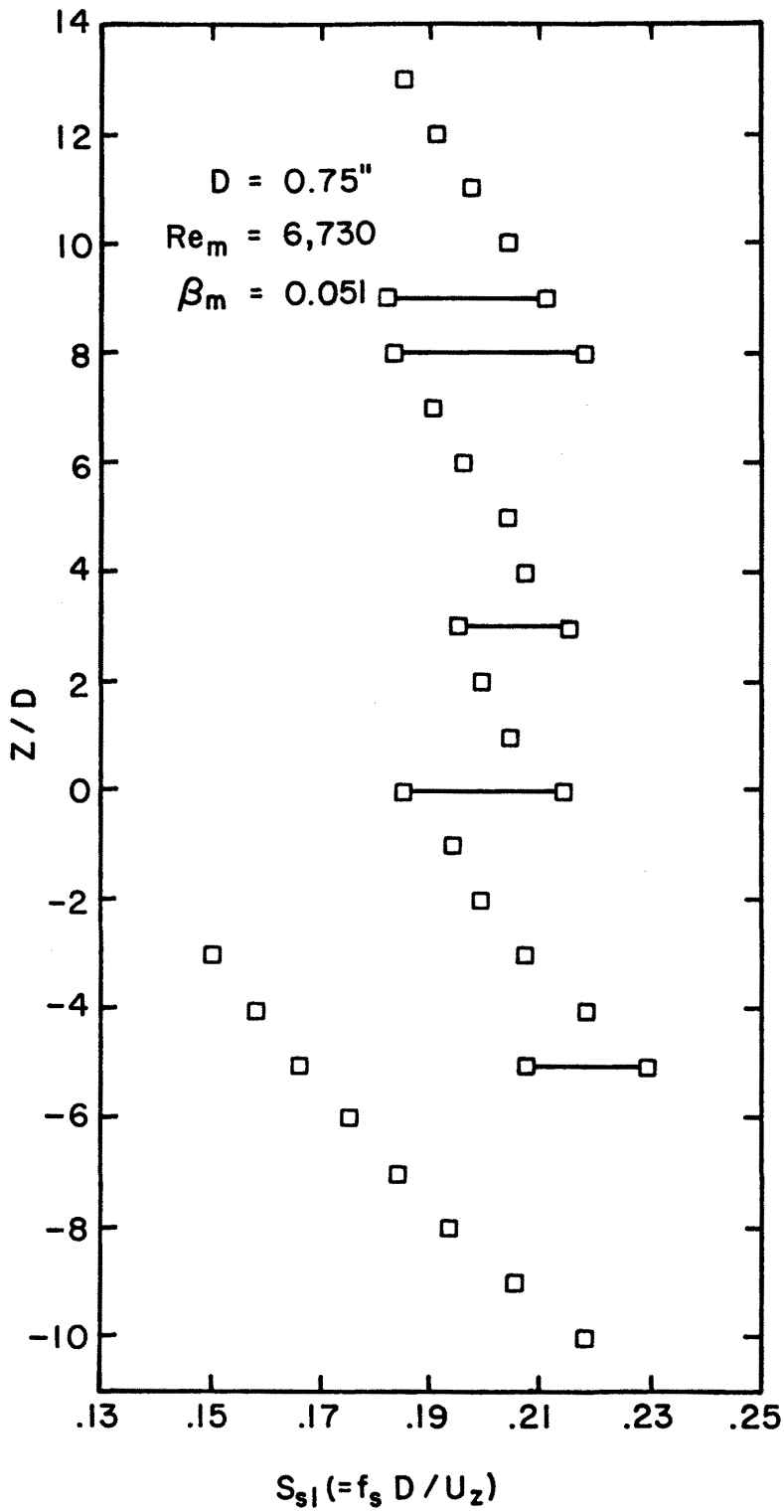

Figure 4.1.50. Spanwise Variation of $S_{s\ell}$ for the Stationary Cylinder with D = 0.75 in., Re_m = 6,730, β_m = 0.051

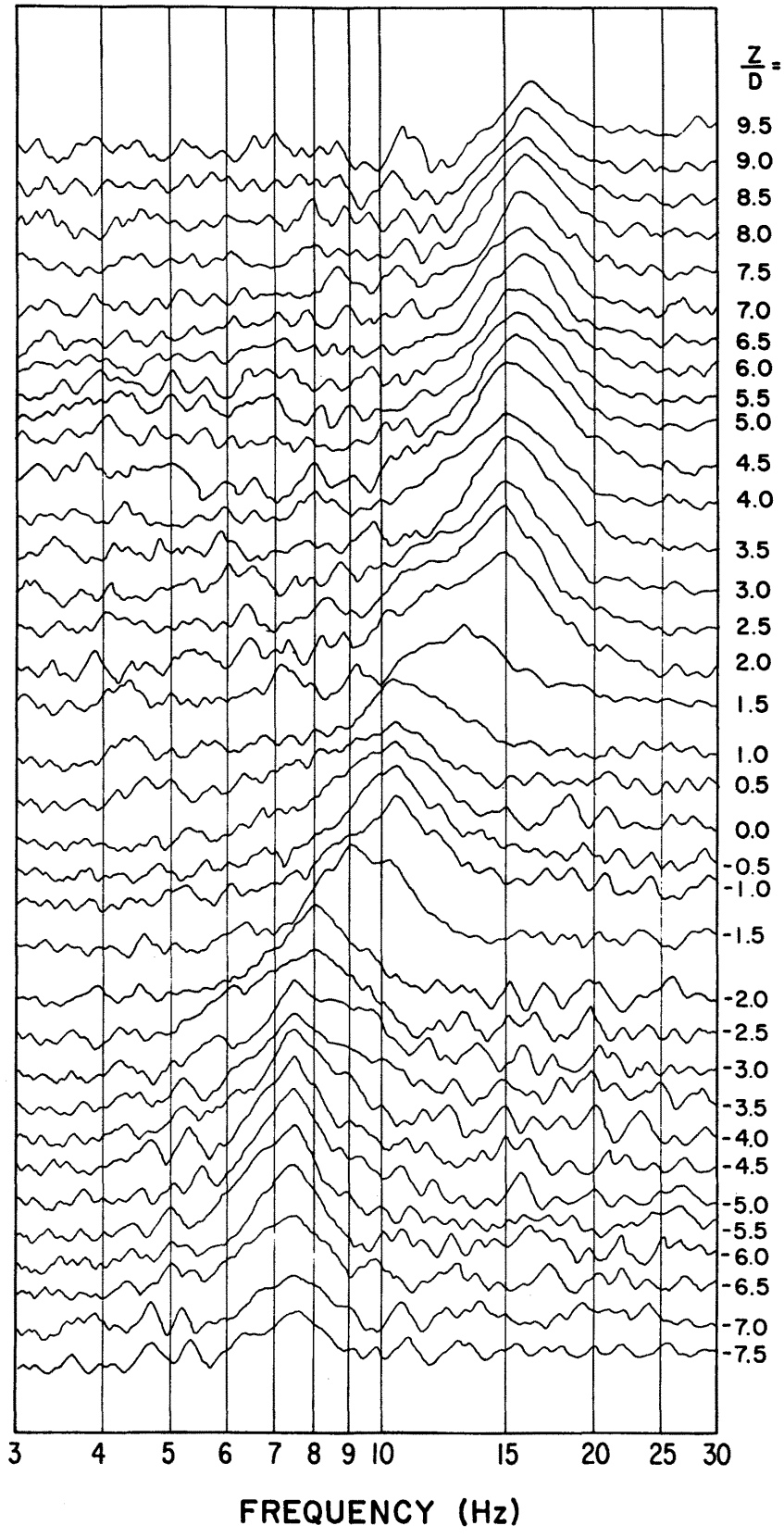

Figure 4.1.51. Frequency Spectra at Various Spanwise Positions for the Stationary Cylinder with D = 1.00 in., Re_m = 1,950, β_m = 0.075

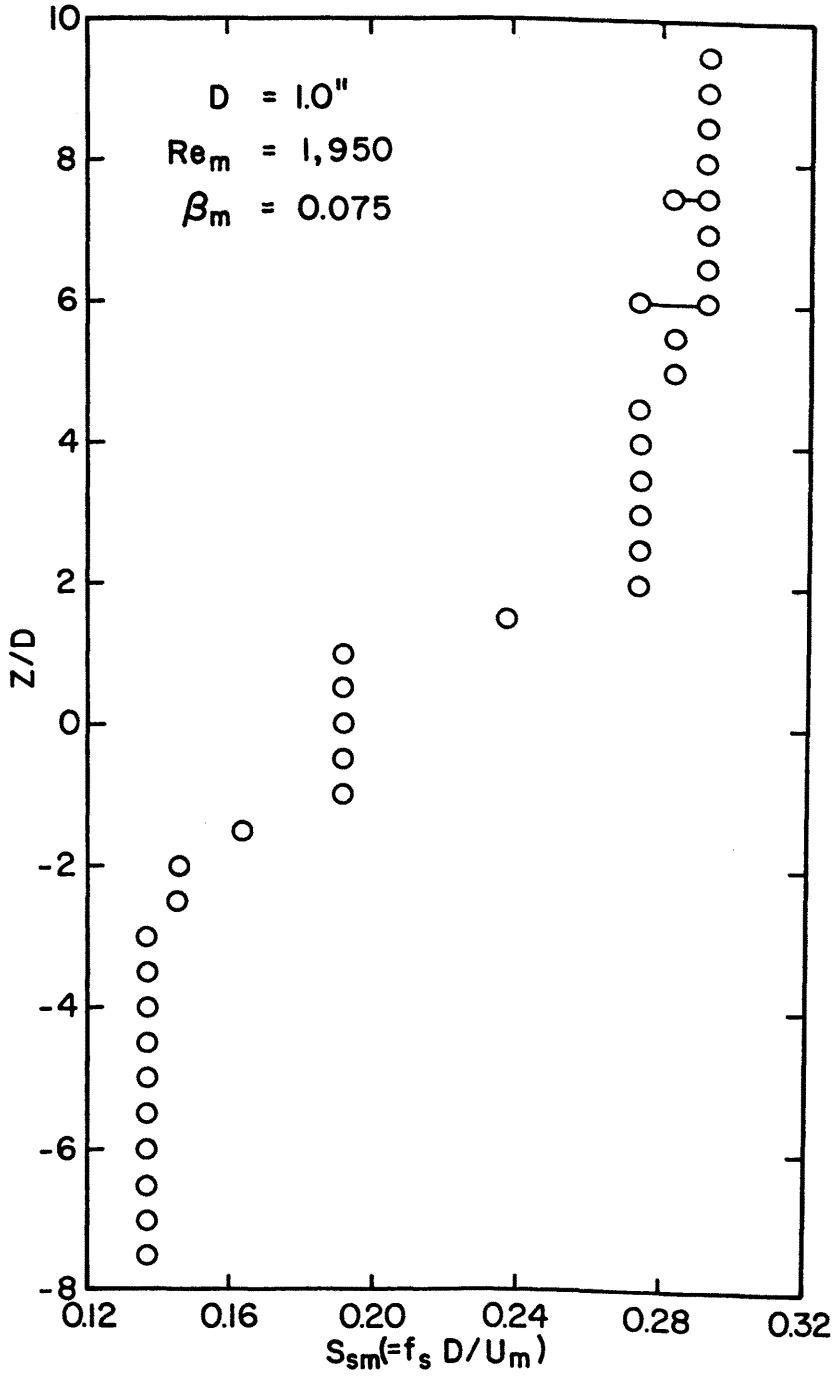

Figure 4.1.52. Spanwise Variation of S_{sm} for the Stationary Cylinder with D = 1.00 in., Re_m = 1,950, β_m = 0.075

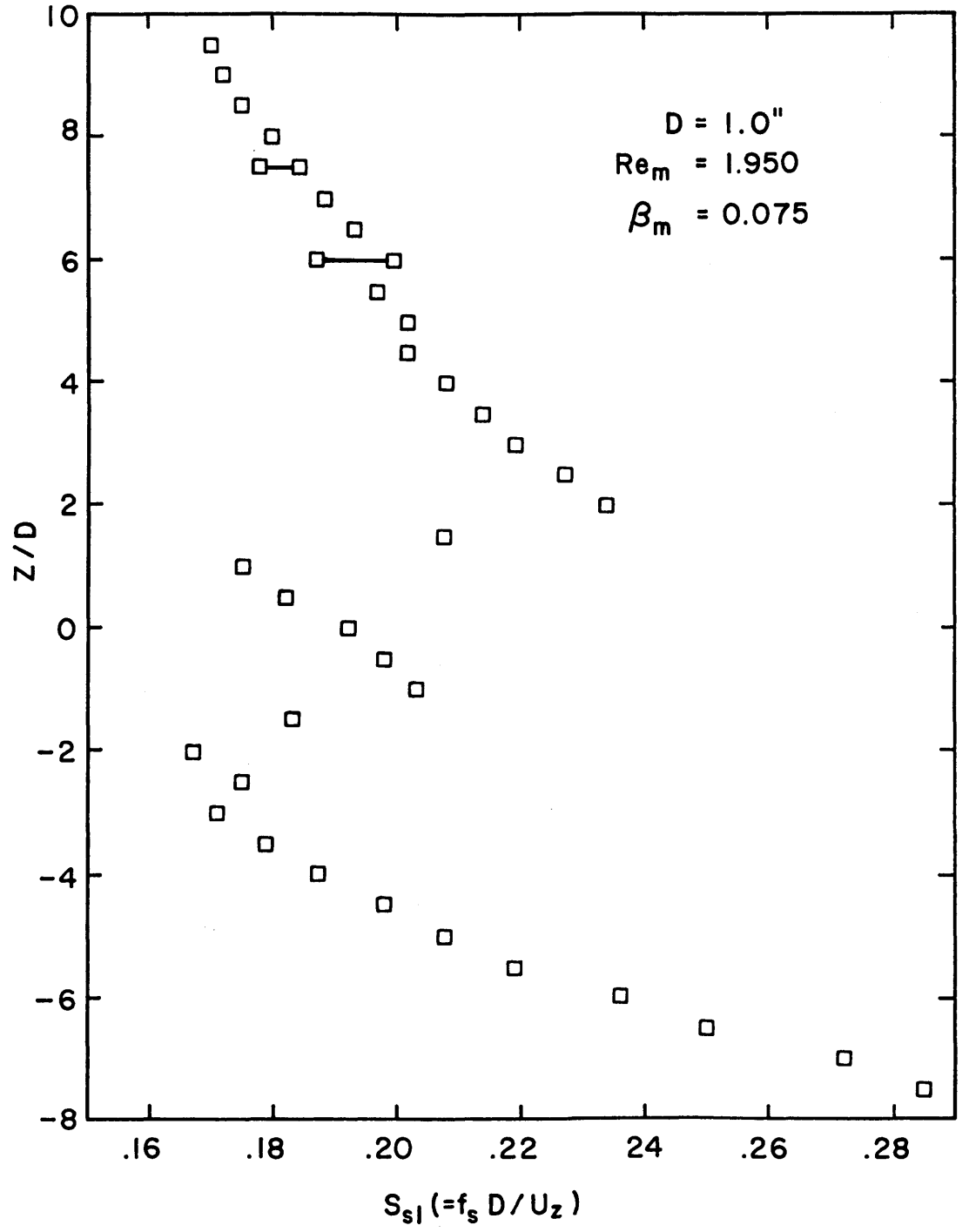

Figure 4.1.53. Spanwise Variation of $S_{s\ell}$ for the Stationary Cylinder with D = 1.00 in., Re_m = 1,950, β_m = 0.075

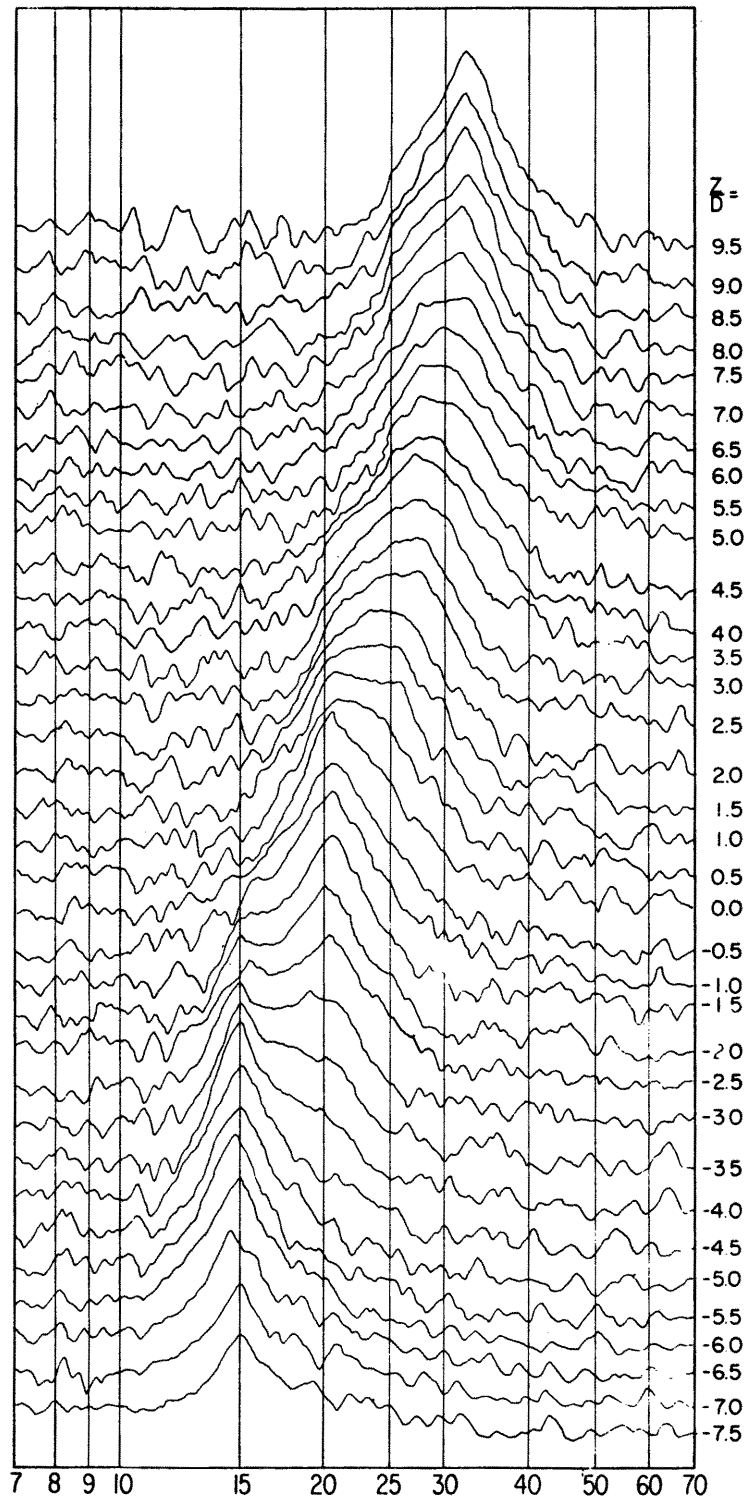

Figure 4.1.54. Frequency Spectra at Various Spanwise Positions for the Stationary Cylinder with D = 1.00 in., Re_m = 3,900, β_m = 0.069

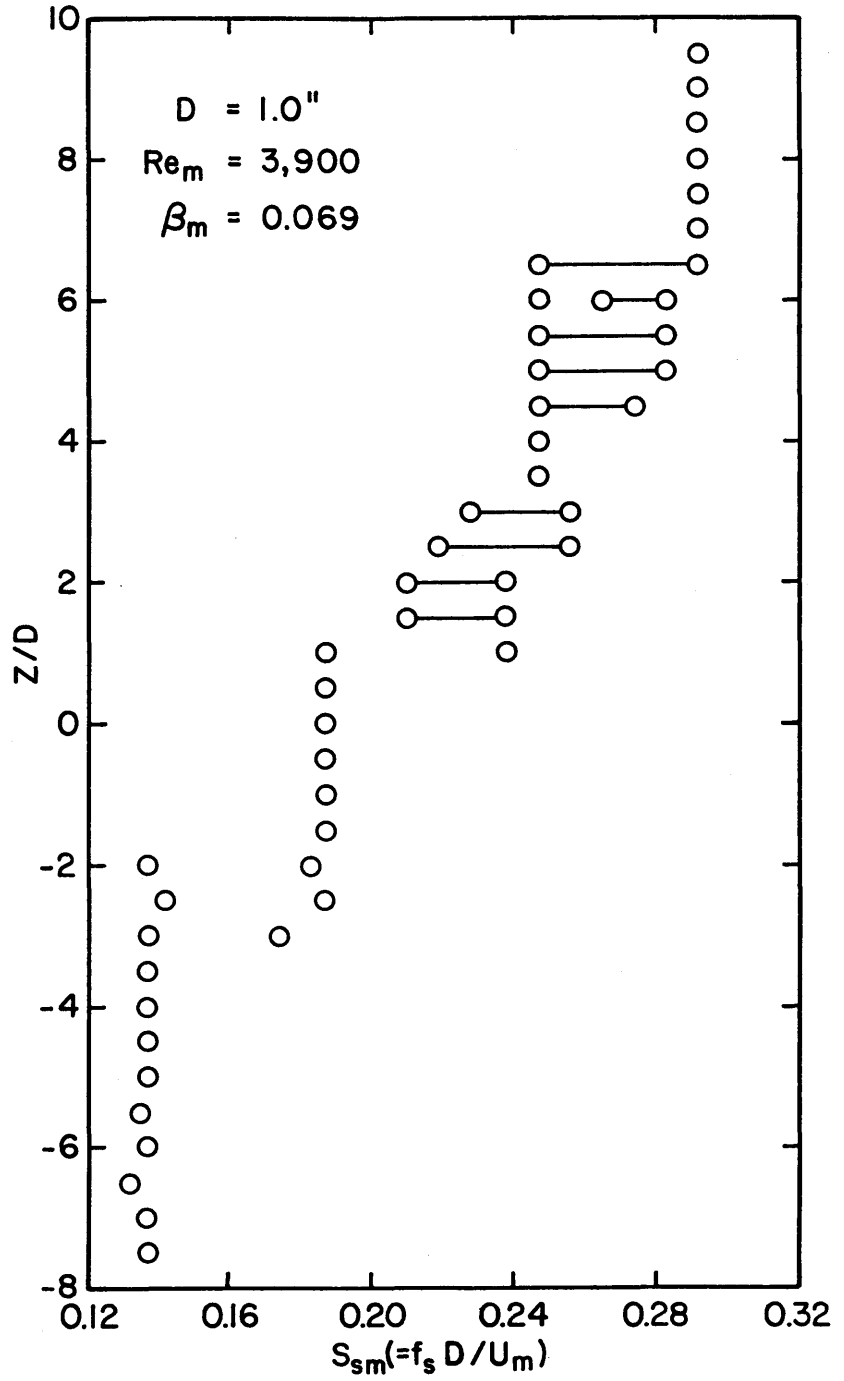

Figure 4.1.55. Spanwise Variation of S_{sm} for the Stationary Cylinder with D = 1.00 in., Re_m = 3,900, β_m = 0.069

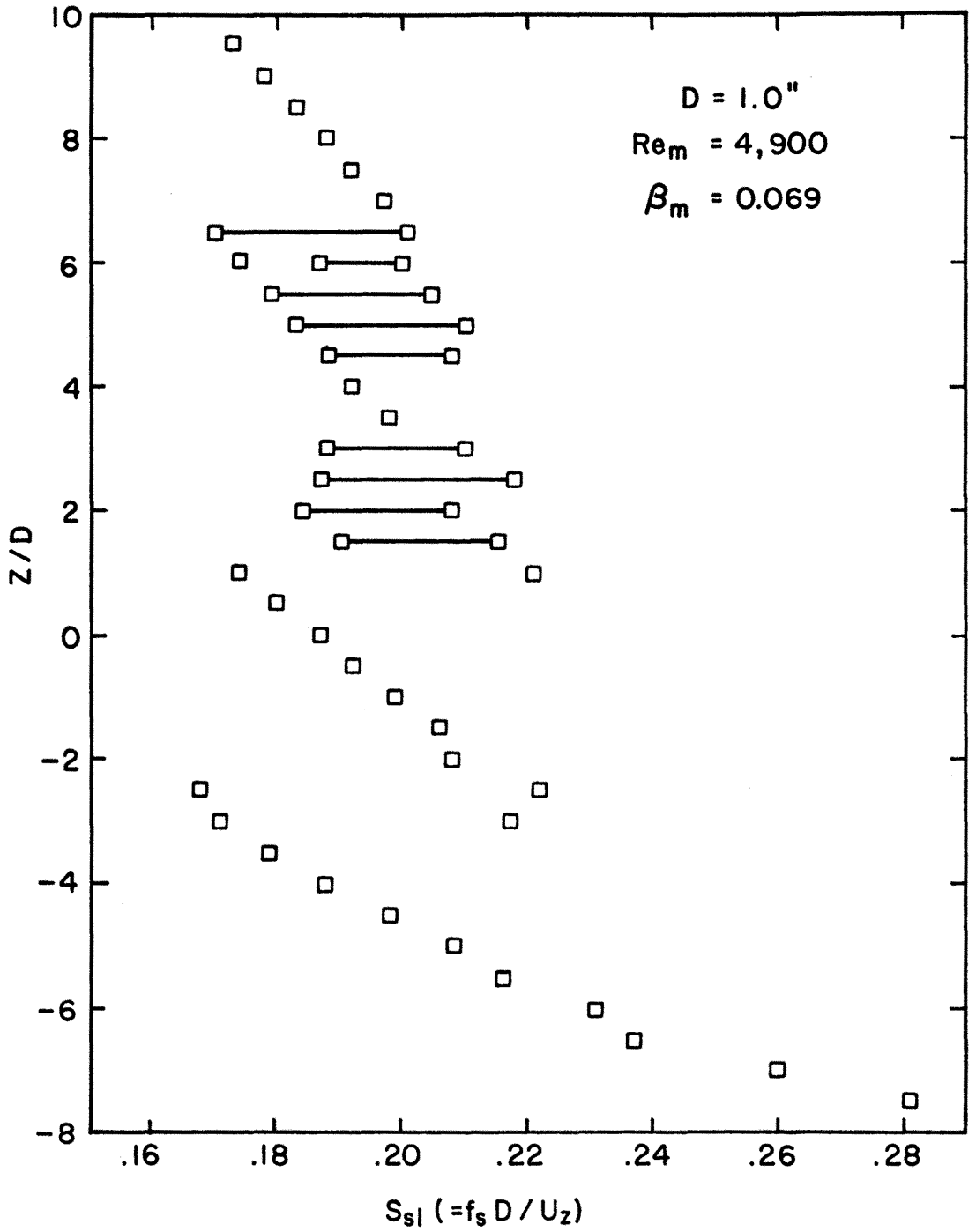

Figure 4.1.56. Spanwise Variation of $S_{s\ell}$ for the Statonary Cylinder with D = 1.00 in., Re_m = 3,900, β_m = 0.069

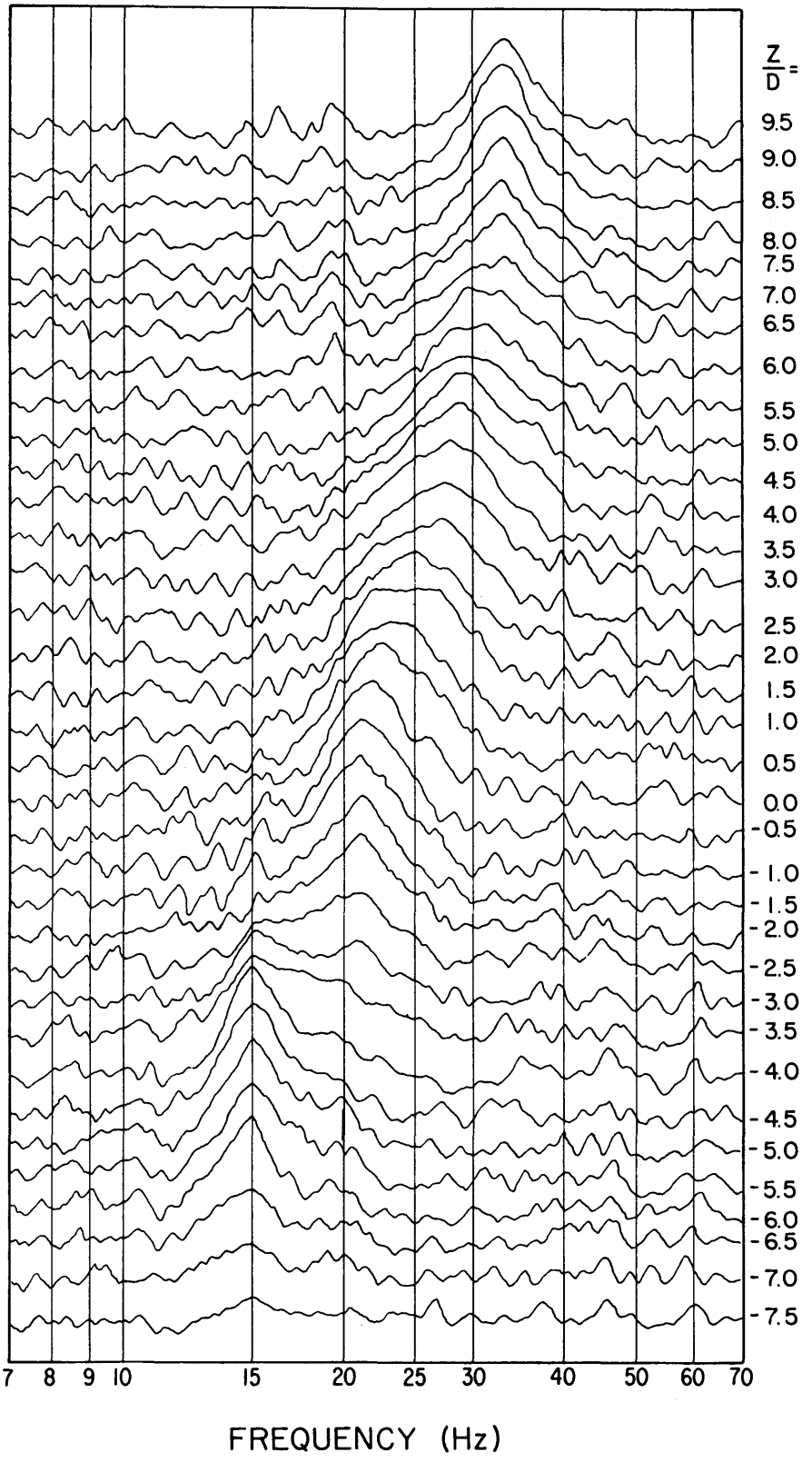

Figure 4.1.57. Frequency Spectra at Various Spanwise Positions for the Stationary Cylinder with D = 1.00 in., Re_m = 3,900, β_m = 0.066 (repeated run)

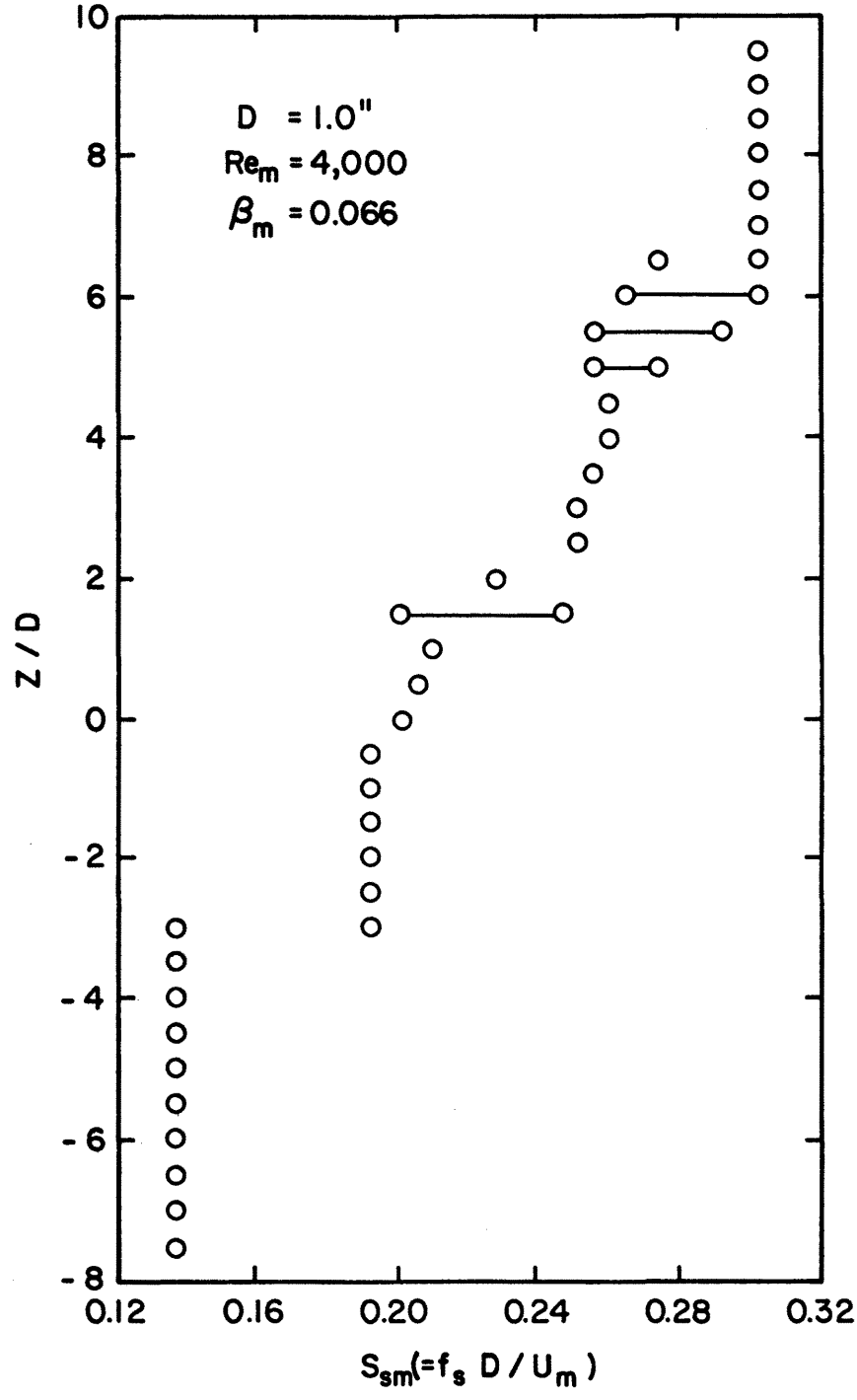

Figure 4.1.58. Spanwise Variation of S_{sm} for the Stationary Cylinder with D = 1.00 in., Re_m = 3,900, β_m = 0.069 (repeated run)

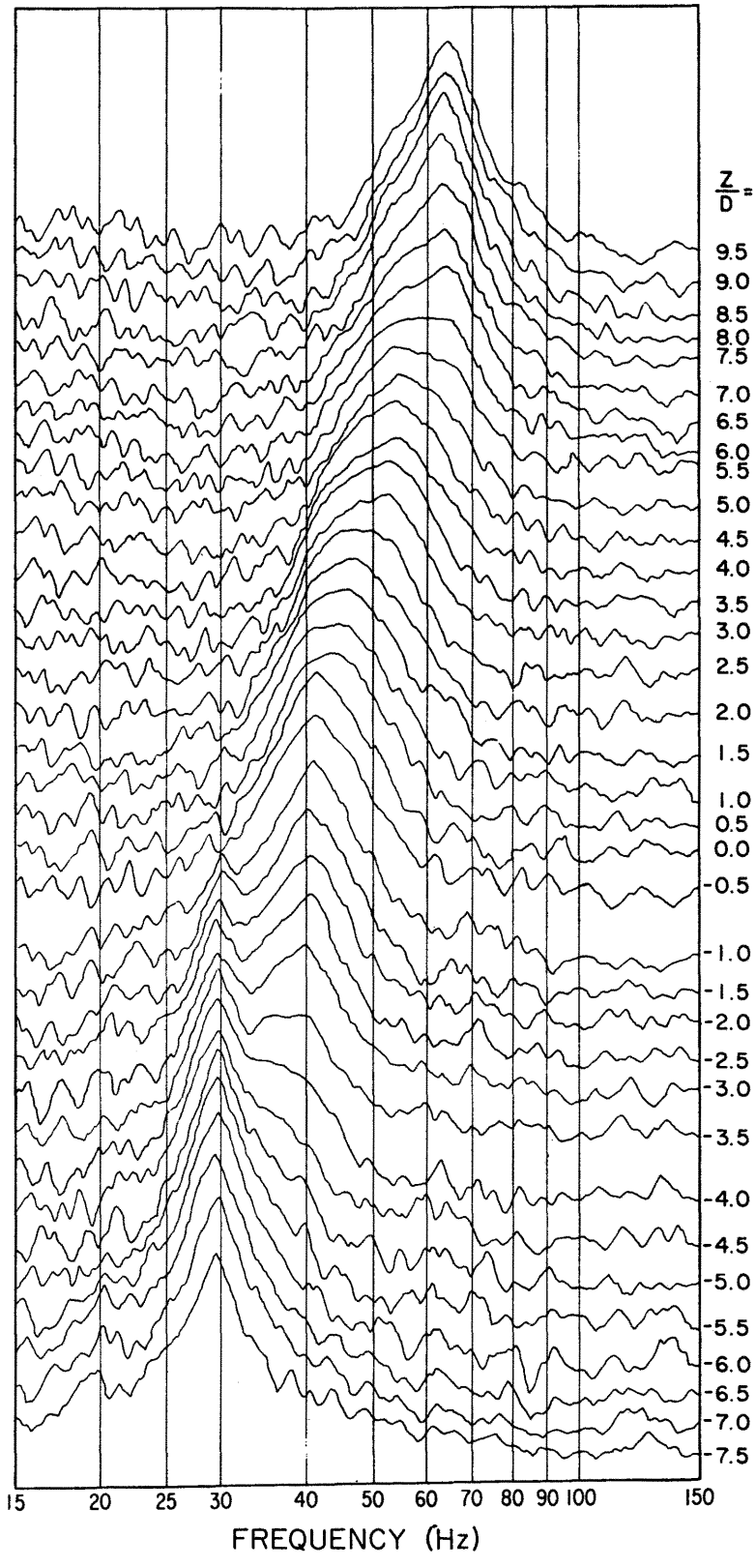

Figure 4.1.59. Frequency Spectra at Various Spanwise Positions for the Stationary Cylinder with D = 1.00 in., Re_m = 7,800, β_m = 0.065

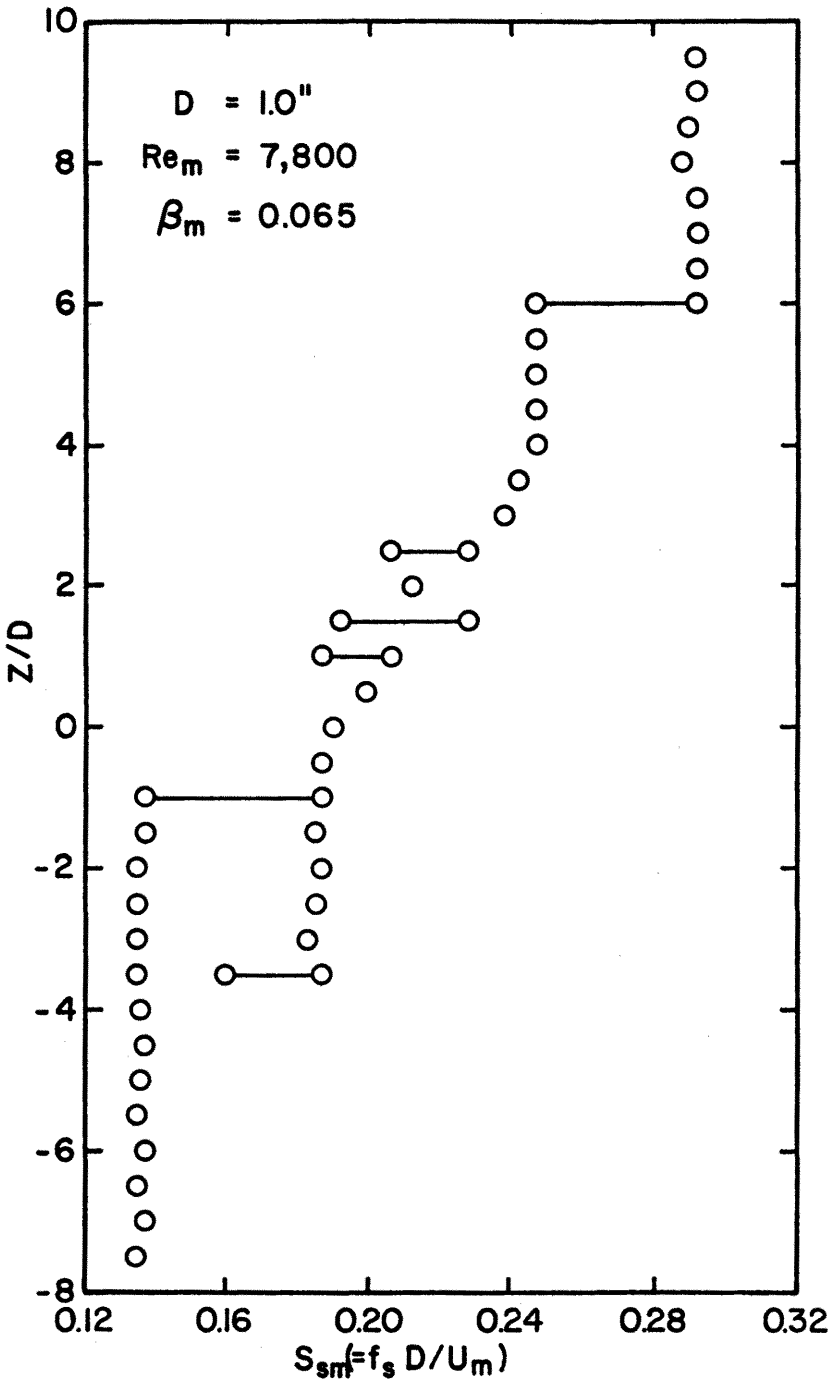

Figure 4.1.60. Spanwise Variation of S_{sm} for the Stationary Cylinder with D = 1.00 in., Re_m = 7,800, β_m = 0.065

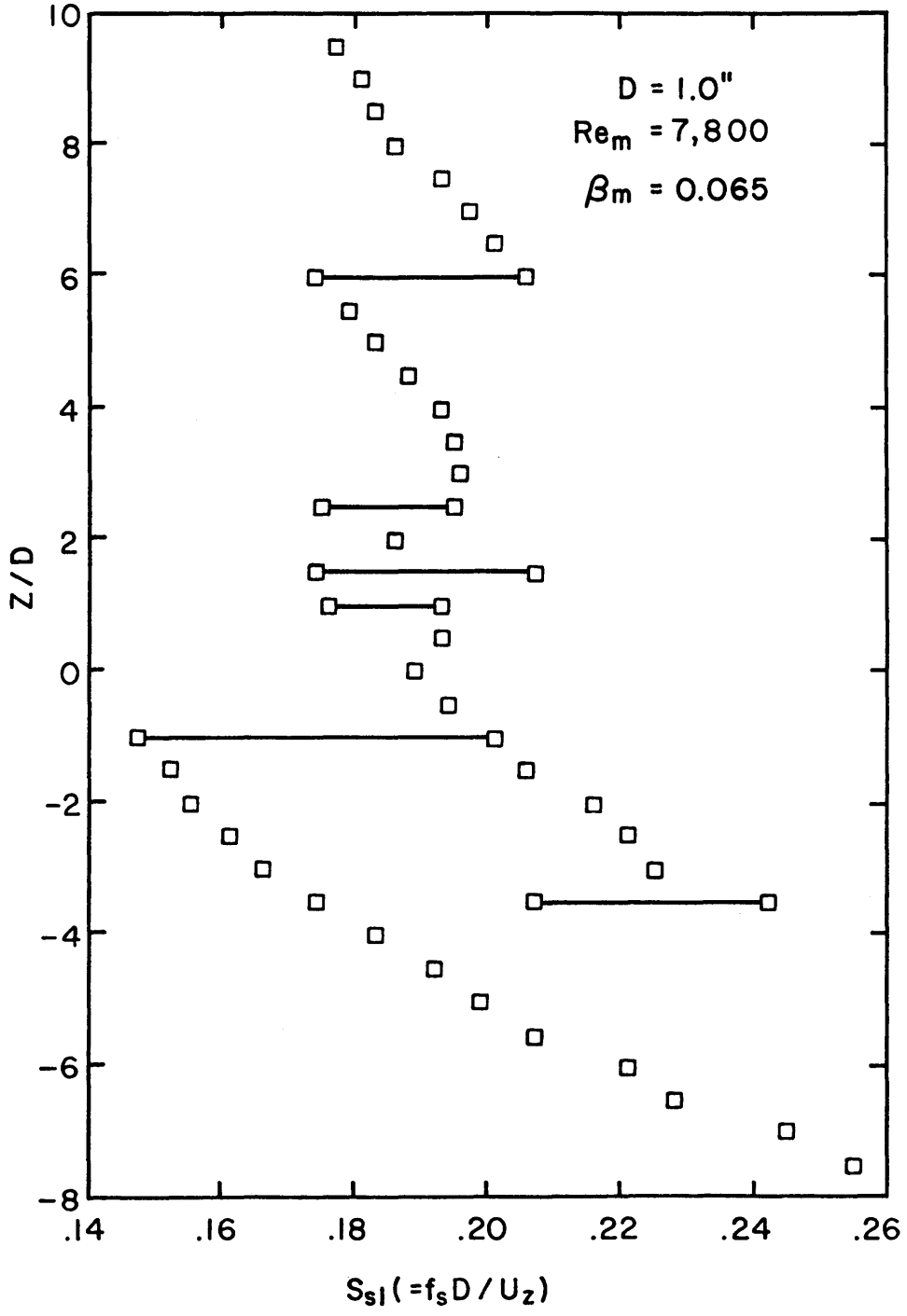

Figure 4.1.61. Spanwise Variation of $S_{s\ell}$ for the Stationary Cylinder with D = 1.00 in., Re_m = 7,800, β_m = 0.065

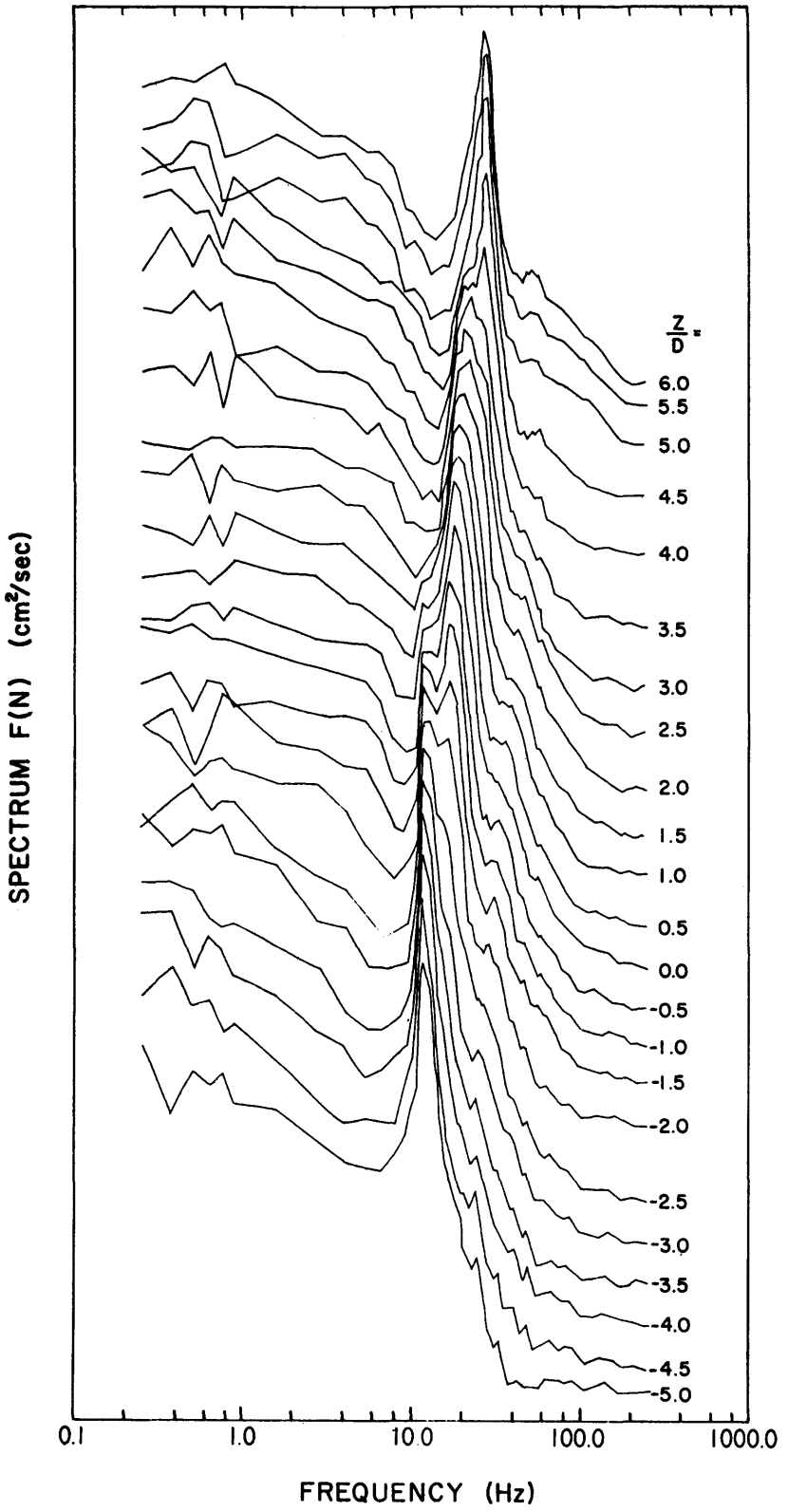

Figure 4.1.62. Frequency Spectra at Various Spanwise Positions for the Stationary Cylinder with D = 1.50 in., Re_m = 7,800, β_m = 0.10 (power spectra density data)

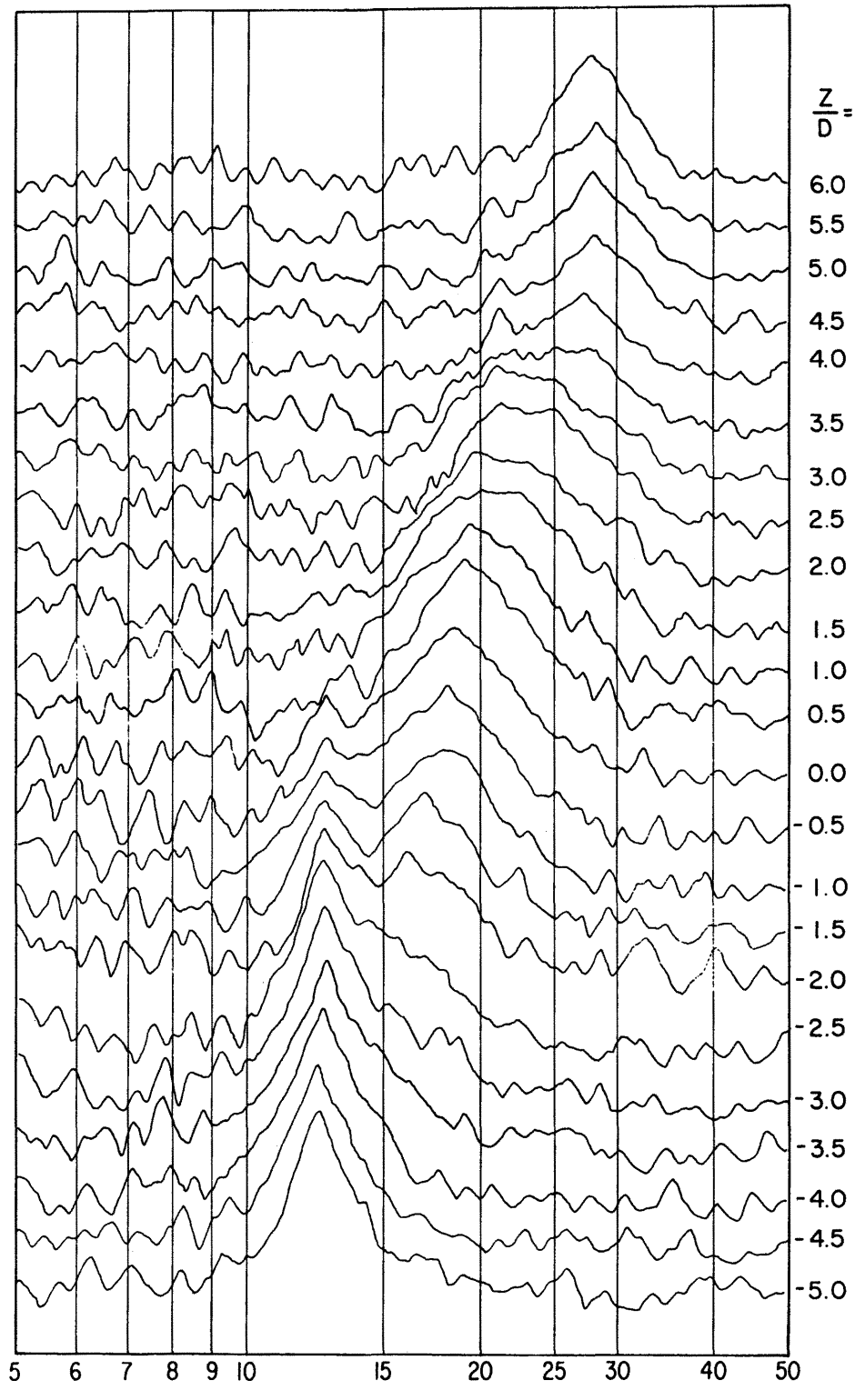

Figure 4.1.63. Frequency Spectra at Various Spanwise Positions for the Stationary Cylinder with D = 1.50 in., Re_m = 7,800, β_m = 0.100

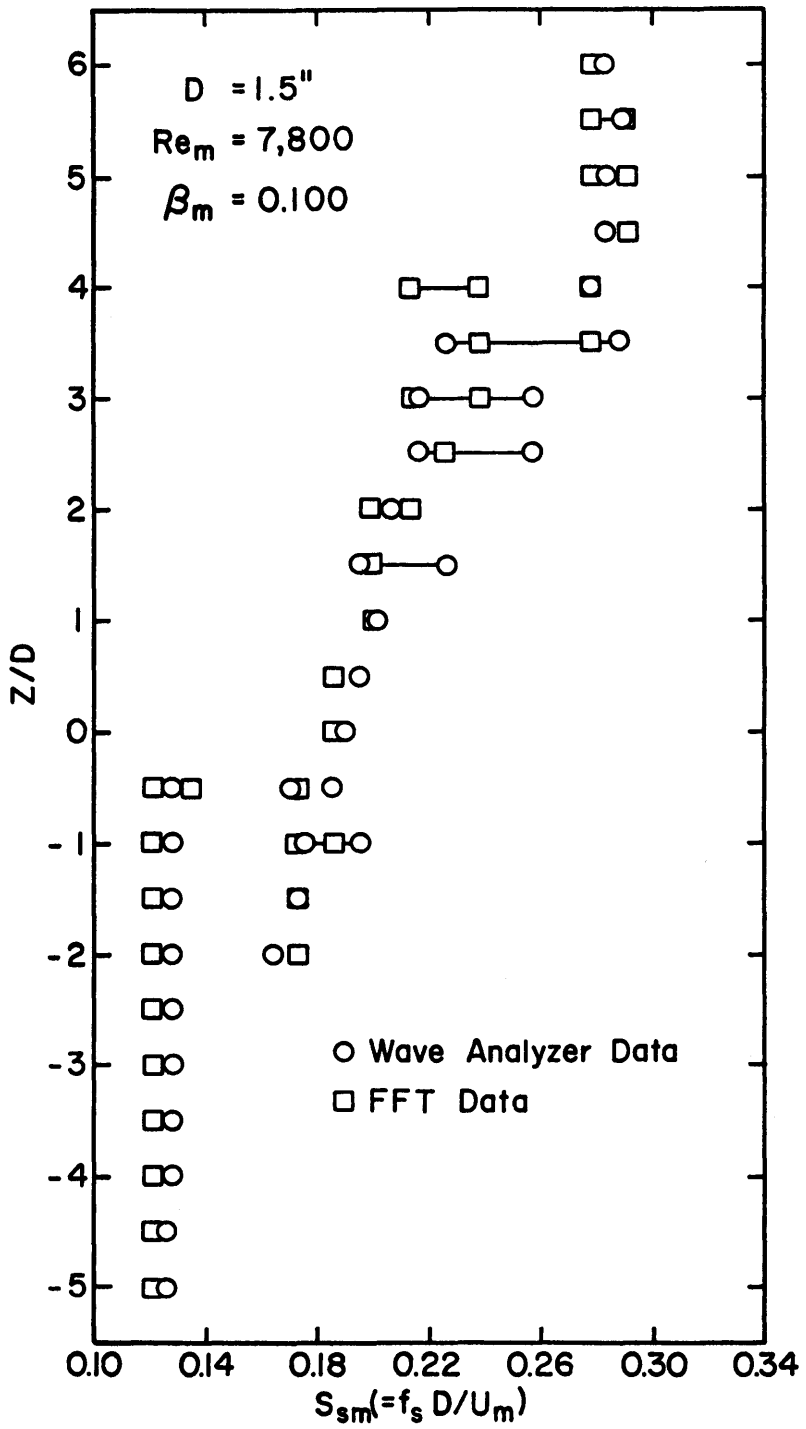

Figure 4.1.64. Spanwise Variation of S_{sm} for the Stationary Cylinder with D = 1.50 in., Re_m = 7,800, β_m = 0.10

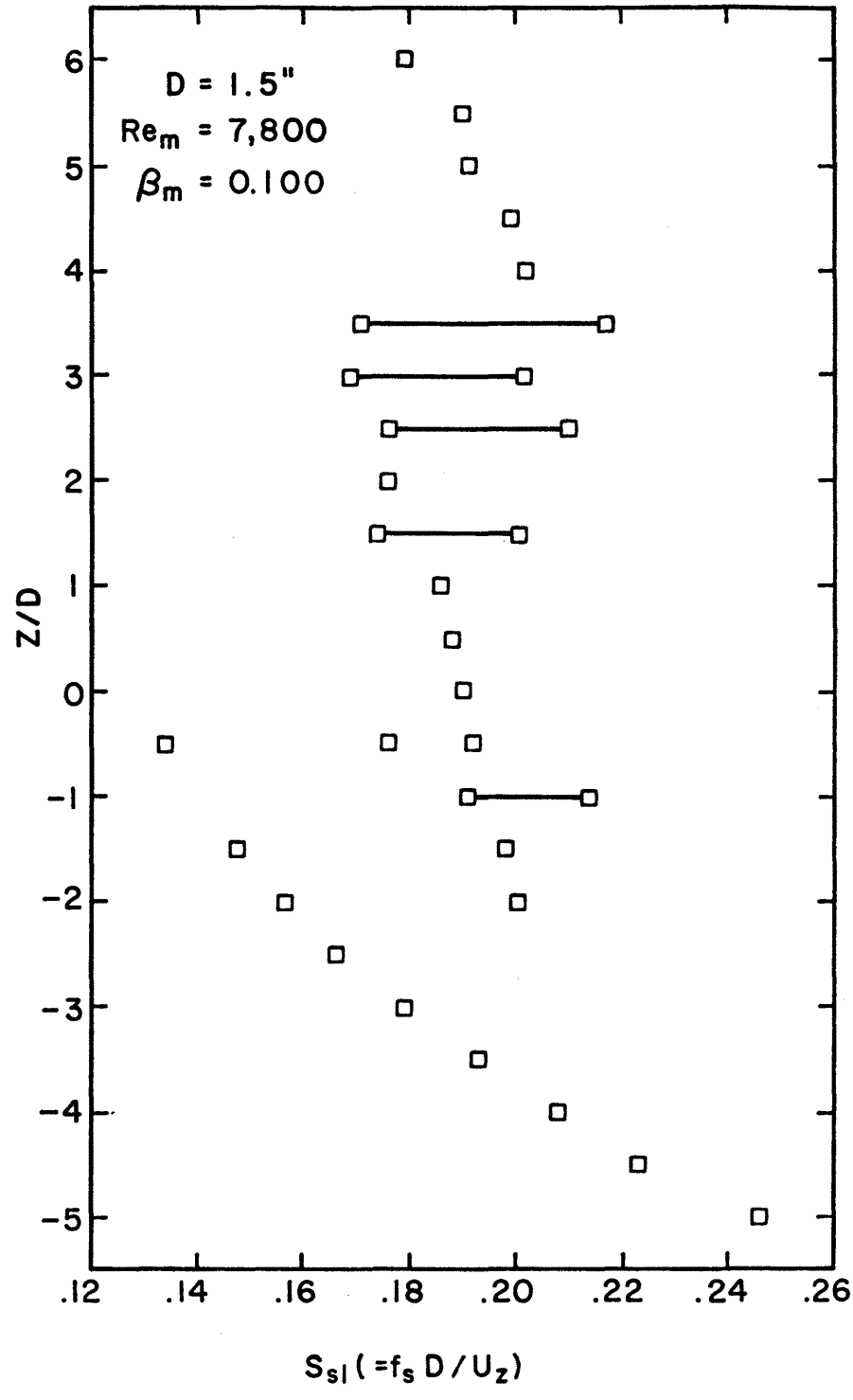

Figure 4.1.65. Spanwise Variation of $S_{s\ell}$ for the Stationary Cylinder with D = 1.50 in., Re_m = 7,800, β_m = 0.10

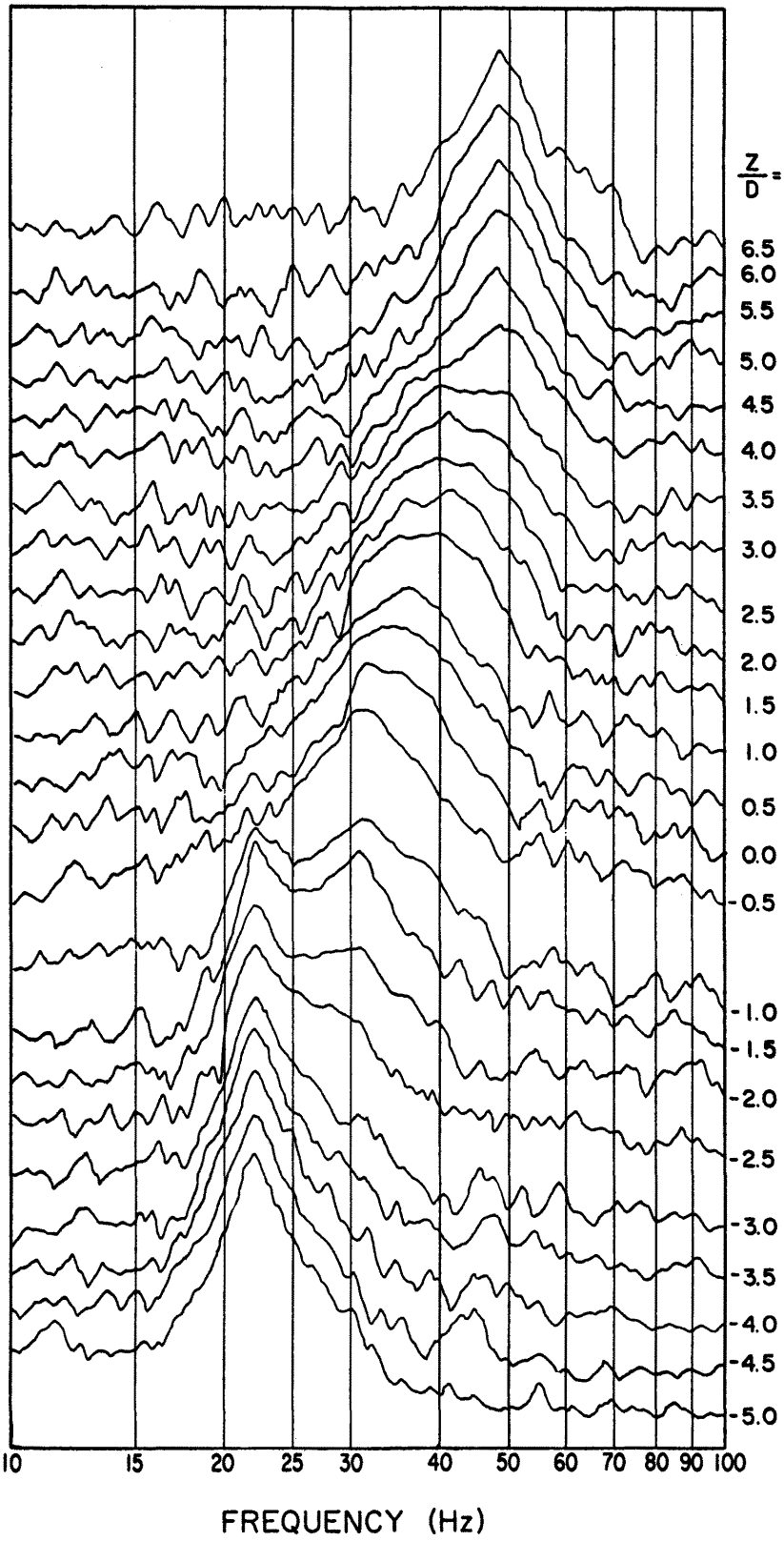

Figure 4.1.66. Frequency Spectra at Various Spanwise Positions for the Stationary Cylinder with D = 1.50 in., Re_m = 13,460, β_m = 0.10

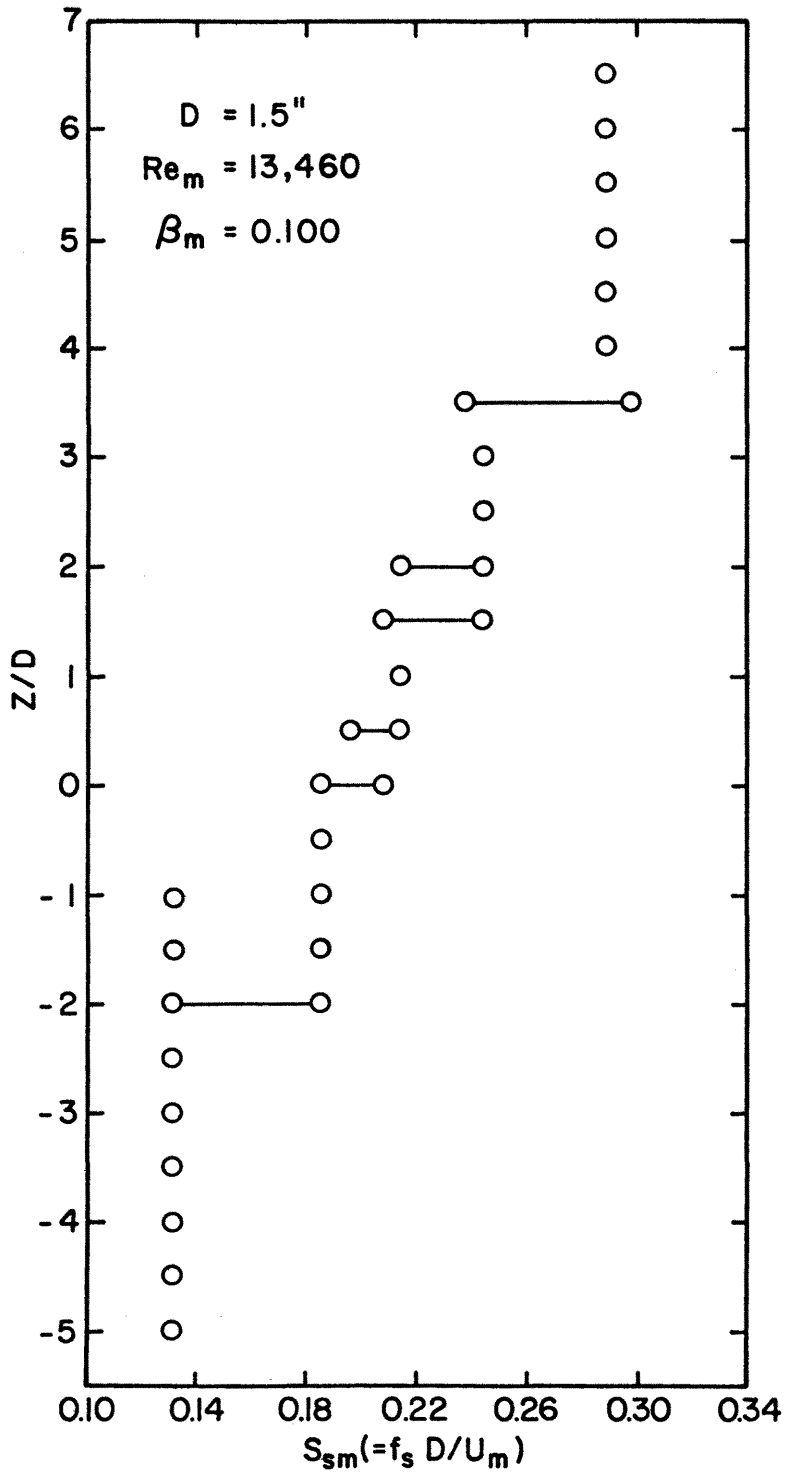

Figure 4.1.67. Spanwise Variation of S_{sm} for the Stationary Cylinder with D = 1.50 in., Re_m = 13,460, β_m = 0.100

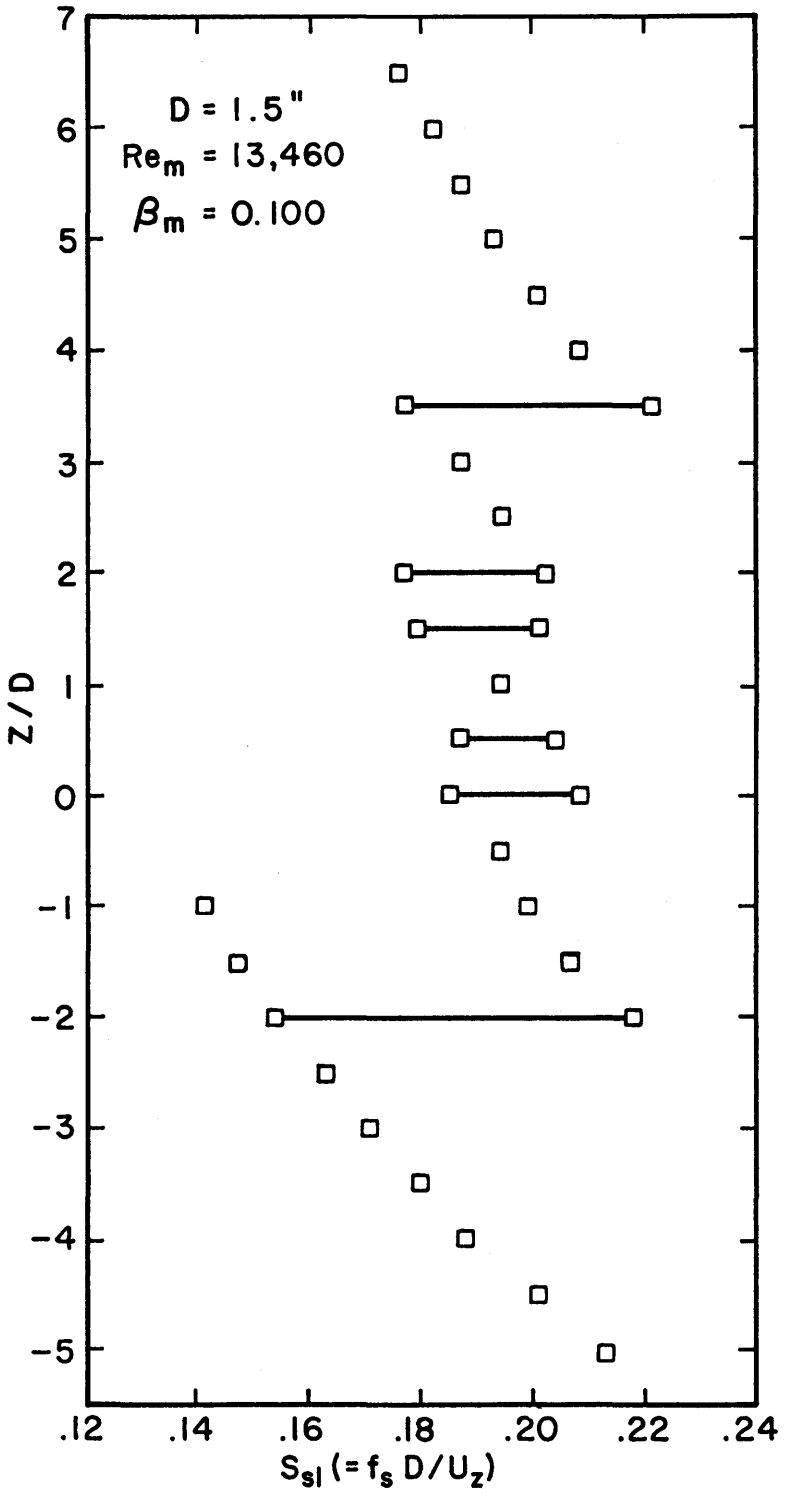

Figure 4.1.68. Spanwise Variation of $S_{s\ell}$ for the Stationary Cylinder with D = 1.50 in., Re_m = 13,460, β_m = 0.10

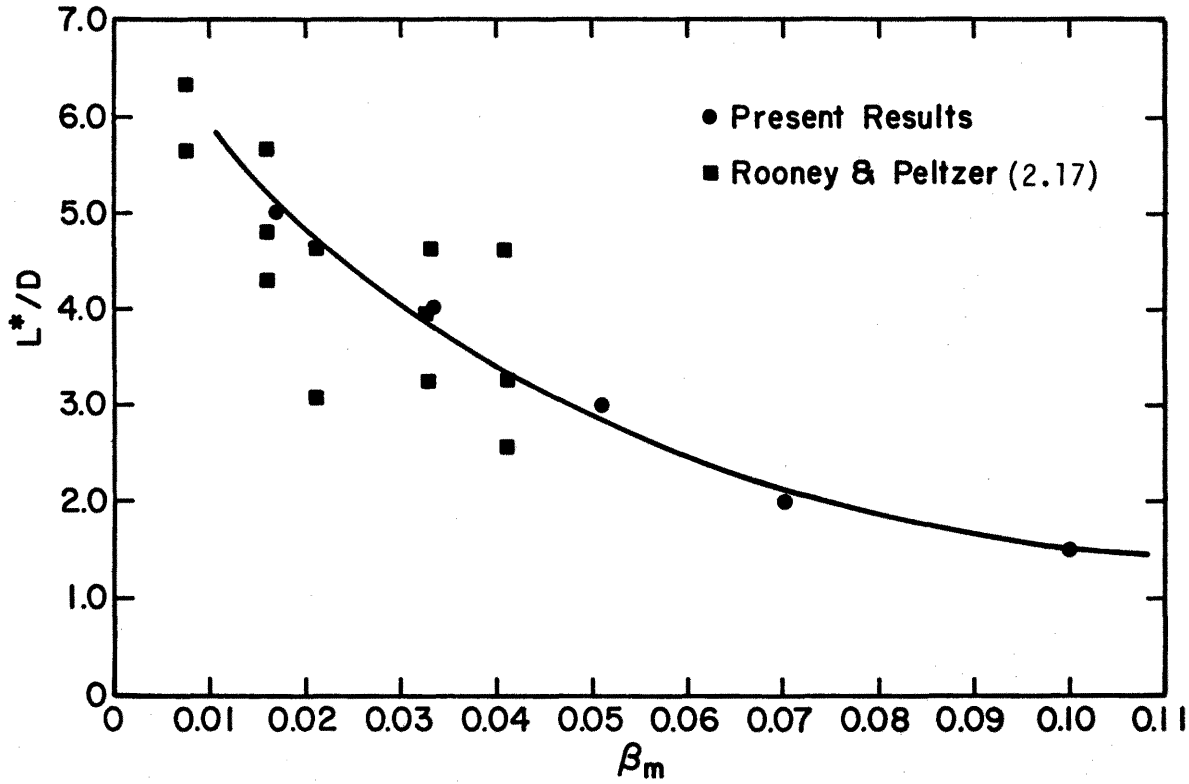

4.1.69 Variation of Cell Length as a Function of Shear Parameter

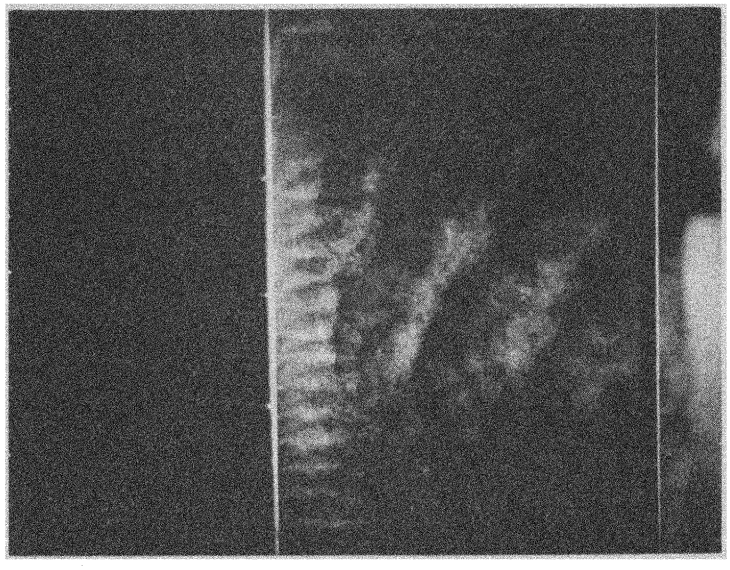

Figure 4.1.70a. Wake Pattern behind a Circular Cylinder with $D = 0.50$ in., $Re_m = 1{,}770$ and $\beta_m = 1.034$

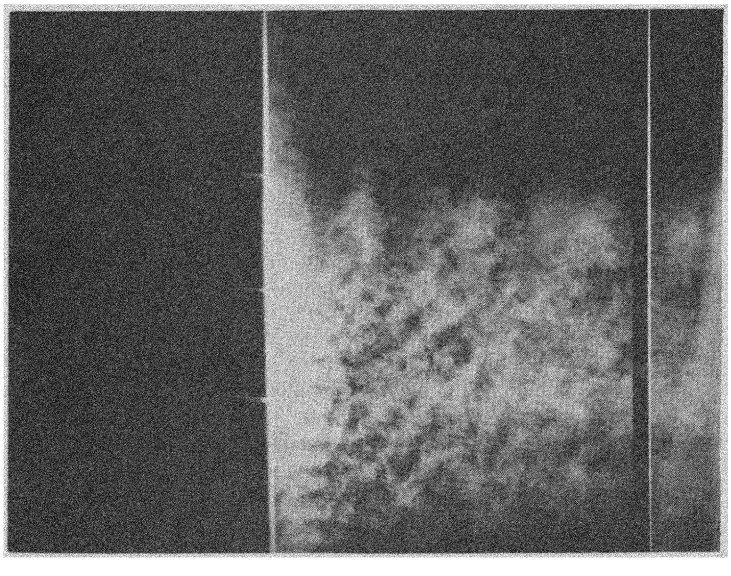

Figure 4.1.70b. Wake Pattern behind a Circular Cylinder with $D = 0.50$ in., $Re_m = 1{,}770$ and $\beta_m = 1.034$

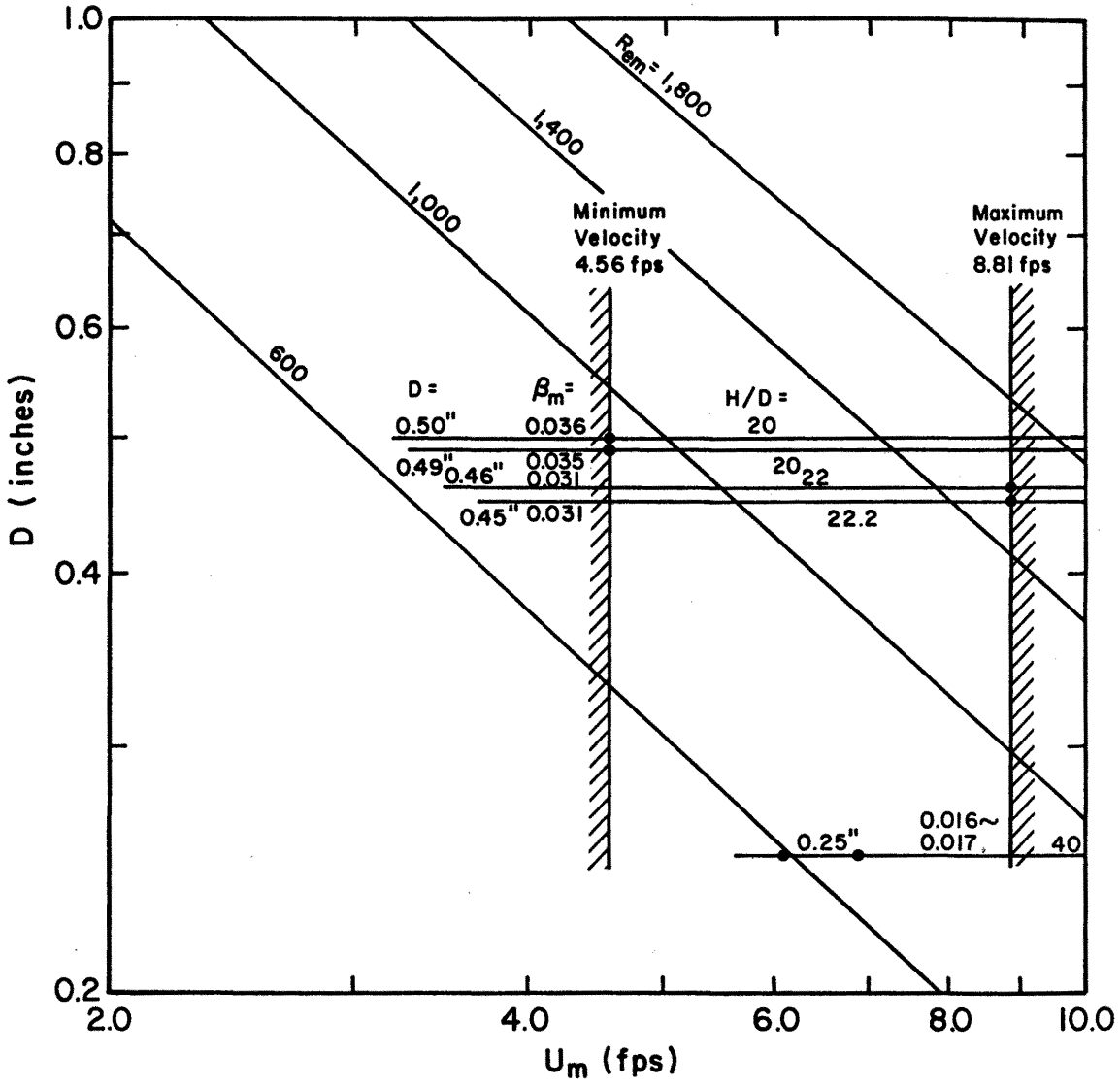

4.2.1 Relation among Experimental Parameters for Cables in Uniform Shear Flows

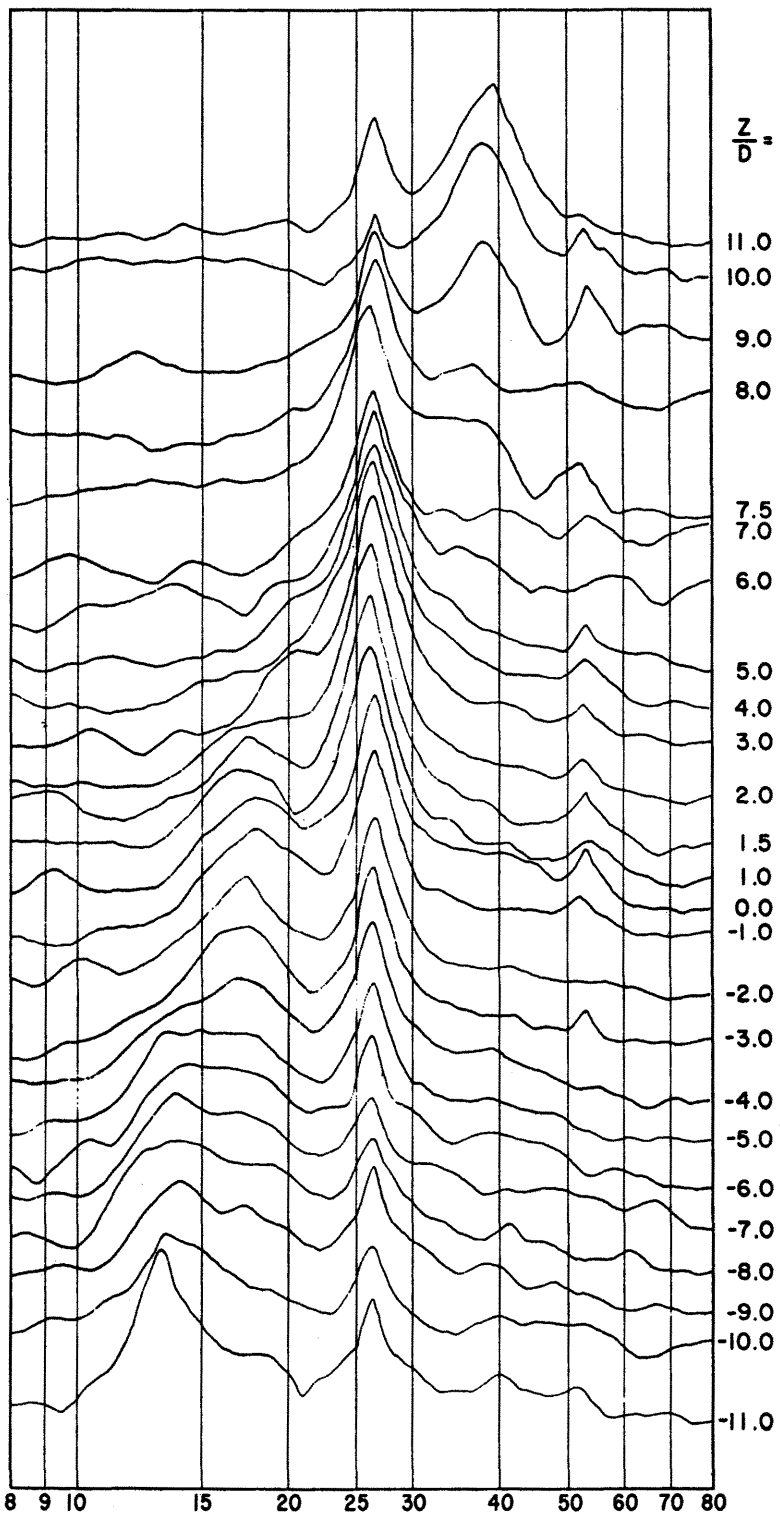

4.2.2 Frequency Spectra at Various Spanwise Positions for an Oscillating Cable with D = 0.49 in., Re_m = 1,000, β_m = 0.35, ℓ/D = 20.0, f_c = 26.5 Hz and a_m/D = 0.6

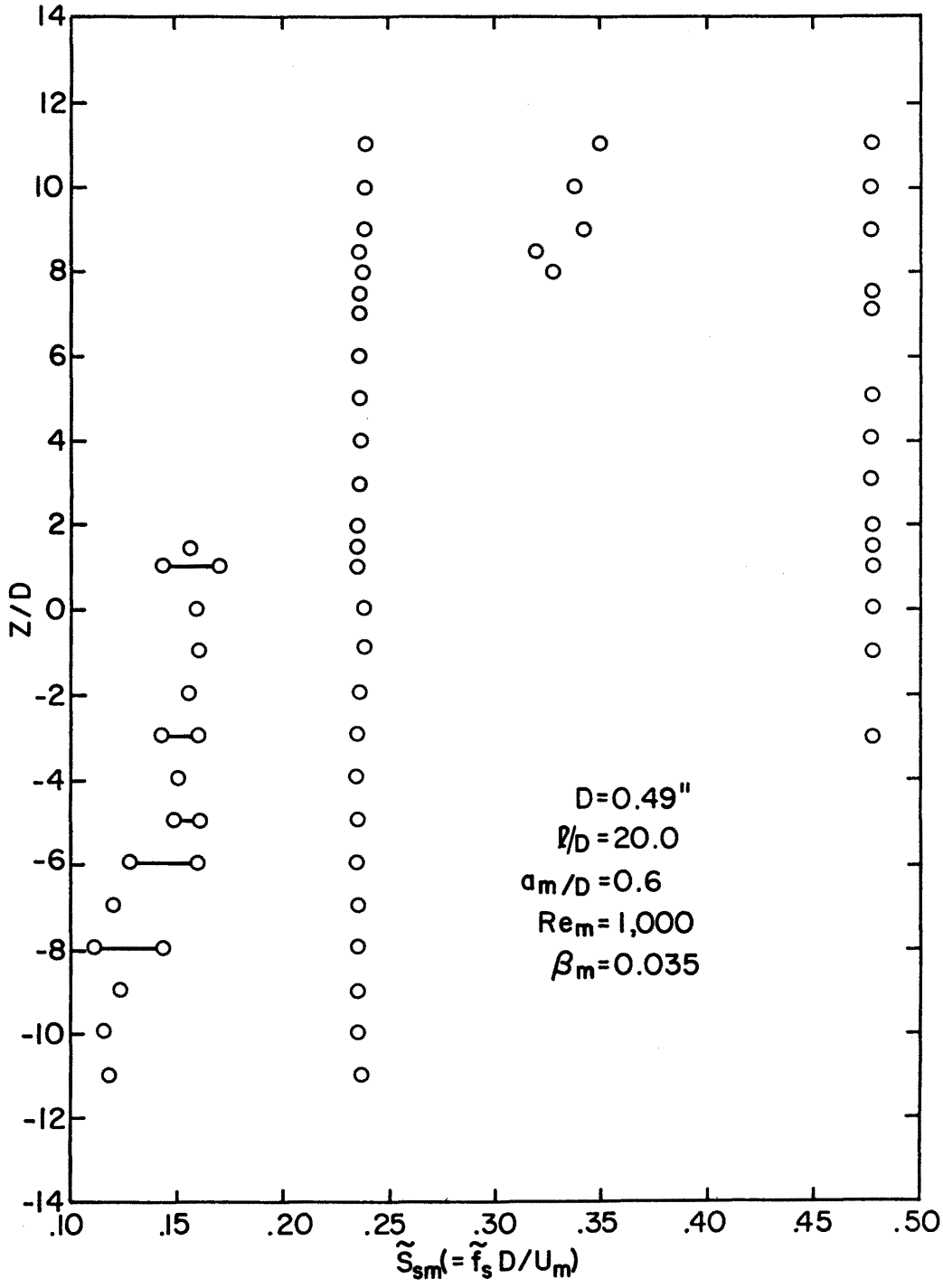

4.2.3 Spanwise Variation of S_{sm} for an Oscillating Cable with D = 0.49 in., Re_m = 1,000, β_m = 0.035, ℓ/D = 20.0, S_{cm} = 0.238, and a_m/D = 0.6

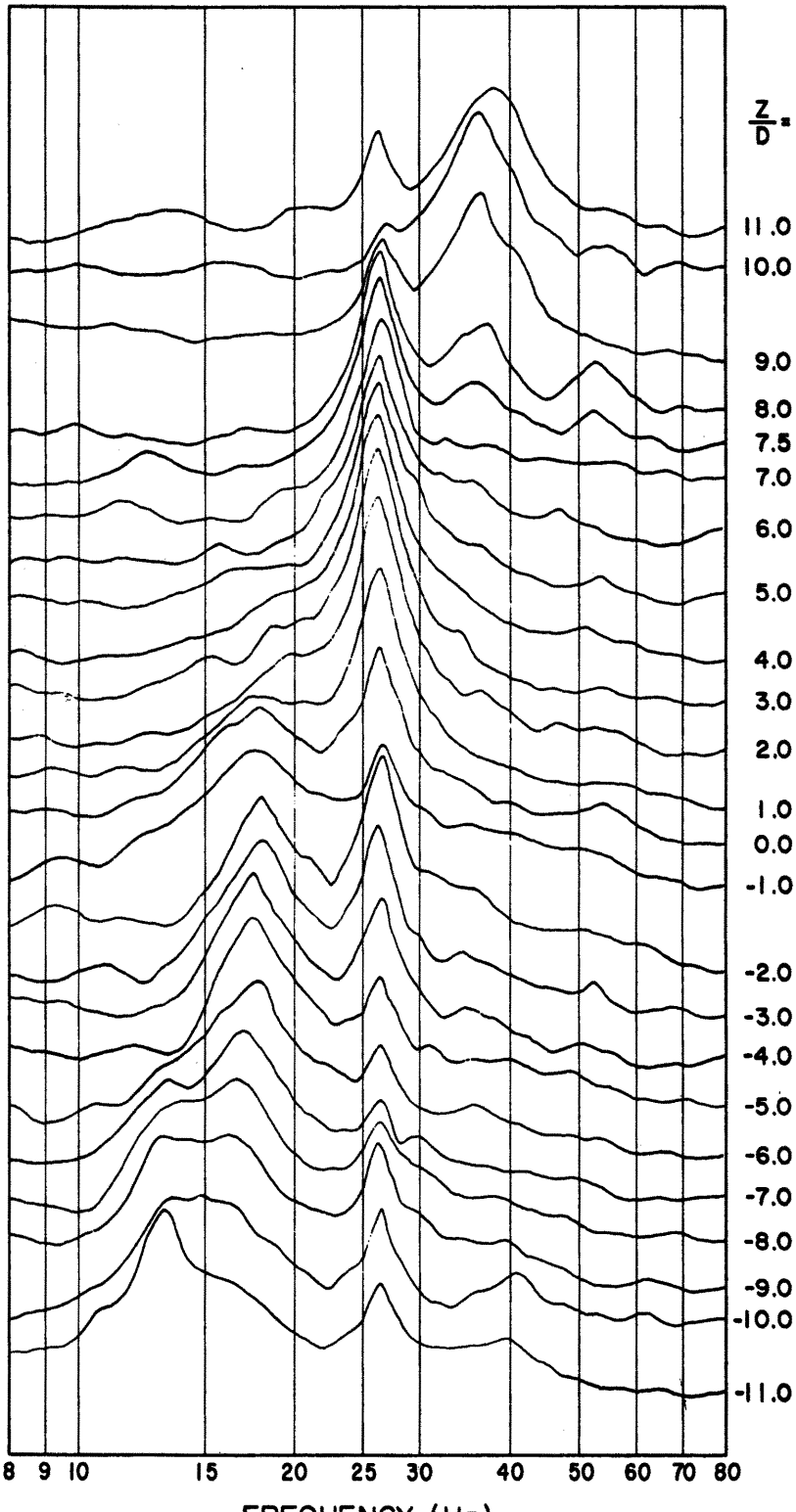

4.2.4 Frequency Spectra at Various Spanwise Positions for an Oscillating Cable with $D = 0.49$ in., $Re_m = 1{,}000$, $\beta_m = 0.35$, $\ell/D = 20.0$, $f_c = 26.5$ Hz and $a_m/D = 0.4$

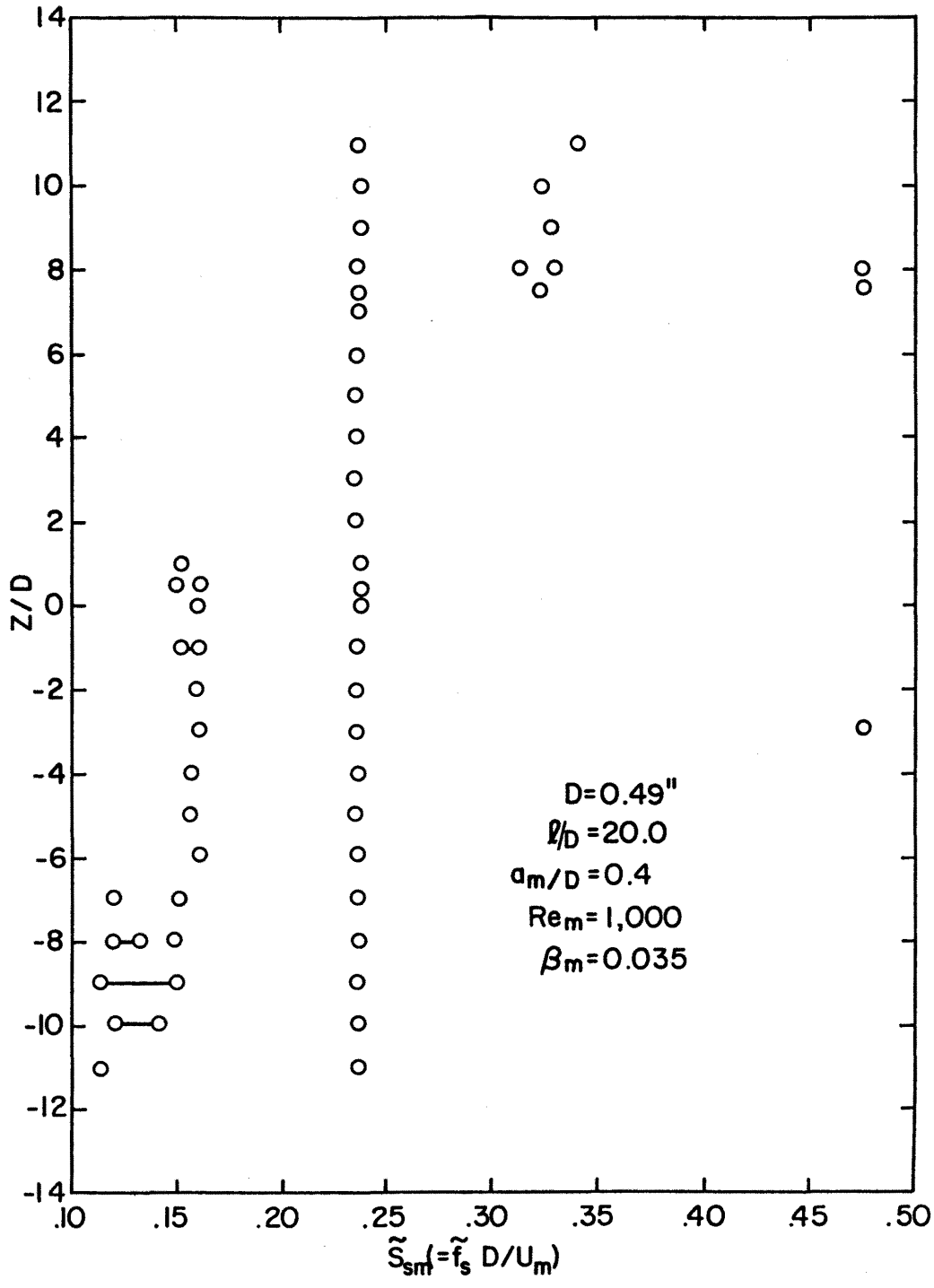

4.2.5 Spanwise Variation of S_{sm} for an Oscillating Cable with D = 0.49 in., Re_m = 1,000, β_m = 0.035, ℓ/D = 20.0, S_{cm} = 0.238, and a_m/D = 0.4

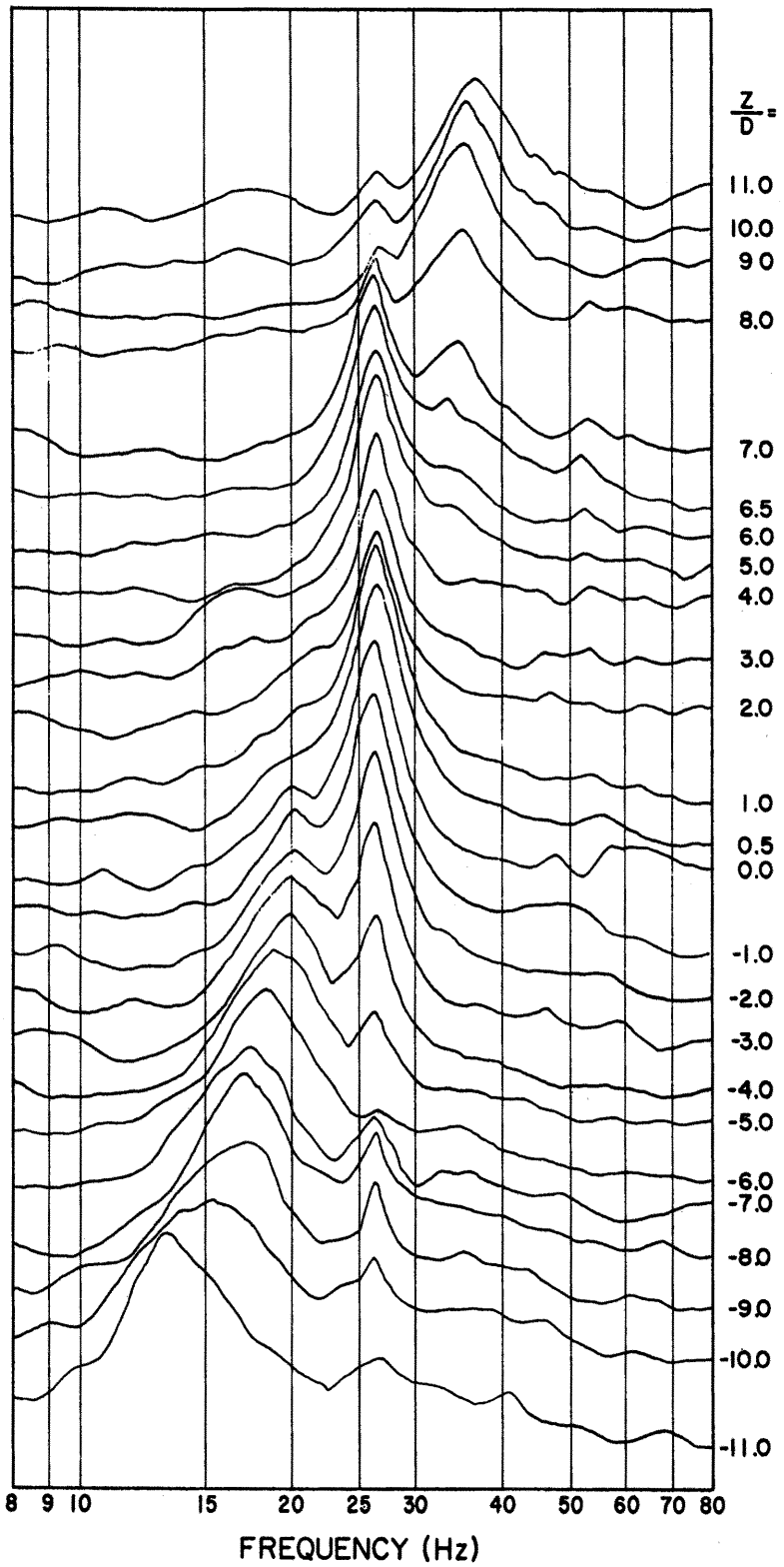

4.2.6 Frequency Spectra at Various Spanwise Positions for an Oscillating Cable with $D = 0.49$ in., $Re_m = 1{,}000$, $\beta_m = 0.035$, $\ell/D = 20.0$, $f_c = 26.4$ Hz and $a_m/D = 0.2$

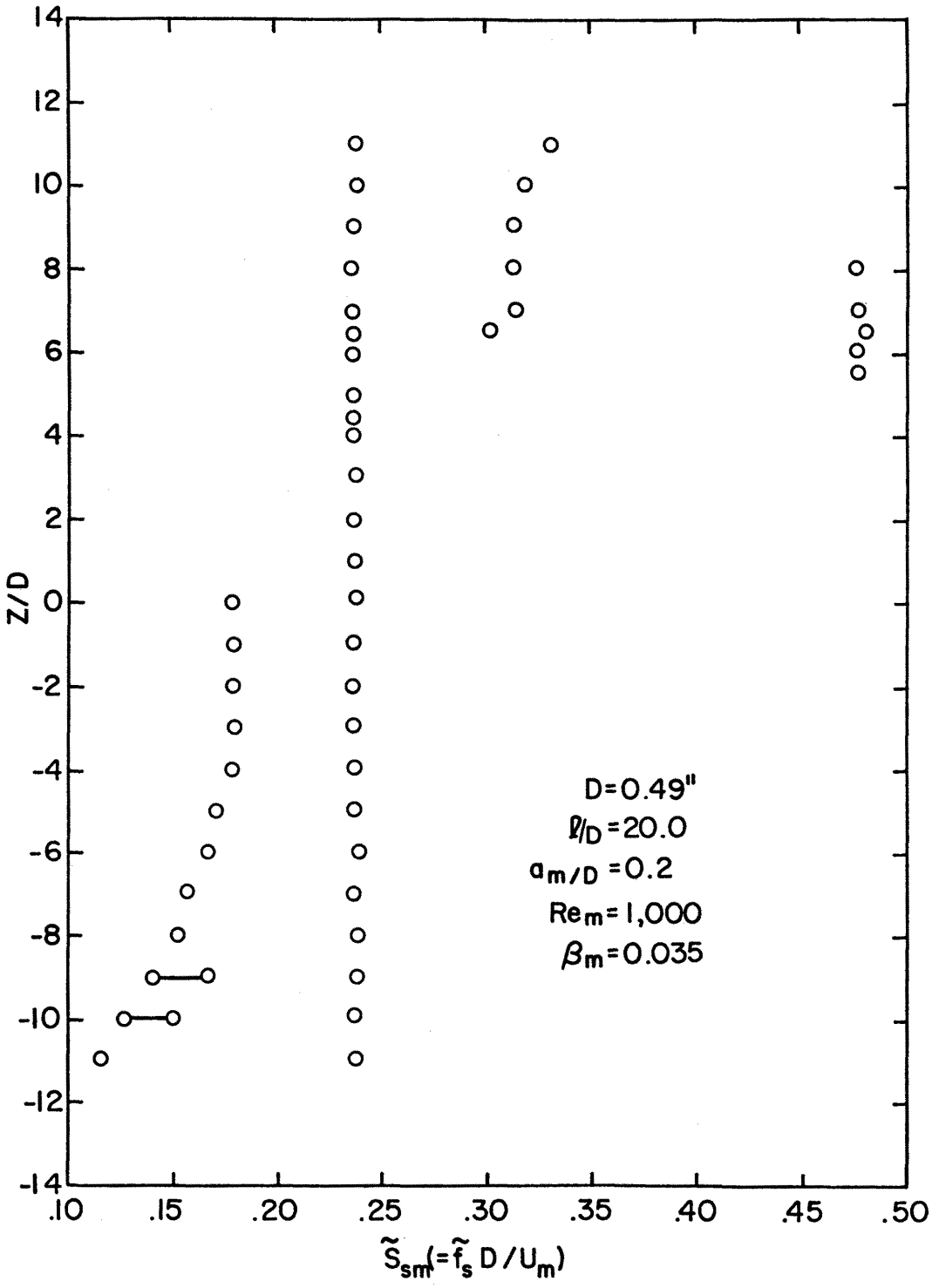

4.2.7 Spanwise Variation of S_{sm} for an Oscillating Cable with D = 0.49 in., Re_m = 1,000, β_m = 0.035, ℓ/D = 20.0, S_{cm} = 0.238, and a_m/D = 0.2

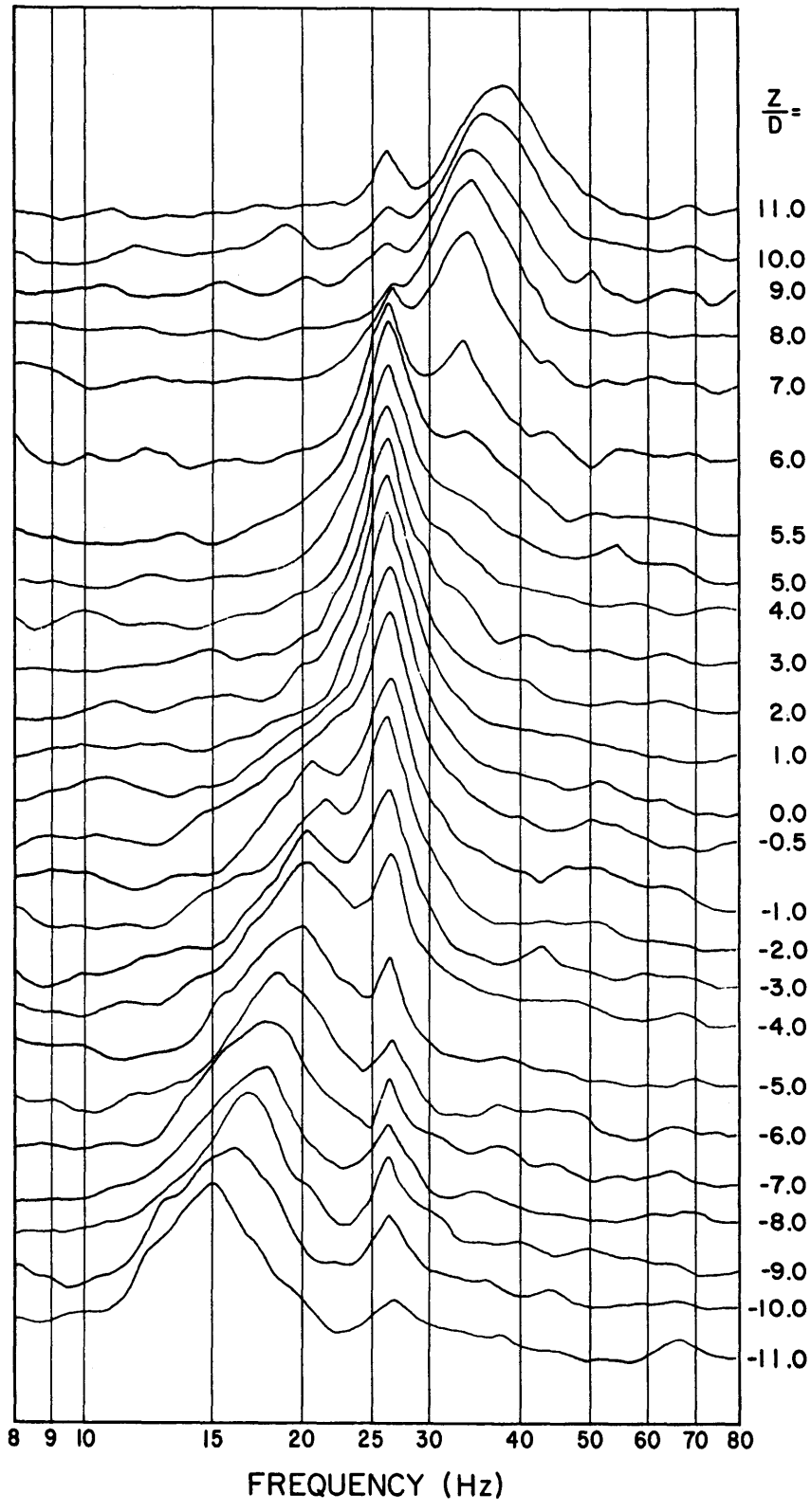

4.2.8 Frequency Spectra at Various Spanwise Positions for an Oscillating Cable with D = 0.49 in., Re_m = 1,000, β_m = 0.038, ℓ/D = 20.0, f_c = 26.5 Hz and a_m/D = 0.1

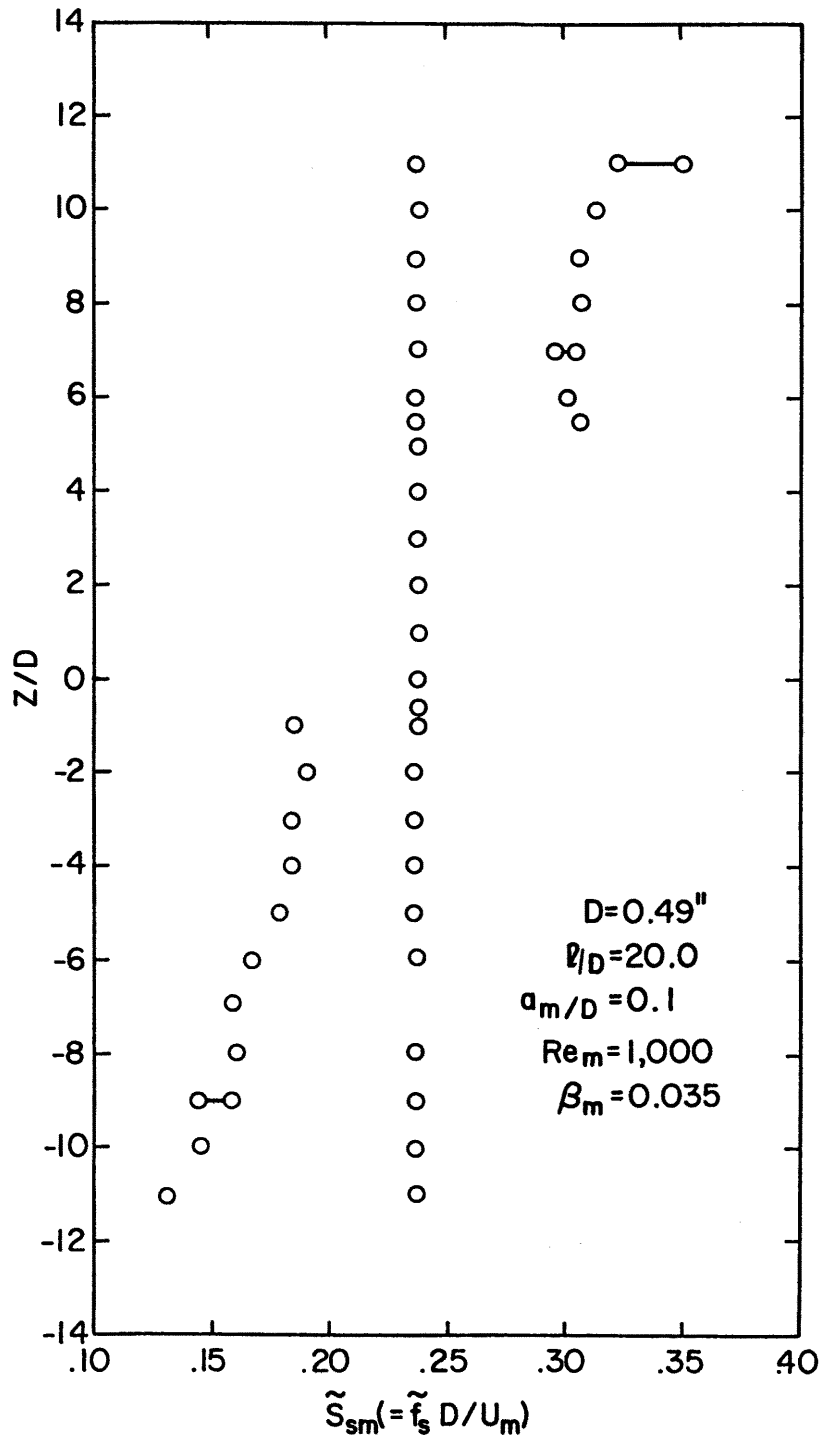

4.2.9 Spanwise Variation of S_{sm} for an Oscillating Cable with D = 0.49 in., Re_m = 1,000, β_m = 0.035, ℓ/D = 20.0, S_{cm} = 0.238, and a_m/D = 0.1

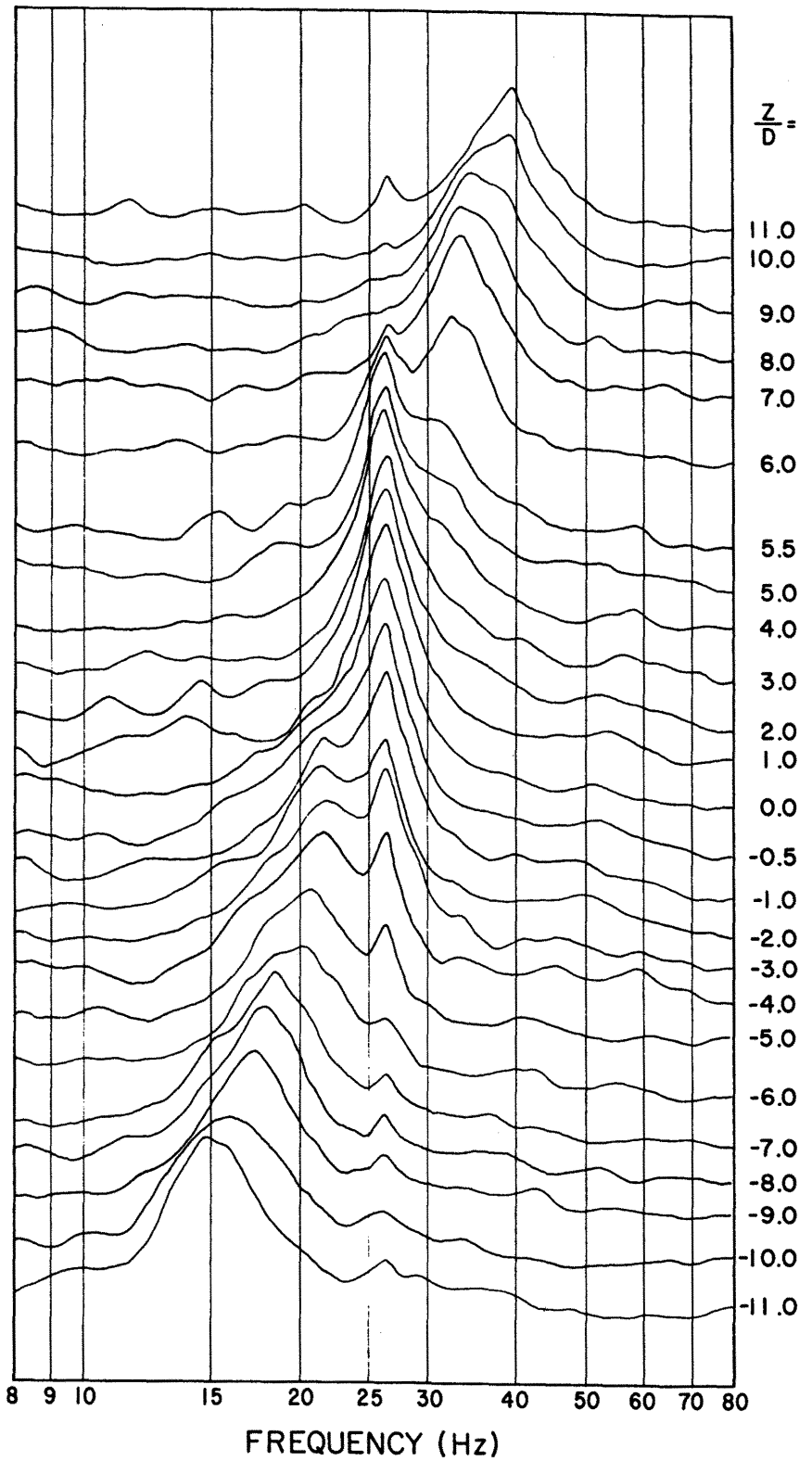

4.2.10 Frequency Spectra at Various Spanwise Positions for an Oscillating Cable with D = 0.49 in., Re = 1,000, β_m = 0.035, ℓ/D = 20.0, f_c = 26.5 Hz and a_m/D = 0.05

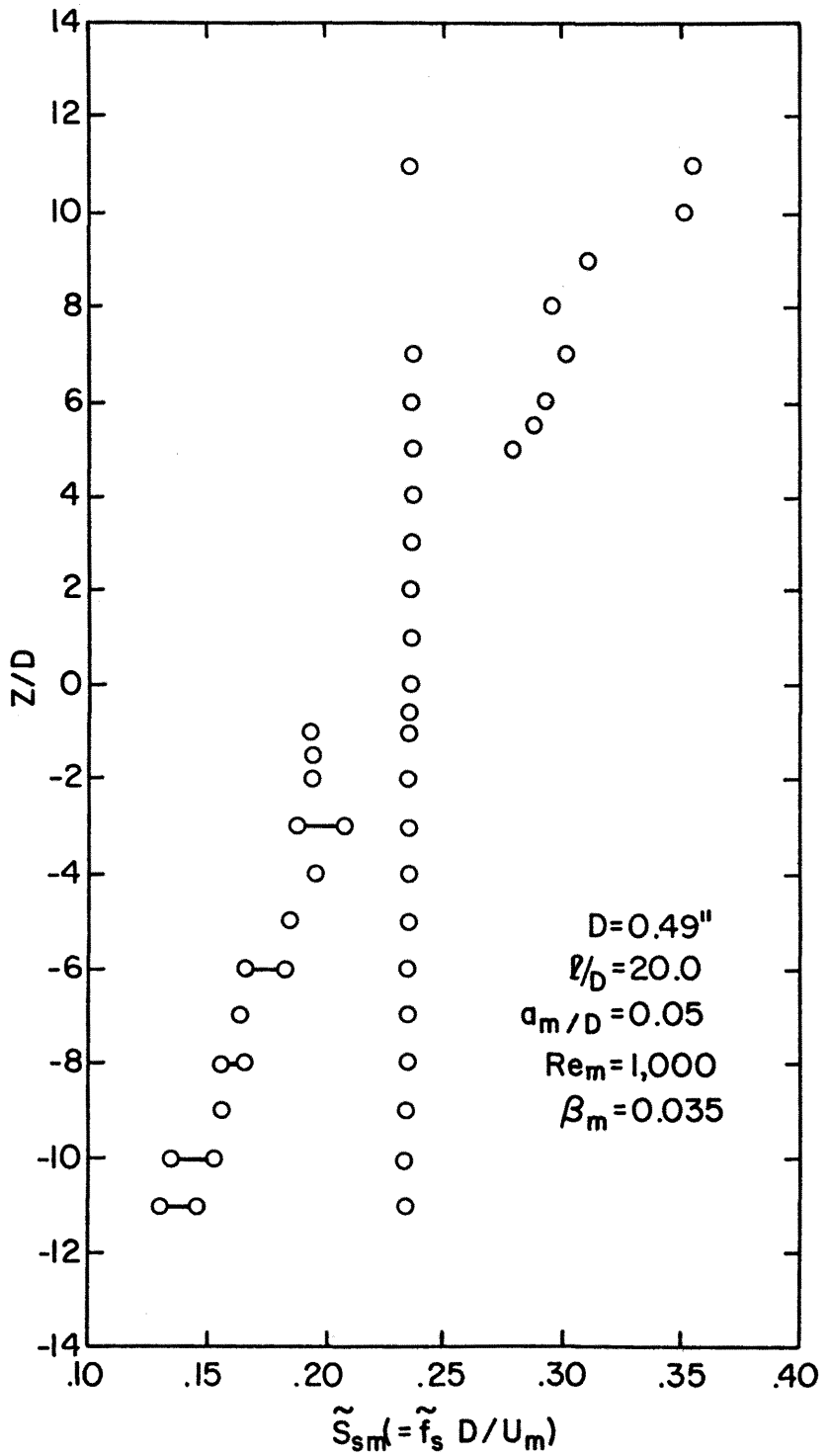

4.2.11 Spanwise Variation of S_{sm} for an Oscillating Cable with D = 0.49 in., Re_m = 1,000, β_m = 0.035, ℓ/D = 20.0, S_{cm} = 0.238, and a_m/D = 0.05

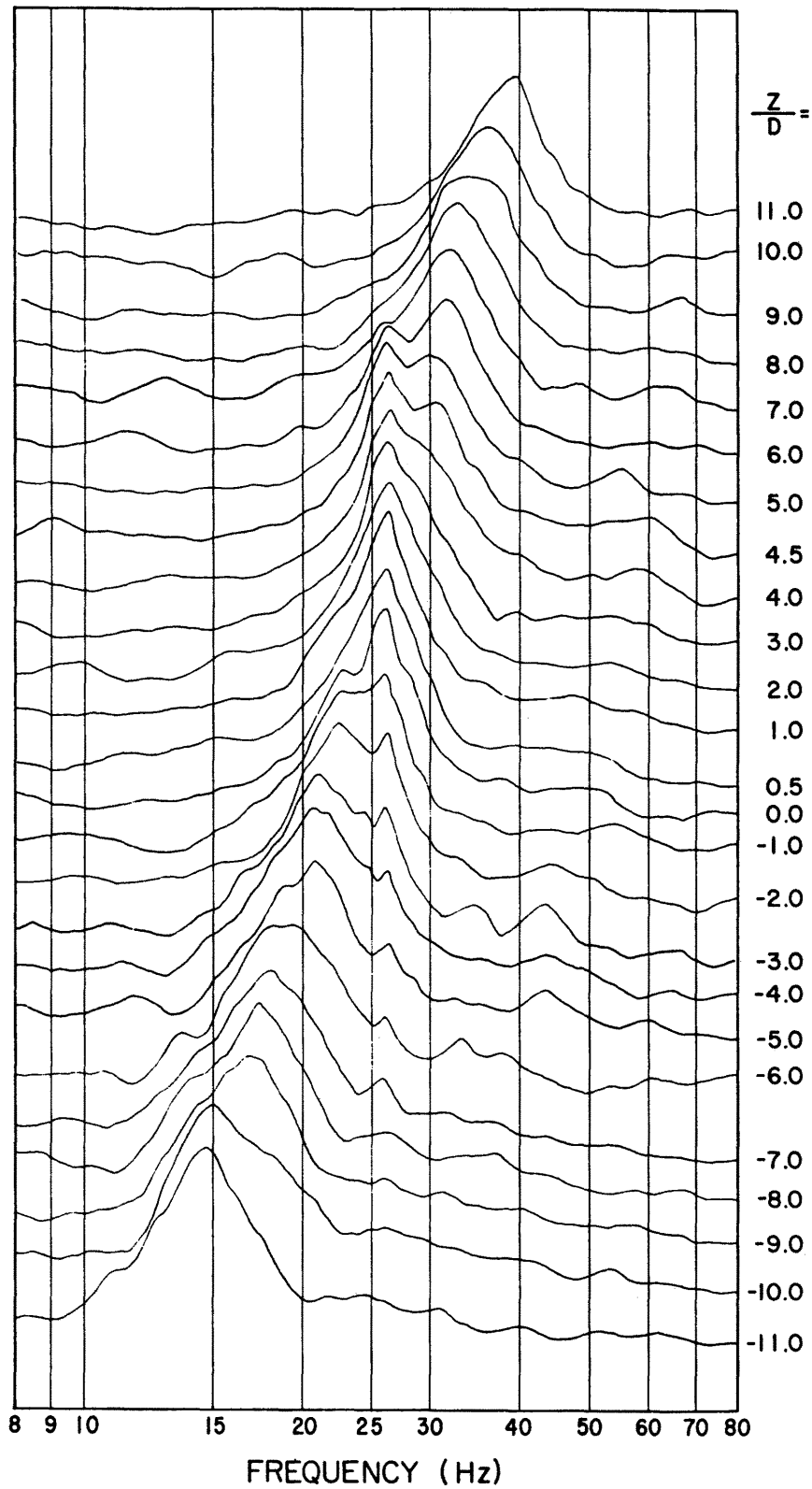

4.2.12 Frequency Spectra at Various Spanwise Positions for an Oscillating Cable with D = 0.49 in., Re_m = 1,000, β_m = 0.035, ℓ/D = 20.0, f_c = 26.5 Hz, and a_m/D = 0.25

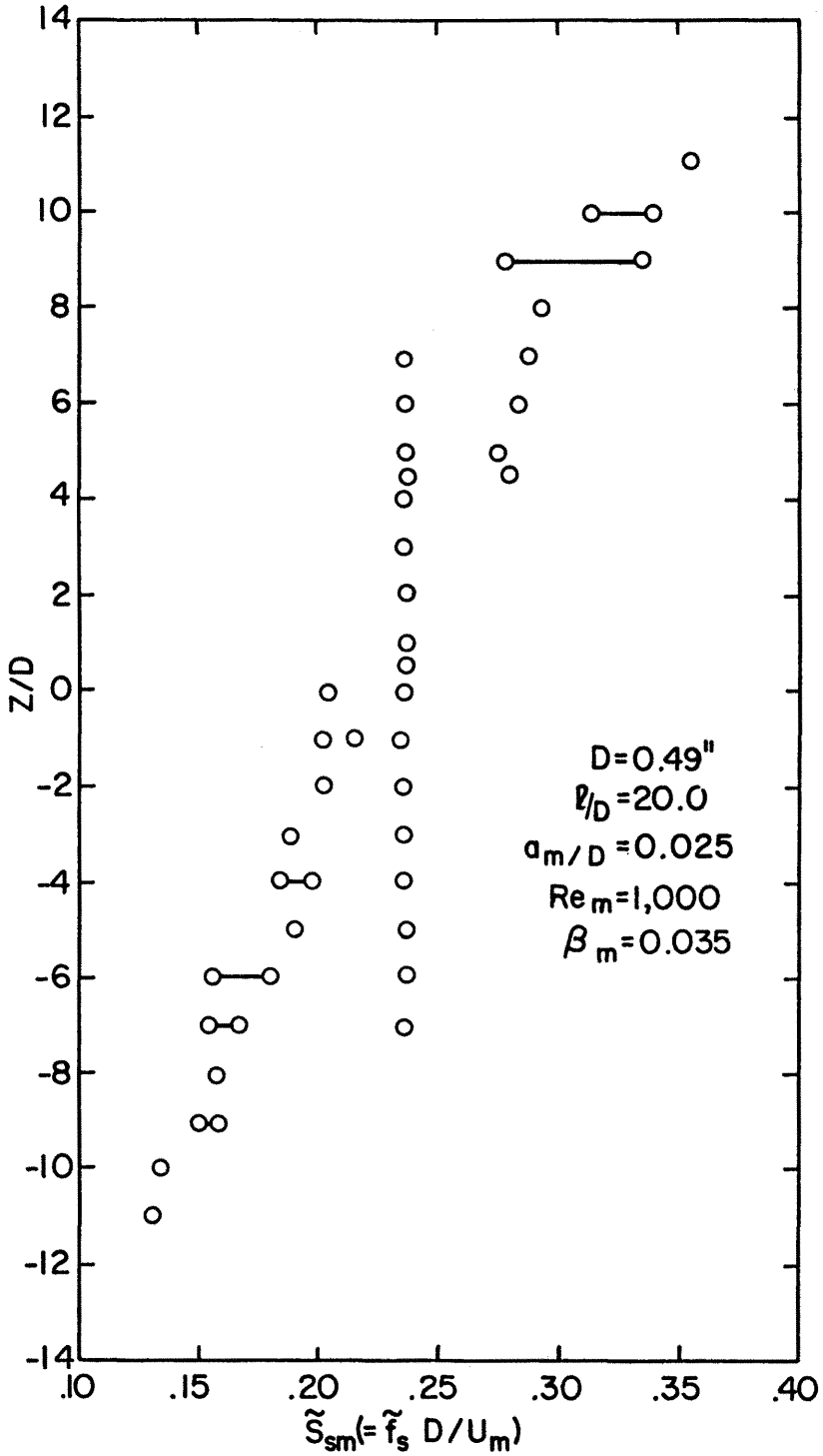

4.2.13 Spanwise Variation of S_{sm} for an Oscillating Cable with D = 0.49 in., Re_m = 1,000, β_m = 0.035, ℓ/D = 20.0, S_{cm} = 0.238, and a_m/D = 0.025

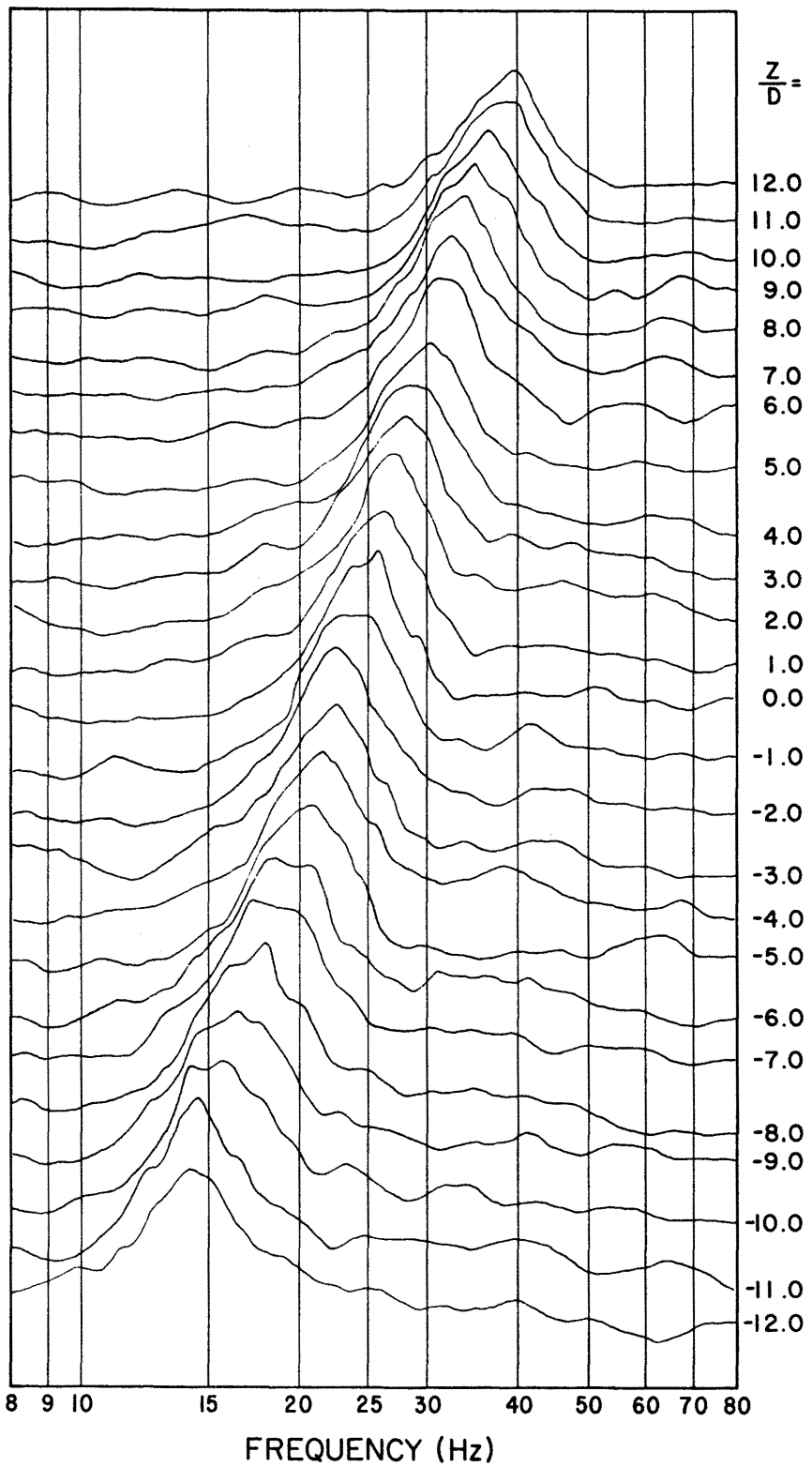

4.2.14 Frequency Spectra at Various Spanwise Positions for an Oscillating Cable with $D = 0.49$ in., $Re_m = 1{,}000$, $\beta_m = 0.035$, $f_c = 0.0$ Hz and $a_m/D = 0.0$

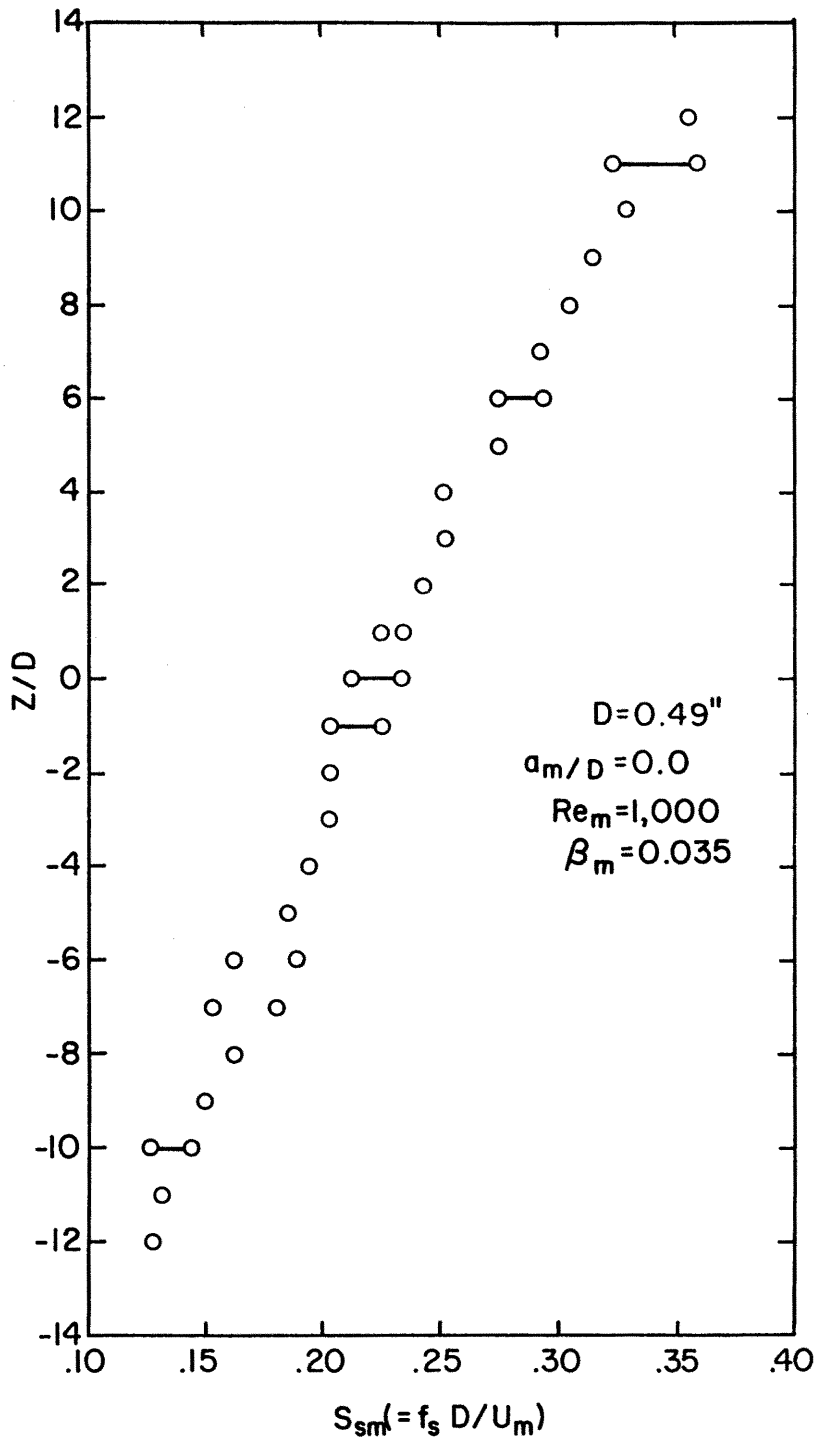

4.2.15 Spanwise Variation of S_{sm} for a Cable with D = 0.49 in., Re_m = 1,000, β_m = 0.035, S_{cm} = 0.0, and a_m/D = 0.0

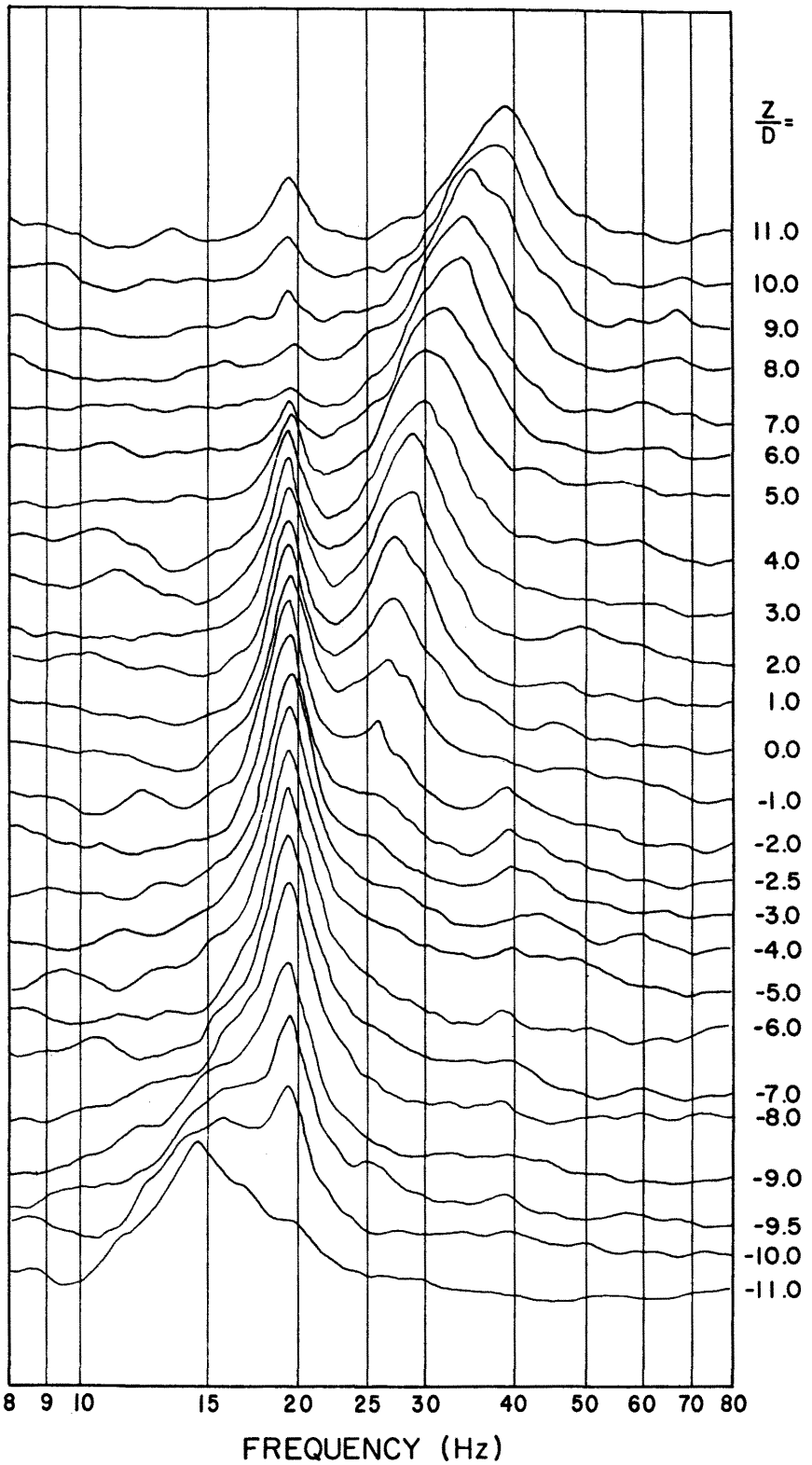

4.2.16 Frequency Spectra at Various Spanwise Positions for an Oscillating Cable with D = 0.50 in., Re_m = 1,000, β_m = 0.036, ℓ/D = 20.0, f_c = 19.5 Hz, and a_m/D = 0.2

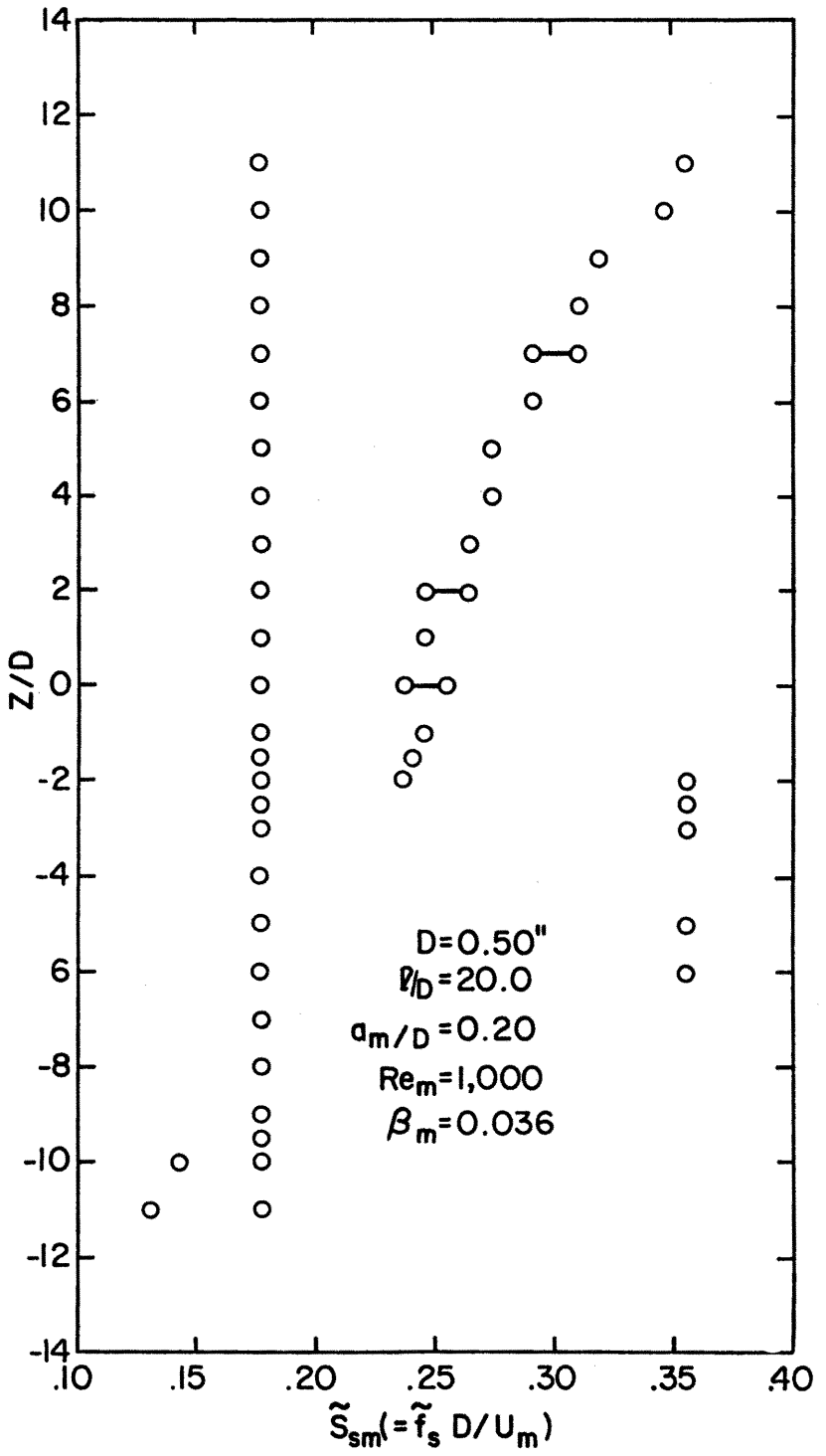

4.2.17 Spanwise Variation of S_{sm} for an Oscillating Cable with D = 0.50 in., Re_m = 1,000, β_m = 0.036, ℓ/D = 20.0, S_{cm} = 0.178, and a_m/D = 0.20

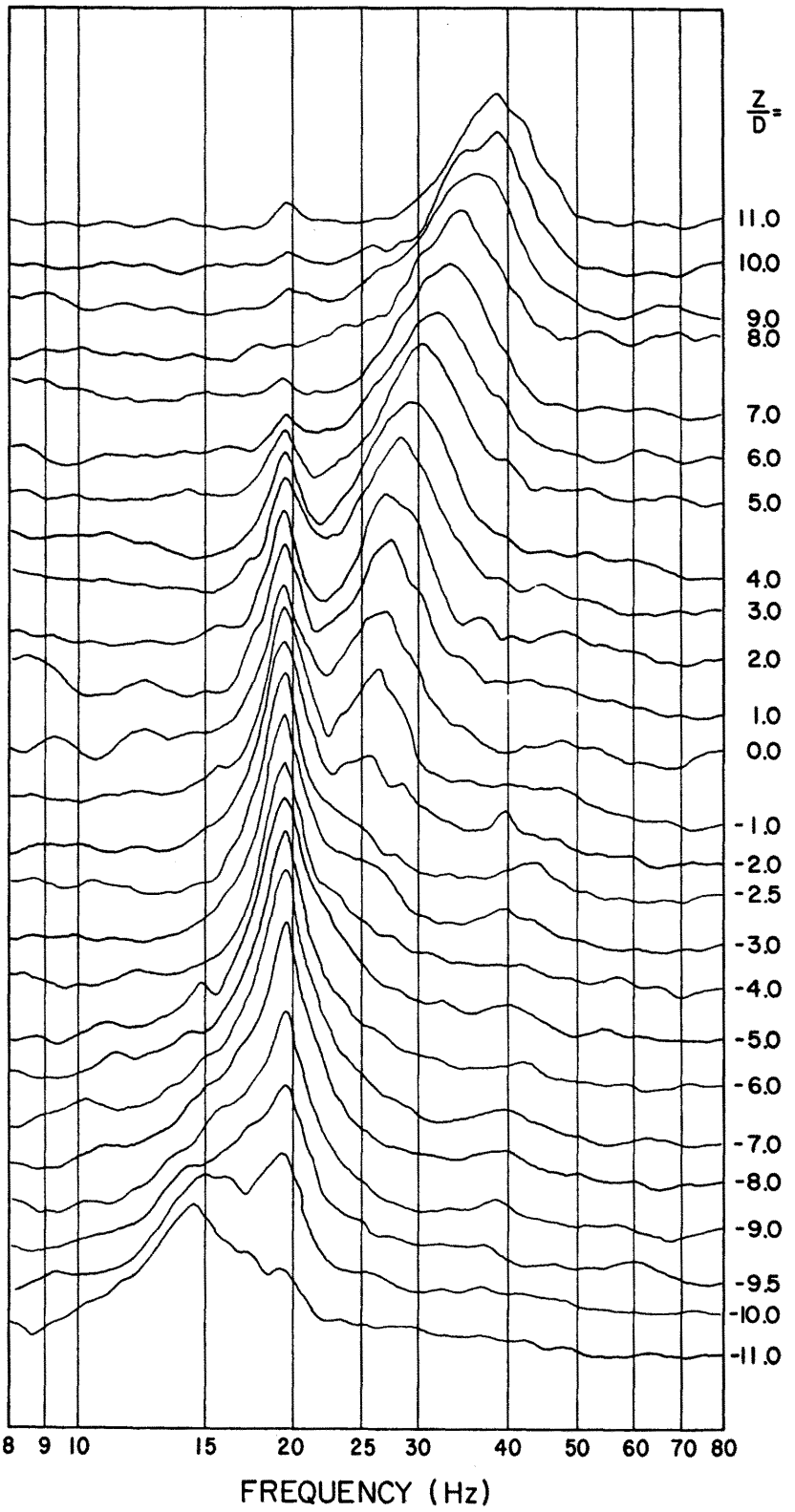

4.2.18 Frequency Spectra at Various Spanwise Positions for an Oscillating Cable with D = 0.50 in., Re_m = 1,000, β_m = 0.036, ℓ/D = 20.0, f_c = 19.5 Hz, and a_m/D = 0.12

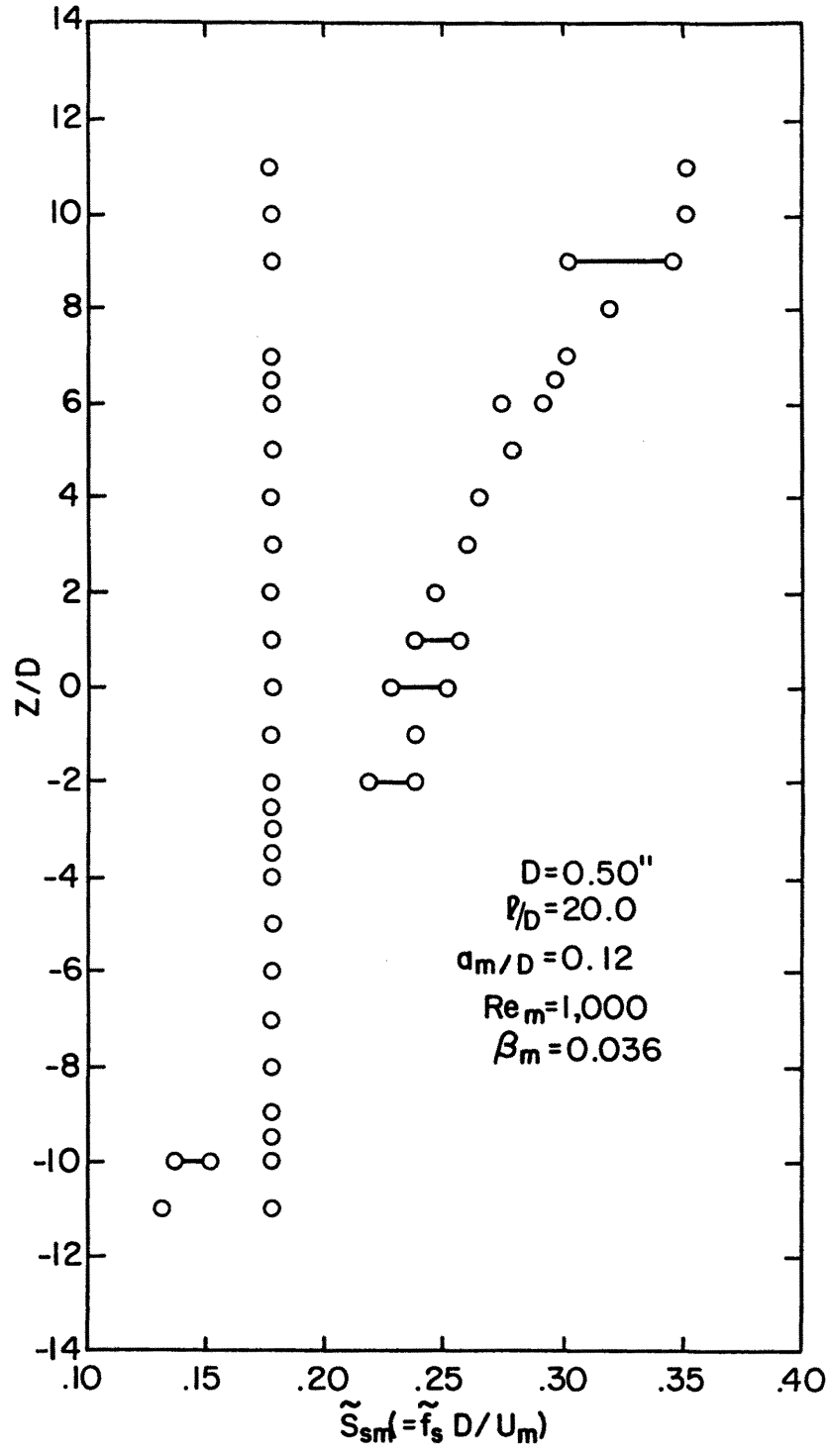

4.2.19 Spanwise Variation of S_{sm} for an Oscillating Cable with D = 0.50 in., Re_m = 1,000, β_m = 0.036, ℓ/D = 20.0, S_{cm} = 0.178, and a_m/D = 0.12

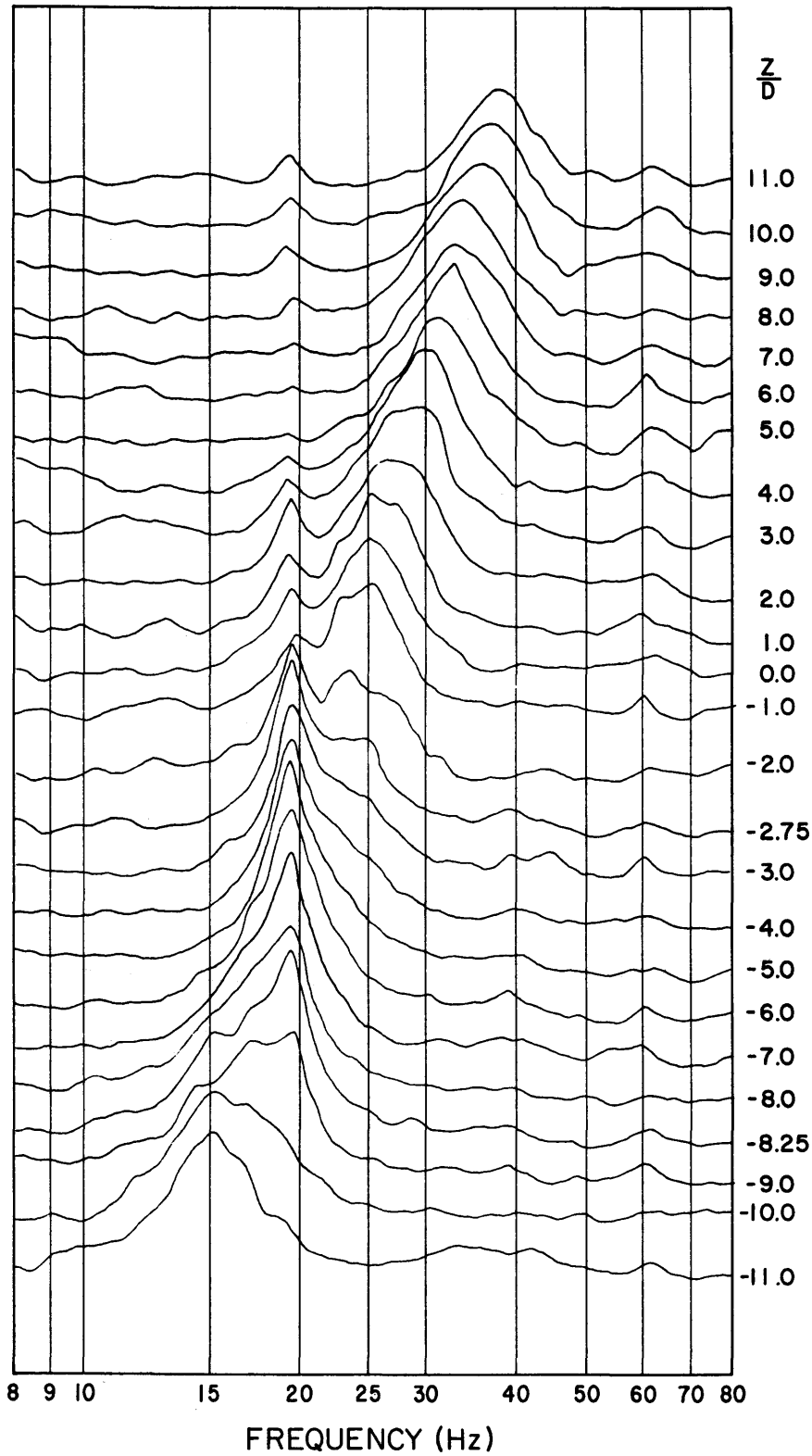

4.2.20 Frequency Spectra at Various Spanwise Positions for an Oscillating Cable with D = 0.50 in., Re_m = 1,000, β_m = 0.036, ℓ/D = 20.0, f_c = 19.5 Hz, and a_m/D = 0.07

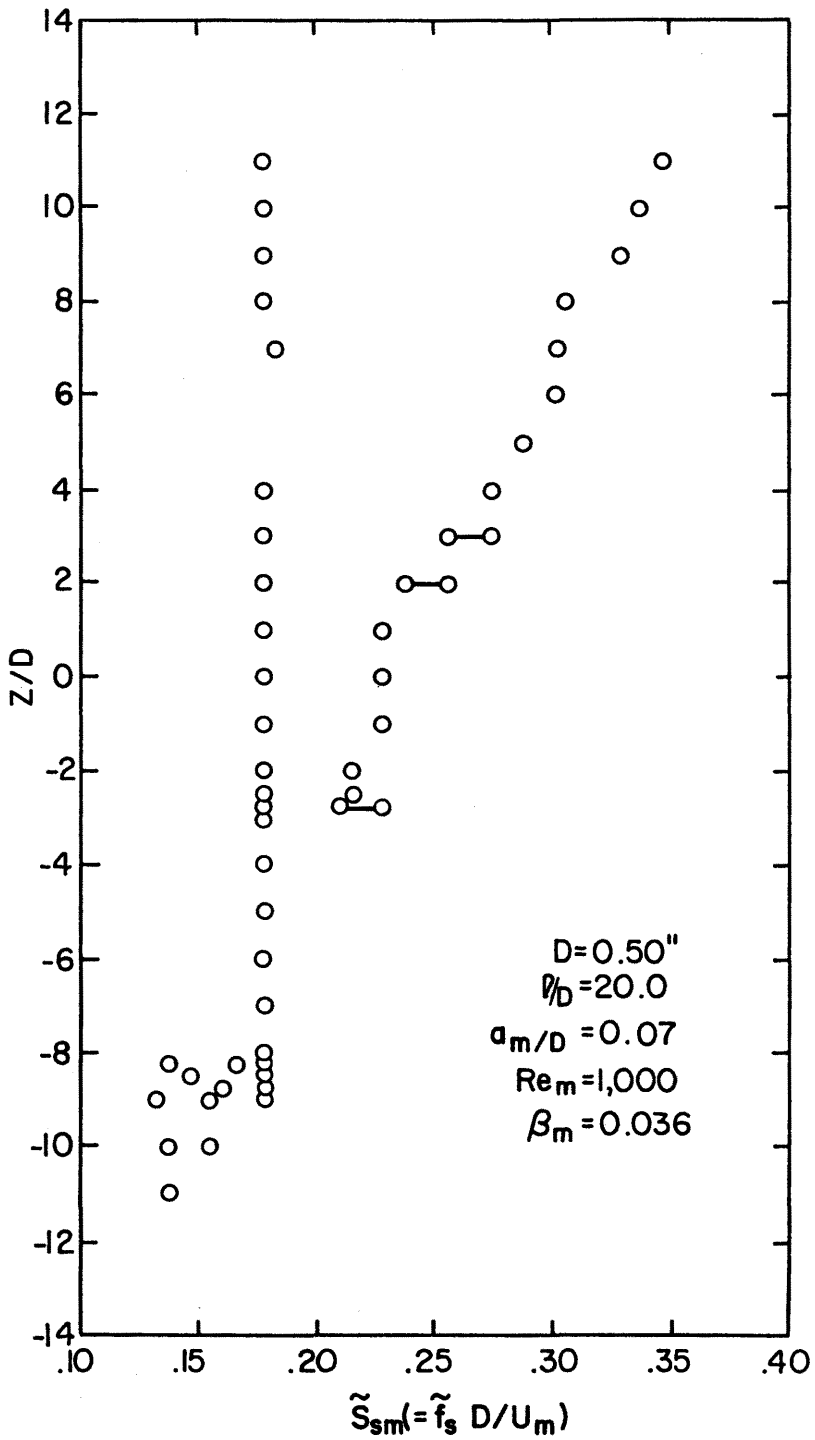

4.2.21 Spanwise Variation of S_{sm} for an Oscillating Cable with D = 0.50 in., Re_m = 1,000, β_m = 0.036, ℓ/D = 20.0, S_{cm} = 0.178, and a_m/D = 0.07

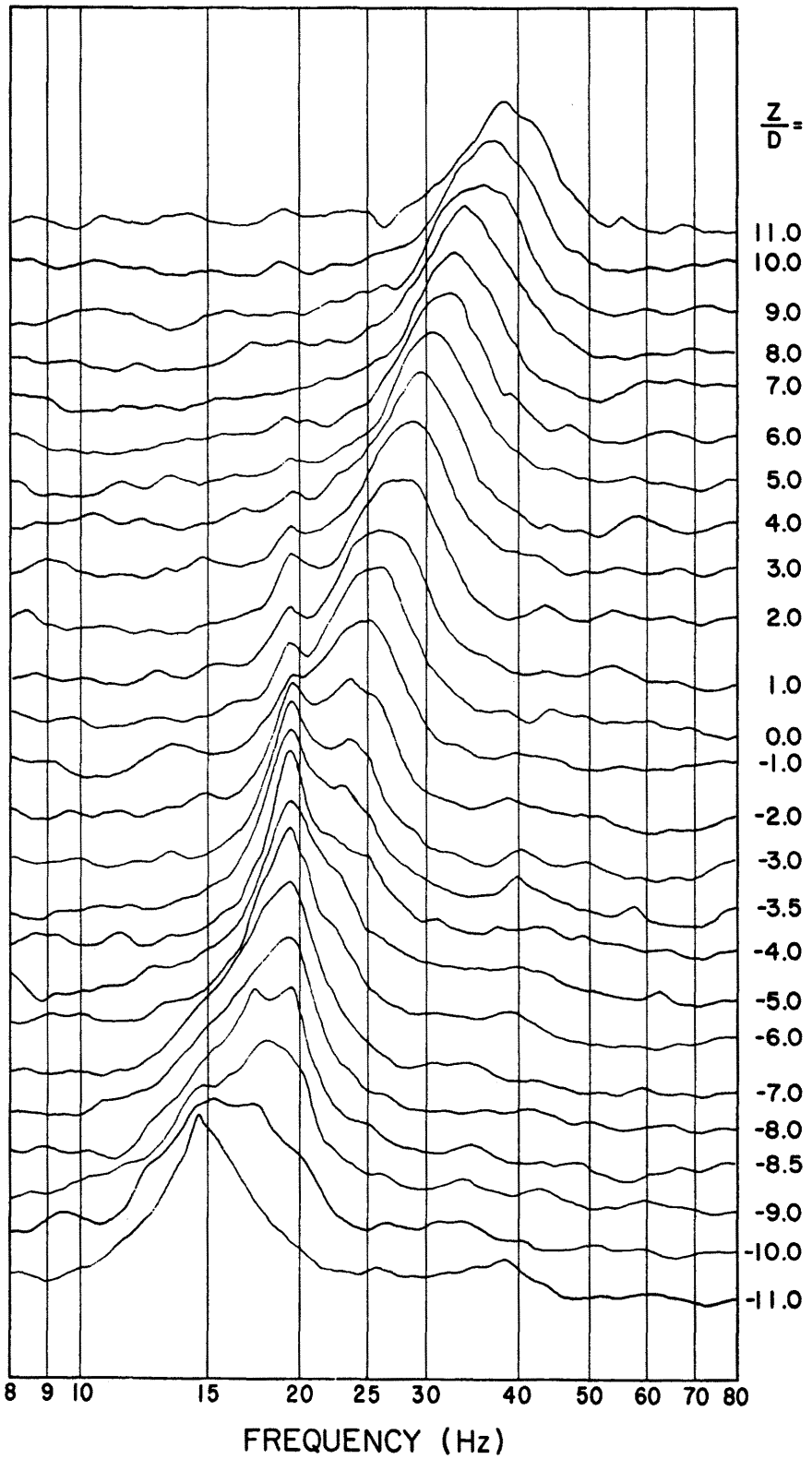

4.2.22 Frequency Spectra at Various Spanwise Positions for an Oscillating Cable with D = 0.50 in., Re_m = 1,000, β_m = 0.036, ℓ/D = 20.0, f_c = 19.5 Hz, and a_m/D = 0.045

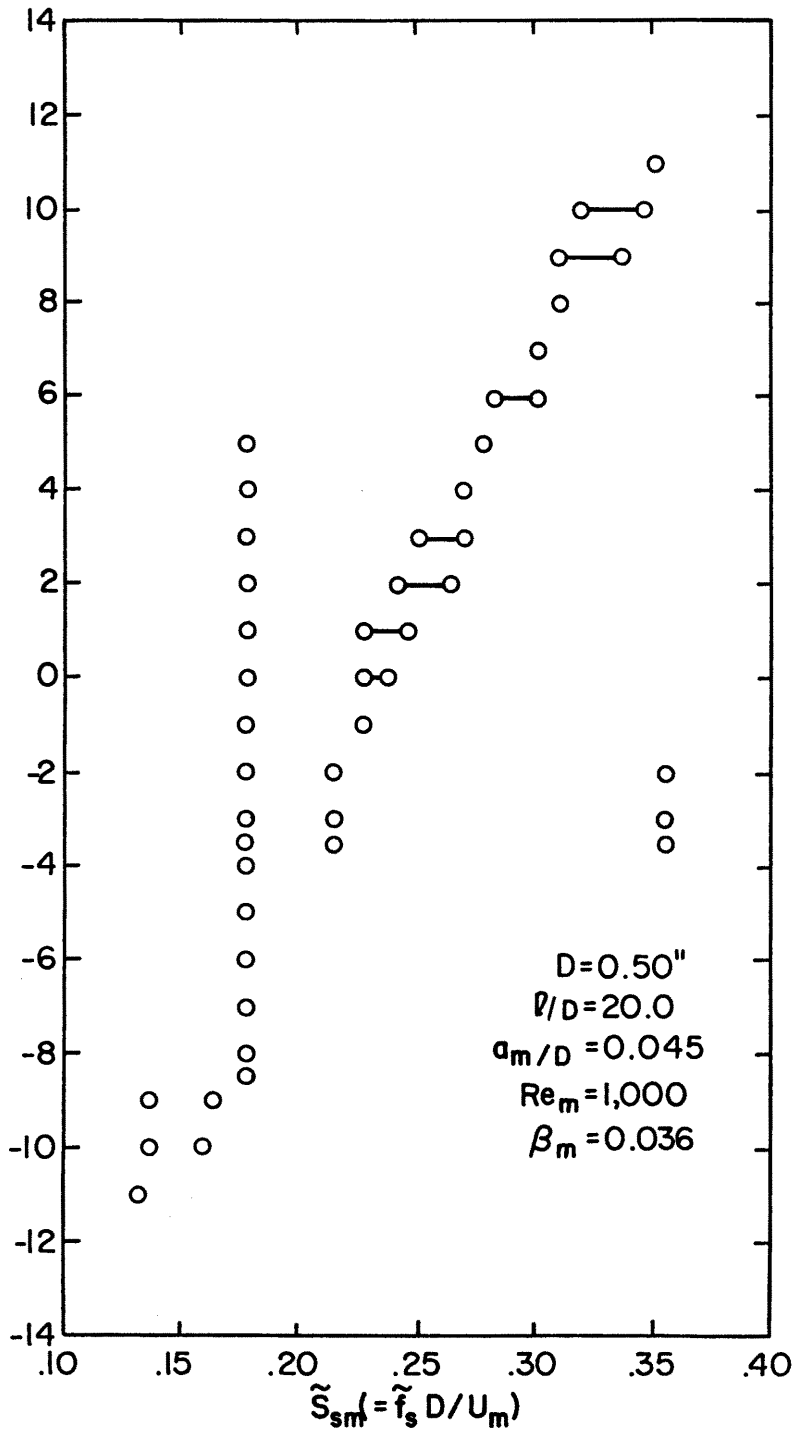

4.2.23 Spanwise Variation of S_{sm} for an Oscillating Cable with D = 0.50 in., Re_m = 1,000, β_m = 0.036, ℓ/D = 20.0, S_{cm} = 0.178, and a_m/D = 0.045

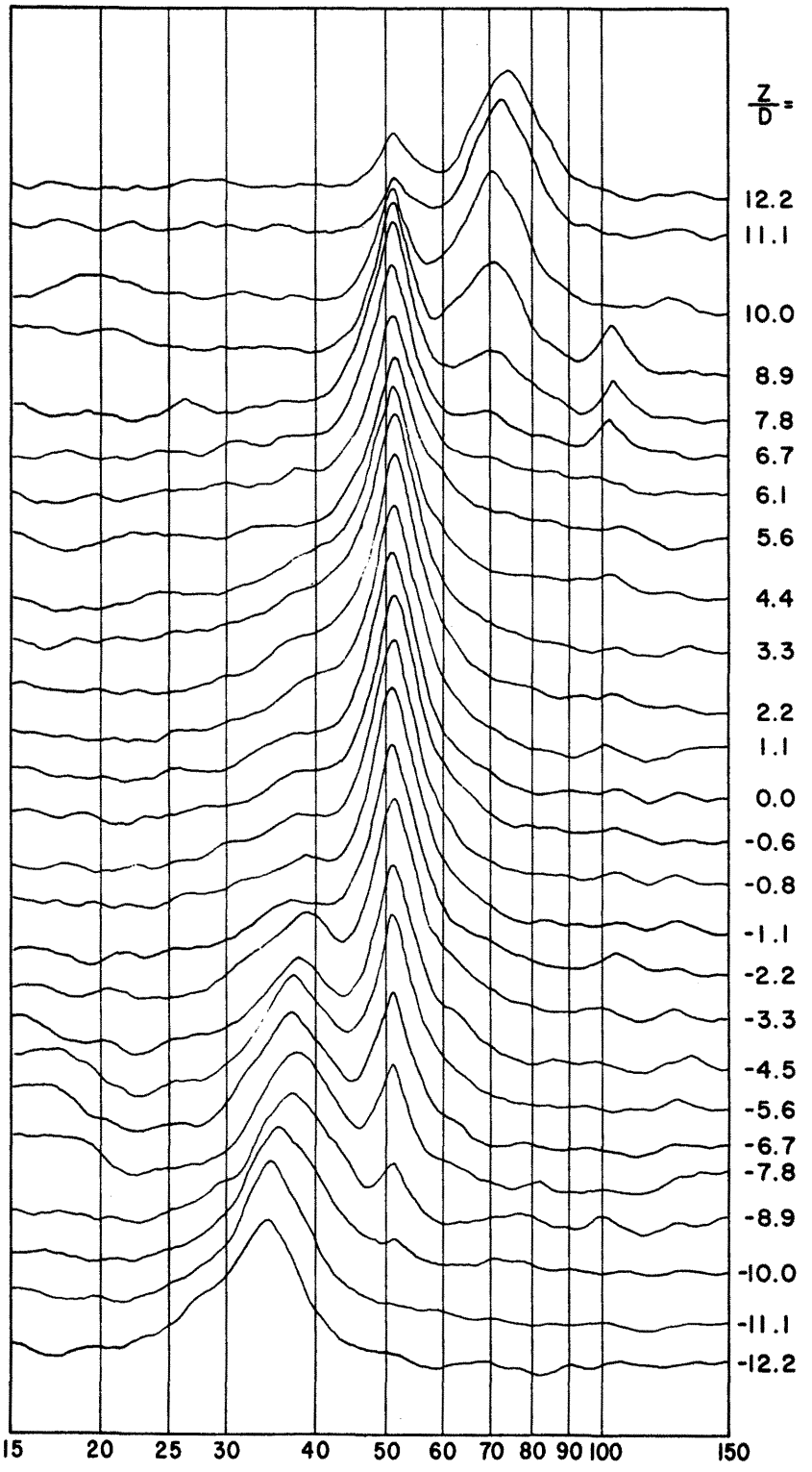

4.2.24 Frequency Spectra at Various Spanwise Positions for an Oscillating Cable with D = 0.45 in., Re_m = 1,700, β_m = 0.031, ℓ/D = 22.2, f_c = 51.0 Hz, and a_m/D = 0.35

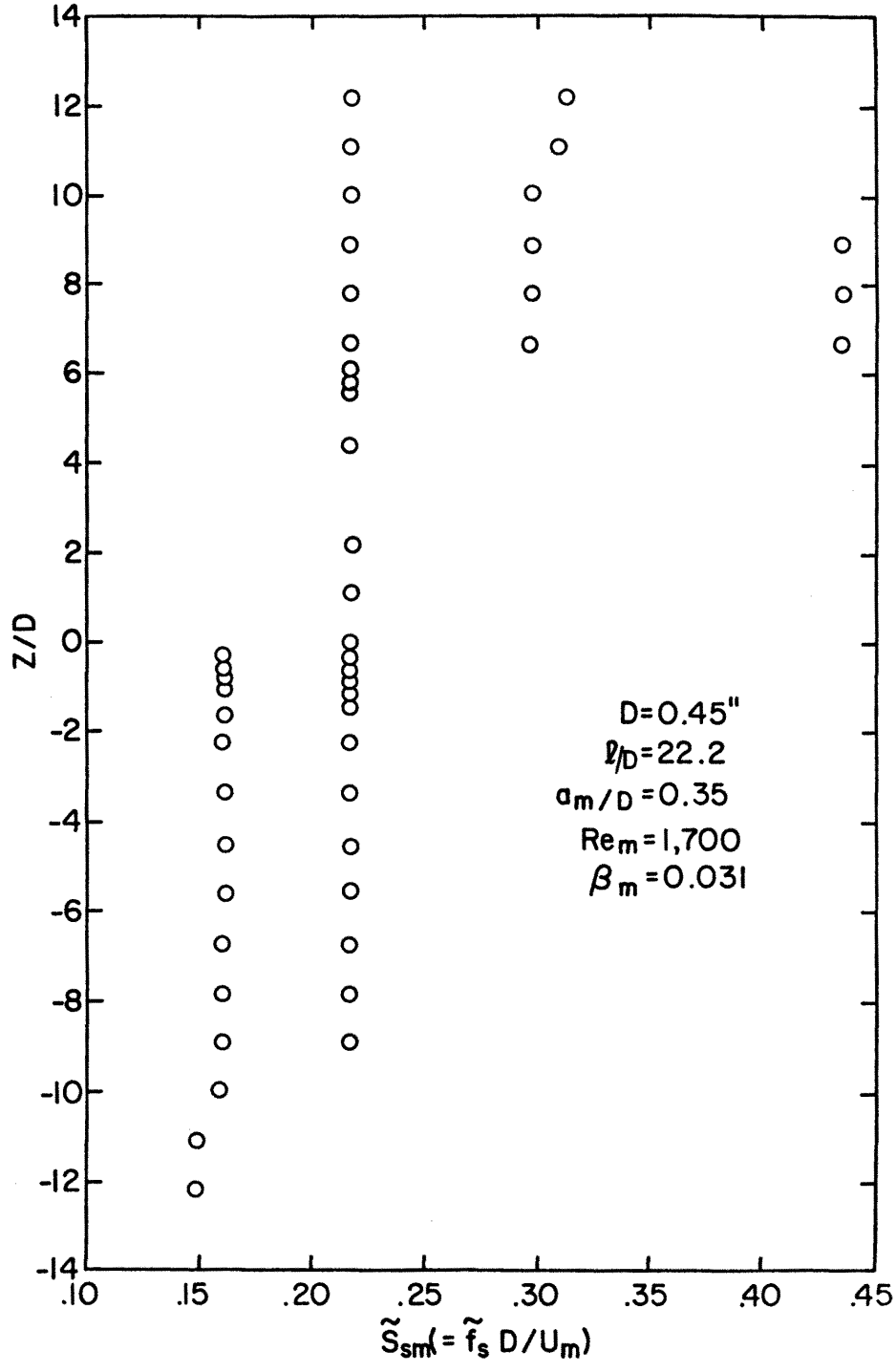

4.2.25 Spanwise Variation of S_{sm} for an Oscillating Cable with D = 0.45 in., Re_m = 1,700, β_m = 0.031, ℓ/D = 22.2, S_{cm} = 0.217, and a_m/D = 0.35

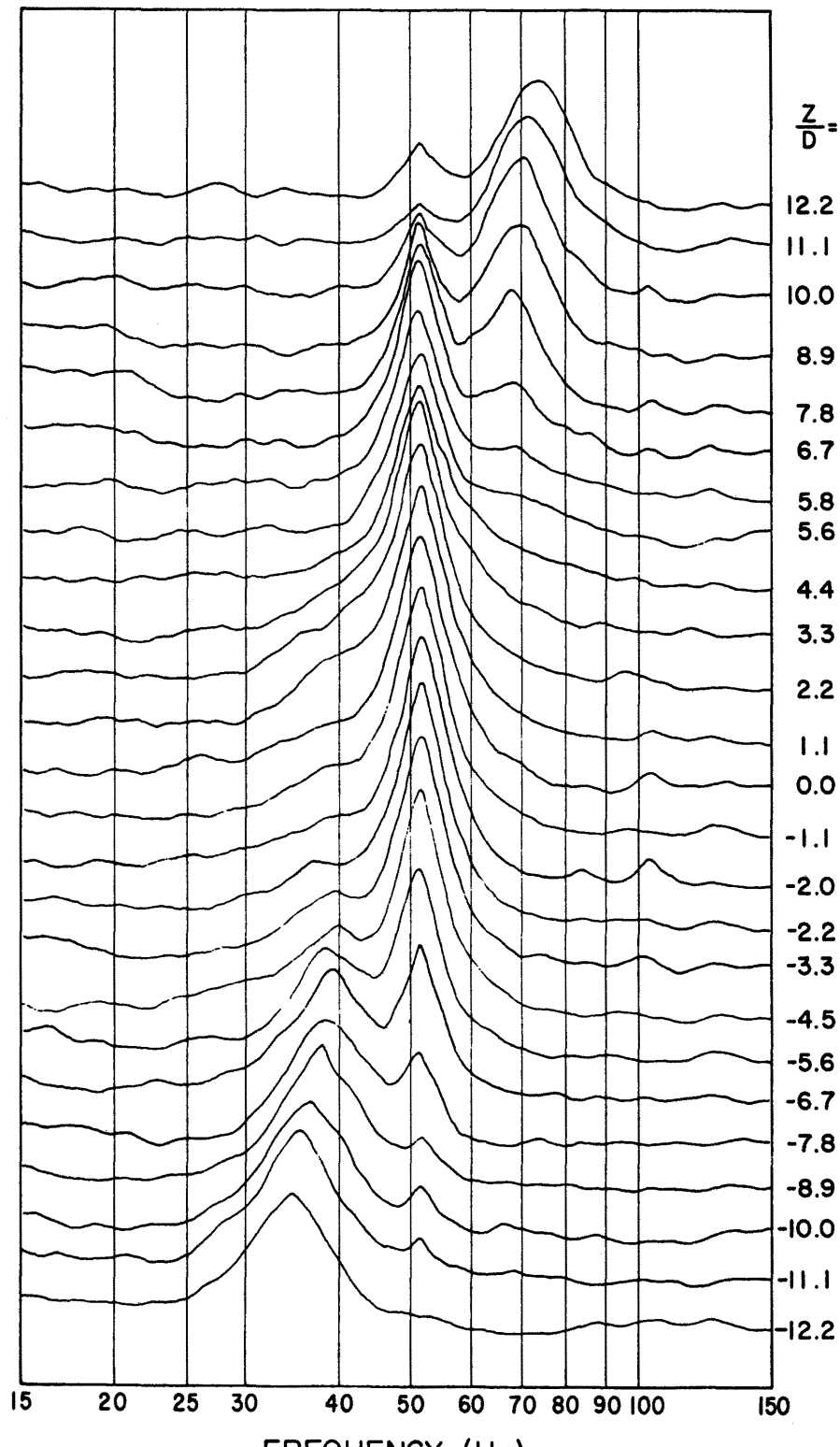

4.2.26 Frequency Spectra at Various Spanwise Positions for an Oscillating Cable with D = 0.45 in., Re_m = 1,700, β_m = 0.031, ℓ/D = 22.2, f_c = 51.0 Hz, and a_m/D = 0.25

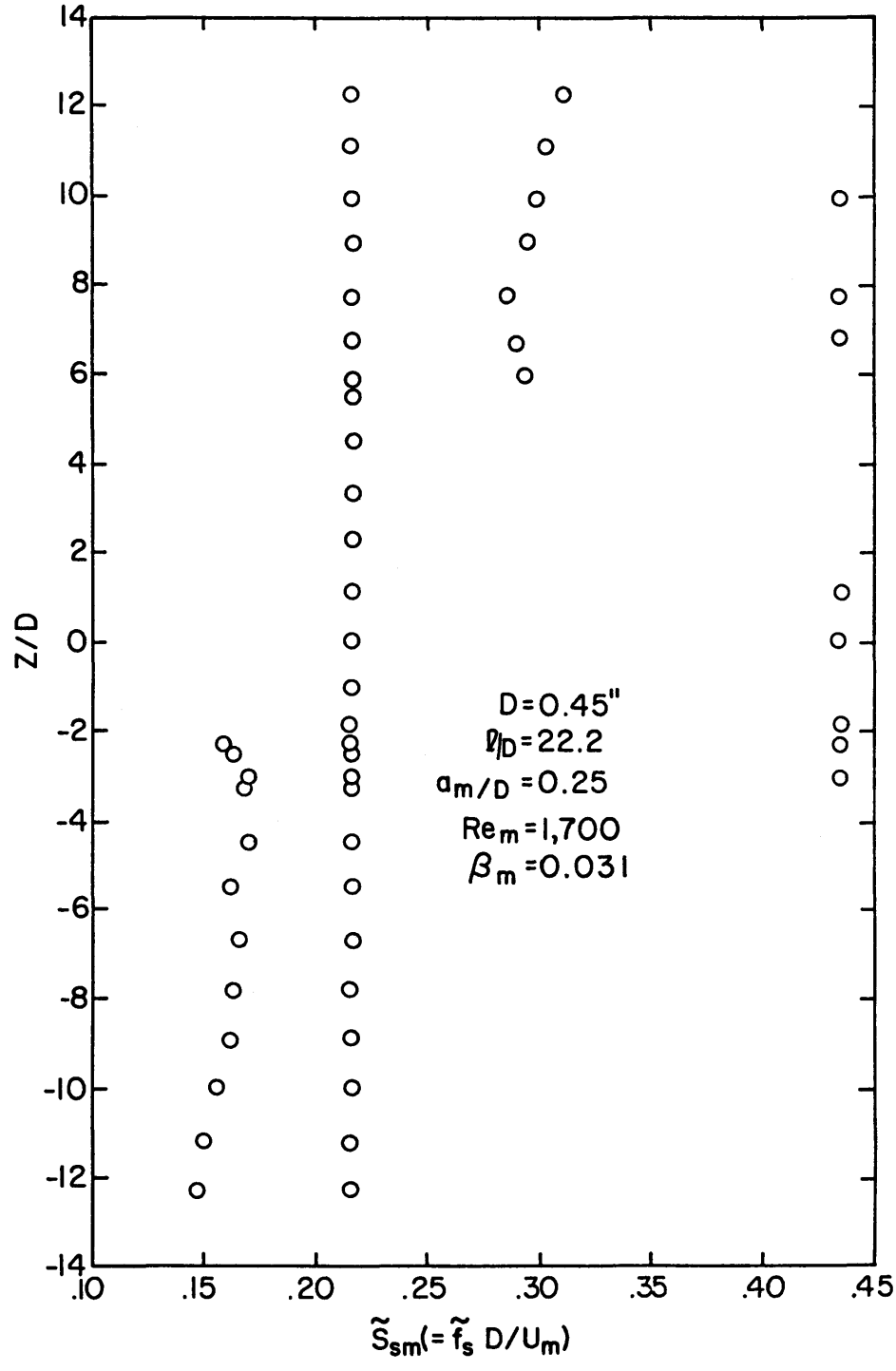

4.2.27 Spanwise Variation of S_{sm} for an Oscillating Cable with D = 0.45 in., Re_m = 1,700, β_m = 0.031, ℓ/D = 22.2, S_{cm} = 0.217, and a_m/D = 0.25

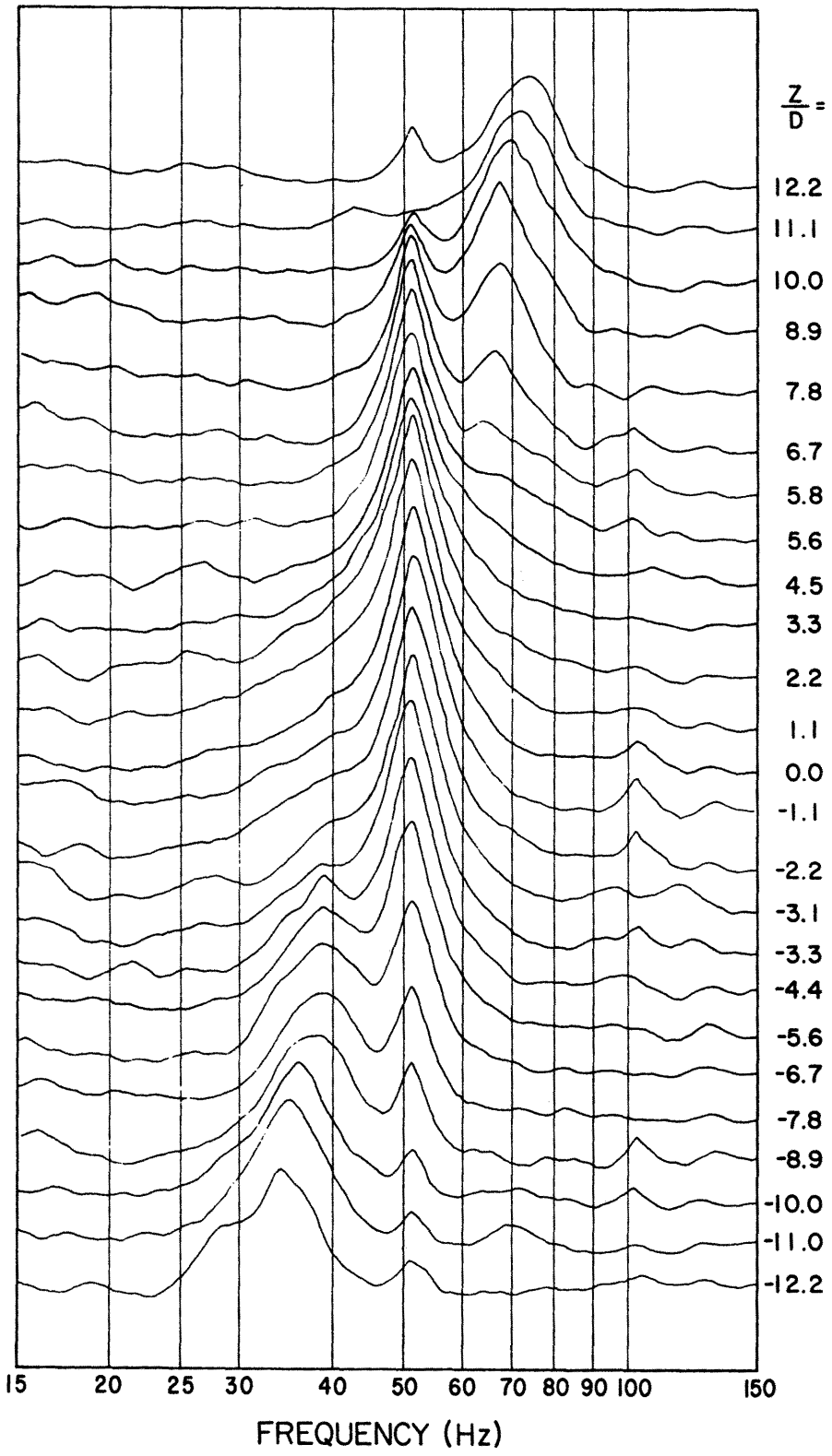

4.2.28 Frequency Spectra at Various Spanwise Positions for an Oscillating Cable with D = 0.45 in., Re_m = 1,700, β_m = 0.031, ℓ/D = 22.2, f_c = 51.0 Hz, and a_m/D = 0.21

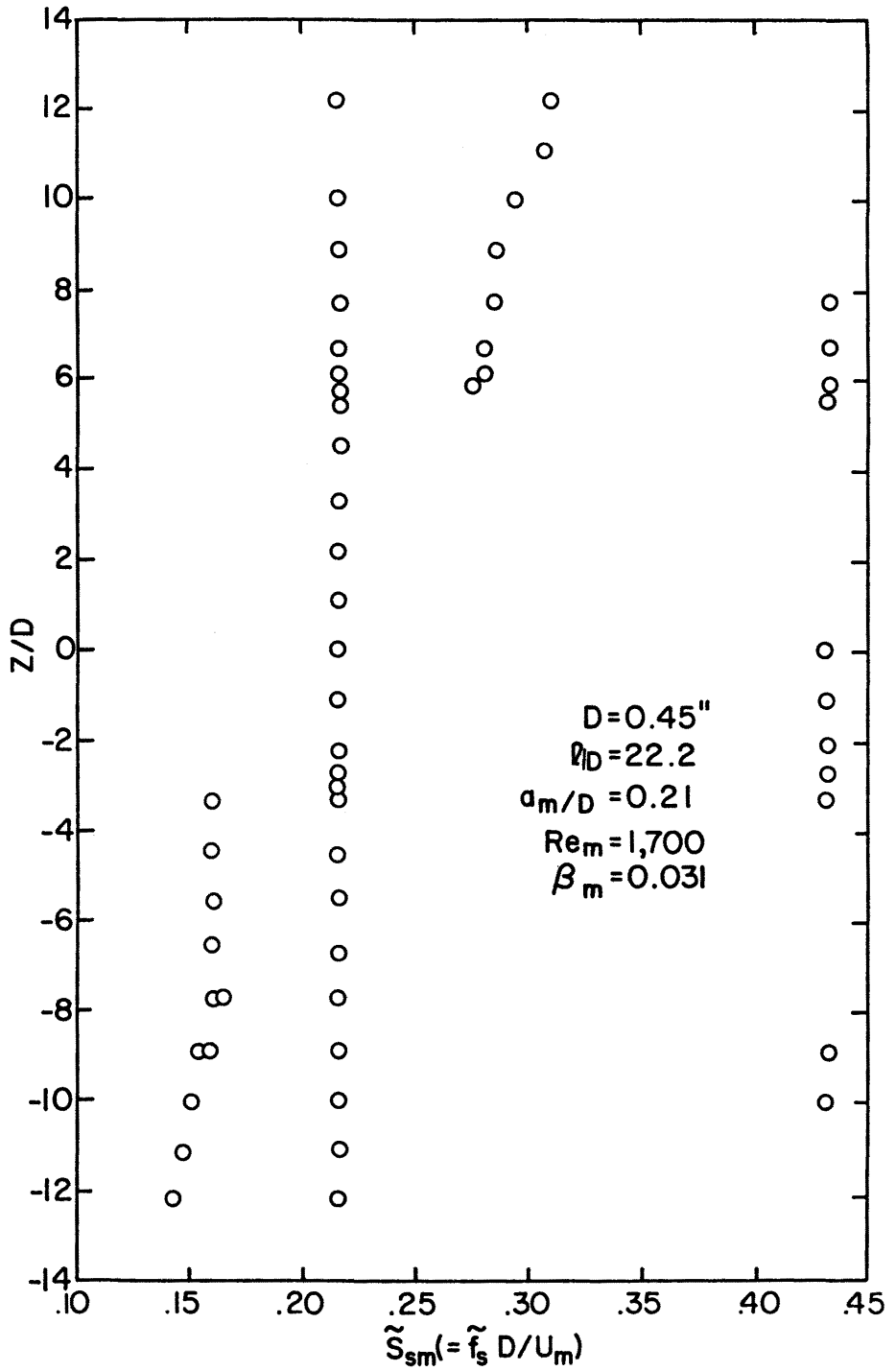

4.2.29 Spanwise Variation of S_{sm} for an Oscillating Cable with D = 0.45 in., Re_m = 1,700, β_m = 0.031, ℓ/D = 22.2, S_{cm} = 0.217, and a_m/D = 0.21

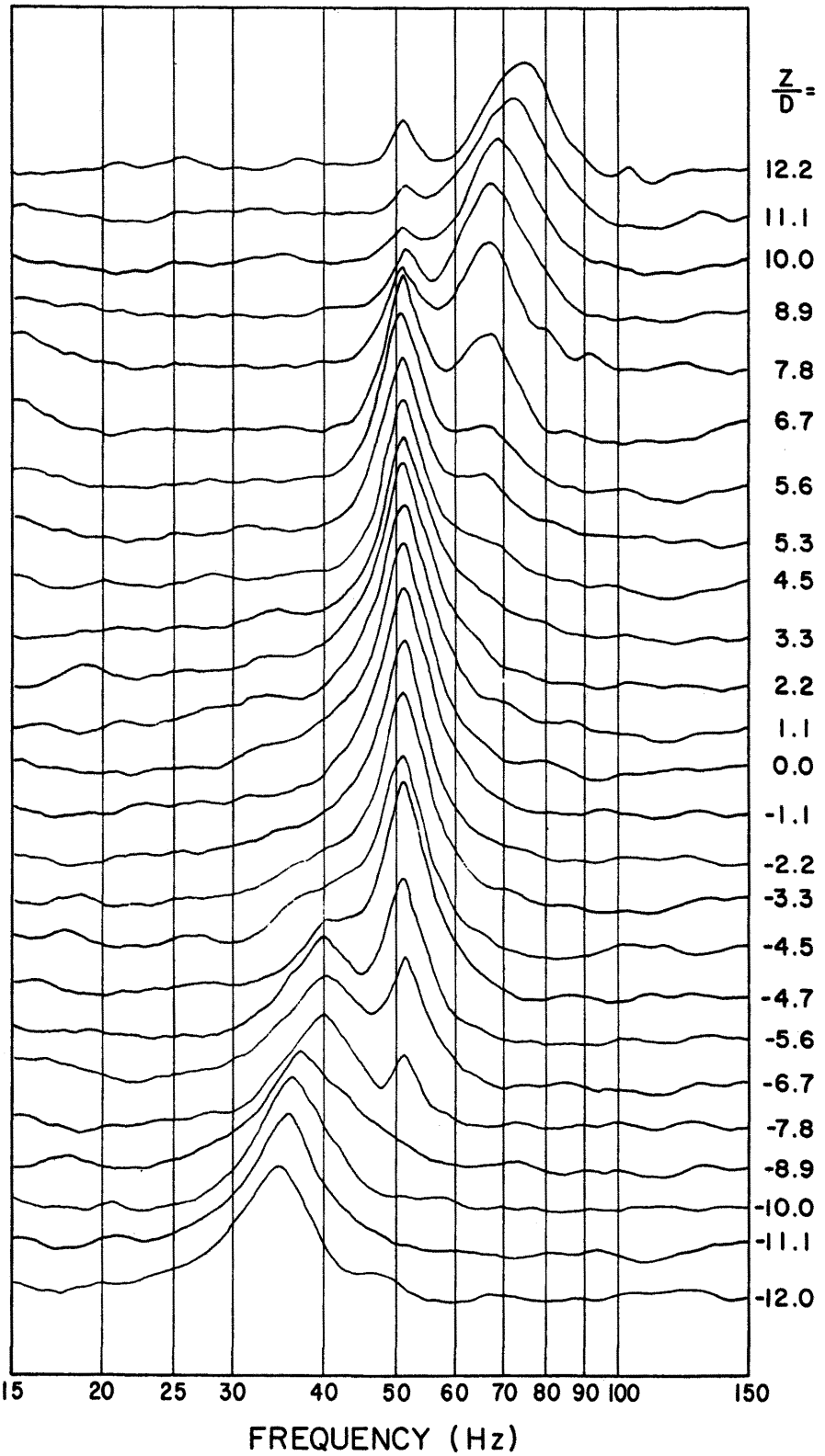

4.2.30 Frequency Spectra at Various Spanwise Positions for an Oscillating Cable with D = 0.45 in., Re_m = 1,700, β_m = 0.031, ℓ/D = 22.2, f_c = 51.0 Hz, and a_m/D = 0.15

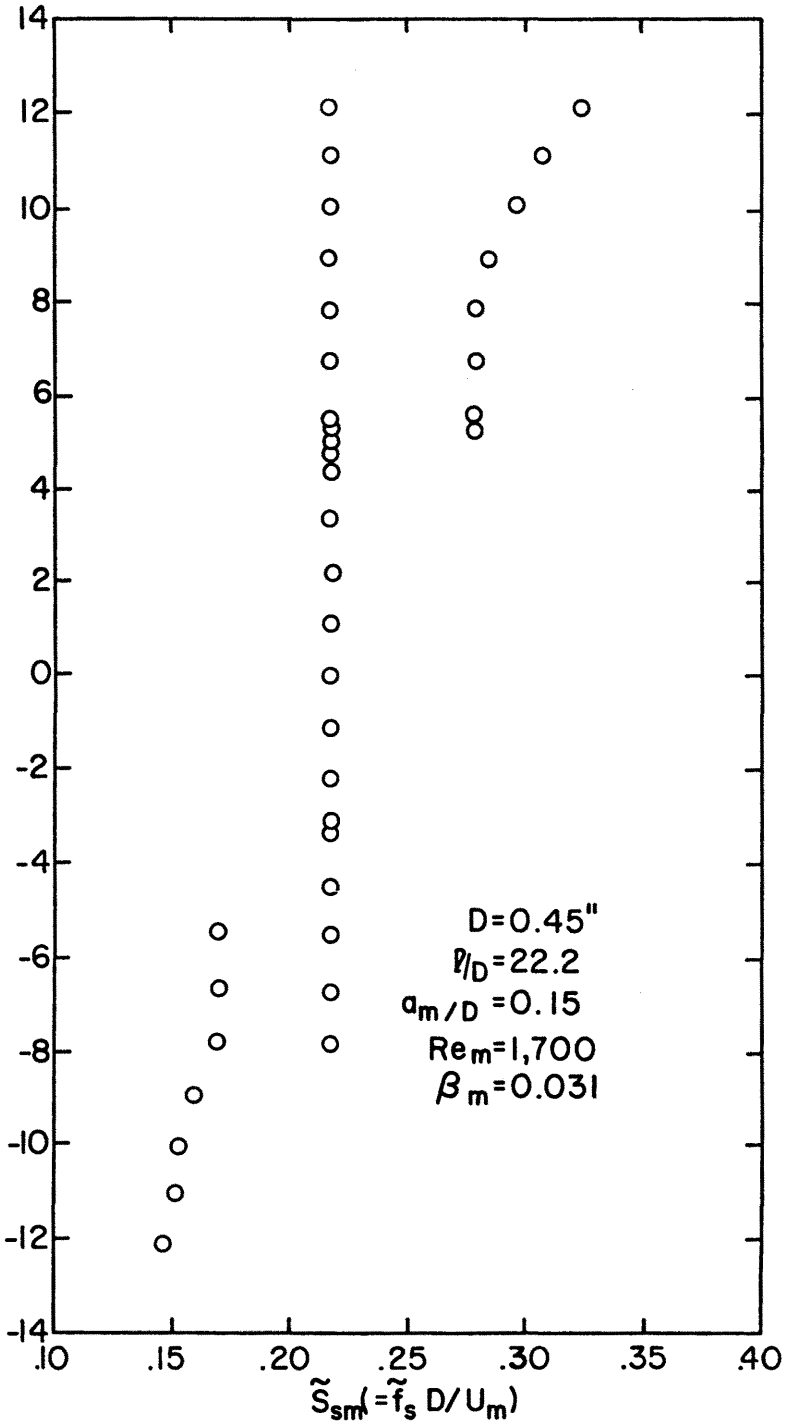

4.2.31 Spanwise Variation of S_{sm} for an Oscillating Cable with D = 0.45 in., Re_m = 1,700, β_m = 0.031, ℓ/D = 22.2, S_{cm} = 0.217, and a_m/D = 0.15

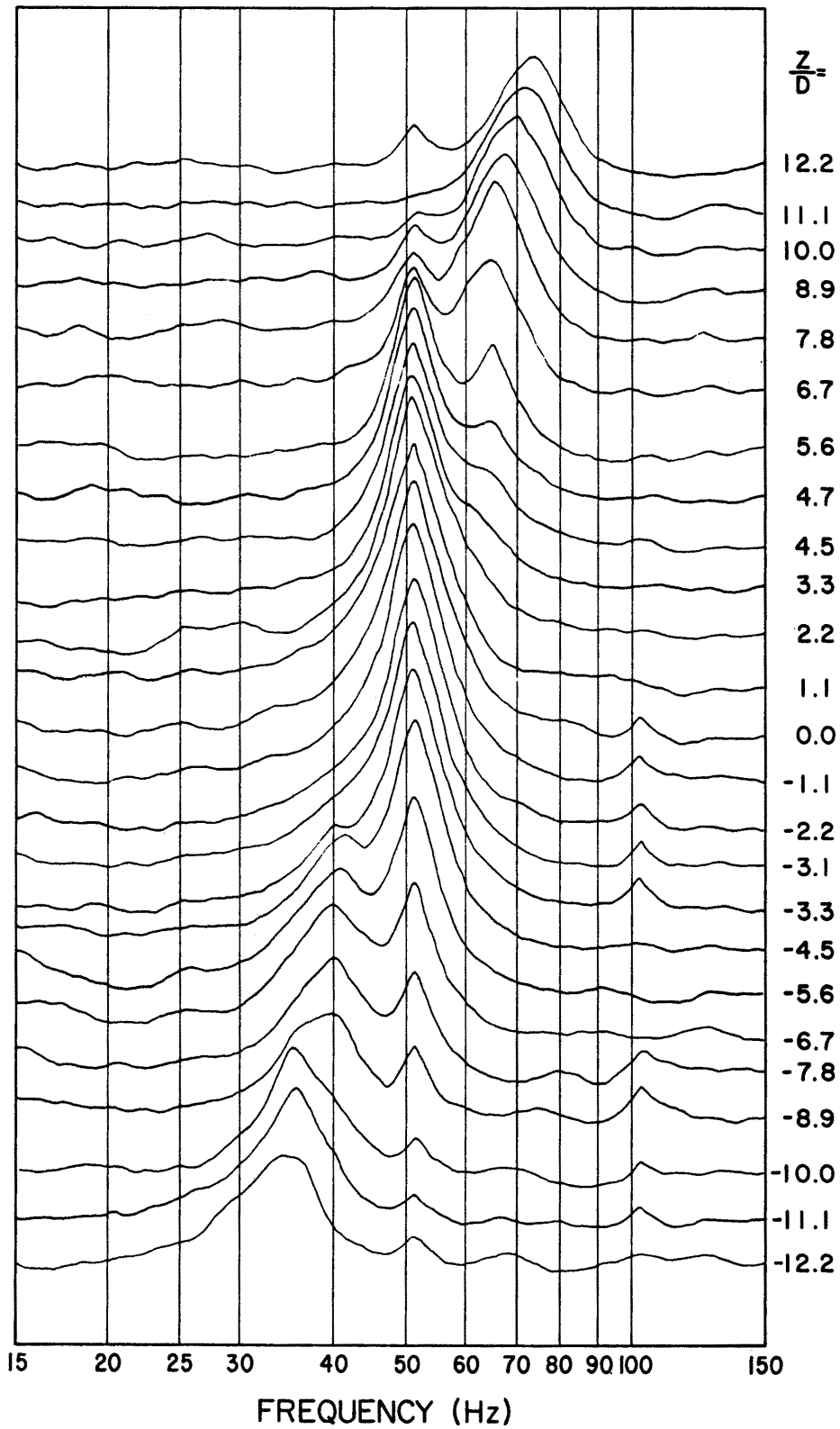

4.2.32 Frequency Spectra at Various Spanwise Positions for an Oscillating Cable with D = 0.45 in., Re_m = 1,700, β_m = 0.031, ℓ/D = 22.2, f_c = 51.0 Hz, and a_m/D = 0.11

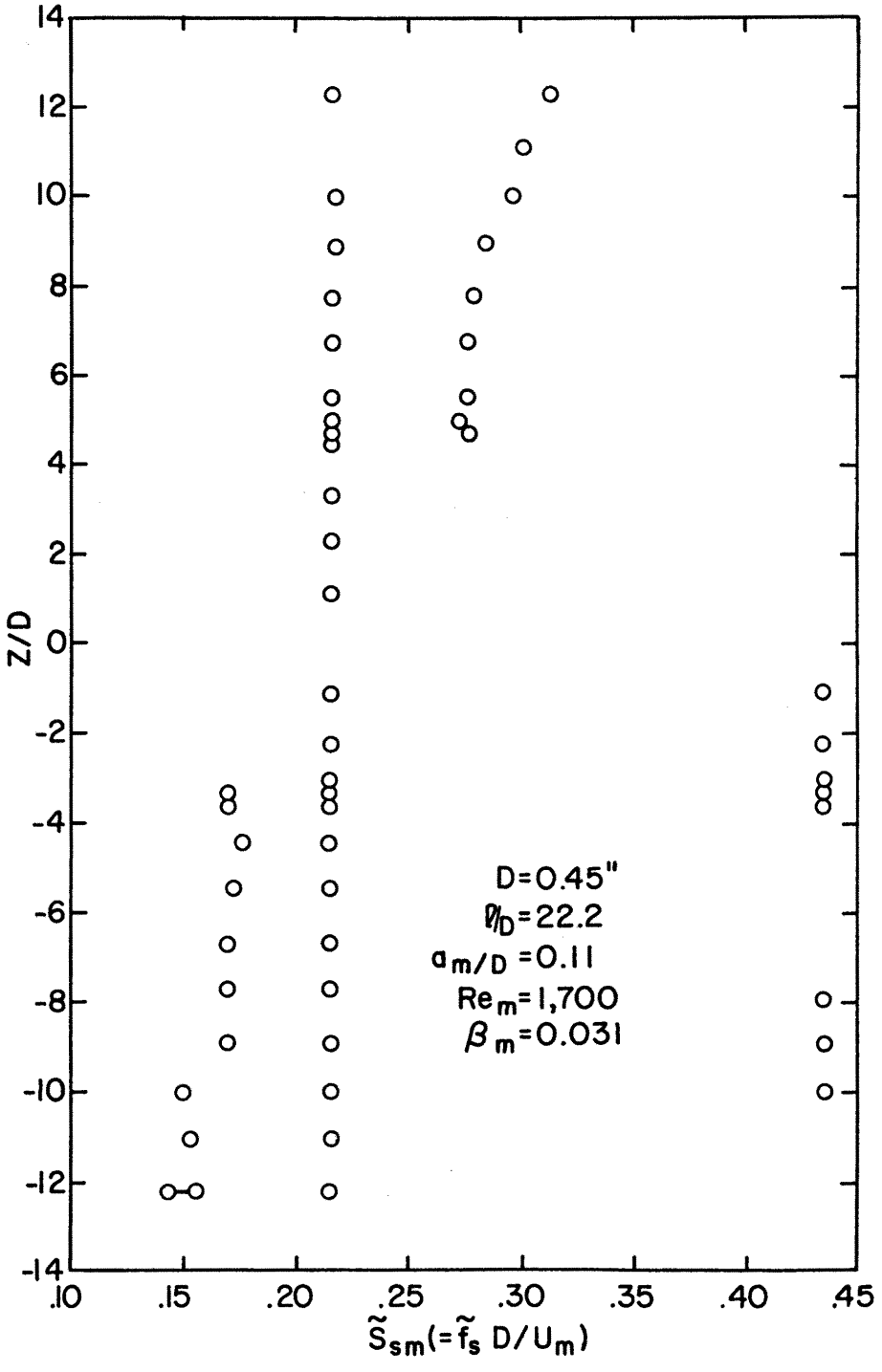

4.2.33 Spanwise Variation of S_{sm} for an Oscillating Cable with D = 0.45 in., Re_m = 1,700, β_m = 0.031, ℓ/D = 22.2, S_{cm} = 0.217, and a_m/D = 0.11

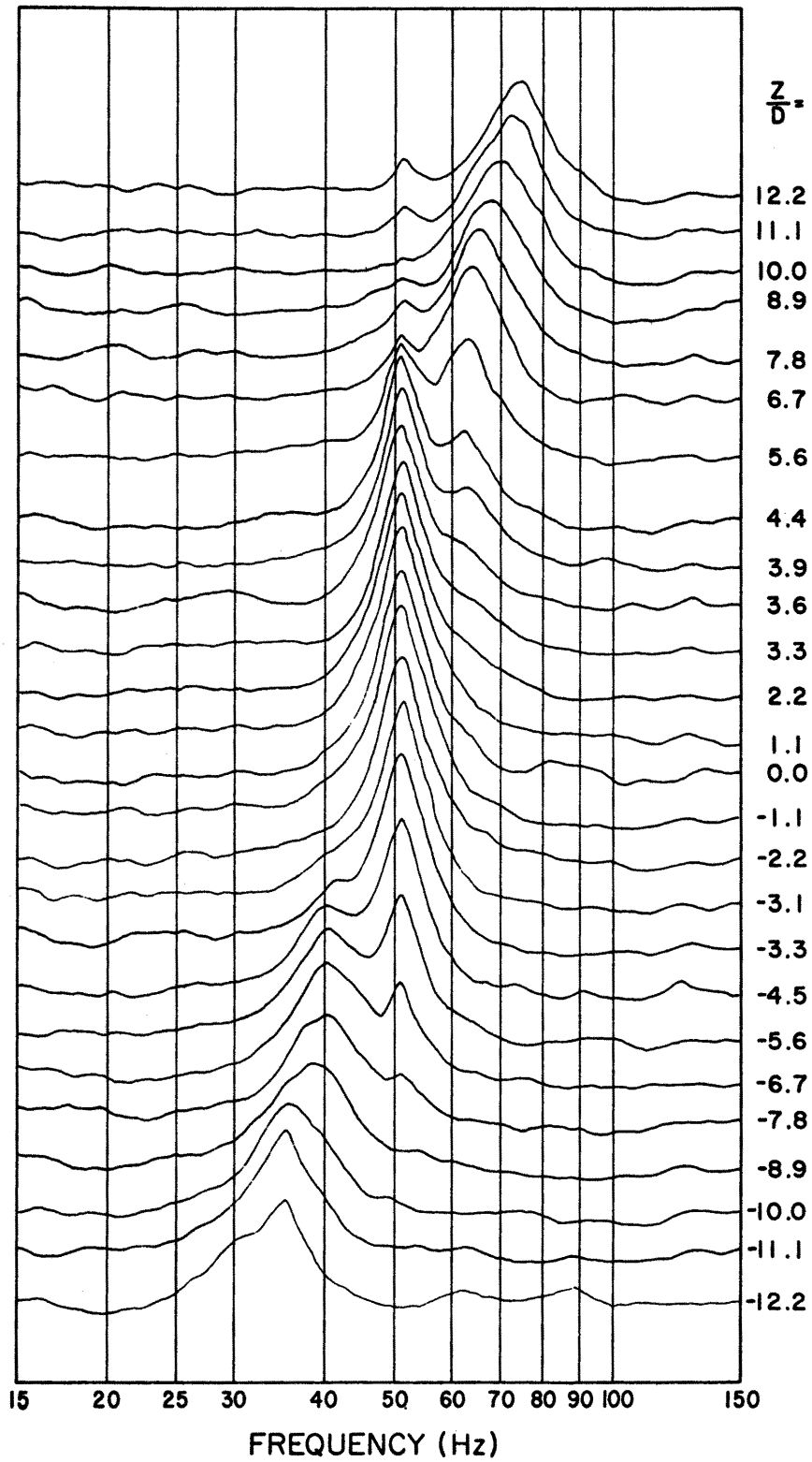

4.2.34 Frequency Spectra at Various Spanwise Positions for an Oscillating Cable with D = 0.45 in., Re_m = 1,700, β_m = 0.031, ℓ/D = 22.2, f_c = 51.0 Hz, and a_m/D = 0.05

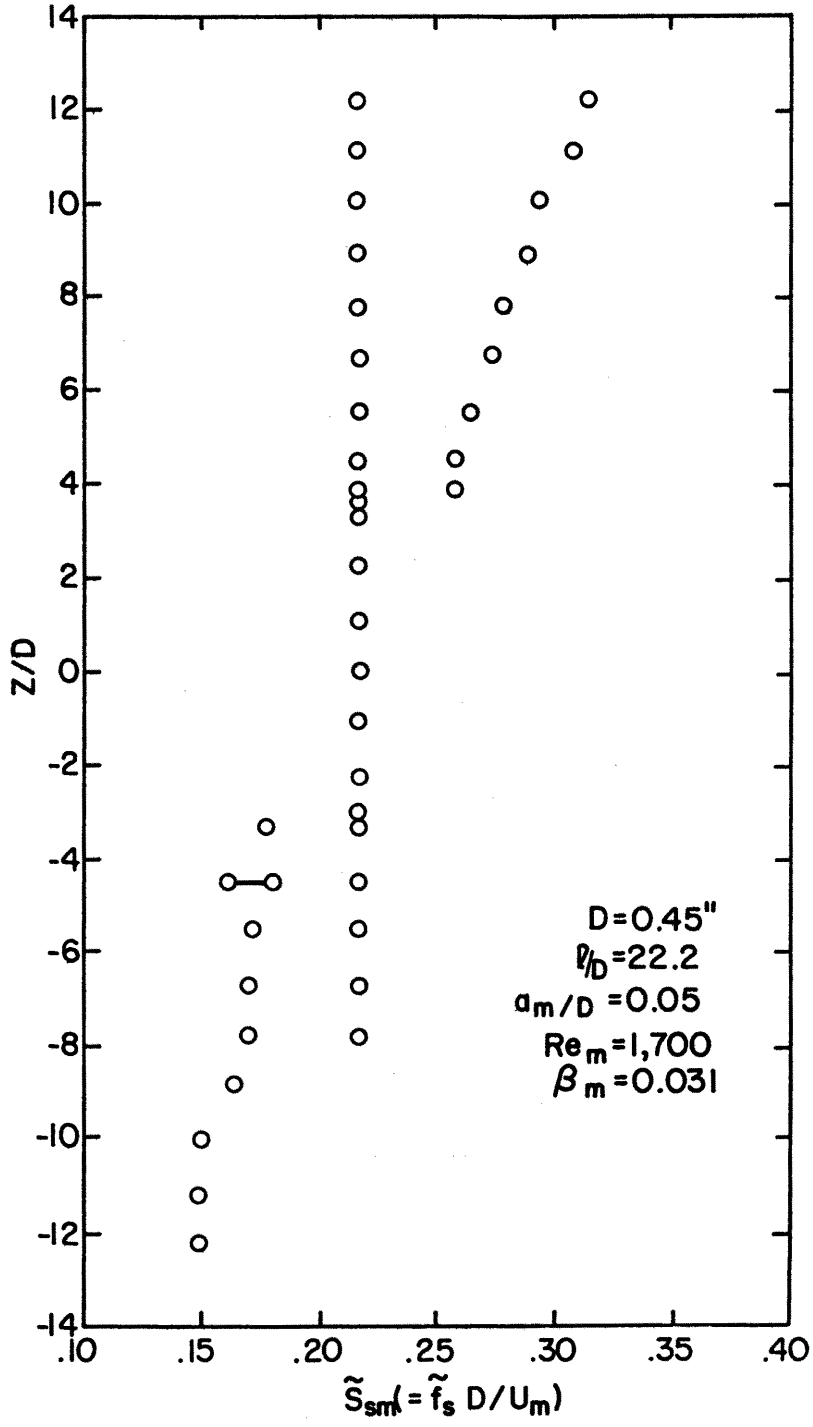

4.2.35 Spanwise Variation of S_{sm} for an Oscillating Cable with D = 0.45 in., Re_m = 1,700, β_m = 0.031, ℓ/D = 22.2, S_{cm} = 0.217, and a_m/D = 0.05

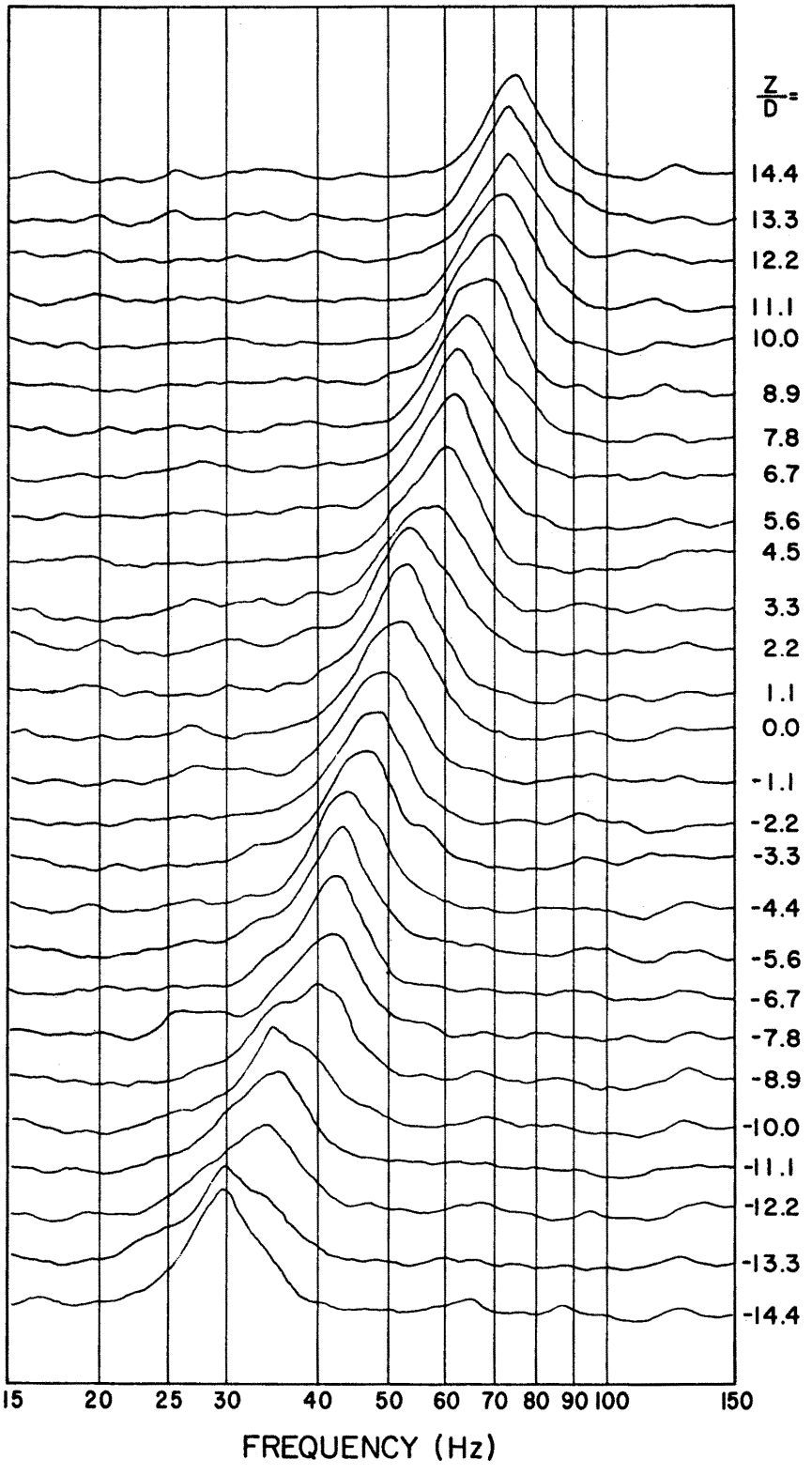

4.2.36 Frequency Spectra at Various Spanwise Positions for a Cable with D = 0.45 in., Re_m = 1,700, β_m = 0.031, f_c = 0.0 Hz and a_m/D = 0.0

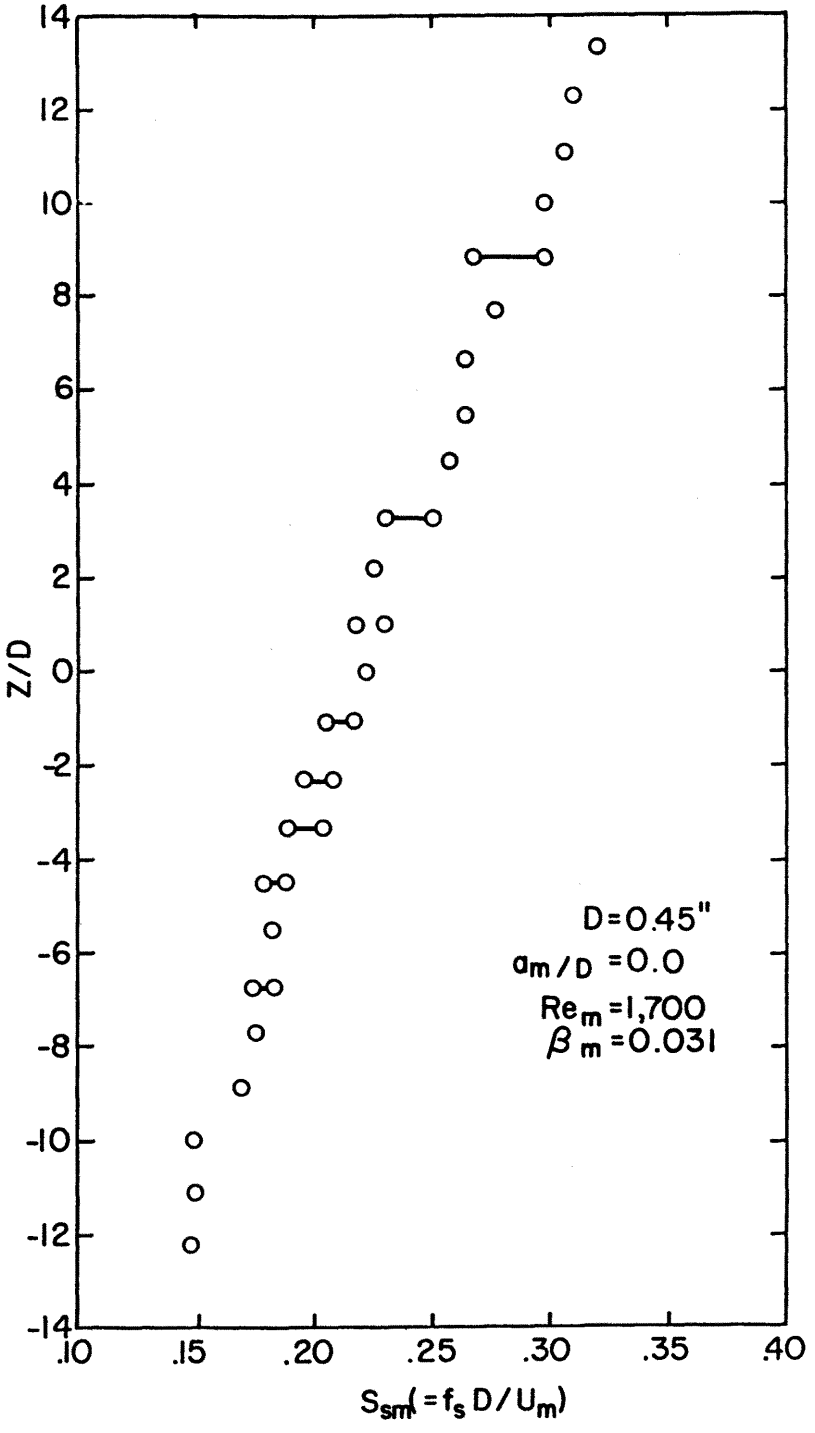

4.2.37 Spanwise Variation of S_{sm} for a Cable with d = 0.45 in., Re_m = 1,700, β_m = 0.031, S_{cm} = 0.0, and a_m/D = 0.0

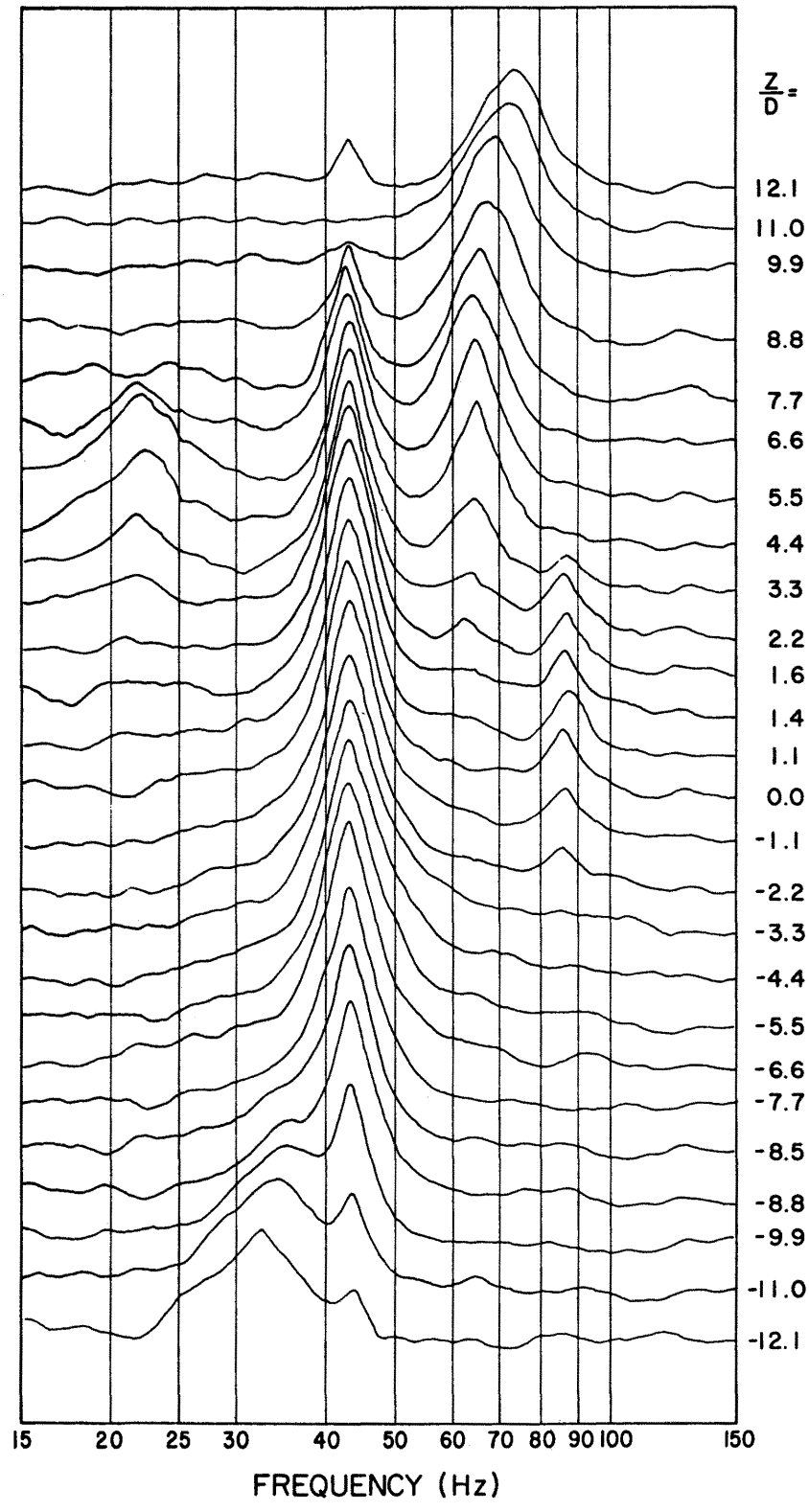

4.2.38 Frequency Spectra at Various Spanwise Positions for an Oscillating Cable with D = 0.46 in., Re_m = 1.725, β_m = 0.031, ℓ/D = 22.0, f_c = 43.0 Hz, and a_m/D = 0.20

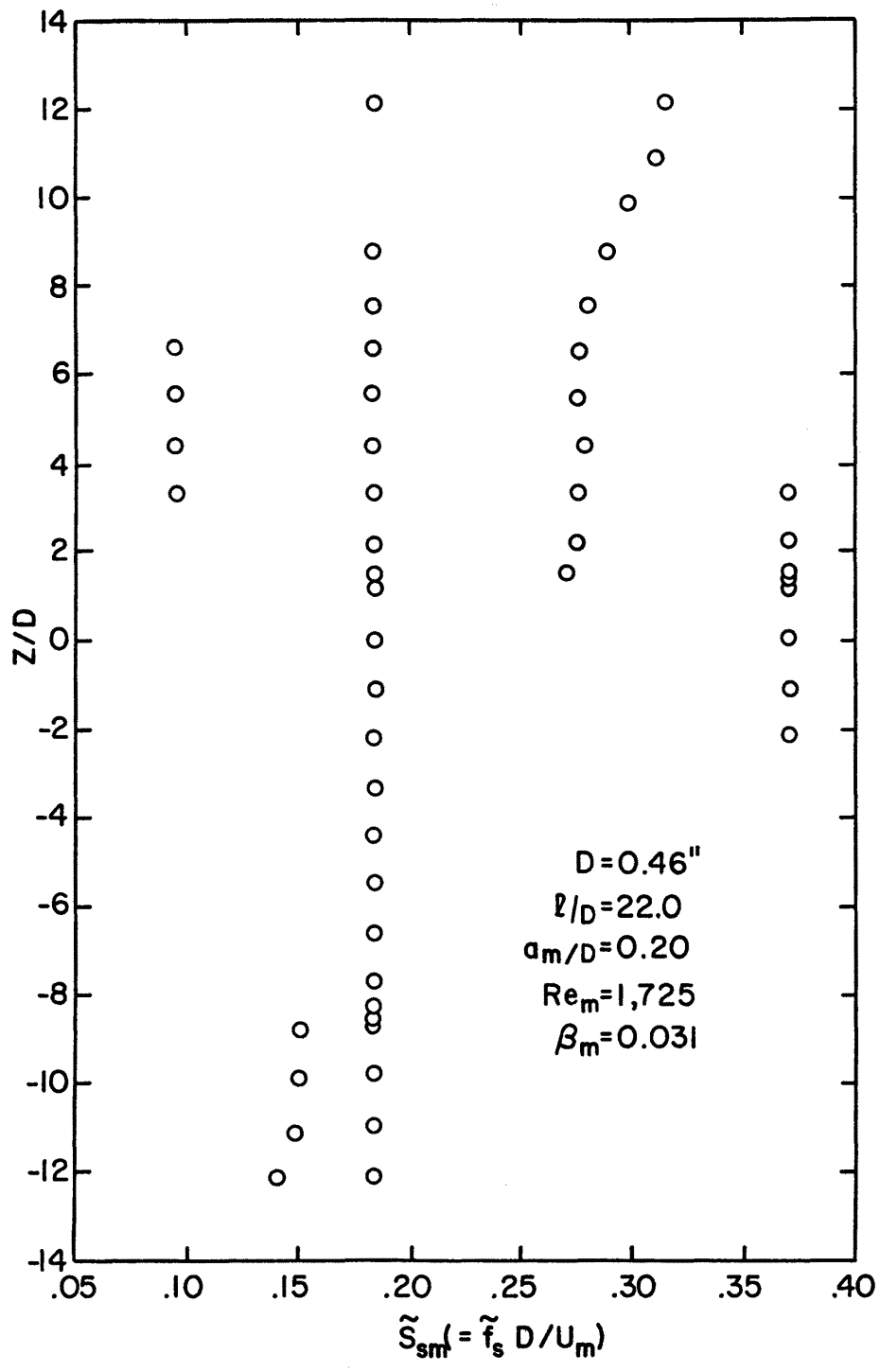

4.2.39 Spanwise Variation of S_{sm} for an Oscillating Cable with D = 0.46 in., Re_m = 1,725, β_m = 0.031, ℓ/D = 22.0, S_{cm} = 0.185, and a_m/D = 0.20

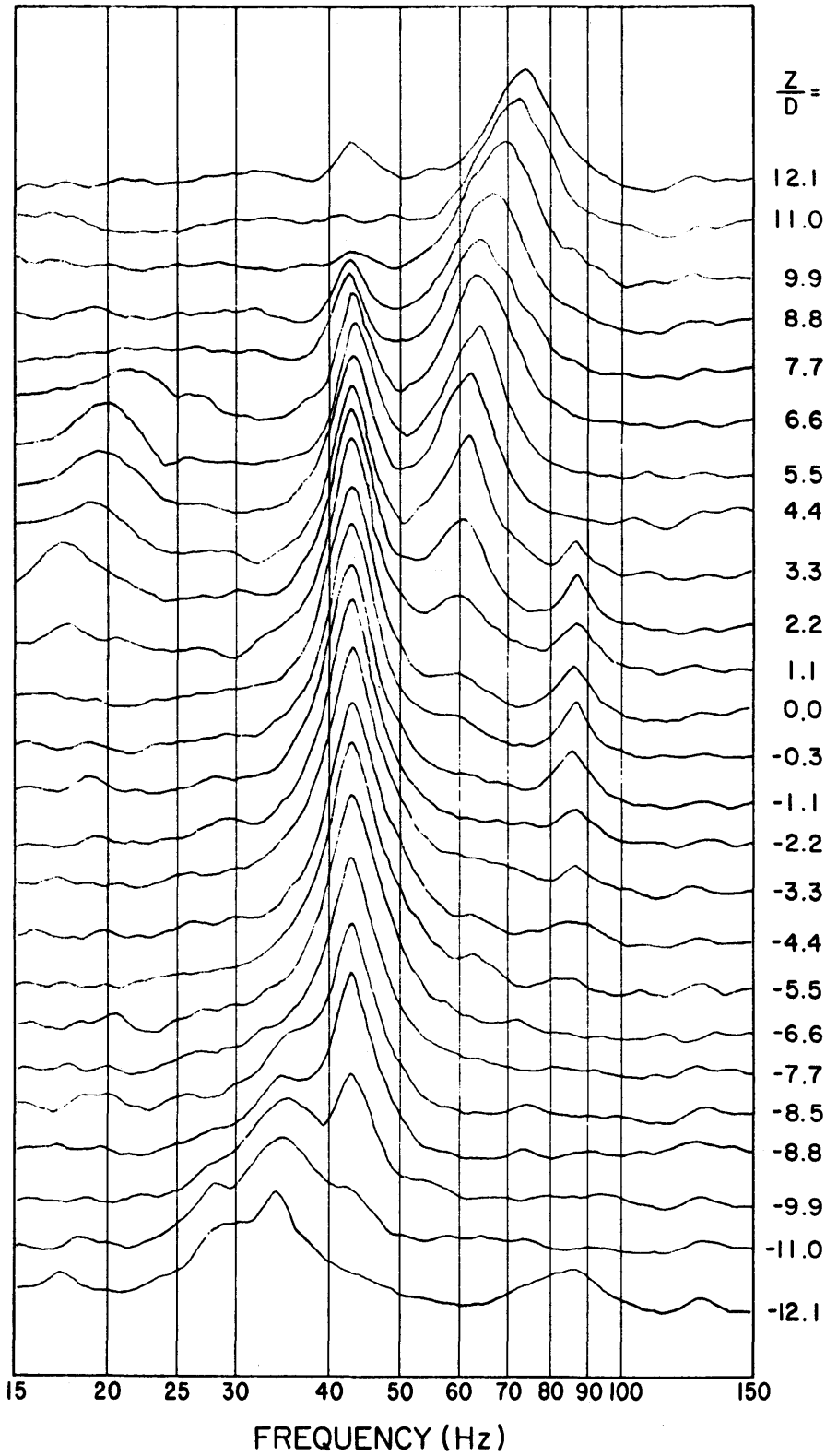

4.2.40 Frequency Spectra at Various Spanwise Positions for an Oscillating Cable with D = 0.46 in., Re_m = 1,725, β_m = 0.031, ℓ/D = 22.0 f_c = 43.0 Hz, and a_m/D = 0.12

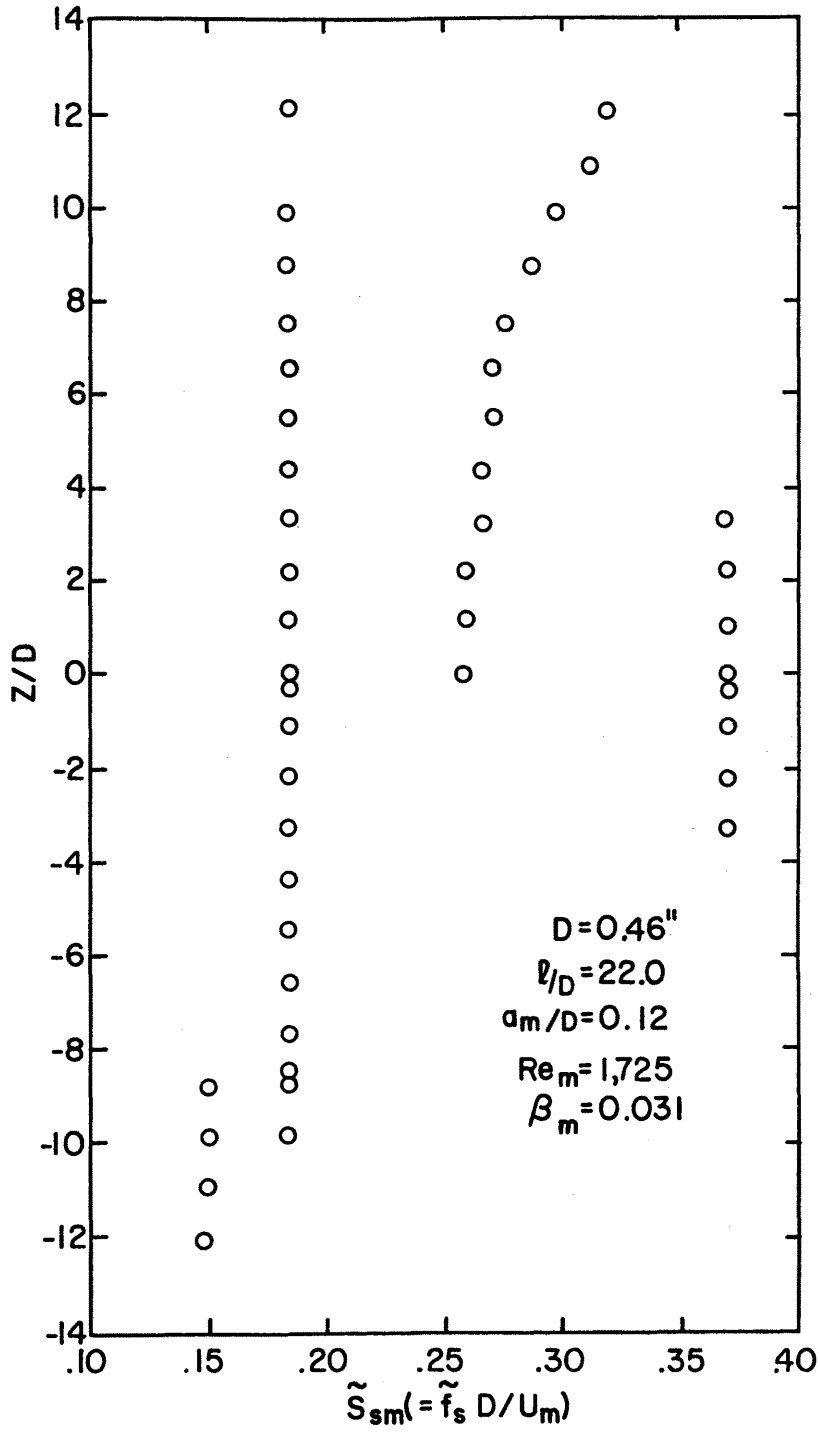

4.2.41 Spanwise Variation of S_{sm} for an Oscillating Cable with D = 0.46 in., Re_m = 1,725, β_m = 0.031, ℓ/D = 22.0, S_{cm} = 0.185, and a_m/D = 0.12

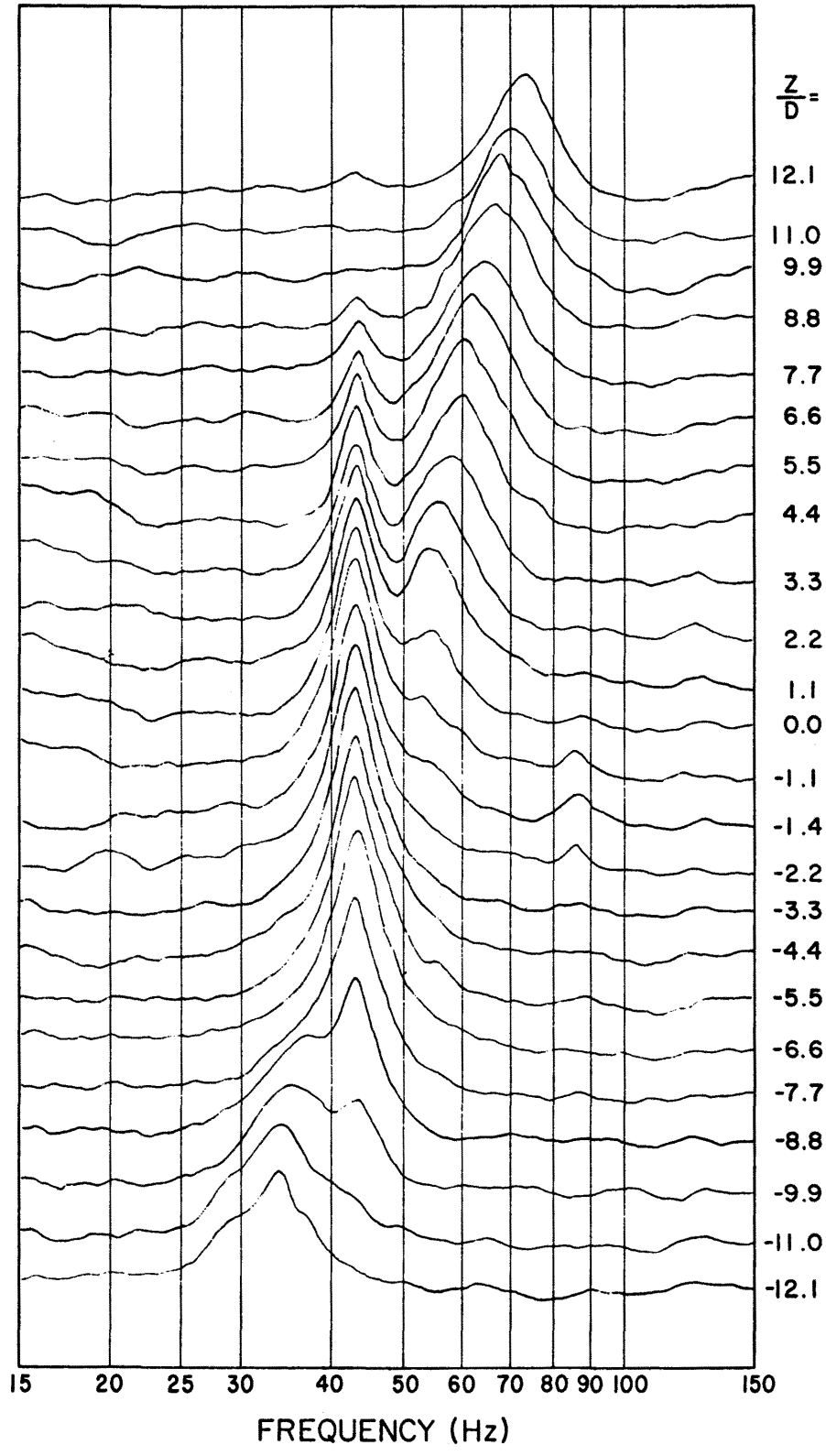

4.2.42 Frequency Spectra at Various Spanwise Positions for an Oscillating Cable with D = 0.46 in., Re_m = 1,725, β_m = 0.031, ℓ/D = 22.0, f_c = 43.0 Hz, and a_m/D = 0.04

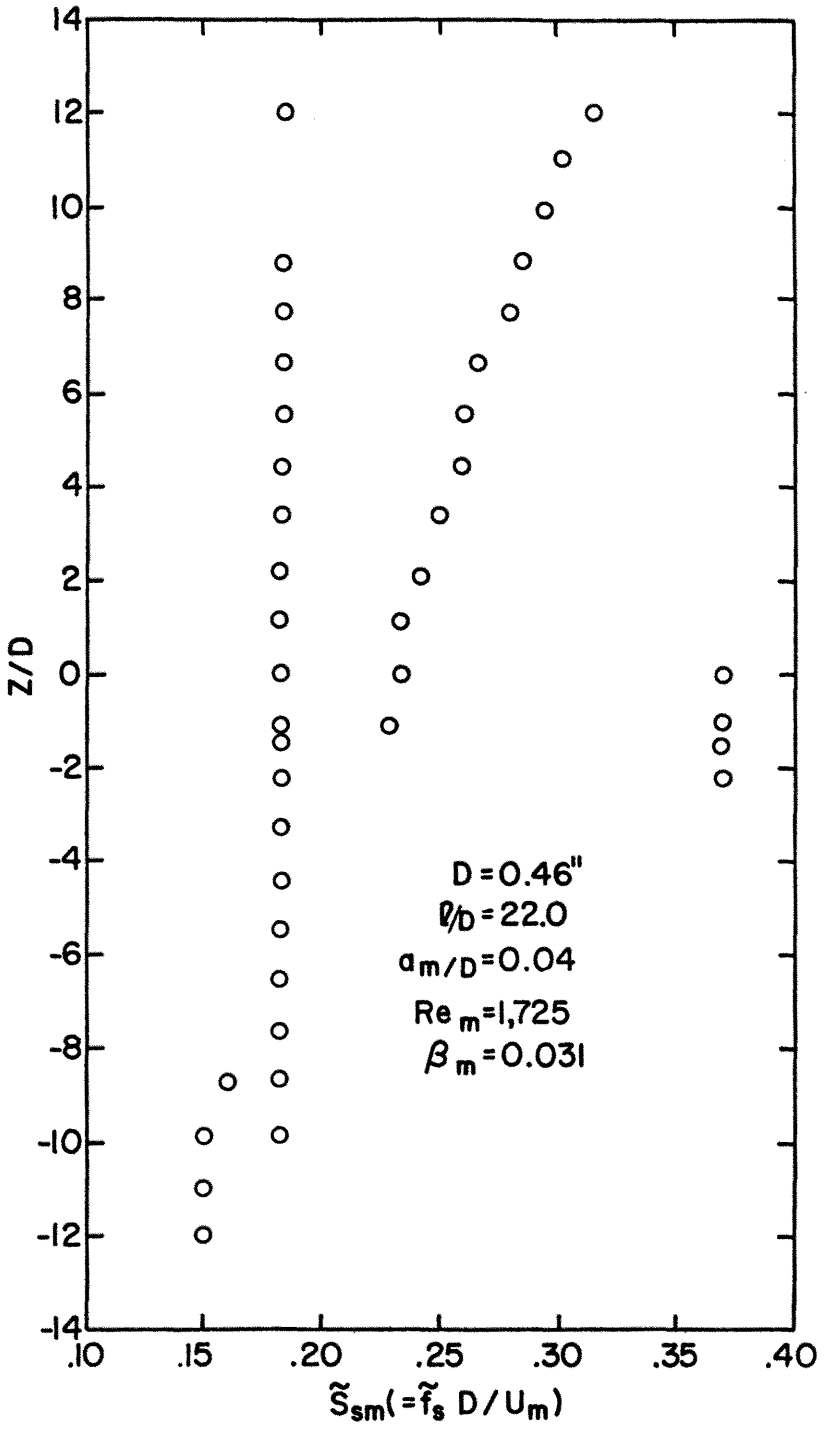

4.2.43 Spanwise Variation of S_{sm} for an Oscillating Cable with D = 0.46 in., Re_m = 1,725, β_m = 0.031, ℓ/D = 22.0, S_{cm} = 0.185, and a_m/D = 0.04

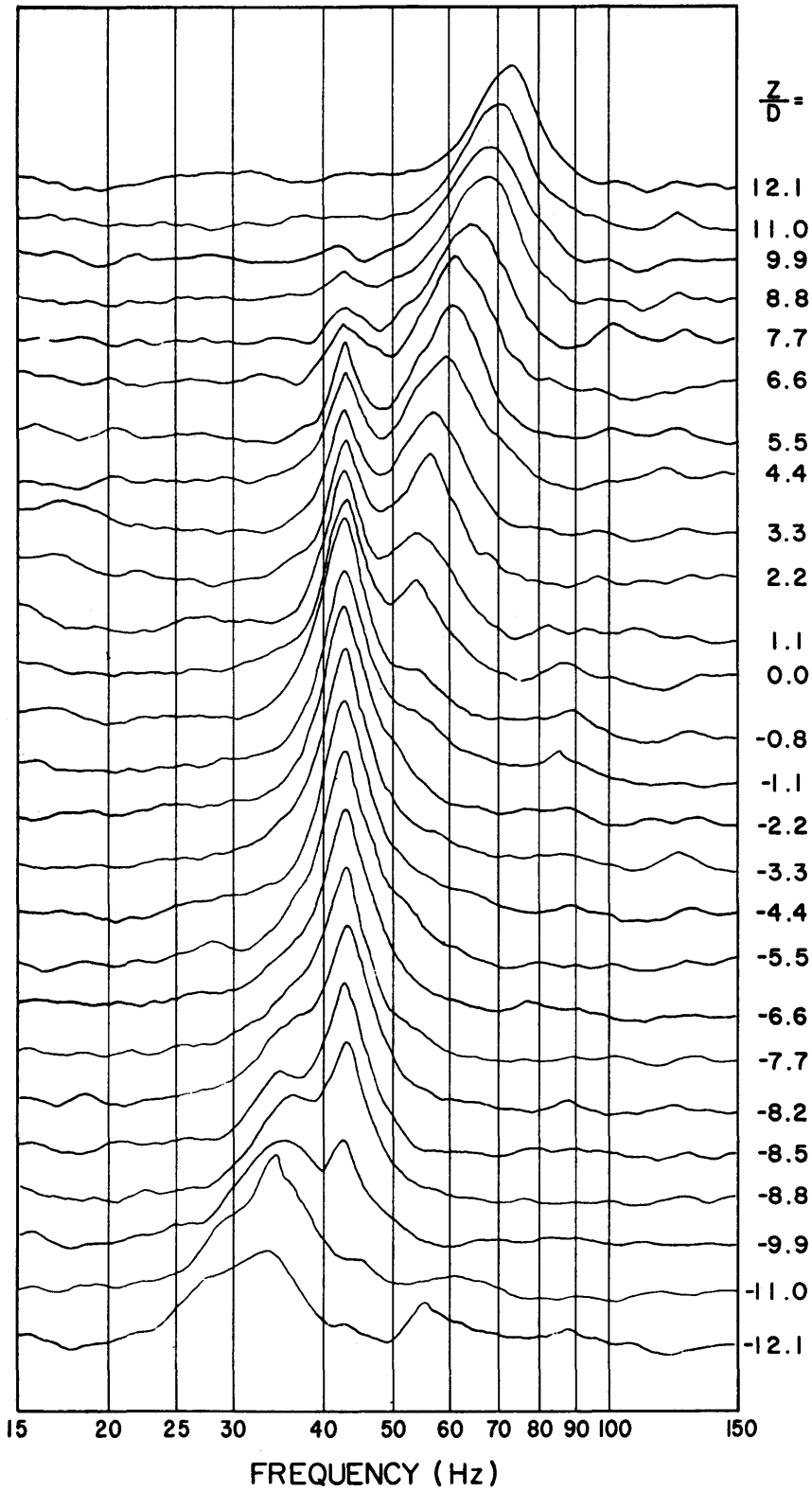

4.2.44 Frequency Spectra at Various Spanwise Positions for an Oscillating Cable with D = 0.46 in., Re_m = 1,725, β_m = 0.031, ℓ/D = 22.0, f_c = 43.0 Hz, and a_m/D = 0.02

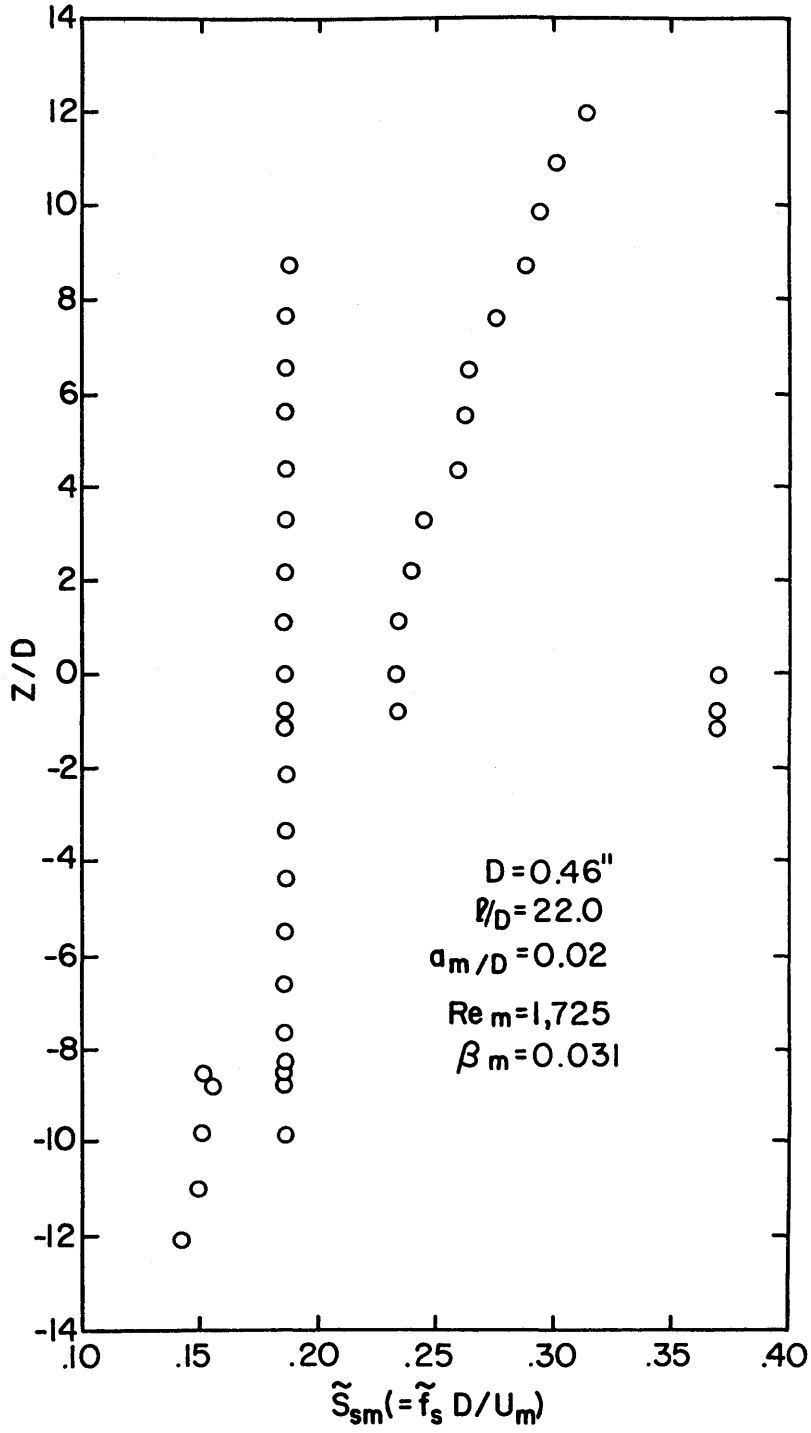

4.2.45 Spanwise Variation of S_{sm} for an Oscillating Cable with D = 0.46 in., Re_m = 1,725, β_m = 0.031, ℓ/D = 22.0, S_{cm} = 0.185, and a_m/D = 0.02

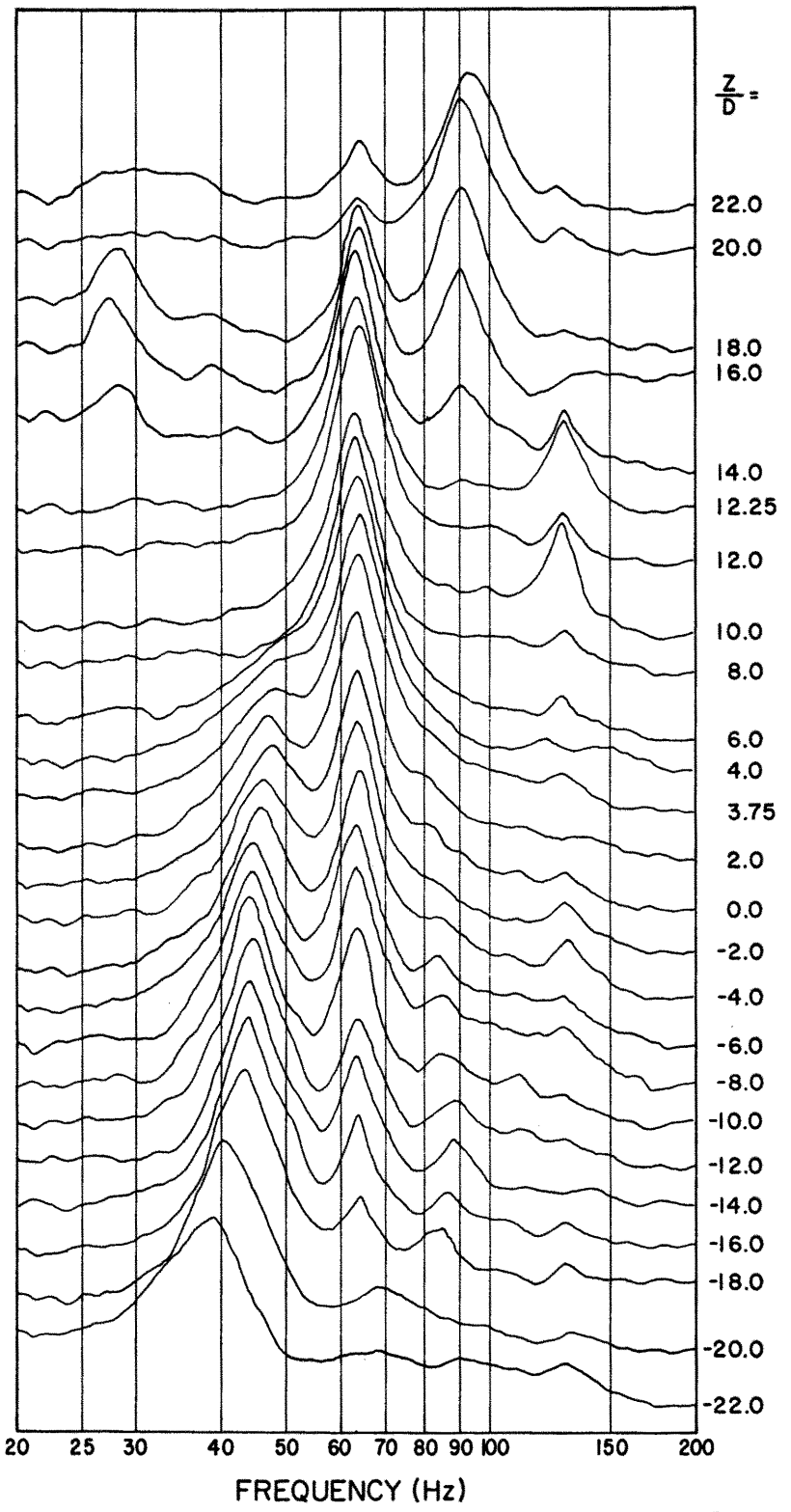

4.2.46 Frequency Spectra at Various Spanwise Positions for an Oscillating Cable with D = 0.25 in., Re_m = 660, β_m = 0.017, ℓ/D = 40.0, f_c = 63.5 Hz, and a_m/D = 0.66

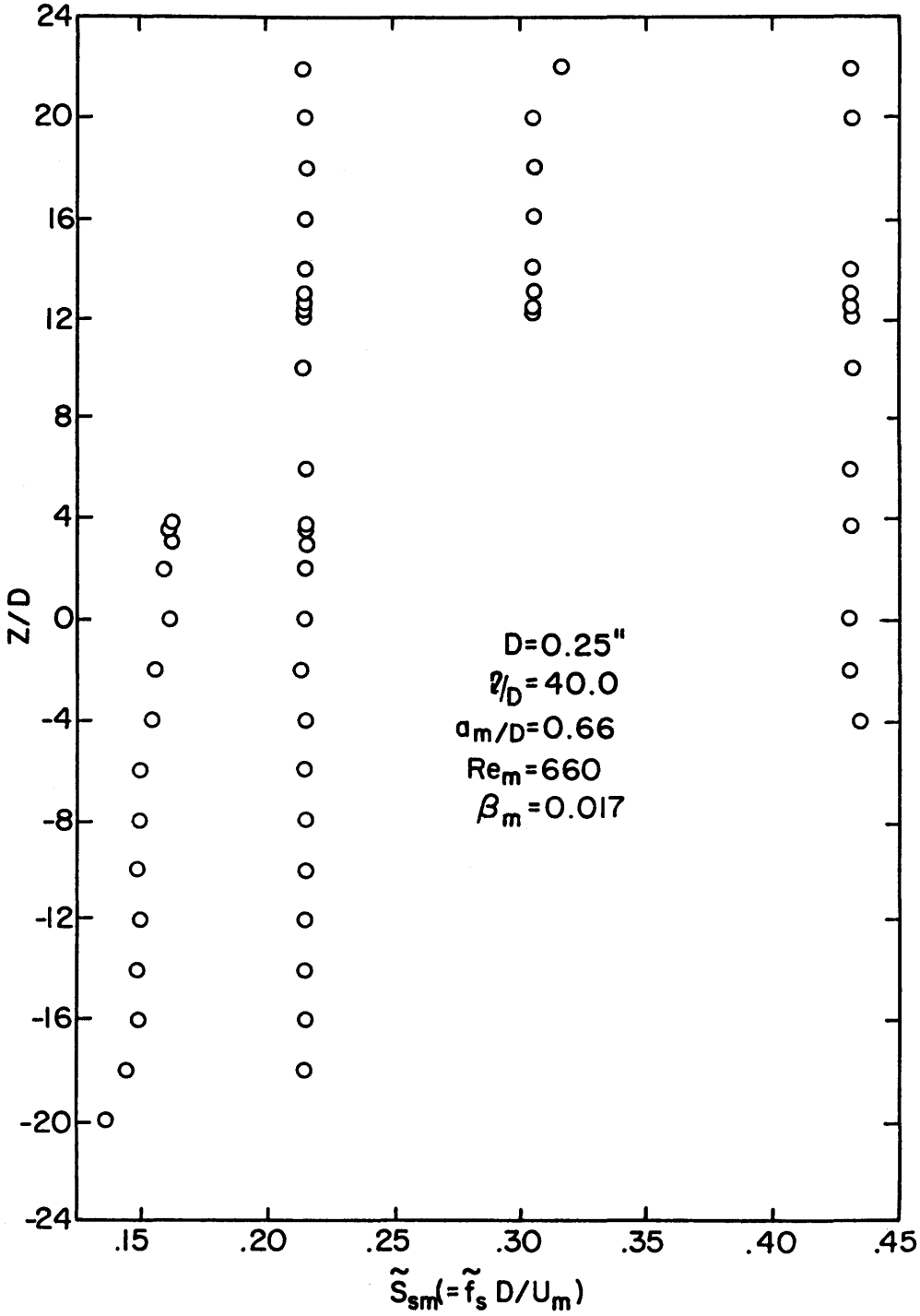

4.2.47 Spanwise Variation of S_{sm} for an Oscillating Cable with D = 0.25 in., Re_m = 660, β_m = 0.017, ℓ/D = 40.0, S_{cm} = 0.216, and a_m/D = 0.66

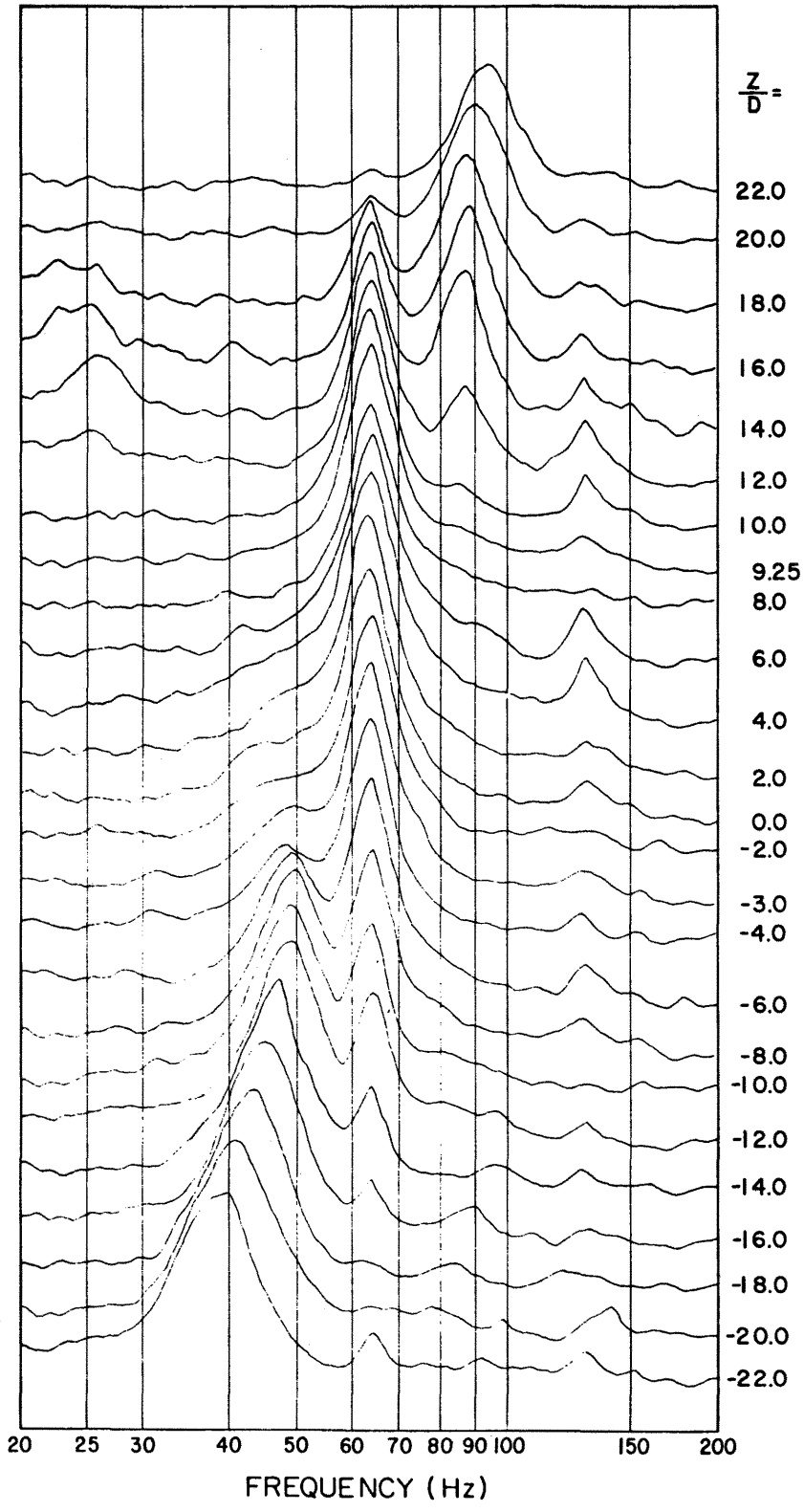

4.2.48 Frequency Spectra at Various Spanwise Positions for an Oscillating Cable with D = 0.25 in., Re_m = 660, β_m = 0.017, ℓ/D = 40.0, f_c = 63.5 Hz, and a_m/D = 0.30

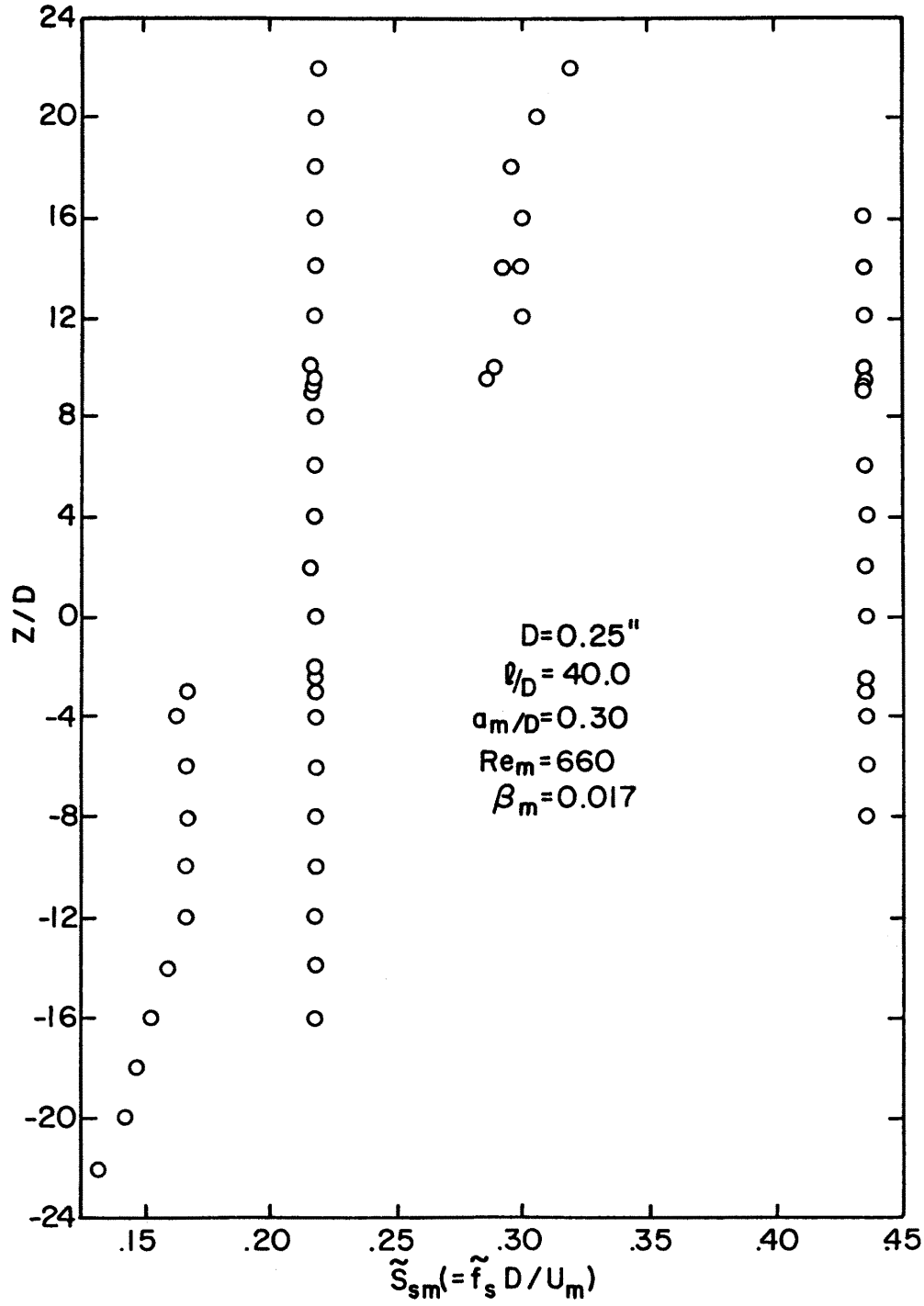

4.2.49 Spanwise Variation of S_{sm} for an Oscillating Cable with D = 0.25 in., Re_m = 660, β_m = 0.017, ℓ/D = 40.0, S_{cm} = 0.216, and a_m/D = 0.30

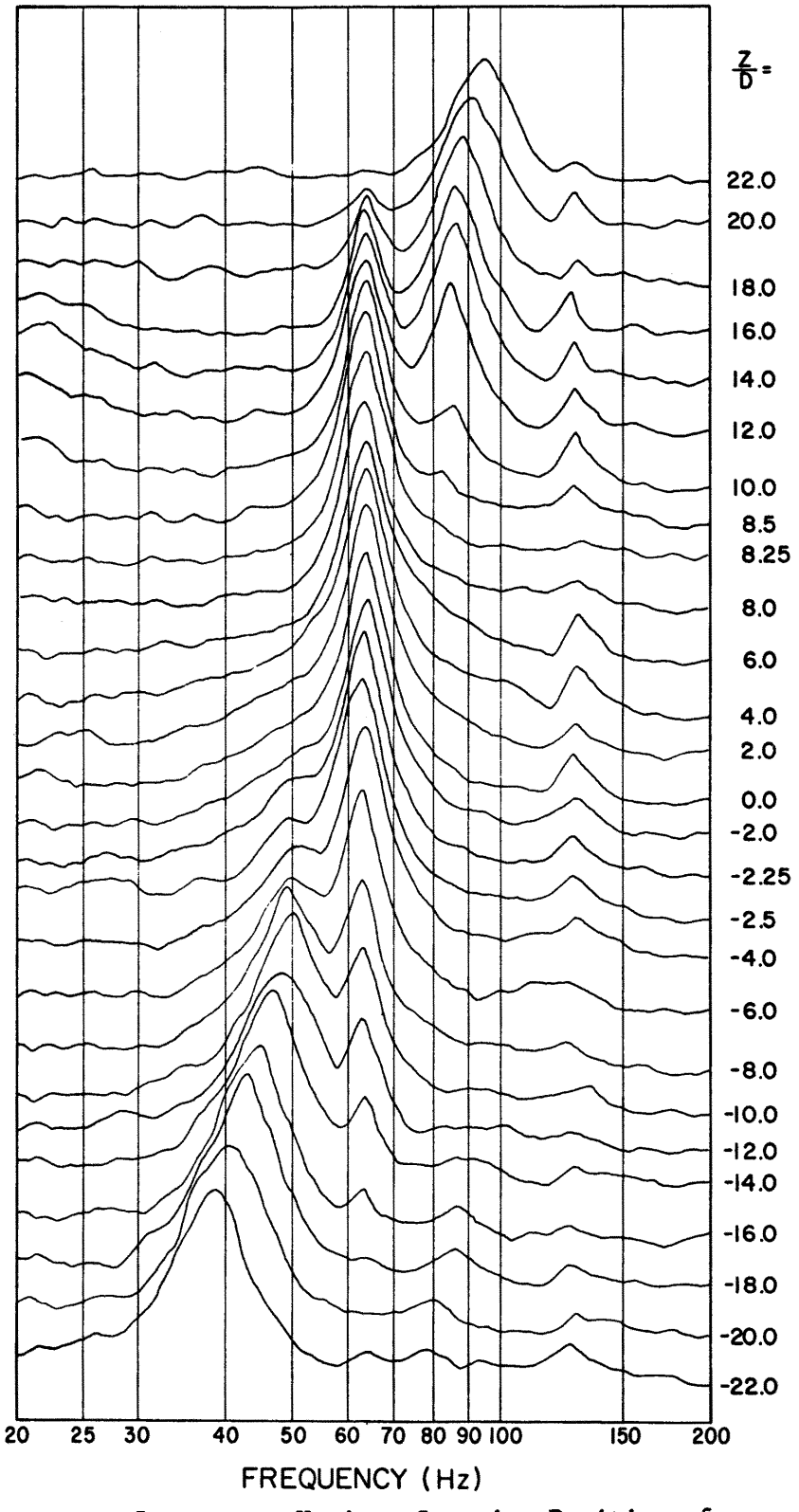

4.2.50 Frequency Spectra at Various Spanwise Positions for an Oscillating Cable with D = 0.25 in., Re_m = 660, β_m = 0.017, ℓ/D = 40.0, f_c = 63.5 Hz, and a_m/D = 0.18.

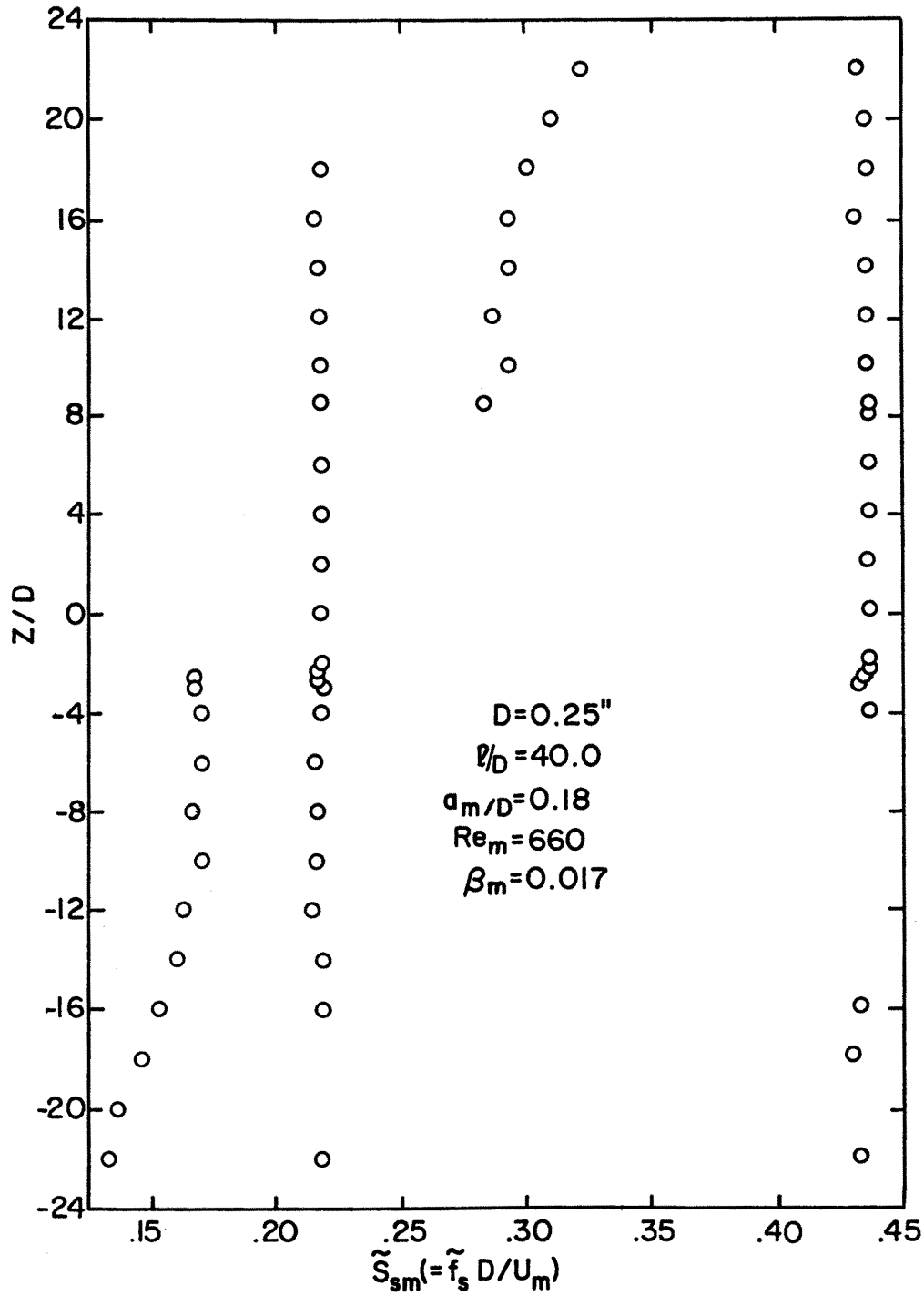

4.2.51 Spanwise Variation of S_{sm} for an Oscillating Cable with D = 0.25 in., Re_m = 660, β_m = 0.017, ℓ/D = 40.0, S_{cm} = 0.216, and a_m/D = 0.18

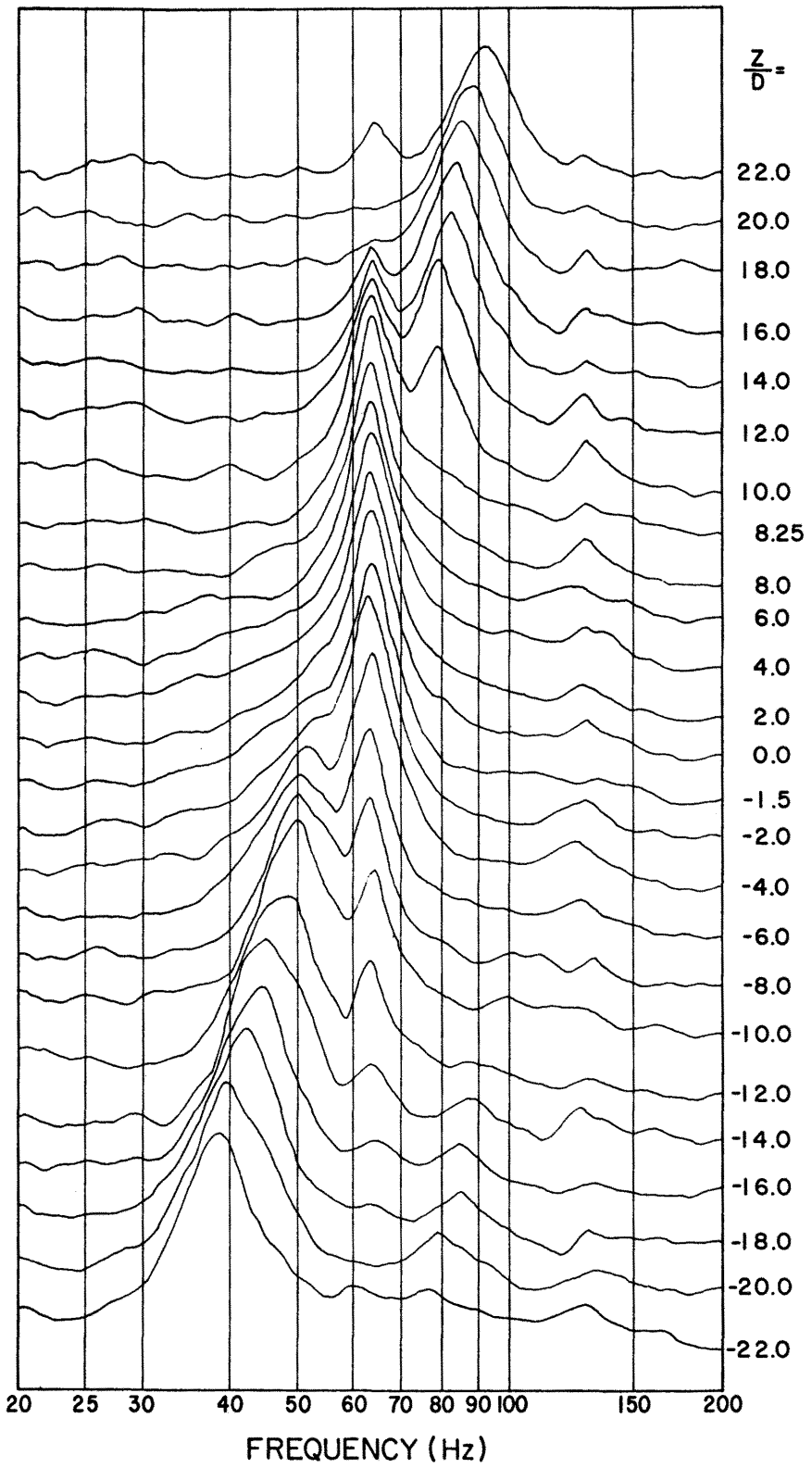

4.2.52 Frequency Spectra at Various Spanwise Positions for and Oscillating Cable with D = 0.25 in., Re_m = 660, β_m = 0.017, ℓ/D = 40.0, f_c = 63.5 Hz, and a_m/D = 0.13

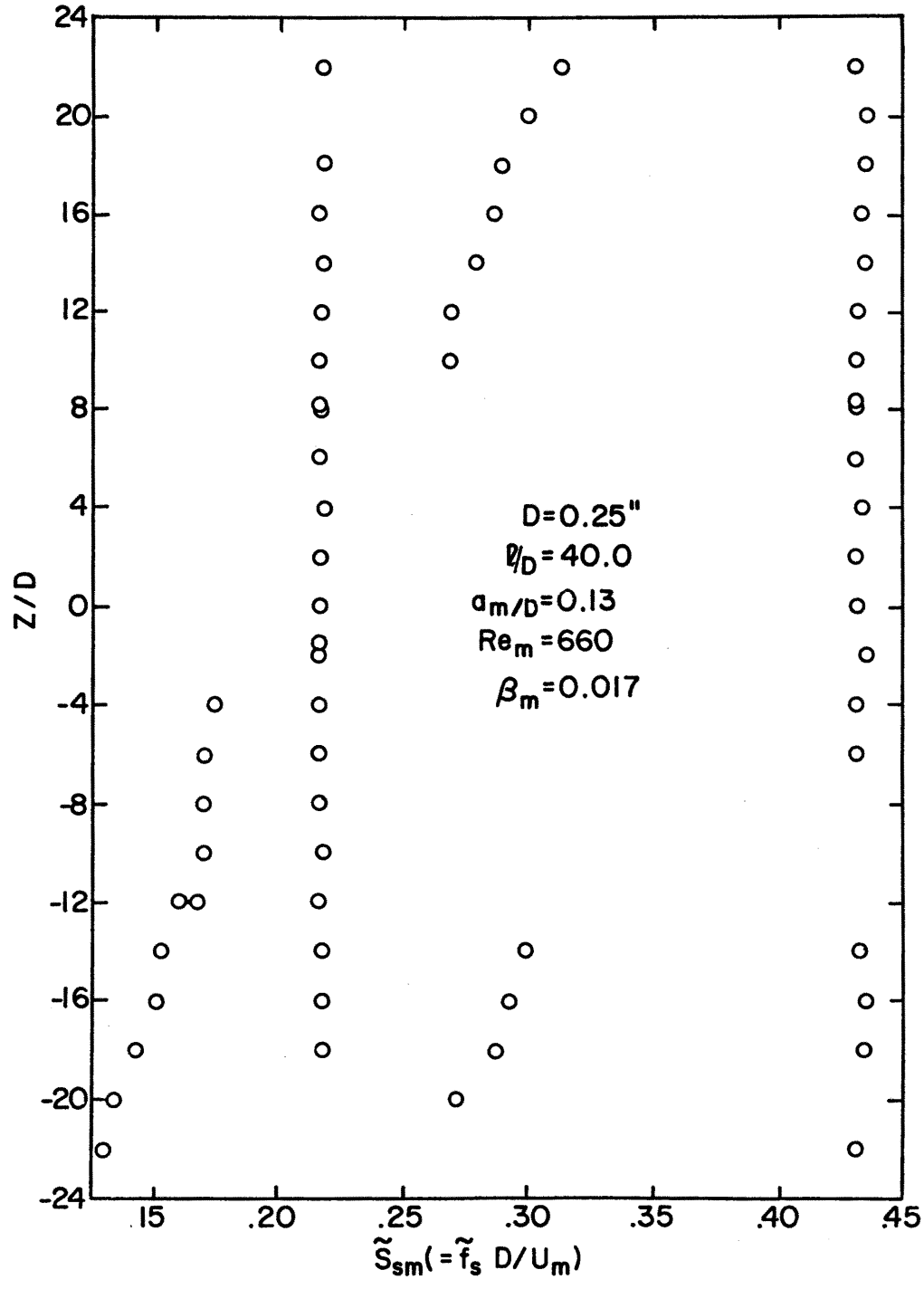

4.2.53 Spanwise Variation of S_{sm} for an Oscillating Cable with D = 0.25 in., Re_m = 660, β_m = 0.017, ℓ/D = 40.0, S_{cm} = 0.216, and a_m/D = 0.13

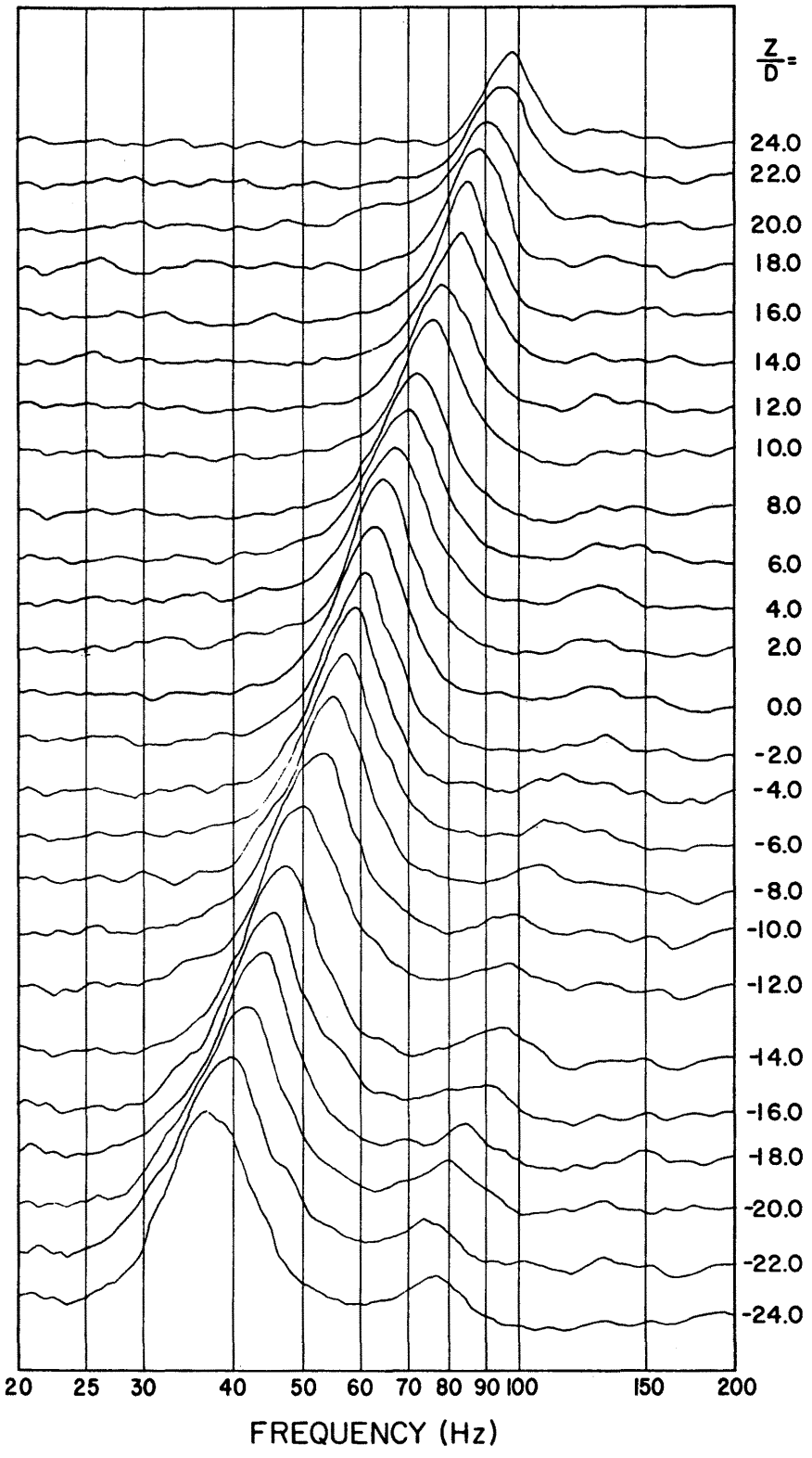

4.2.54 Frequency Spectra at Various Spanwise Positions for a Cable with D = 0.25 in., Re_m = 660, β_m = 0.017, f_c = 0.0 Hz, and a_m/D = 0.0

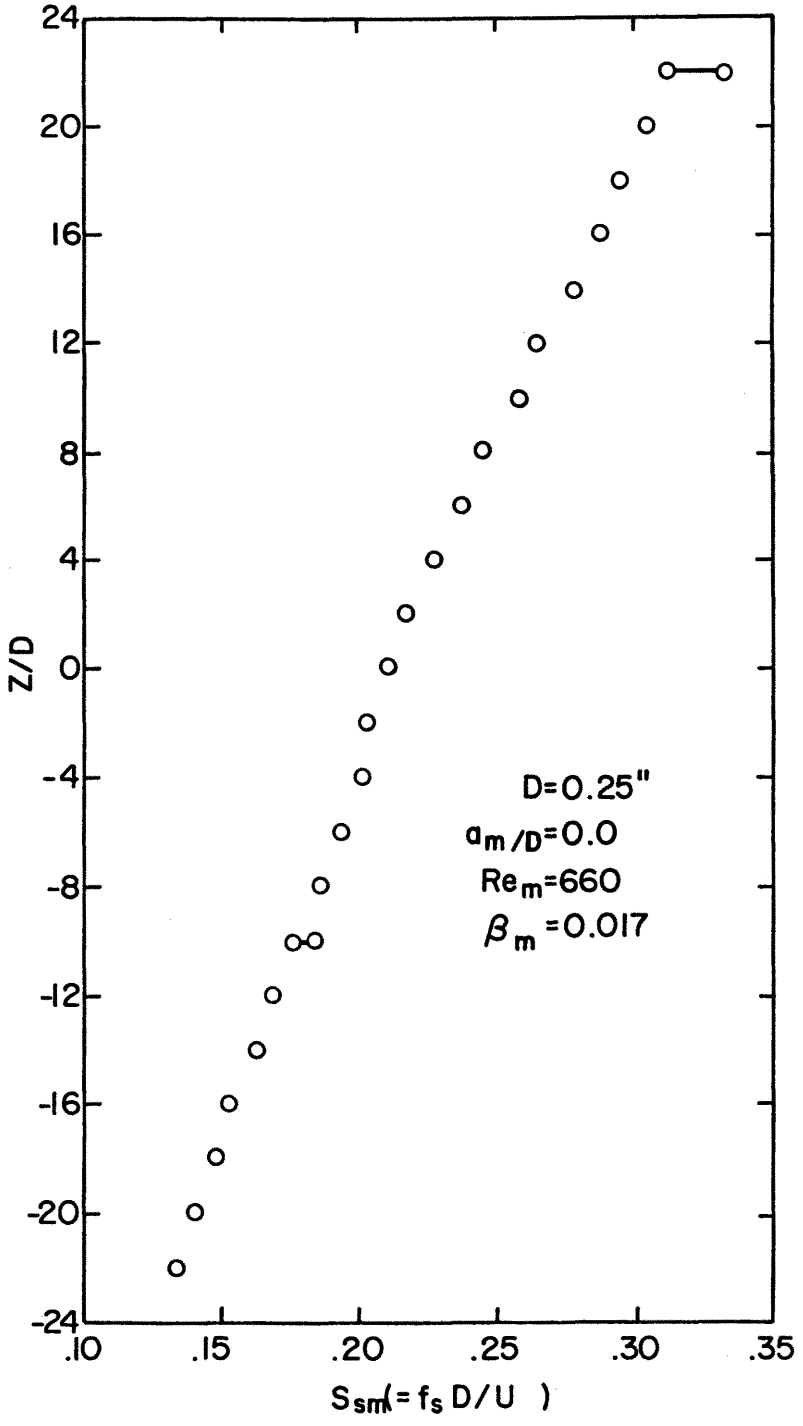

4.2.55 Spanwise Variation of S_{sm} for a Cable with D = 0.25 in., Re_m = 660, β_m = 0.017, S_{cm} = 0.0 and a_m/D = 0.0

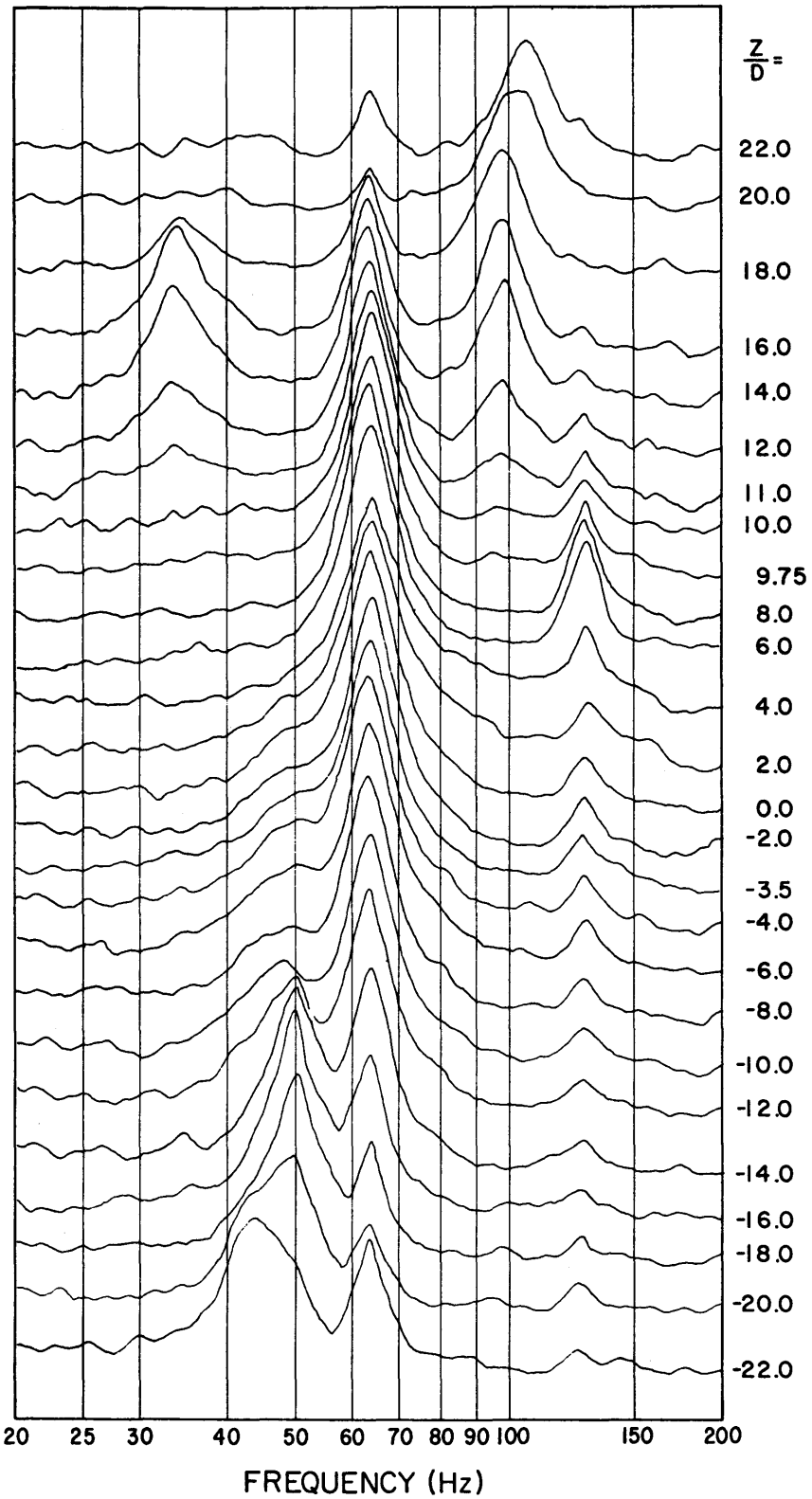

4.2.56 Frequency Spectra at Various Spanwise Positions for an Oscillating Cable with D = 0.25 in., Re_m = 735, β_m = 0.016, ℓ/D = 40.0, f_c = 63.5 Hz, and a_m/D = 0.63

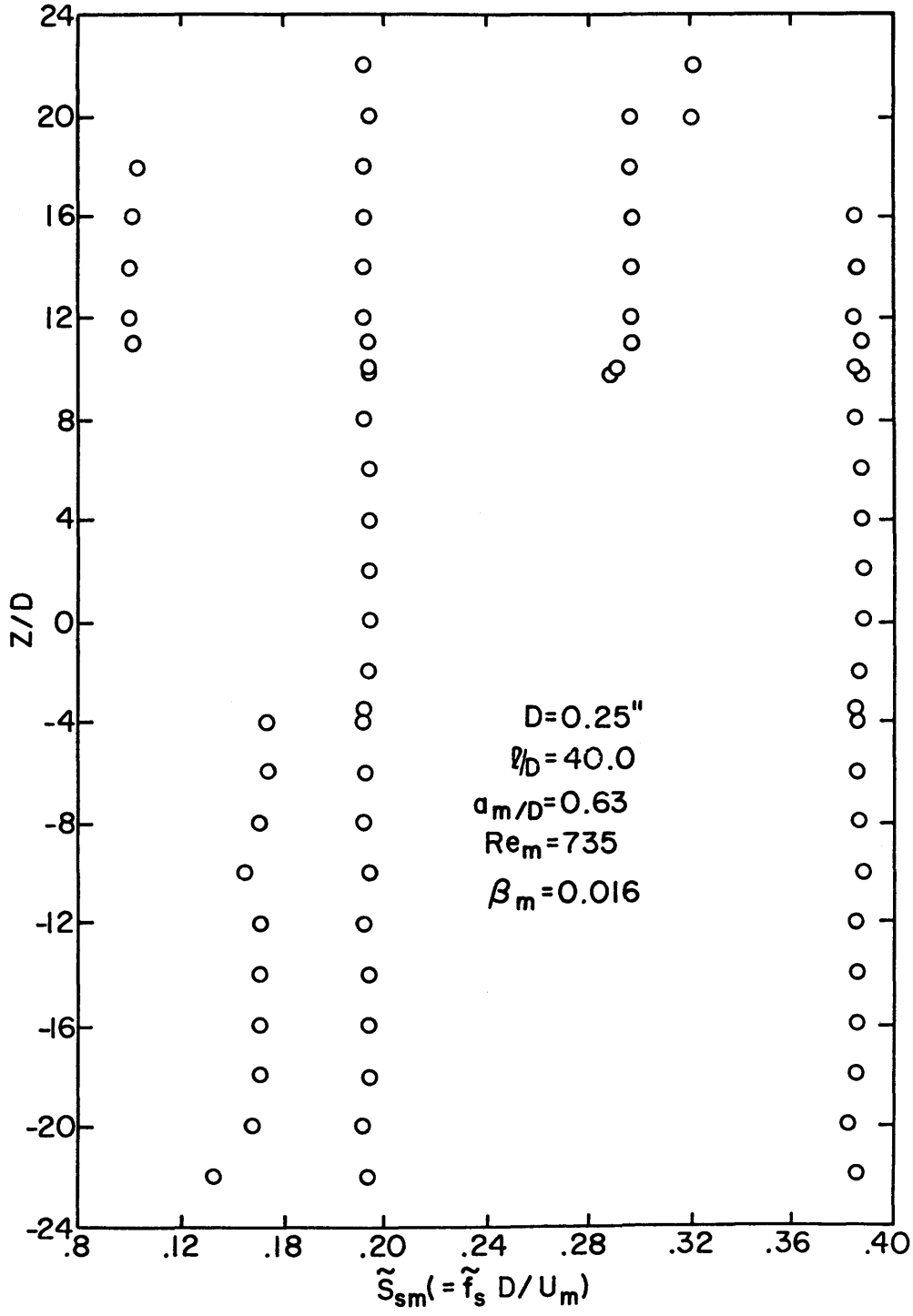

4.2.57 Spanwise Variation of S_{sm} for an Oscillating Cable with D = 0.25 in., Re_m = 735, β_m = 0.016, ℓ/D = 40.0, S_{cm} = 0.192, and a_m/D = 0.63

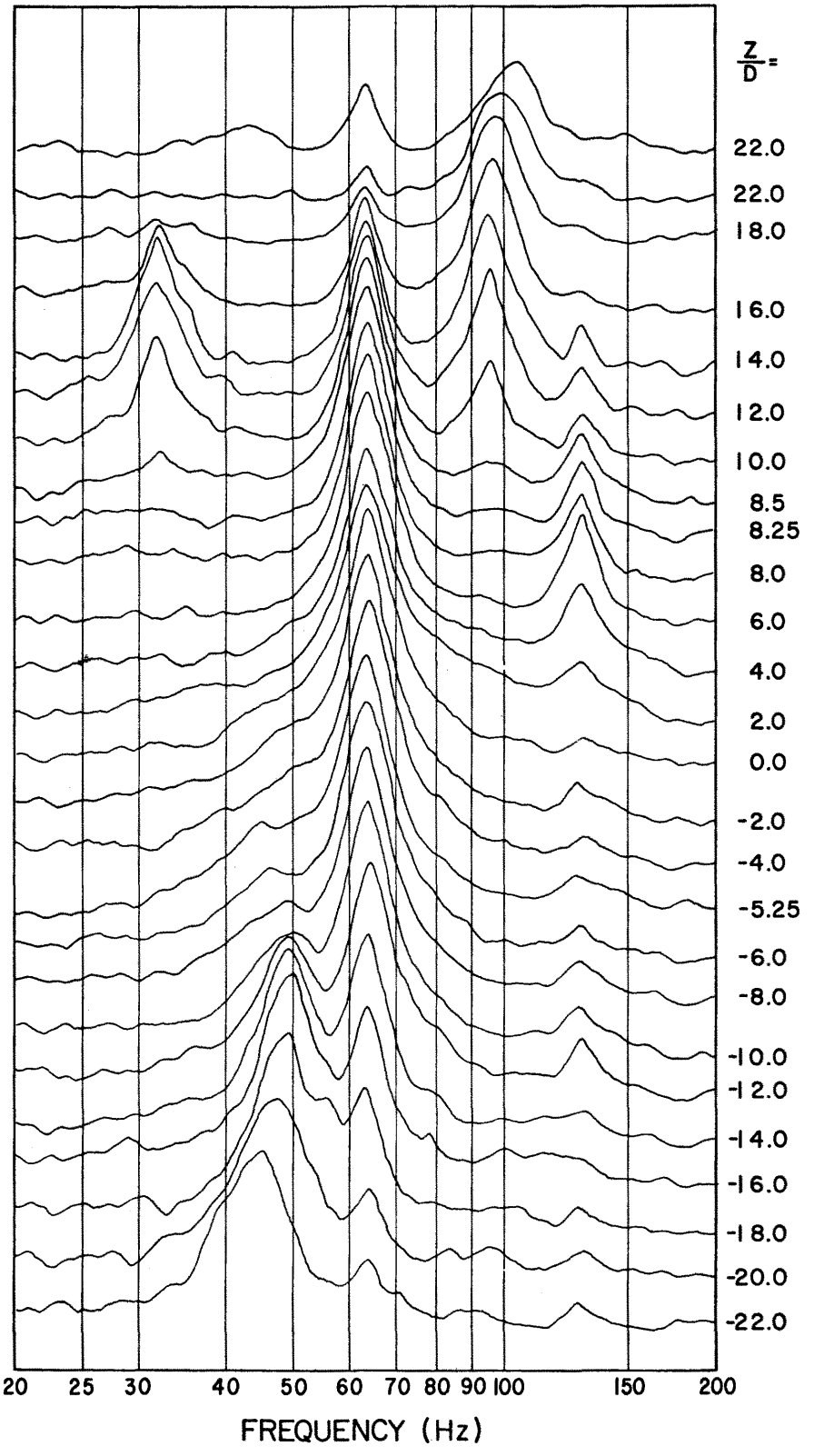

4.2.58 Frequency Spectra at Various Spanwise Positions for an Oscillating Cable with D = 0.25 in., Re_m = 735, β_m = 0.016, ℓ/D = 40.0, f_c = 63.5 Hz, and a_m/D = 0.47

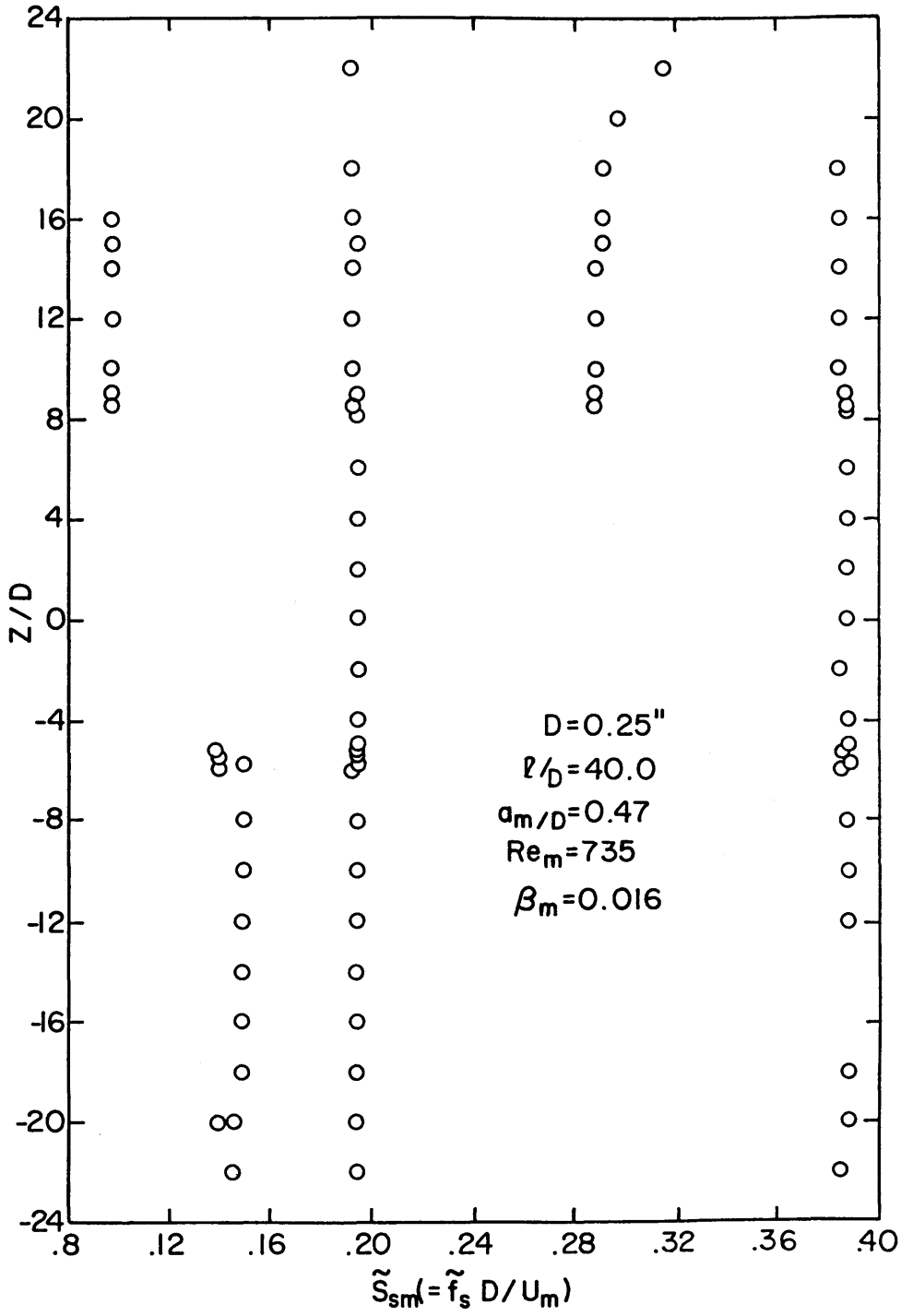

4.2.59 Spanwise Variation of S_{sm} for an Oscillating Cable with D = 0.25 in., Re_m = 735, β_m = 0.016, ℓ/D = 40.0, S_{cm} = 0.192, and a_m/D = 0.47

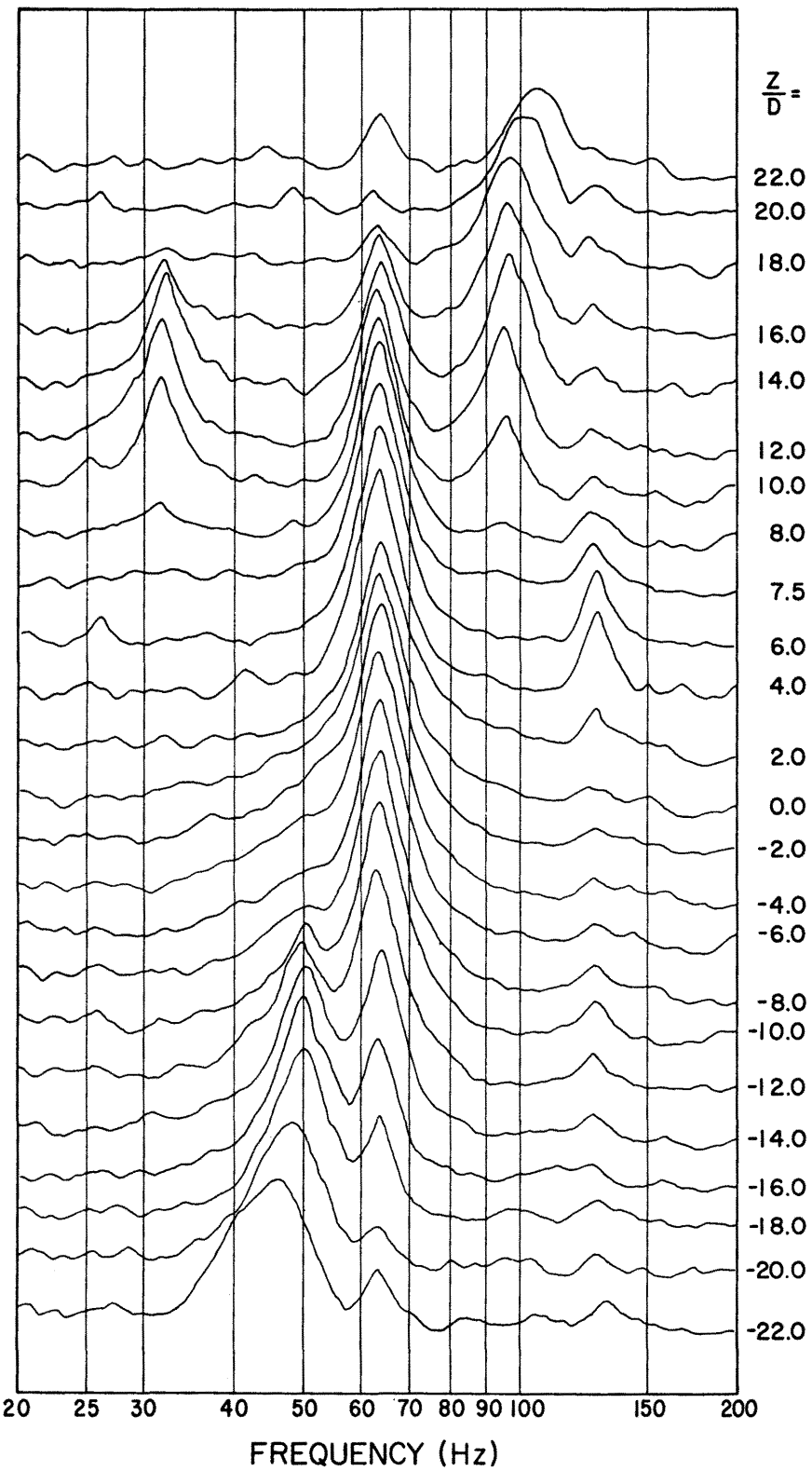

4.2.60 Frequency Spectra at Various Spanwise Positions for an Oscillating Cable with D = 0.25 in., Re_m = 735, β_m = 0.016, ℓ/D = 40.0, f_c = 63.5 Hz, and a_m/D = 0.37

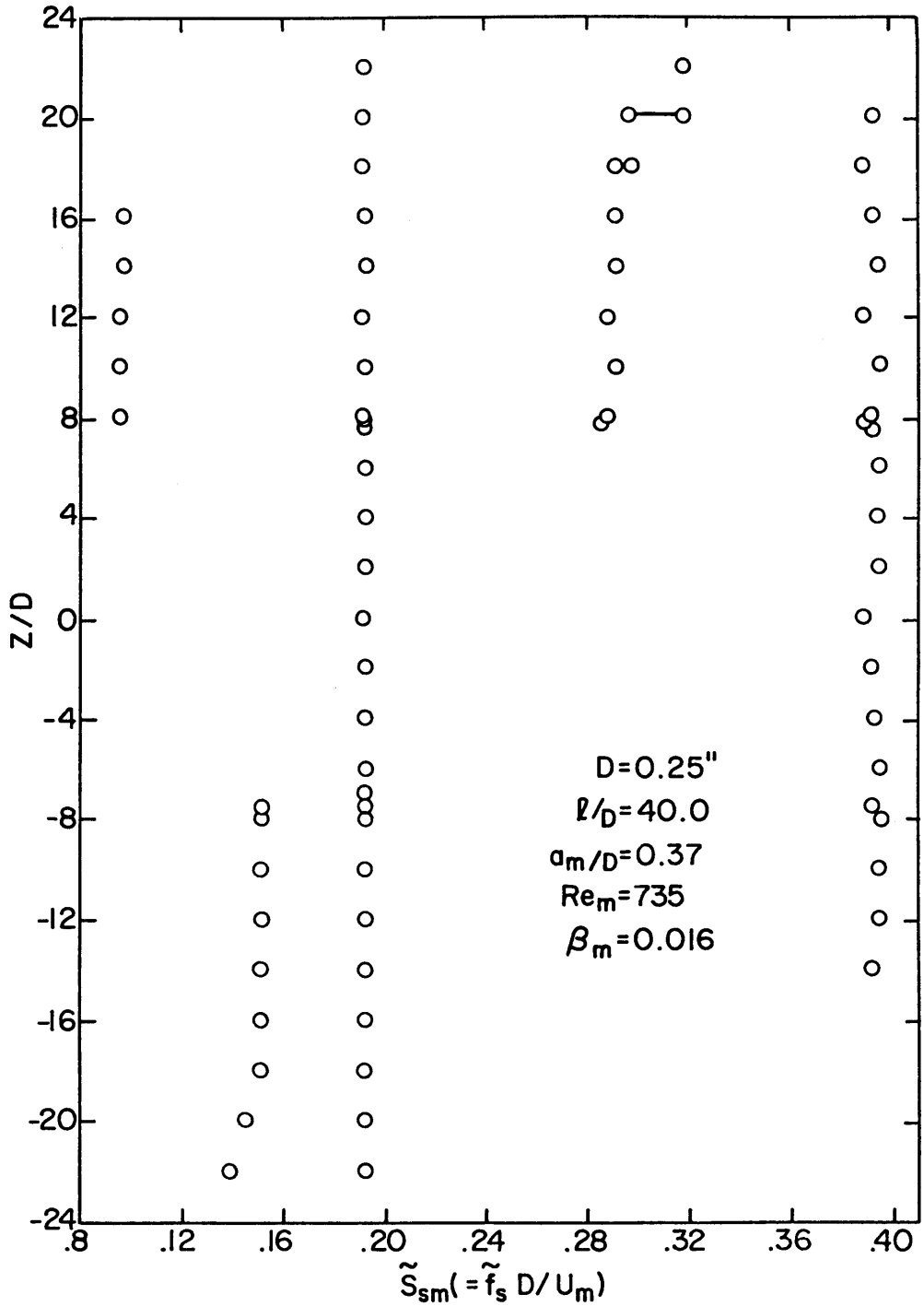

4.2.61 Spanwise Variation of S_{sm} for an Oscillating Cable with D = 0.25 in., Re_m = 735, β_m = 0.016, ℓ/D = 40.0, S_{cm} = 0.192, and a_m/D = 0.37

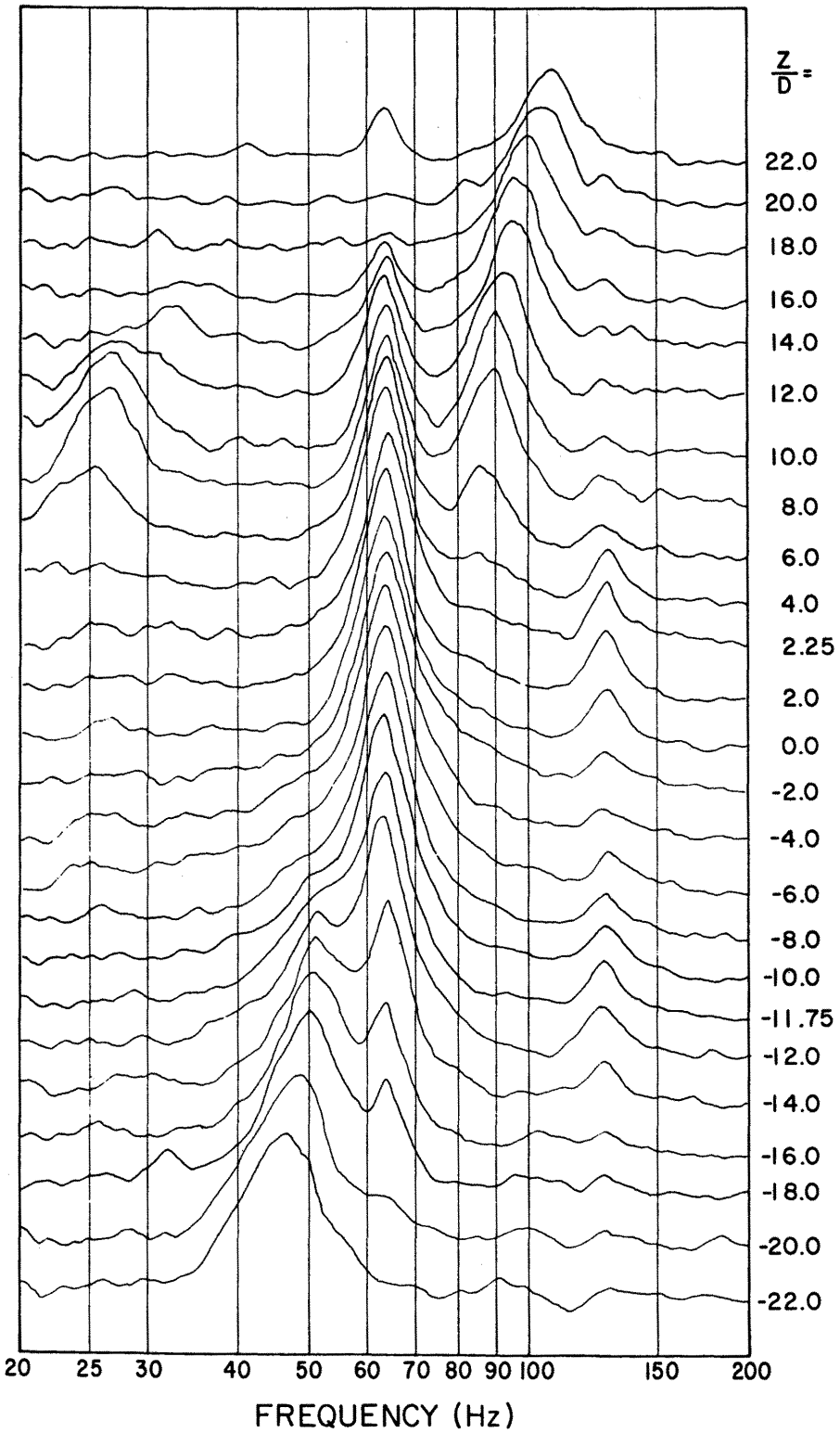

4.2.62 Frequency Spectra at Various Spanwise Positions for an Oscillating Cable with D = 0.25 in., Re_m = 735, β_m = 0.016, ℓ/D = 40.0, f_c = 63.5 Hz, and a_m/D = 0.23

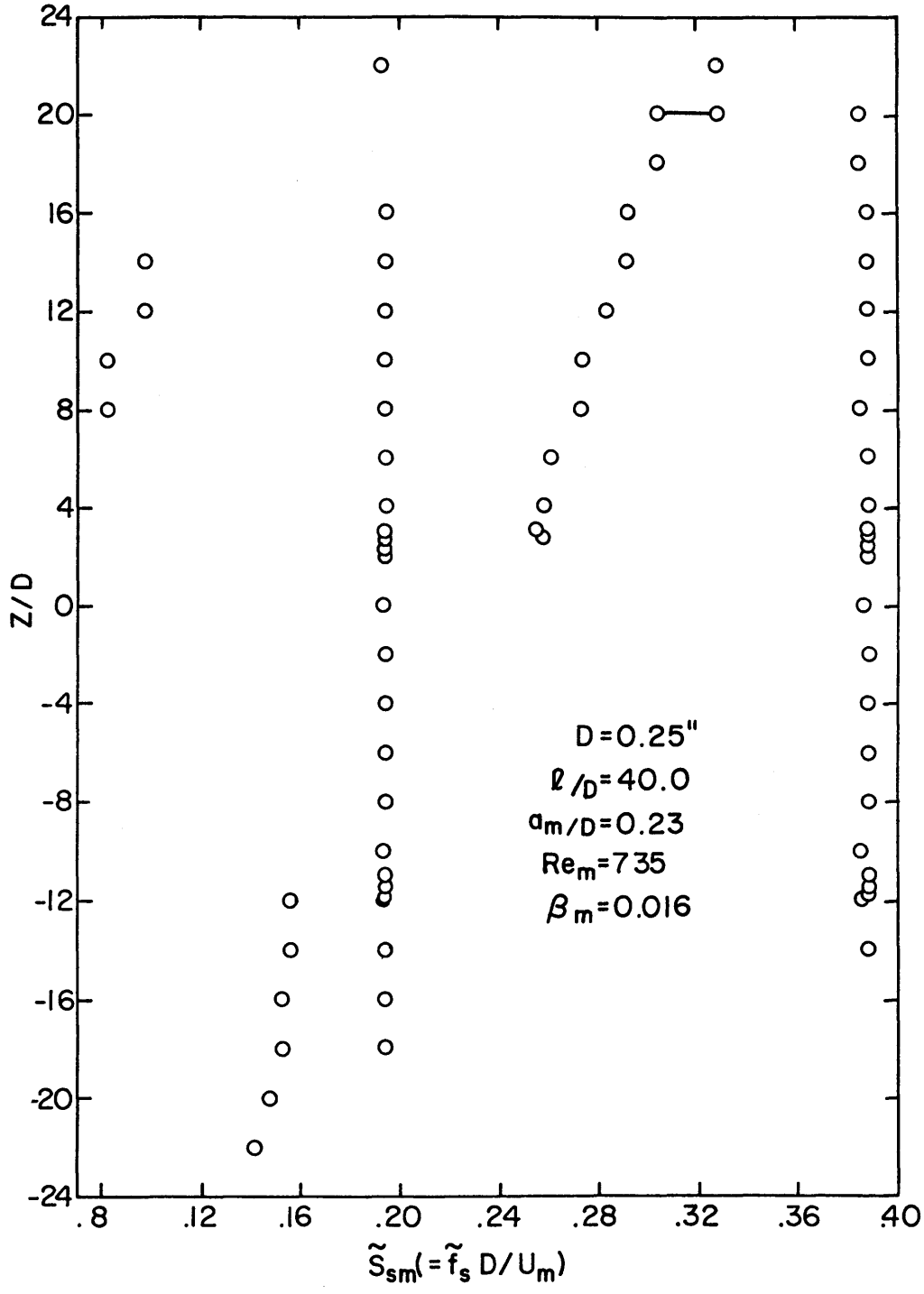

4.2.63 Spanwise Variation of S_{sm} for an Oscillating Cable with D = 0.25 in., Re_m = 735, β_m = 0.016, ℓ/D = 40.0, S_{cm} = 0.192, and a_m/D = 0.23

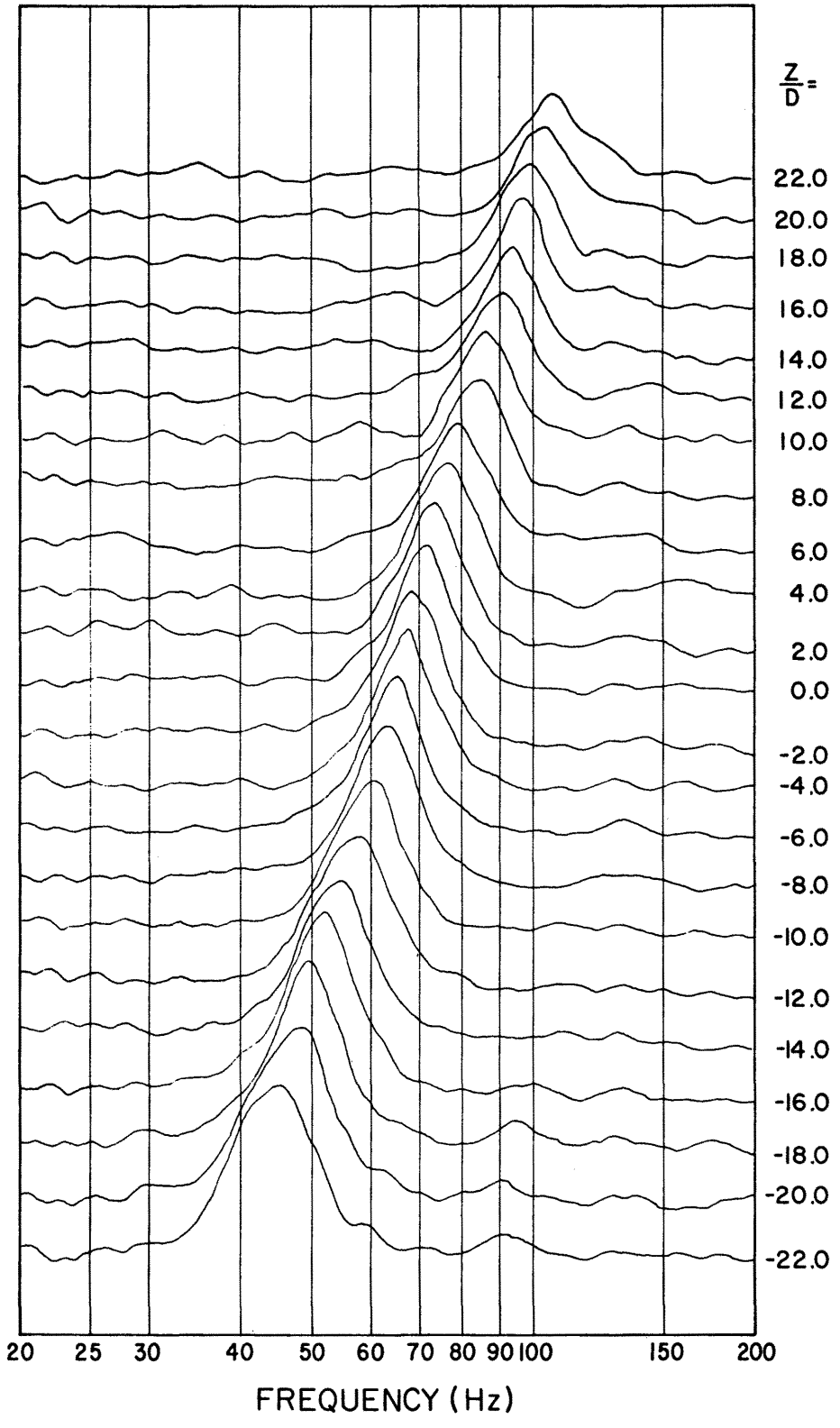

4.2.64 Frequency Spectra at Various Spanwise Positions for a Cable with D = 0.25 in., Re_m = 735, β_m = 0.016, f_c = 0.0 Hz, and a_m/D = 0.0

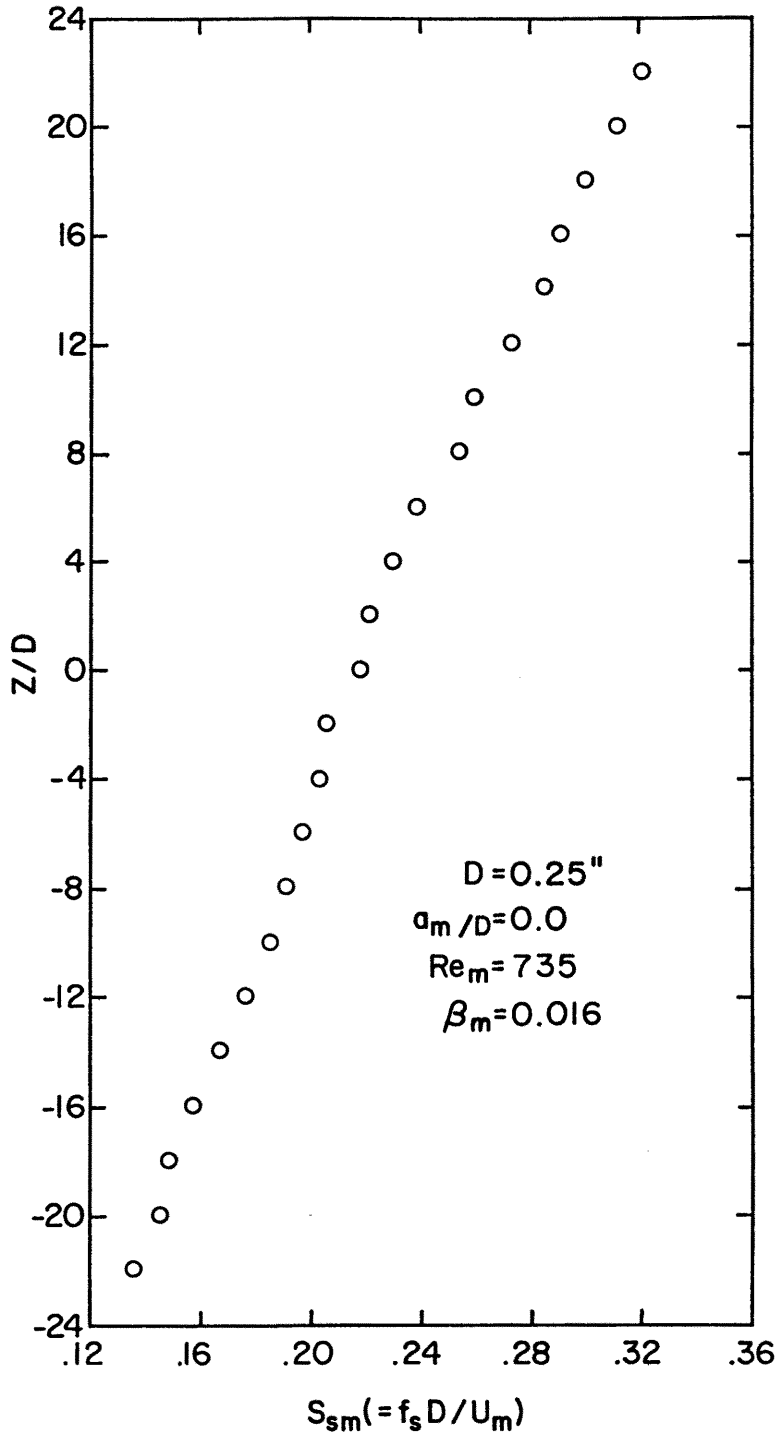

4.2.65 Spanwise Variation of S_{sm} for a Cable with D = 0.25 in., Re_m = 735, β_m = 0.016, S_{cm} = 0.0 and a_m/D = 0.0

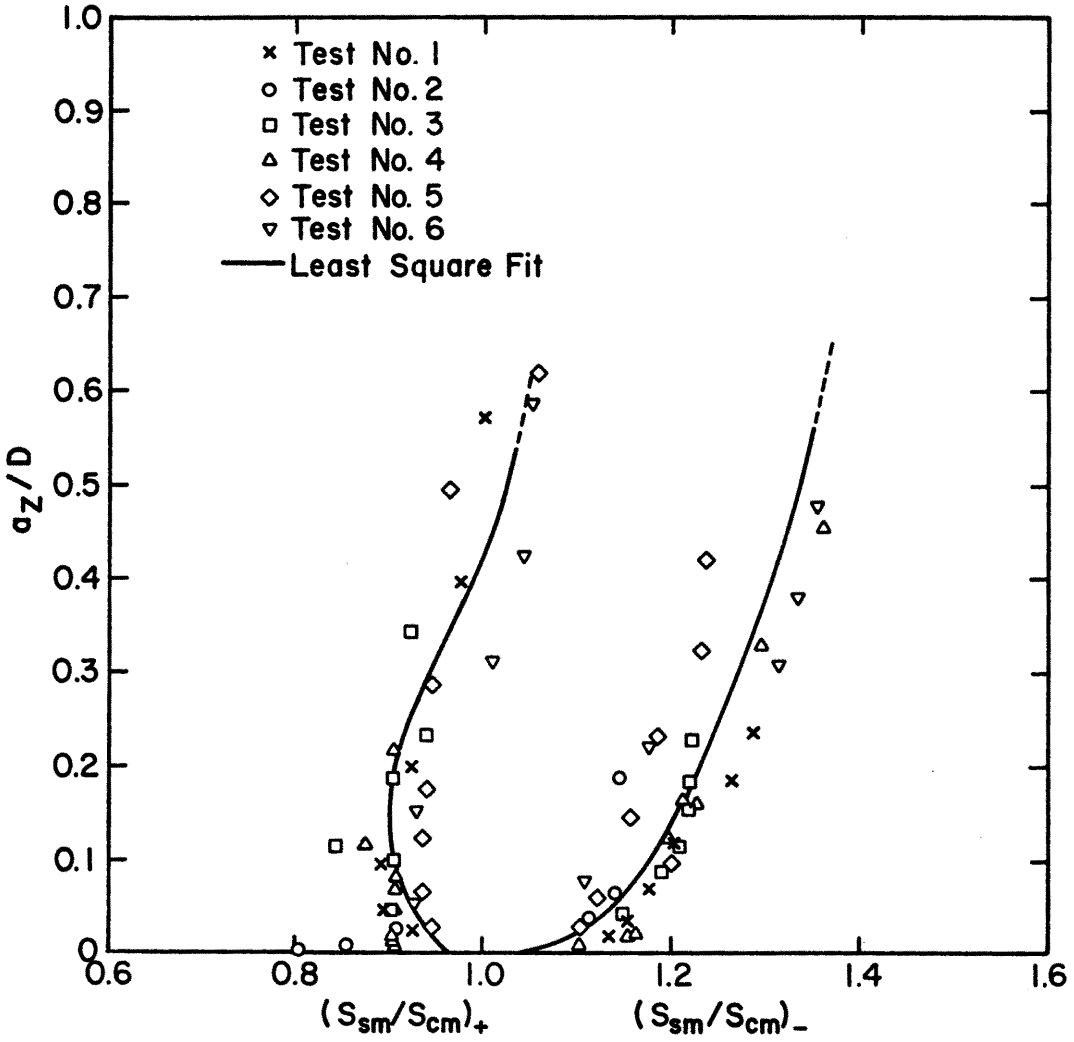

4.2.66 The Ratio of S_{sm}/S_{cm} in the Boundary Zones of Primary Locking-On in Shear Flows for Different a_z/D

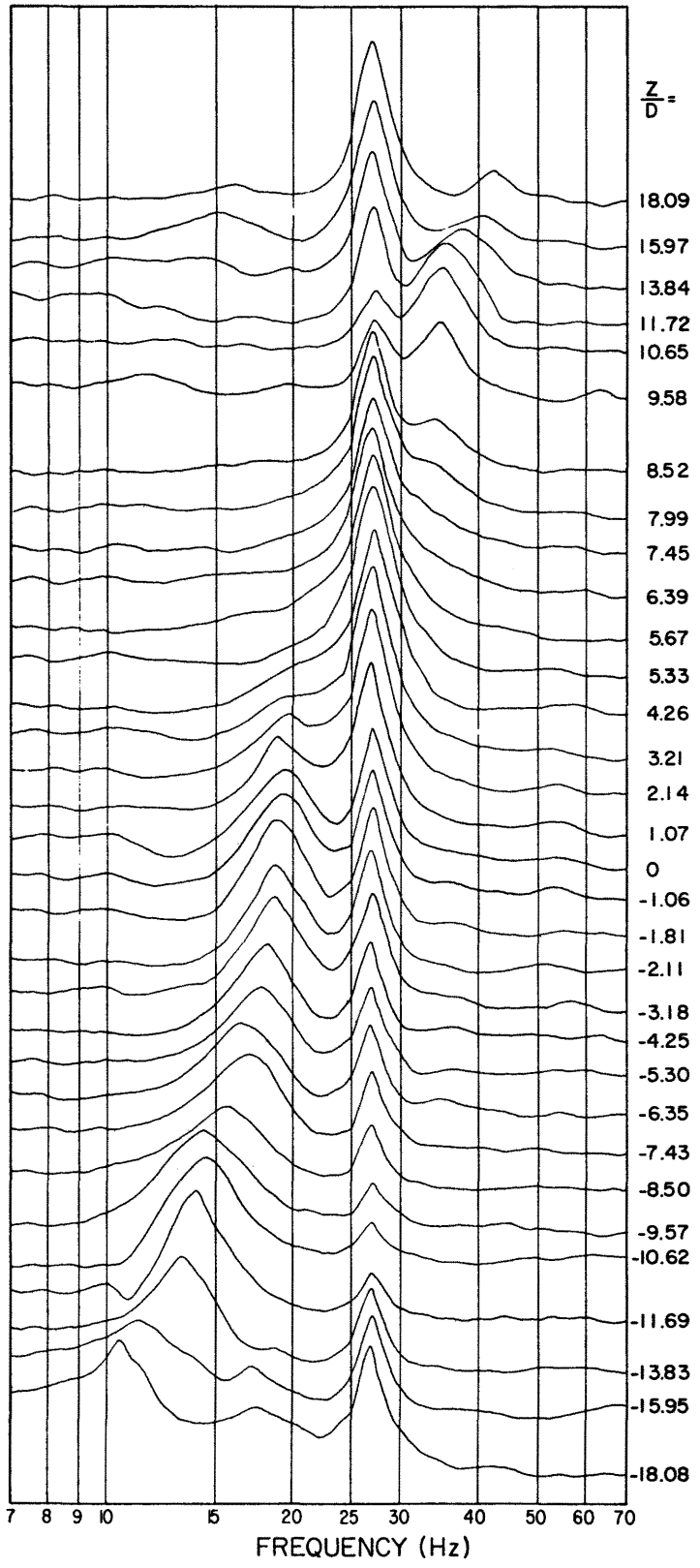

4.2.67 Frequency Spectra at Various Spanwise Positions for an Oscillating Cable with D = 0.48 in., Re_m = 960, β_m = .034, ℓ/D = 21.3, f_c = 27.0 and a_m/D = 0.45 (for Flow Visualization Study)